eman ta zabal zazu
Euskal Herriko Unibertsitatea
Universidad del País Vasco

EUSKAL HERRIKO UNIBERTSITATEA / UNIVERSIDAD DEL PAÍS VASCO

Facultad de Ciencia y Tecnología

Departamento de Química Inorgánica

Advanced anode materials for sodium ion batteries: $H_2Ti_3O_7$ and T^MNCN (T^M =Mn^{2+}, Fe^{2+}, Co^{2+}, Ni^{2+}, $Cu^{2+}$and Zn^{2+}) carbodiimides

A dissertation submitted to the University of the Basque Country in partial fulfillments of the requirements for the degree of Ph.D.

By

Mr. Aitor Eguía Barrio

Thesis Advisors:

Dr. Elisabet Castillo Martínez

Prof. Teófilo Rojo Aparicio

2016

Table of contents

Abstract

The current energy consumption system is strongly dependent on fossil fuels. The contaminant emissions and the future depletion of these non-renewable sources are the main drawbacks. These facts make necessary a gradually change towards to renewable energy sources that can cover the demand of energy. The use of stationary energy storage systems will help enhance the flexibility, minimize power fluctuations and ease the integration of renewable power generation, which is intrinsically variable, into a stable and controlled grid. Already there are pilot stationary energy storage systems in the MWh range that have been deployed in several places worldwide, based on Li-ion technology. However, the need to look for cheaper and safer high energy density electrochemical devices able to sustain the large scale storage of renewable energy sources is moving the focus of research from the lighter lithium ion into the cheaper and more abundant sodium ion based systems. The main handicap of this technology is that Na^+ does not insert into graphite and hard carbon is plagued by slow diffusion and an end-of-charge potential very close to the plating of Na° with risk of dendrites. Therefore, there is a need of finding new anode materials for sodium ion batteries.

In this work, two families of materials were investigated in order to solve the lack in the anode materials for sodium ion batteries: titanates and transition-metal carbodiimides. Titanates have layers big enough where sodium ions can diffuse easily while the presence of the $(N=C=N)^{2-}$ bond creates channels for the sodium ions insertion in transition-metal carbodiimide.

The transference of the good electrochemical behaviour of $H_2Ti_3O_7$ observed in lithium to sodium ion batteries was the aim of the study. The material was synthesized using $Na_2Ti_3O_7$ as precursor and characterized as pure phase confirmed by X-Ray Diffraction (XRD). The morphology and thermal stability were studied by scanning electron microscopy (SEM) and thermogravimetric analysis (TGA), respectively. The reported structure for this phase did not include the atomic positions of the protons. Therefore, the employment of complementary techniques such as Neutron Diffraction, solid state Nuclear Magnetic Resonance and Infrared (FTIR) was required with the objective of finding the locations of the protons. The electrochemical properties were tested for sodium ion batteries. The

kinetics and the mechanism of the electrochemical reaction were characterized by galvanostatic intermittent titration technique (GITT) and in-situ XRD, respectively.

Different synthesis methods were carried out. Synthesis in organic media and solid state route were carried out for MnNCN, while Schlenk techniques were used for FeNCN, CoNCN and NiNCN as well as $Co_{1-x}Fe_xNCN$ solid solution samples. Synthesis in aqueous media was performed for CuNCN and ZnNCN. All transition-metal carbodiimides were synthesized as pure phase confirmed by XRD. The morphology and the identification of NCN bond were analysed by SEM and FTIR, respectively. The electrochemical performance of these materials was carried out for sodium and lithium ion batteries. The mechanism and irreversibility of the electrochemical process; and the study of the SEI layer formation in sodium ion batteries were studied for CuNCN. A thermodynamic discussion of the family of transition-metal carbodiimides was performed in order to compare the theoretical and experimental results.

Finally, a selected compound of each family was tested in a sodium ion full cell using a layered oxide as cathode material in order to evaluate the possible application of these phases for a future prototype.

Resumen

La tesis doctoral resumida en esta memoria se ha realizado en la Universidad del País Vasco (UPV/EHU) en el Departamento de Química Inorgánica del Campus de Bizkaia. Sin embargo, el análisis de estudios concretos detallados en el manuscrito ha requerido el uso de diferentes instituciones.

La realización de este trabajo se ha desarrollado bajo la supervisión de la Dra. Elisabeth Castillo Martínez y el Prof. Teófilo Rojo Aparicio.

Este trabajo ha consistido en el desarrollo de los materiales para ser utilizados como ánodos para baterías de ion sodio. Para ello, diferentes familias de materiales inorgánicos se han estudiado.

Capítulo 1. Introducción

En la introducción se describe de manera resumida la fuerte dependencia de los combustibles fósiles en el actual sistema energético. La producción de desechos contaminantes y la limitada abundancia de estas fuentes de energía provocan una necesidad de la utilización de fuentes de energía renovables. El desarrollo de sistemas de almacenamiento de energía permite paliar la diferencia entre el periodo generación y le momento de la demanda. A pesar de que el sistema de almacenamiento de energía mayoritario es la hidroeléctrica, el uso de baterías aumenta la densidad energética que se puede almacenar. A día de hoy, las baterías de litio son las más utilizadas en la actualidad pero se está promoviendo el cambio hacia sistemas que sean más baratos y favorables para el medio ambiente. Por ello, se ha comenzado la transferencia de conocimiento de este tipo de baterías hacia a las baterías de ion sodio. En este sentido, los materiales análogos al litio pueden ser utilizados como cátodos, mientras que el grafito no tiene las mismas prestaciones como ánodo que en las baterías de litio. Por este motivo, la búsqueda de un ánodo en baterías de ion sodio que permita compensar la diferencia en términos de densidad energética que presenta la tecnología de litio ion.

En este trabajo dos familias de materiales han sido estudiados: $H_2Ti_3O_7$ y las carbodiimidas de metales de transición.

Capítulo 2. Experimental: Métodos de síntesis y técnicas de caracterización

En este capítulo se detallan todos los métodos de síntesis desarrollados en esta tesis, así como la descripción del montaje de las baterías tipo Swagelok o tipo "botón". Además se expone una breve descripción sobre las técnicas de caracterización utilizadas y sus detalles experimentales.

Capítulo 3. Resolución de la estructura y comprensión del mecanismo electroquímico de $H_2Ti_3O_7$

El compuesto $H_2Ti_3O_7$ se sintetizó y se obtuvo como fase pura por difracción de rayos X. La estructura reportada no tenía situados los protones por lo que se realizaron medidas de difracción de neutrones. Del refinamiento conjugado de los rayos X y de los neutrones se encontraron las posiciones atómicas de los 3 tipos protones. Además, a partir de las técnicas de espectroscopía de Resonancia Magnética Nuclear (RMN) e InfraRroja (IR) se caracterizó sus entornos. También se analizó la estabilidad térmica del material con medidas de termogravimetría. El material se descompuso desde 120 ^oC perdiendo moléculas de agua a diferentes temperaturas formando $H_2Ti_6O_{13}$ como intermedio y TiO_2 como producto final a 550 ^oC.

La caracterización electroquímica de este compuesto no proporcionó resultados satisfactorios. Este material exhibió baja capacidad y una alta irreversibilidad a pesar de alto coeficiente de difusión ($1.68 \cdot 10^{-11}$ cm^2/s, 5 veces mayor que el del $Na_2Ti_3O_7$). A través del estudio *ex-situ* e *in-situ* de los electrodos ciclados se observó que $H_2Ti_3O_7$ presentaba una transición estructural durante la inserción de iones sodio a una estructura tipo $Na_2Ti_3O_7$ explicando la mala reversibilidad observada. Tras observar esta transición estructural, se decidió ciclar el material en el rango que estaba reportado para $Na_2Ti_3O_7$. El compuesto exhibió una capacidad similar en los primeros ciclos pero su ciclabilidad era mejor. Dada su mejora en la ciclabilidad, se llevó a cabo un análisis de RMN *ex-situ* obteniendo $Na_{1.8}H_{0.2}Ti_3O_7$ como estequiometría en el compuesto.

Capítulo 4. Caracterización estructural y estudio cinético de la reacción de conversión en ZnNCN y CuNCN

La síntesis de las carbodiimidas de zinc y cobre se sintetizaron en disolución acuosa obteniendo dichas fases como puras confirmadas por rayos X. Además se observó que el cobre estaba coordinado en octaedros con 6 diferentes cadenas de NCN. Este octaedro mostraba una distorsión en el eje axial debido a la presencia del efecto Jahn-Teller. La morfología fue estudiada por microscopía electrónica de barrido (MEB) y se asignaron las bandas activas (la deformación y la tensión asimétrica) en espectroscopía infrarroja. La estabilidad térmica de estos compuestos se estudió por rayos X de 25^{o}C a 800^{o}C al aire y atmosfera inerte. El compuesto CuNCN se descompuso a 200 ^{o}C en oxido de cobre cuando se calentó al aire mientras que cuando se calentó en atmosfera inserte se convirtió en cobre metálico. En cambio, el compuesto ZnNCN se transformó en óxido de zinc al calentarse al aire y fue estable hasta 800 ^{o}C calentada en atmosfera inerte.

En el estudio del mecanismo de reacción electroquímica de estos compuestos se observó un comportamiento característico de los materiales que reaccionan por reacciones de conversión (alta polarización, capacidades altas, irreversibilidad grande en el primer ciclo,..). A través de experimentos ex-situ e in-situ se observó como el material se convertía en amorfo a medida que reaccionaba, también característico de las reacciones de conversión. El EPR del CuNCN mostró que se reducía de Cu^{2+} a Cu^{0}, mientras que en carga el cobre metálico solo era capaz de oxidarse a Cu^{+}, contribuyendo a la irreversibilidad del primer ciclo. A la vista de los primeros resultados, se analizó la descomposición del electrolito donde el NaFSI se descomponía formando NaF y la reversibilidad de los procesos electroquímicos mediante medidas potenciostáticas en la carbodiimida de cobre.

Capítulo 5. Estudios estructurales, electroquímicos y termodinámicos de MnNCN, FeNCN, CoNCN y NiNCN

La síntesis de la carbodiimida de manganeso se llevó a cabo a través de dos métodos diferentes. El primero mediante síntesis en estado sólido y el segundo consistió en un intercambio iónico de litio y manganeso en medio orgánico. Las diferentes síntesis proporcionaron una fase pura cristalina con mayor tamaño de partícula para la síntesis de estado sólido confirmado por MEB. Sin embargo, con la síntesis en medio orgánico se

obtuvo un menor tamaño de partícula que también se observó en el difractograma de rayos X. Las carbodiimidas de hierro, cobalto y níquel se sintetizaron por técnicas Schlenk a partir de las hidrogeno cianamidas en sales fundidas. Las muestras cristalinas se obtuvieron como fases puras a través de rayos X y se observó por MEB que las muestra de hierro tenía menor tamaño de partícula mientras que CoNCN y NiNCN tenían mayor tamaño y una forma más regular. Mediante el análisis de los espectros de IR se asignaron las bandas de deformación y tensión asimétrica de las carbodiimidas y se relacionaron con las distancias de enlace metal-nitrogeno y nitrógeno-carbono obtenidas en los refinamientos respectivamente.

La caracterización electroquímica de estos materiales se estudió para litio y para sodio. En la carbodiimida de manganeso se observó una gran diferencia en el comportamiento electroquímico en la utilización de ambas muestras. La de menor tamaño de partícula experimentó actividad electroquímica con grandes valores de capacidad pero mucha polarización. FeNCN, CoNCN y NiNCN mostraron un comportamiento electroquímico similar al que estaba reportado para litio en los óxidos análogos (FeO, CoO y NiO respectivamente). Se obtuvieron altos valores de capacidad para todas las muestras pero la retención de la capacidad fue muy pequeña para CoNCN y NiNCN. Esta diferencia se puede atribuir al mayor tamaño de partícula de estas muestras en comparación con FeNCN y MnNCN.

Por tanto, la carbodiimida de hierro mostró las mejores prestaciones electroquímicas debido a su menos irreversibilidad en el primer ciclo, su gran ciclabilidad y su baja polarización para ser un sistema que opera a través del mecanismo de conversión. Por último, la electroquímica de estos compuestos es discutida y relacionada con la termodinámica de estos compuestos.

Capítulo 6. Caracterización estructural y electroquímico de $Co_{1-x}Fe_xNCN$

Debido a la gran capacidad observada en CoNCN y la gran estabilidad que mostró FeNCN se prepararon muestras con diferentes contenidos de la disolución sólida $Co_{1-x}Fe_xNCN$. Las muestras de la disolución solida no habían sido publicadas ni testadas electroquímicamente previamente. Los compuestos fueron caracterizados como fases puras y los parámetros de celda de estos materiales se relacionaban siguiendo la ley de Vegard. Se observó la morfología de las muestras en el microscopio electrónico de transmisión (MET). Las partículas con mayor contenido de cobalto en su composición, mostraban bordes más regulares. Por difracción de electrones, se observó la presencia de

monocristal en la zona analizada y los planos (h k l) correspondientes fueron indexados. En las medidas magnéticas, se observó una diferente temperatura de orden donde la muestra de estequiometría $Co_{0.54}Fe_{0.46}NCN$ era antiferromagnética a temperatura ambiente y la otra tenía la temperatura de orden por debajo (283 K). La espectroscopía Mössbauer observó el mismo comportamiento. Para determinar el contenido de Fe^{3+} se calentaron las muestras a 350 K para tenerlas en zona paramagnétia y así poder refinar el espectro. Se obtuvo un 20 % de Fe^{3+}.

La caracterización electroquímica de estos materiales se estudió para litio y para sodio por primera vez. Los materiales exhibieron un comportamiento electroquímico similar al FeNCN. Mostraron mayores valores de capacidad y su retención era parecida a la del FeNCN. Por tanto, se incrementó la capacidad de las muestras en comparación con FeNCN pero además se obtuvieron menor polarización y mayor retención de la capacidad que el CoNCN. Estos materiales son buenos candidatos para ser probados como ánodos en baterías de ion sodio y de ion litio.

Capítulo 7. Desarrollo de celdas completas de ion sodio

Por último, se estudió la posible aplicación de estos materiales en celdas completas. Debido a los problemas que conlleva el operar con celdas con sodio metálico, un material de cada familia trabajada en esta tesis fueron analizados utilizando como cátodo óxido laminar de sodio. Se comprobó la importancia de hacer el balance de masa de cara al aprovechamiento del material y a poder observar en ambos compuestos los procesos electroquímicos caracterizados previamente en celdas con sodio. En este análisis se llegó a la conclusión de que a pesar de la mayor polarización que presentaba el FeNCN, éste mostraba mayores valores de densidad energética (157 Wh/Kg) y mejor ciclabilidad que el titanato protonado (136 Wh/Kg).

Capítulo 8. Conclusiones y perspectivas

En este capítulo se detallan las conclusiones más generales derivadas de este trabajo y se expone el posible trabajo que se puede realizar en el futuro como continuación a este trabajo.

1.-Introduction

The actual energetic system is strongly dependant on fossil fuels, including oil, natural gas and coal. 80% of the worldwide energy consumption is based on fossil fuels (Figure 1.1)[1] but there are two big issues associated with their consumption. In one hand they release carbon dioxide, nitrogen dioxide, sulphur dioxide, carbon monoxide, etc. which can lead to serious environmental issues such as air pollution. On the other hand, they are non-renewable sources of energy so their availability and price are not constant. In fact, the price will increase meanwhile the resources are going to be depleted.

It thus seems that the energetic system is gradually moving from fossil fuels towards renewable energy sources. Despite the fact that they represent the 11% of the primary energy reserve of the world, their use will increase in the near future due to their unlimited advantages such as they are inexhaustible and they do not produce dangerous wastes. The issue of these sources is that energy generation is intermittent and it does not exactly match with consumption time. Therefore, there is a need to find suitable electrical energy storage devices to take full advantage of the energy produced in non-consuming periods.

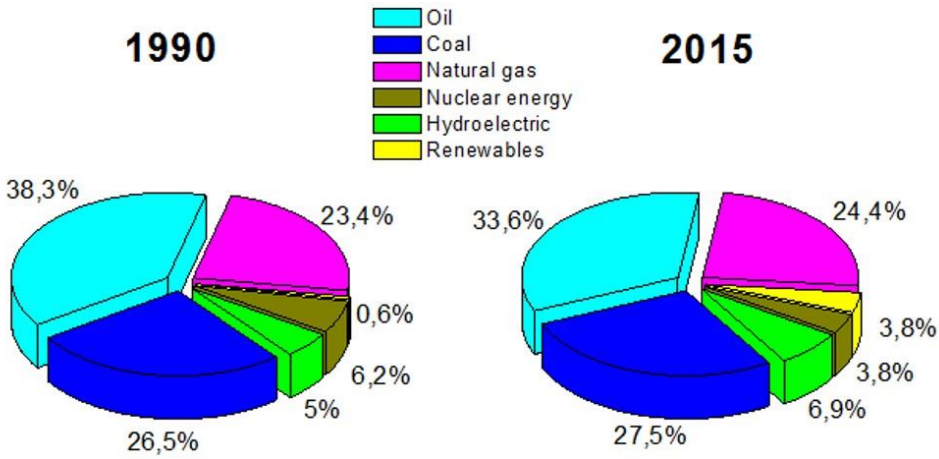

Figure 1.1. Energetic world consumption difference between 1990 and 2015 by BP statistics[1]. The energy primary sources represented in the graph are: oil (cyan), coal (dark blue), natural gas (pink), nuclear energy (dark yellow), hydroelectricity (green) and renewables (yellow).

Electrical energy storage systems have been part of our society for many years, for large scale applications pumped hydro represents nearly 99% of the worldwide energy stored (Figure 1.2) and 3% of the actual energy generation[2]. Pump hydro storage is based on two water reserves at different heights. During the charge process (at off-peak demand) the water is pumped to the upper level. However, during the discharge process, the water goes to the lower level powering a turbine that provides the transformed energy[3]. Besides, compressed air system is another good candidate for large scale applications as well. In this system, electricity is used to compress air and store it and when the energy is needed, the compressed air is mixed with natural gas, burned and expanded in a modified gas turbine[4]. The main drawback of these two systems is the price of the installation.

For medium and small scale applications electrochemical energy storage such as secondary batteries and supercapacitors are more suitable. These systems work through the differential voltage between two electrodes.

Batteries store the electric energy through redox reactions between anode and cathode. Rechargeable batteries, especially Li-ion batteries, can provide high energy density. However, supercapacitors work by physical adsorption of the ions above the surface of electrode. These devices can supply large power and have long cycle life. The Ragone plot (Figure 1.3) summarizes well the difference between supercapacitors and the different types of batteries in terms of energy density (total amount of charges) and power density (charges per instant).

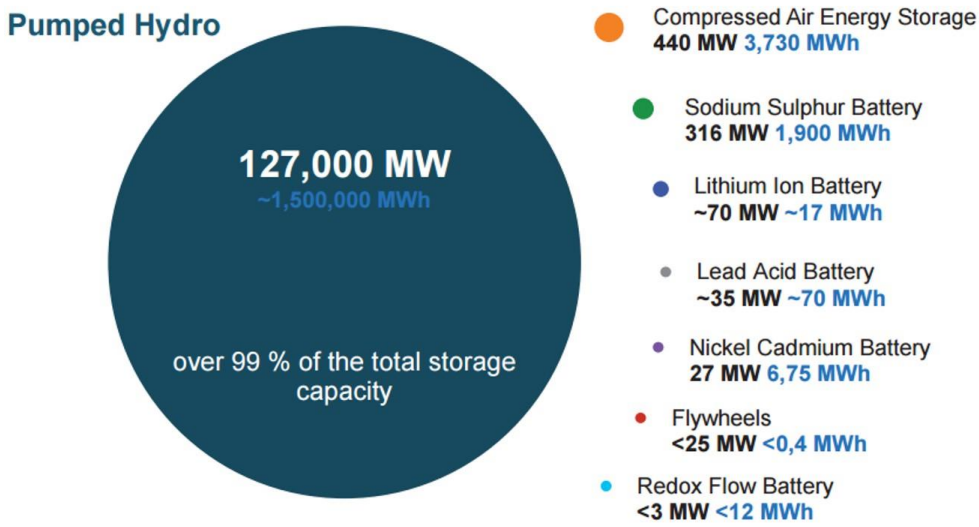

Figure 1.2. Worldwide installed storage capacity for the different electrical energy systems[2].

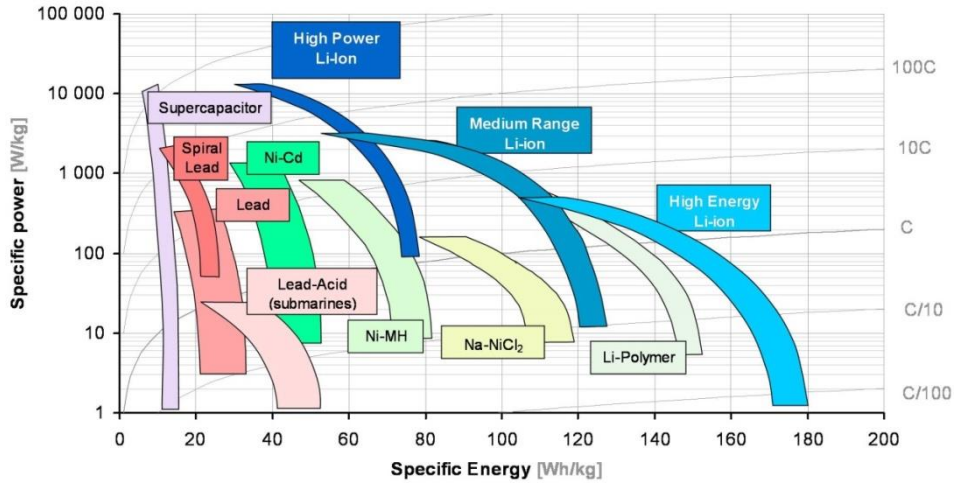

Figure 1.3. Ragone plot of the ratio of the specific energy and specific power of batteries and supercapacitors. Source: Genport.it[5]

The higher energy density that batteries are able to store makes them a more promising solution for energy storage applications.

1.1- Secondary Batteries for electrical energy storage

Rechargeable batteries are widely used electrical energy storage (EES) technologies in industry and daily life. They can be used in many different applications, such as power quality, energy management, ride-through power and transportation systems[6]. Table 1.1 describes the commercial rechargeable batteries and what are the chemical processes that occur inside the battery as well as their resulting voltage difference. The commercial rechargeable battery systems can be classified in two main categories depending on the type of electrolyte (liquid or solid) used. Sodium-sulphur and sodium-nickel chloride[7] operate with beta alumina (solid electrolyte). Nevertheless, lead-acid, alkaline nickel-cadmium and nickel-metal hydride batteries work in aqueous electrolyte, while lithium ion batteries and beyond Li-ion batteries (still at research or development stages) work in organic liquid electrolyte.

Rechargeable batteries store electrical energy through reversible electrochemical reactions in its electrodes allowing the device to be used several times after the charging process. The amount of stored energy density is related to the difference of the voltage between two electrodes (anode and cathode) and their specific capacity, which is dependent on the number of electrons involved in the electrochemical reaction and the molecular weight of the electrode materials.

Sodium-sulphur and sodium-nickel chloride batteries own high energy density, excellent cycle life and use low-cost materials. The drawback of these technologies is the need to operate at high temperatures (300^{o}C) with the risk of working with molten sodium and the maintenance problems of the insulator. These disadvantages make them less viable option as a grid energy storage solution compared to other more feasible grid energy storage solutions.

On the other hand, the energy density that lead-acid, alkaline nickel-cadmium and nickel-metal hydride batteries are able to store is much lower (Figure 1.3). Also, while lead-acid systems suffer corrosion problems decreasing the life time of the batteries, nickel cadmium devices contain toxic metals and are environmentally unfriendly. The nickel-metal hydride batteries present a critical charge generating more heat and must be controlled carefully.

Li-ion batteries seem to be the most promising technology because they are able to store high energy density (volumetric and gravimetric) with better maintenance despite their expensive manufacturing.

In the field of secondary batteries, the first lithium ion battery was commercialized by Sony Co. [8]. Since then, they have undergone tremendous development due to their high energy density [9] especially for portable applications. There are many different shapes of container in the commercialized lithium ion batteries (Figure 1.4).

Table 1.1. Rechargeable batteries, the reactions inside them and the nominal voltage obtained due to the electrochemical reactions.[6]

Battery type	Chemical reactions at anodes and cathodes	Unit voltage
Lead–acid	$Pb + SO_4^{2-} \Longleftrightarrow PbSO_4 + 2e^-$	2.0 V
	$PbO_2 + SO_4^{2-} + 4H^+ + 2e^- \Longleftrightarrow PbSO_4 + 2H_2O$	
Lithium-ion	$C + nLi^+ + ne^- \Longleftrightarrow Li_nC$	3.7 V
	$LiXXO_2 \Longleftrightarrow Li_{1-n}XXO_2 + nLi^+ + ne^-$	
Sodium–sulfur	$2Na \Longleftrightarrow 2Na^+ + 2e^-$	~2.08 V
	$\chi S + 2e^- \Longleftrightarrow \chi S^{2-}$	
Nickel–cadmium	$Cd + 2OH^- \Longleftrightarrow Cd(OH)_2 + 2e^-$	1.0–
	$2NiOOH + 2H_2O + 2e^- \Longleftrightarrow 2Ni(OH)_2 + 2OH^-$	1.3 V
Nickel–metal hydride	$H_2O + e^- \Longleftrightarrow 1/2H_2 + OH^-$	1.0–
	$Ni(OH)_2 + OH^- \Longleftrightarrow NiOOH + H_2O + e^-$	1.3 V
Sodium nickel chloride	$2Na \Longleftrightarrow 2Na^+ + 2e^-$	~2.58 V
	$NiCl_2 + 2e^- \Longleftrightarrow Ni + 2Cl^-$	

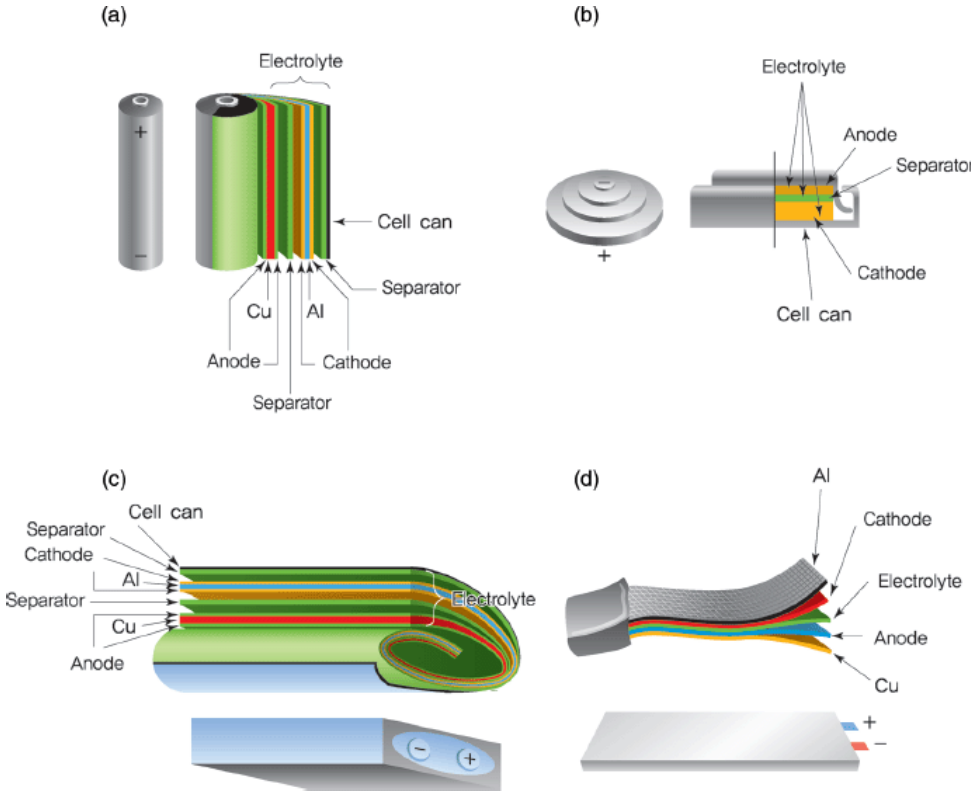

Figure 1.4. Different shape of containers of the commercial lithium rechargeable batteries: cylindrical (a), coin (b), prismatic (c) and pouch (d) cells.[9]

1.2- Na-ion batteries: Emerging technology in Rechargeable Batteries for stationary applications

Research on sodium ion batteries started even before (1980) and they were studied in parallel to lithium ion batteries[10,11]. In that time, sodium ion technology did not attract much attention because the lower energy density which can be stored in comparison with lithium ion batteries. The lower energy density obtained is partly due to the heavier weight of sodium compared to lithium, but mostly based on the smaller voltage of the Na^+/Na (E^0=2.71 Volts *vs* Standard Hydrogen Electrode) instead of the Li^+/Li (E^0=3.04 Volts *vs* S.H.E.). However, this voltage difference only applies if metallic lithium and sodium are used as the anode. Moreover, the long-term economic viability of large-scale Li-ion energy storage systems needs taking into consideration the global lithium reserves[12] due to the availability, production, recycling and geographical/political constraints of

lithium[13]. Moreover, in the last years, much progress has been done in sodium ion batteries[14] as it can be seen in the increment of publications related to this topic (Figure 1.5). There are several advantages of this technology respect to the lithium ion batteries, such as the lower price and the higher abundance of sodium resources, which can partially mitigate the big demand of the lithium ion battery technology, especially for stationary applications, where the weight of the device is not of primary importance. So, the development of both lithium and sodium ion batteries can be complementary for portable and stationary energy storage respectively.

The operation of the sodium ion batteries is based on the same concepts of lithium ion batteries. During the charge, the sodium ions of cathode materials are deinserted (oxidazing the transition metal of the cathode material) and they are diffusing through the electrolyte up to the anode material where they are inserted, causing its reduction, while electrons are moved from anode to cathode by an external circuit. Likewise, during the discharge process, sodium ions and electrons are diffusing from anode to the cathode and the opposite redox processes are occurring. These processes can be observed in Figure 1.6. The use of non-aqueous electrolytes enables the use of electrodes with large voltage difference between the electrodes. This option causes a big step in the rechargeable batteries increasing a lot the energy density which can be stored in the devices. The rate of the applied current is very important because it affects in the kinetics of the reactions and in the same way in the amount of energy stored. Commonly, this rate is named C-Rate and it is expressed in mA/g and gives the information of how long it takes the fully charge or discharge of the battery. For example, a C-Rate of C/10 means that the battery will be completely charged or discharged in 10 hours[15].

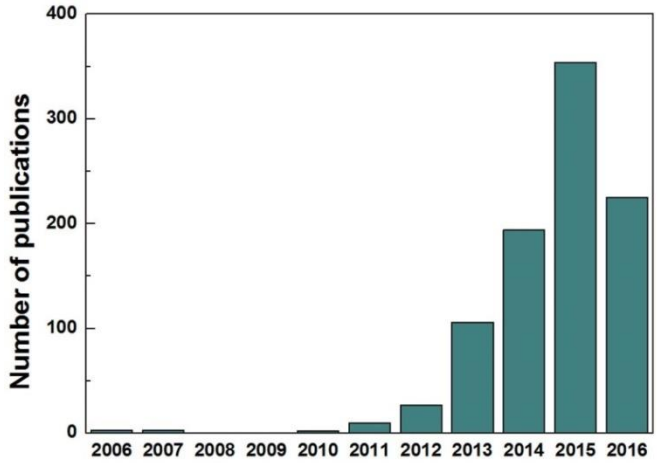

Figure 1.5. Number of publications per year in sodium ion batteries for the las 10 years (data obtained from Web of Science FECYT in August 2016).

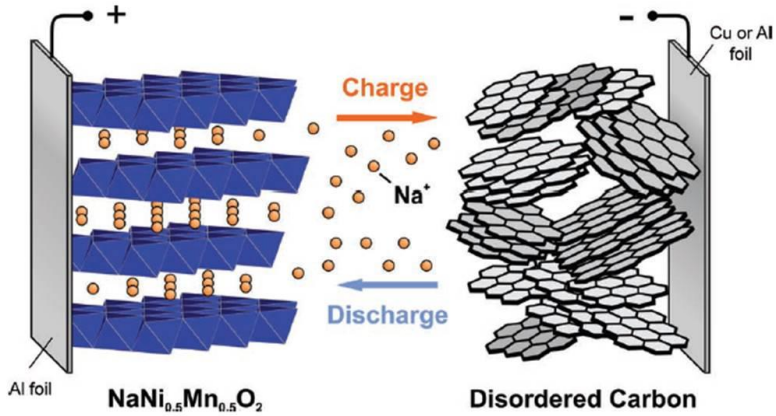

Figure 1.6. Schema of a sodium ion battery based on a $NaNi_{0.5}Mn_{0.5}O_2$ as cathode material and disordered carbon as anode material[22].

An advantage of sodium ion batteries is that both current collectors can be of aluminium due to the stability of aluminium in the voltage range of (0-5 V *vs* Na^+/Na), whereas lithium alloys with aluminium at 0.6 Volts *vs* Li^+/Li[16]. The use of aluminium instead of copper (used in Li-ion batteries) decreases 7 times the price of current collectors as well as the total weight of the electrode[17].

In spite of the similar chemistry involved in lithium and sodium ion batteries, the larger size (Table 1.2) of the Na ions (1.02 Å) cause big differences in the intercalation behaviour in the crystal structure. Using the same host structure, the electrochemical performance in sodium ion batteries is often worse than in lithium ion batteries. An example is the better performance in terms of voltage and capacity of $LiCoO_2$ in lithium ion batteries[17] compared to Na_xCoO_2, which is the sodium analogue, for sodium ion batteries[18] (Figure 1.7). However, the biggest issue in sodium-ion batteries is that graphite cannot be utilized as a low voltage insertion host of Na ions[19]. This fact makes that finding a suitable anode material for sodium-ion batteries is a key main challenge in the development of this technology.

Table 1.2. Main differences between sodium and lithium ion battery technologies in terms of energy density, size and melting point.

	Na	**Li**
Energy density	90 Wh/kg	150 Wh/kg
Ionic radius	1.02 Å	0.76 Å
Melting point	97.8°C	180.5°C
Price (for carbonates) [14,20]	0.07-0.37 €/kg	4.11-4.49 €/kg
Abundance[21,22]	30000 ppm	20 ppm

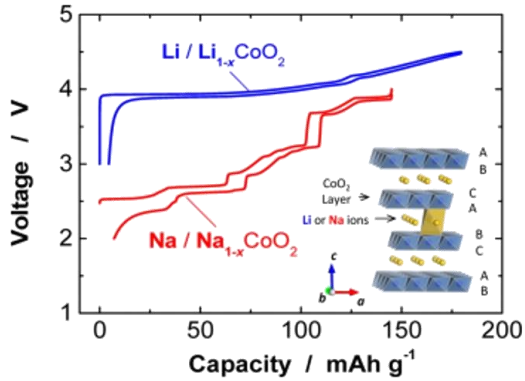

Figure 1.7. Comparison of charge/discharge processes of $Li/LiCoO_2$ (blue) and Na/Na_xCoO_2 (red cells) and the structure with the CoO_2 layers and the Li/Na positions in the interlayers[22].

1.2.1- Cathode materials

In the positive electrode materials (cathodes), the intercalation chemistry of sodium is more similar to that of lithium, and it allows using the lithium analogue compounds for sodium ion cells. Depending on the need of the high voltage or high capacity values, cathode materials used so far in sodium-ion prototype devices are fluorophosphates of vanadium and layered oxides:

1.2.1.1- Vanadium fluorophosphates

Phosphate polyanion based materials have been reported as promising cathode materials for sodium-ion batteries. The phosphate group $(PO_4)^{3-}$ has a strong inductive effect that moderates the energetic of the transition metal redox couple to generate relatively high operating potentials for these compounds[23]. Moreover, the addition of the fluoride ion to the phosphate materials further increases the operating voltage because the inductive effect of the fluoride adds to that of the phosphate[24]. Due to their high operating voltage, batteries assembled using these materials as cathodes are able to store large amounts of energy. Three different phases have been deeply studied in literature: $NaVPO_4F$, $Na_3(VO)_2(PO_4)_2F$ and $Na_3V_2(PO_4)_2F_3$.

- $NaVPO_4F$

$NaV(PO_4)F$ with tetragonal structure can achieve 82 mAh/g of reversible capacity which is 2/3 of the theoretical capacity (143 mAh/g) and relatively high average voltage (4 Volts *vs* Na^+/Na)[25]. Capacity retention in half cells can be improved by partial substitution of Vanadium by Aluminum[26] and Chromium[27] in the low-temperature phase.

- $Na_3(VO)_2(PO_4)_2F$

The framework structure of $Na_3(VO)_2(PO_4)_2F$ consists of VO_5F octahedra and PO_4 tetrahedra (Figure 1.8). This material can provide 110 mAh/g and it presents high reaction voltages distributed in two plateaux of the same length at 3.6 and 4.1 Volts *vs* Na/Na^+[25].

- $Na_3V_2(PO_4)_2F_3$

The framework structure of $Na_3V_2(PO_4)_2F_3$ consists of VO_4F_2 octahedra and PO_4 tetrahedra. $Na_3V_2(PO_4)_2F_3$ can deliver 120 mAh/g of reversible capacity with excellent cyclability with the appearance of two voltage plateaux at 3.7 and 4.2 Volts *vs* Na/Na^+[28,29]. Moreover, as this compound is isostructural to $Na_3(VO)_2(PO_4)_2F$, solid solutions such as $Na_3V_2(PO_4)_2O_{1.6}F_{1.4}$ have been prepared providing 130 mAh/g with excellent capacity retention due to the small volume expansion (less than 3%)[30].

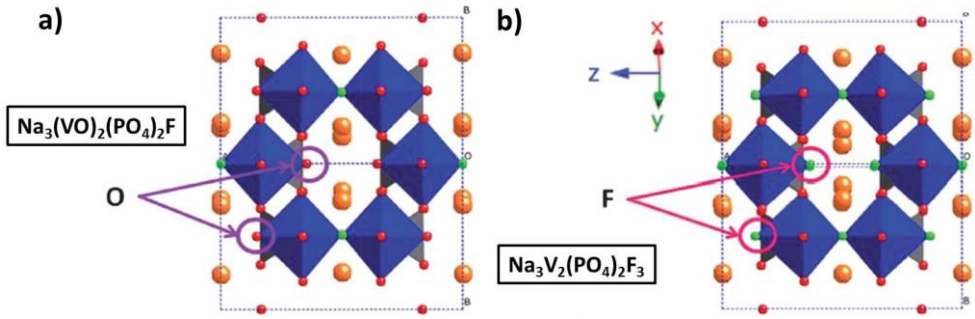

Figure 1.8. Different structures of $Na_3(VO)_2(PO_4)_2F$ (a) and $Na_3V_2(PO_4)_2F_3$ (b) where the difference in the octahedra is observed by the substitution of 2 fluoride groups (F^-) by 2 oxide groups (O^{2-}) (reproduced from ref.24).

1.2.1.2 Layered oxides

Layered oxides which general formula can be summarize as Na_xTMO_2 are composed of repeating sheets of T^MO_6 (T^M=transition metal) layers where Na-ions are in between the oxide layers[31]. This sodium layered oxides can be synthesized forming different ordered structures although the same formula unit. They are called O3, P2 or P3-phases, where the letter indicates the oxygen environment where Na is located (O: octahedral, P: prismatic) and the number points out the number of layers that compose a unit cell[32]. The O3-phase composition usually corresponds to the Na_xTMO_2 with higher content of sodium ions ($0.7 \leq x \leq 1$) and the order of the layer stacking of is ABCABC. On the other hand, $Na_{0.7}TMO_2$ composition is usually called as P3-phase and the layer of TMO_2 are distributed as ABBCCA while for $Na_{0.5}TMO_2$ (P2-phase) the layer stacking follows the ABBA sequence (Figure 1.9).

The electrochemical behavior of these compounds is strongly influenced by the structure adopted by the layered oxide because the stability of the ordered layers of the compound and the kinetics are affected by the environment surrounding Na ions. In fact, better electrochemistry is obtained when the layered oxide is a P2-structure versus the O3-phase. This is due to the lower diffusion barrier and higher ionic conductivity[33] of the P2 phase in spite of the higher capacity achieved by the O3-structure due to the higher sodium content in the pristine phase.

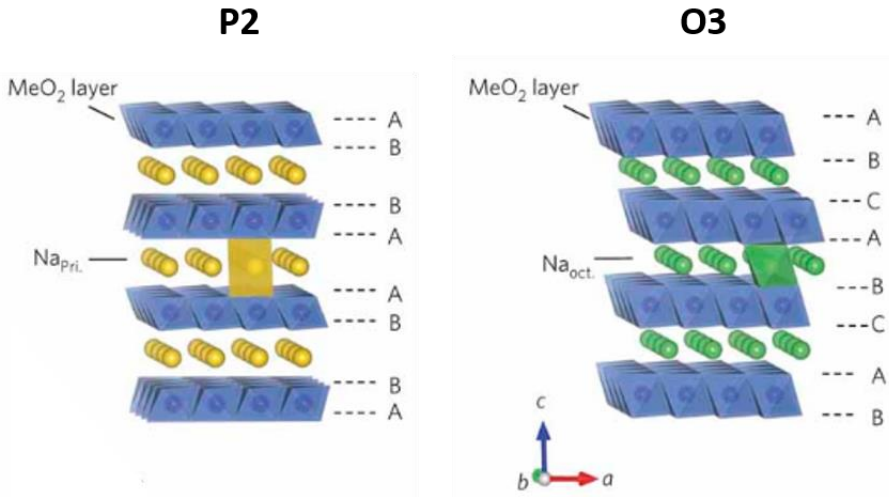

Figure 1.9. Structural differences between P2 and O3 structures modified from ref.[34].

In the Na_xTMO_2, the material composition can be made up by just a single transition-metal, by two different transition-metals or even by a higher number of transition-metals in the same formula. The introduction of lithium in the atomic positions of both sodium and transition-metal can also result beneficial increasing the average voltage and the capacity of the battery. The average voltage and the capacity of the most studied layer oxides is described in Figure 1.10.

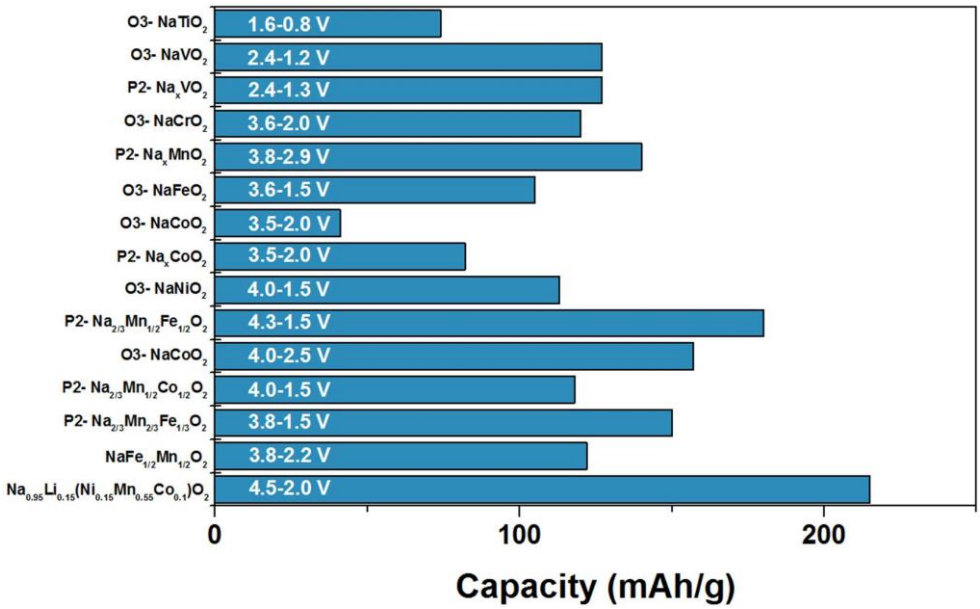

Figure 1.10. Bar diagram of the different layer oxides where the capacity is described in the "x" axis and the voltages at which materials operate are pointed out inside the bars (figure modified from ref.31).

1.2.2- Anode materials

The chemistry of negative electrodes of sodium ion batteries is quite different in comparison with lithium ion technology. In lithium ion batteries graphite and silicon are the most suitable anodes because of their low voltage plateau, high reversible capacity (and short first cycle irreversible capacity) and good cyclability[35]. However, in sodium ion batteries graphite is not able to intercalate sodium effectively and silicon is not able to incorporate sodium ion like in lithium systems despite the fact that *V.L.Chevrier and G.Ceder*[36] DFT calculations predicted the plateau for the formation of NaSi at 0.15 Volts *vs* Na^+/Na. The incorporation of new materials is necessary in the negative electrode in order to take the advantage of this technology.

Up to date, many different kinds of compounds have been proposed as anode materials for sodium ion batteries. The most significant families can be classified into carbon materials, alloys, transition metal oxides and organic compounds[37]:

1.2.2.1- Carbon materials

The first studies were based on the graphite due to the suitable behaviour for lithium ion batteries but it was observed that the same material was not able to insert sodium ions[38]. Experimentally, the maximum sodium insertion for graphite was only to form NaC_{70}, in contrast to lithium into graphite (LiC_6). The intercalation of lithium into the graphite occurs at lower voltages[39] than 0.4 V[40]; so the same process for sodium cells can be expected to occur at similar voltages. Due to the difference between the standard voltage of reduction of sodium and lithium ions into the corresponding metal[41] , this process could ideally occur below the sodium electroplating (below 0 Volts *vs* Na^+/Na) and therefore it would not be observed. However, it has been observed that graphite can co-intercalate Na-ions with solvent molecules[42] and it can solve the mismatch between sodium ions size and the graphite interlayer distance. The co-intercalation of solvated sodium ions in the graphite is possible using a high donor number electrolyte, such as ether-based electrolytes[43].

In this context, early research was focused on different carbonaceous materials that can avoid this problem and are electrochemically active. Hard carbons (non-graphitic carbons) seem to be the most promising material[44] owing to its highly disordered structure and large interlayer distance (Figure 1.11a).

They can reach high capacity (300 mAh/g[45] or even a bit more[46]) through a sloping region due to the insertion of sodium ions between the layers and a long plateau region at very low potential plateau (less than 0.1 V) which can be attributed to the insertion of sodium ions into the nonporous of hard carbon[47]. This mechanism was confirmed by wide angle in situ X-ray scattering[48] and ^{23}Na-NMR more recently[49]. As this plateau is close to the sodium electroplating potential (0 Volts *vs* Na^+/Na) (Figure 1.11b), the kinetic effects have to be seriously taken into account. The use of fast current rates causes an increment of polarization in the charge and discharge processes and the discharge voltage could move to voltages below sodium electroplating and consequently the electrochemical activity would not appear. In that case, hard carbon could be not reduced by sodium ions as it happens in graphite

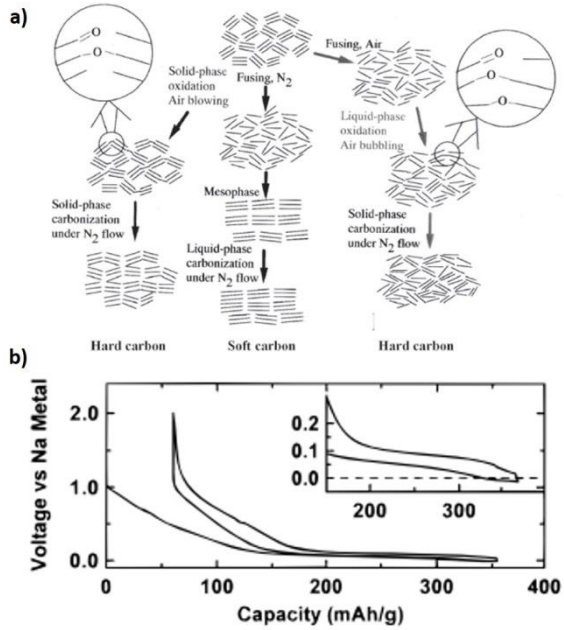

Figure 1.11. Different ordered carbons soft (graphitizing) and hard (non-graphitizing) carbon (a) and electrochemical curve of hard carbon for sodium ion batteries (b) making the zoom in the sodium electroplating[44].

1.2.2.2- Alloys

Another group of materials which have good electrochemical behavior are those materials which alloy with sodium. Their high theoretical capacity but in sodium ion batteries they cannot reach the capacity that they get in lithium ion batteries. While, in lithium ion batteries silicon is the material which exhibited higher capacity (and the theoretical is around 3675 mAh/g) at very low plateau[50], in sodium ion batteries silicon is not active. As it was explained before, this could be due to having the plateau responsible of the alloying of silicon below the sodium electroplating. Sodium ions cannot incorporate into silicon to form sodium-rich alloy phases with higher capacity than carbon-based materials. However, the rest of the elements of group 14 (tin and germanium) and group 15 (phosphorous and antimony) are electrochemically active and show large capacity values with high reversibility (Figure 1.12). While tin alloys form three intermediate compounds ($NaSn_5$, NaSn and Na_3Sn)[36] and final $Na_{15}Sn_4$ was detected after full sodiation[51,52], it was experimentally observed that during the discharge of germanium, this reacts to form NaGe. In fact, nanowires and nanorods shapes activated by lithium can reach high capacity (369 mAh/g) which is the theoretical for NaGe[53]. The microstructure

of germanium is thus important because a large porous structure partially avoids the critical cracking of the electrodes.

On group 15, red phosphorous is the allotrope which experimentally shows better electrochemical performance. It is stable, commercially available and it provides high theoretical capacity (2596 mAh/g). Experimentally, only 1890 mAh/g[54] were achieved with a very low voltage plateau (0.4 V *vs* Na^+/Na), which can enable a high energy density full cell. Also, antimony is a promising anode with a high theoretical capacity[55] (660 mAh/g for the formation of Na_3Sb). During the discharge, it forms several amorphous Na-Sb compounds and ends up becoming hexagonal Na_3Sb with a quite stable capacity of 610 mAh/g [56,57].

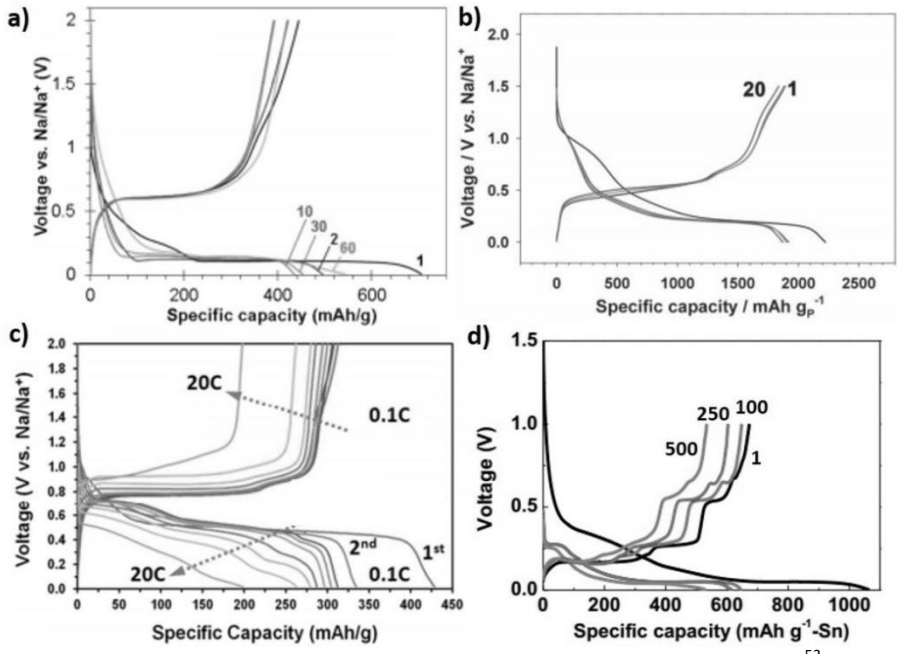

Figure 1.12. Electrochemical behaviour of the different composites: germanium[53] (a), red phosphorous[54] (b), antimony[55] (c) and tin[57] (d).

Nevertheless, the main disadvantages of these compounds are the large volume expansion which can damage the electrodes, their high cost and the possibility of forming unsafe products, in the case of antimony and phosphorous electrodes are exposed to water sources, such as the hydrides (SbH_3 or PH_3) or the trouble of tin handling. For germanium, the main drawback is the sluggish kinetics and poor cyclability[58]. These reasons do not make these compounds the most suitable anodes for sodium ion batteries because the sodium ion battery technology was invented with the goal of being large scale environmentally friendly energy storage systems.

1.2.2.3- Transition metal oxides

This family of compounds can be divided into two main groups. The first group includes the transition-metal oxides which work through conversion reactions. The reaction mechanism is summarized in the displacement of the metal oxide ion (where metal = Mn, Fe, Co, Ni, Cu and Mo) reducing its native elemental metal, and the formation of sodium oxide. Moreover, if the transition metal oxide contains tin or antimony, once the metal is formed, it can also alloy with sodium providing the sum of the capacity obtained in the conversion reaction and the capacity which come from the alloying process. The main advantages of these anodes are the high capacities and the lower voltage plateau exhibited. On the other hand large hysteresis and poor cyclability experimentally observed probably due to the volume expansion of the electrodes during the whole electrochemical process are their main drawbacks and do not make them the best candidates for a full cell of sodium ion batteries. In this family of materials, the most interesting electrode materials are the α-Fe_2O_3 and Fe_3O_4 due to their high theoretical capacities and their very low cost[59].

Fe_2O_3 prepared as a porous nanocomposite shows a sloppy profile (a sharp plateau at least is not appeared) with a capacity of 640 mAh/g of which only 400 mAh/g are reversible[60]. This evidences that the full conversion reaction could not occur in this case. Due to harsh changes that accompany this reaction, the electrodes could suffer a strong volume change which could affect the cyclability of this material. However, a composite with graphene nanosheets improve the capacity retention but requires the addition of a large weight of inactive material, about 37% of weight[59] (Figure 1.13a).

In a different way, Fe_3O_4 has some kinetic problems resulting in a discharge capacity of 643 mAh/g (this is 67% of the theoretical capacity) from which just 366 mAh/g is reverted in the first charge[61]. This material also shows a capacity fading with a capacity of 250 mAh/g after the first 10 cycles (Figure 1.13b)[62]. These values are quite lower compared to the capacities obtained for lithium ion batteries.

Conversion reactions usually present attractive large theoretical specific capacities but high voltage hysteresis and strong capacity fading due to the volume expansion which the electrodes suffer hinder their application in commercial devices.

On the other hand, the second group involves basically different structures of titanates which mostly react through intercalation reaction. Titanium-based materials have emerged as promising anode materials for sodium ion batteries due to their low cost, chemical stability and good cyclability for a long-term usage. However, the capacity is not as high as desired for an anode material of a rechargeable alkali ion battery.

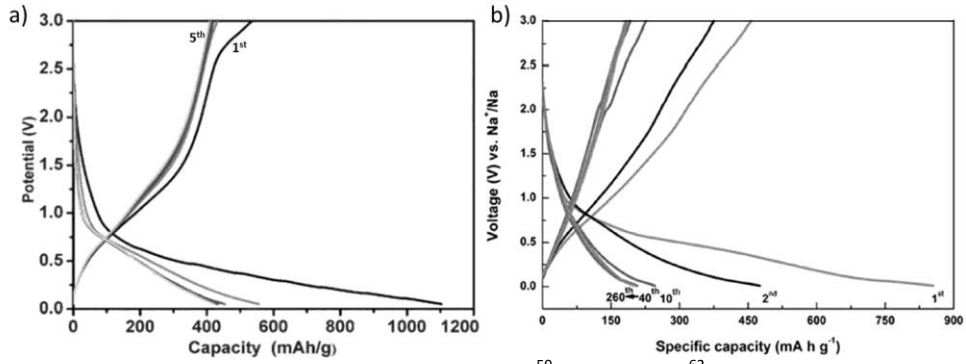

Figure 1.13. Galvanostatic voltage profile of Fe_2O_3 (a)[59] and Fe_3O_4 (b)[62] for sodium ion batteries from 0.05-3.0 and 0.01-3.0 Volts vs Na^+/Na respectively.

Amongst these materials, the first studies were focused on titanium oxide polymorphs and lithium titanates (specially the spinel-type $Li(Li_{1/3}Ti_{5/3})O_4$), which had been very well studied as anode materials for lithium ion batteries. However, up to 2010, just three titanates compounds had been reported to be a good candidate as anode for sodium ion batteries: i) Na_xTiO_2[63] working at relatively low potentials of 0.8-1.6 Volts *vs* Na^+/Na but with small capacity values 55 mAh/g; ii) NASICON-type $NaTi_2(PO_4)_3$ and iii) titanium sulphide with high intercalation voltages, of about 0.9 and 2.10 Volts *vs* Na^+/Na [64] and 1.40 and 2.10 Volts *vs* Na^+/Na [65] respectively.

Since then, titanates have been studied as anodes due to the lower potential for the reduction of Ti^{4+}/Ti^{3+} in oxides versus phosphates or sulphates due to the inductive effect of the polyanionic anion, being the oxidation state 4+ the most stable. The first studies were focused on the different polymorphs of TiO_2. These structures are based on different links of TiO_6 octahedra, so different polymorphs of TiO_2 crystallize in different crystalline systems such as tetragonal for anatase and rutile with space groups as $I4_1/amd$ (141) and $P4_2/mnm$ (136) respectively and ortorhombic for brookite with *Pbca* (61) space group (Figure 1.14).

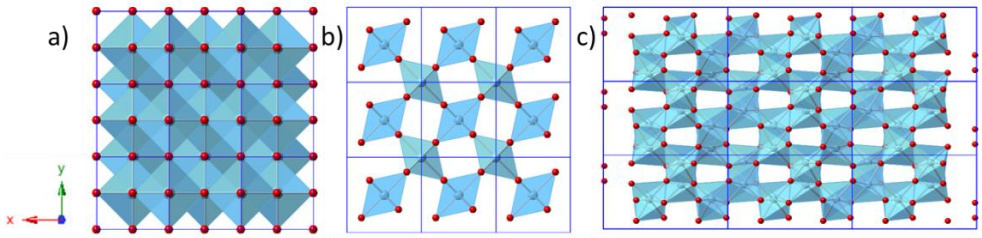

Figure 1.14. Different types of structures of TiO_2: anatase (a), rutile (b) and brookite (c) in the (001) axis. Red balls are the oxygen atoms and the blue polyhedral is the TiO_6 octahedra blocks with titanium atoms in the centre of the octahedra.

In lithium ion batteries, lithium titanate spinel-type $Li(Li_{1/3}Ti_{5/3})O_4$) has quite good electrochemical performance for sodium ion batteries. It has a reversible plateau with capacity of 155 mAh/g at 0.7 Volts vs Na^+/Na[66]. The main drawback of operating at this voltage is that below 1 Volt vs Na^+/Na, the electrolyte decomposes forming the solid electrolyte interphase, known as SEI, and causing capacity fading.

Nowadays, the most studied titanate as anode for sodium ion batteries is $Na_2Ti_3O_7$ ($P2_1/m$) because it has laminar structure (see Figure 1.15a) and is able to intercalate reversibly two sodium ions at relatively low voltage (0.3 Volts vs Na^+/Na). This material has a theoretical capacity of 177 mAh/g and it is able to achieve capacities close to the theoretical at current rate of C/10 [67].

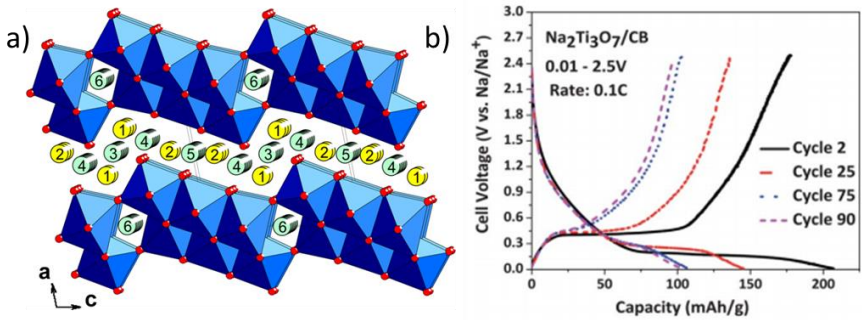

Figure 1.15. $Na_2Ti_3O_7$ structure with blue octahedra of TiO_6, yellow spheres of the sodium ions in the structure and the green spheres of the possible location of the inserted sodium ions (a); and the discharge/charge galvanostatic curves of sodium titanate upon cycling (b)[68].

An important issue for low-potential oxides is the high irreversible capacity observed in the first cycle and the big capacity fading upon cycling (Figure 1.15b). A large irreversible capacity is typically observed in the initial cycle because of the electrolyte decomposition[68] (more difficult to study in Na ion cells because the decomposition products are more soluble in the Na^+ based electrolyte[19]) and the SEI film-forming process at the titanium oxide surface (and carbon black) similar to carbon materials discussed above. Capacity degradation is attributed to the insufficient surface passivation of the particles of $Na_2Ti_3O_7$[69]. However, it was shown by *A.Rudola et al*[70] that $Na_2Ti_6O_{13}$ using carbon black as conductive carbon led to only 70 mAh/g of reversible capacity but it was very stable upon cycling suitable for testing in a full-cell.

1.2.2.4- Organic materials

During the last years, the research on organic materials has been attracted attention due to their abundant resources and structural flexibility. Moreover they are environmental-friendly which is the one of the most important goals of large-scale production of electrode materials for batteries. In this sense, *M.Armand et al*.[71] developed di-lithium

terephthalate based on conjugated di-carboxylate showing good electrochemical properties. Moving to the sodium analogue terephthalate ($Na_2C_8H_4O_4$), it was observed that they can reach a reversible capacity of 250 mAh/g at 0.3 Volts *vs* Na^+/Na[72] (see Figure 1.16a). This capacity can be attributed to the insertion of two sodium ions in the structure and recently, its capacity retention was improved making hybrid electrodes with graphene[73].

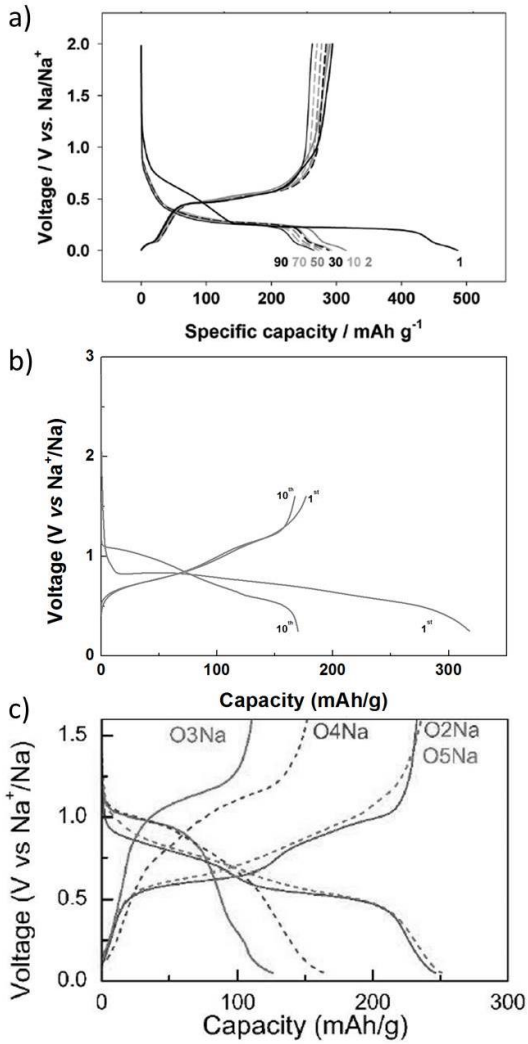

Figure 1.16. Electrochemical characterization of organic anodes in Na-ion batteries. Galvanostatic voltage profiles of disodium-terephthalates[72] (a), Poly-Schiff bases [74] (b) and Oligomeric-Schiff bases[75] (c).

Another type of organic materials tested as anode for sodium ion batteries are Poly-Schiff bases. Their electrochemical activity is based on (-N=CH-Ar-HC=N-) active unit and the aromaticity in this planar structure is stabilized because it follows the 4n+2 Hückel´s rule. Poly-Schiff bases show high capacities of 200 mAh/g at 0.8 Volts *vs* Na^+/Na[74] as can be seen in Figure 1.16b. Besides, Oligomeric-Schiff bases, hybrids between carboxylates and poly-Schiff, improve the electrochemical properties of Poly-Schiff bases due to the 0.2 volts lower voltage for sodium insertion and because they also exhibit higher capacity values (260 mAh/g)[75] (Figure 1.16c).

.

Table 1.3. Summary of the capacity, voltage and polarization of the different families of anode materials studied for sodium ion batteries.

Family	Material	Capacity	Average voltage	Polarization	Reference
		mAh/g	V *vs* Na^+/Na	Volts	
Carbons	Hard carbon**	250 mAh/g	0.3	0.05	[47]
Alloys	Ge/C**	369	0.3	0.5	[53]
	P/C**	1890	0.4	0.4	[54]
	Sb/C**	576	0.75	0.3	[55,56]
	Sn/C***	600 mAh/g	0.3	0.3	[57]
T^M oxides	Fe_2O_3	250	1.1	1.12	[60]
	Fe_3O_4**	250	1.3	1	[61,63]
	$Na_2Ti_3O_7$*	177	0.5	0.2	[68]
Organics	Carboxylates**	300	0.5	0.25	[72]
	Poly-Schiff**	170	0.85	0.3	[74]
	Oligomers	260	0.75	0.15	[75]

*Cycle 5 / **Cycle 10 / ***Cycle 100

Table 1.3 are summarizes the reported capacities and voltages for the most studied anode materials for sodium ion batteries. The main goal of an anode material is to operate at lower voltages with the highest possible capacities and in case of Na-ion batteries, being of low cost. The cyclability is also an important property in order to achieve high cycle life in the batteries. To date hard carbons are the materials that best meet most of the required electrochemical properties.

1.3- New anode materials for sodium ion batteries

The lack of a material that meets all criteria to be a good anode material in sodium ion batteries encourages the search of alternative negative electrodes suitable for a prototype of sodium ion battery. In the search of new materials that can operate as anode for lithium and sodium ion batteries, compounds such as titanates and different ordered carbons are the most preferred because the alkali metals can be easily inserted in their structure and the voltage at which the insertion is occurring is relatively low. Therefore, the aim of this work is to get new compounds which are able to improve the electrochemical performance and reduce the cost of the more used anode materials up to now. Two families of anode materials will be studied in this thesis:

1.3.1- $H_2Ti_3O_7$ as anode material for sodium ion batteries

$H_2Ti_3O_7$ (*C*2/*m*) has a structure closely related to that of $Na_2Ti_3O_7$ ($P2_1/m$) and it is synthesized by ionic exchange from the sodium titanate. During the proton/sodium exchange in acidic media there is a shift of the layers along the *b* axis resulting in a doubling of the unit cell and changing the symmetry. These changes are mostly reflected in the value of the *a* parameter of the unit cell in Figure 1.17.

Despite the smaller unit cell per formula unit. Regarding the better electrochemical behaviour, in terms of capacity, of $H_2Ti_3O_7$ vs $Na_2Ti_3O_7$ for lithium ion batteries[76] and the similar structure compared to $Na_2Ti_3O_7$, protonated titanate seems to be a very promising anode for sodium ion batteries. $H_2Ti_3O_7$ has a plateau at 1.5 Volts *vs* Li^+/Li so considering the theoretical difference of 0.3 Volts between the oxidation potential of both alkali metals, it could be possible that the plateau of the insertion of sodium ions could be at 1.2 Volts *vs* Na^+/Na, which is above the voltage for electrolyte decomposition. A big issue of this material is that although the capacity of the first cycle is 174 mAh/g (insertion of about 1.64 Li ions in the material), it decreases upon cycling. The working average voltage also decays 0.2 Volts in the first 3 cycles. This is good for anode materials but as *J. Akimoto et al.* suggested[76]. The drop in voltage could be due to the ionic exchange of some Li^+ and H^+ because they saw some $Li_2Ti_3O_7$ in the X-Ray Diffraction pattern of an electrode after cycling. This proton/lithium ion exchange could also be the reason of the capacity fading upon cycling. Moreover, the Li^+ ion insertion into the $Li_2Ti_3O_7$ structure obtained from $Na_2Ti_3O_7$[77], does not show good performance and it still continues with a big capacity fading.

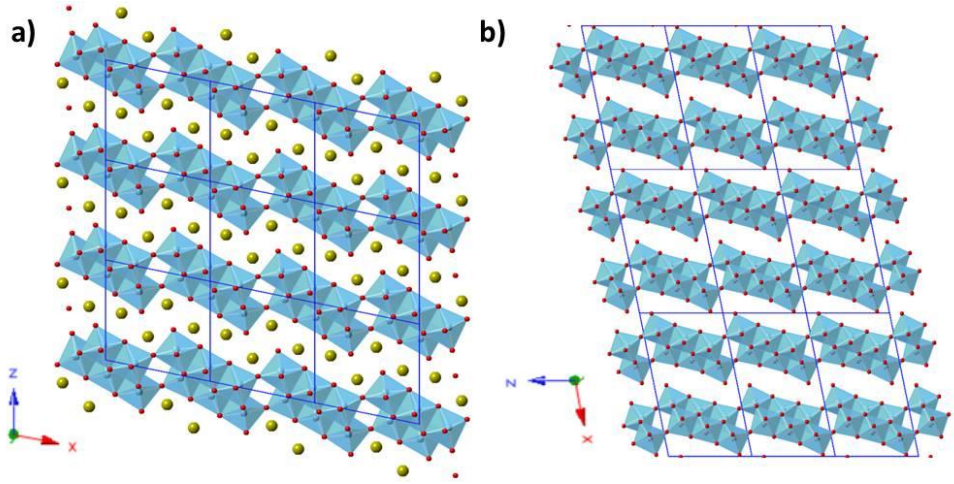

Figure 1.17. View along of the 101 plane of the structures of $Na_2Ti_3O_7$ (a) and $H_2Ti_3O_7$ (b) $A_2Ti_3O_7$. Red balls are the oxygen atoms, blue polyhedra are the TiO_6 octahedra and the yellow spheres are the sodium ions. Note that protons are missing in $H_2Ti_3O_7$, as their location was not known until this research work.

1.3.2- Transition-metal carbodiimides as anode materials for sodium and lithium ion batteries

Transition-metal carbodiimides are metalorganic compounds where transition metals are bonded to the molecular $(-N=C=N-)^{2-}$ group. They were synthesized for the first time in 2005[78]. Following Pearson´s Hard Soft Acid Base (HSAB) principle[79], and since all transition metals (M= Mn, Fe, Co, Ni, Cu and Zn) are hard cations, they prefer to form compounds with the carbodiimide ($^{-}N=C=N^{-}$) configuration. Nevertheless, metals such as lead [80] or silver[81] prefer the cyanamide configuration ($N\equiv C-N^{2-}$). Even so, it has been reported that mercury metal can adopt both configurations, depending on the pH of the solution at which the material has been synthesized[82]. Some examples of the different distances of metal-nitrogen (M-N), nitrogen-carbon (N-C) and the angle formed between nitrogen-carbon-nitrogen (NCN) due to the cyanamide or carbodiimide configuration can be seen in Table 1.4. There can be seen the differences in the configuration of the NCN bond: nitrogen-carbon distances and the angle of the NCN chain. While in iron carbodiimide the nitrogen-carbon bonds are equal and the length is 1.22 Å, which is in agreement with a nitrogen carbon double bond, in lead cyanamide both distances are not equal and the lengths are 1.25 Å and 1.17 Å correspondingly for the single and triple nitrogen carbon bonds. Also the steric hindrance plays a very important role and cations such proton that is very hard following the HSAB principle, prefers the cyanamide configuration ($N\equiv C-N^{2-}$).

Table 1.4. Characteristics of some examples of cyanamides and carbodiimides with the corresponding metal or hydrogen nitrogen distance, nitrogen-carbon distances (in the case of cyanamides s=single N-C and t=triple NΞC) and the angle formed by the NCN atoms.

Material	Type of NCN	M-N (Å)	N-C (Å)	N-C-N (º)	References
CaNCN	Carbodiimide	2.45	1.25	180	83
FeNCN	Carbodiimide	2.20	1.22	180	84
ZnNCN	Carbodiimide	1.98/2.04	1.23	177	85
HgNCN	Carbodiimide	2.07	1.23	172.4	86
HgNCN	Cyanamide	2.11	1.12 (s)/1.35 (t)	161	82
H_2NCN	Cyanamide	0.9	1.15 (s)/1.32 (t)	178.1	87
PbNCN	Cyanamide	2.33	1.17 (s)/1.25 (t)	178.4	88

The carbodiimide group ($^{-}$N=C=N^{-}) has many similarities with the oxide group (O^{2-}) and has been referred as a pseudochalcogenide. Both have the same charge (2-) and similar electronegativity values, namely 3.36 for the carbodiimide group and 3.47 for the oxide[89]. The structure of the transition metal carbodiimides present some similarities with the corresponding oxides with a small distortion due to the different size due to the monoatomic vs triatomic character of the oxide and carbodiimide group (Figure 1.18). However, the lower electronegativity values of carbodiimide group and larger charge delocalization cause the bond with transition metal to be more covalent[90]. In fact, seeing the molecular orbitals diagram of $[NCN]^{2-}$ ligand and the atomic orbital of the O^{2-} it can be seen that the electronic gap should be a bit narrower for carbodiimides than for oxides, because the HOMO (high occupancy molecular orbital) is at higher energy for the carbodiimide[90] group than for the oxide group (Figure 1.19).

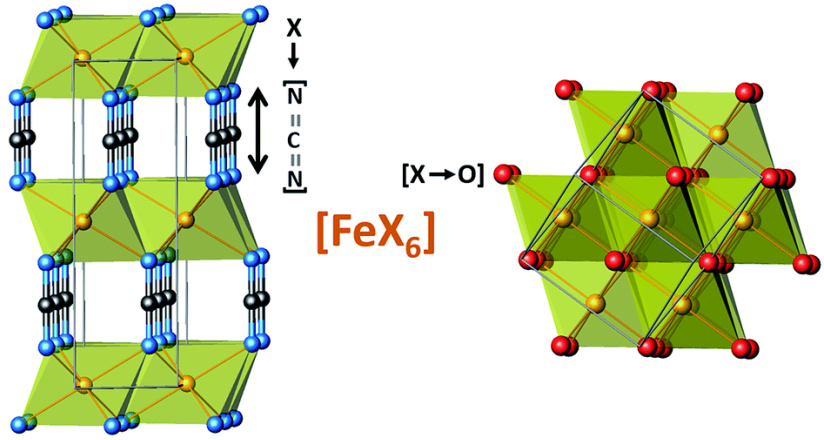

Figure 1.18. Iron carbodiimide and iron oxide structures. Light blue spheres are the nitrogen atoms, the black spheres are carbon atoms, the brown spheres are iron atoms and red spheres are oxygen atoms.

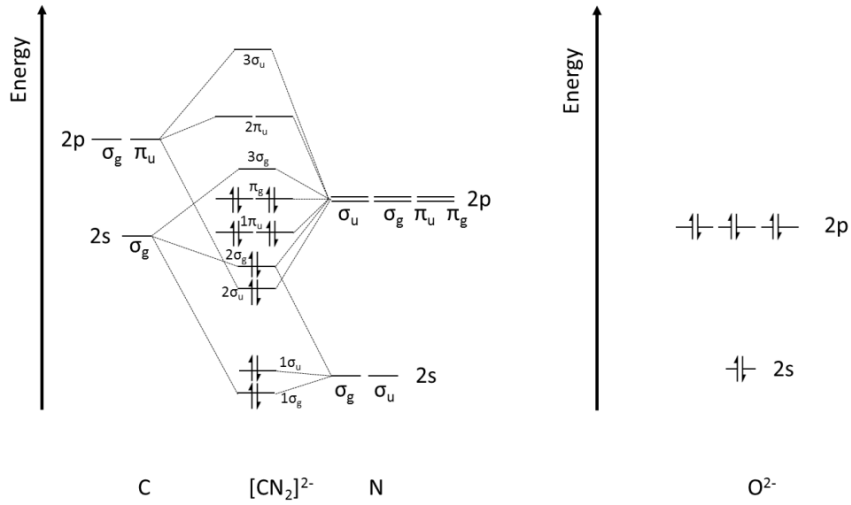

Figure 1.19. Schematic representation of the molecular orbitals of carbodiimide group in the left and the atomic orbitals of oxide group in the right.

The industrial application of these materials is still unknown. Up to now, the works based on transition-metal carbodiimides have been focused on reporting their synthesis methods, as well as their structure and studying the antiferromagnetic properties of these materials. While MnNCN, FeNCN, CoNCN, NiNCN and CuNCN show a typical antiferromagnetic behavior, ZnNCN does not show long range magnetic ordering, since the Zn^{2+} cation has a full shell electronic configuration with 10 electrons in its *d* orbital. It is important to mention the different Neel temperatures observed for each compounds. MnNCN and CuNCN exhibit low Néel temperatures (around 30 K[78] and 75 K[91] respectively). On the other hand, FeNCN, CoNCN and NiNCN show relatively high Néel temperatures (345 K[84], 255 K[92] and 360 K). Apart from their magnetism nothing has been reported about the carbodiimides as electrode for batteries or for any electrochemical energy storage application. Therefore, owing to their structure and other properties such as magnetism somewhat similar to that of oxides these compounds seem to be suitable for the study as electrode materials. Their small molecular weight could indeed results in a large specific capacity.

1.4- Scope of the thesis

In this thesis and in the search of new anode materials, the protonated titanate $H_2Ti_3O_7$ and the whole family transition-metal carbodiimides have been studied as anode materials for sodium ion batteries and their results are presented.

In this context, the electrochemical properties of a material that had already shown to be a successful anode in Lithium ion batteries, $H_2Ti_3O_7$, were measured for sodium batteries and the results are presented in this thesis. The main goal to achieve with this sample is to observe a plateau at 1.2 Volts *vs* Na^+/Na and a capacity close to the theoretical (C_{th}=208mAh/g for the insertion of 2 sodium ions).

On the other hand, the family of transition metal carbodiimides, somewhat analogues to transition metal oxides and not explored before for their electrochemical performance seem to be good candidates for the intercalation of lithium and sodium ions which could easily diffuse within the empty tunnels of these structures. The main drawback of transition metal carbodiimides is that they do not have any alkali metals in the structure and thus alkali ion de-insertion is not possible.

The main tasks that have been developed in this work are based on:

- Synthesis and physicochemical characterization of protonated titanate $H_2Ti_3O_7$ in order to elucidate the proton positions on the structure.
- Study of the electrochemical performance of protonated titanate as anode for sodium ion batteries.
- Synthesis and structural characterization of known transition-metal carbodiimides TMNCN (TM=Mn^{2+}, Fe^{2+} Co^{2+}, Ni^{2+}, Cu^{2+} and Zn^{2+}) as well as the novel solid solution $Co_{1-x}Fe_xNCN$ (x=0.36 and 0.46).
- Study of the electrochemical properties of transition-metal carbodiimides for first time as anodes for sodium/lithium ion batteries.
- Elucidate the mechanism of the electrochemical reaction of $H_2Ti_3O_7$ and transition-metal carbodiimide during their cycling in a Na-ion battery.
- Study the application of the characterized anodes in full cell using $Na_{0.67}[Mg_{0.005}Ni_{0.25}Mn_{0.7}]O_2$ as reference cathode material.

The introduction and rational behind this research work has been described in this chapter (Chapter 1). The performed synthesis methods, the assembly of electrochemical cells and characterization techniques used are explained in detail in Chapter 2. Chapter 3 covers the characterization of the structure and electrochemistry of protonated titanate ($H_2Ti_3O_7$). The study of transition metal carbodiimides were divided in three different chapters. In Chapter 4, late transition metal (copper and zinc) carbodiimides are contrasted in detail due to the differences in their electrochemical behaviours. Chapter 5 covers d5-d8 manganese, iron, cobalt and nickel carbodiimides, which exhibit similar electrochemical properties, as well as a global discussion of the electrochemical performances of all transition metal carbodiimides. The $Co_{1-x}Fe_xNCN$ solid solution is characterized in depth in Chapter 6. In Chapter 7 the operation of the studied anodes in a full cell is described. Finally, the general conclusions derived from this work are detailed in Chapter 8.

1.5- References

[1] BP Statistical Review of World Energy 2016; bp.com/statisticalreview (Access June 2016)

[2] Electric Power Research Institute: Electric Energy Storage Technology Options White Paper, 2010.

[3] B. Steffen and C. Weber; "Optimal operation of pumped-hydro storage plants with continuous time-varying power prices"; *European Journal of Operational Research*, 2016, **252** (1) 308.

[4] C. Dötsch: Electrical energy storage from 100 kW – State of the art technologies, fields of use. 2nd Int. Renewable Energy Storage Conference, Bonn/Germany, 22 Nov 2007.

[5] http://blog.genport.it/?p=133 (Access May 2016)

[6] X. Luo, J. Wang, M. Dooner and J. Clarke; "Overview of current development in electrical energy storage technologies and the application potential in power system operation"; *Applied Energy* 2015, **137** (1), 511.

[7] J. L. Sudworth; "The sodium/nickel chloride (ZEBRA) battery"; *J.Power Sources* 2001, **100**, 149.

[8] Y. Nishi; "Lithium ion secondary batteries; past 10 years and the future"; *J. Power Sources*, 2001, **100**, 101.

[9] J. M. Tarascon and M. Armand; "Issues and challenges facing rechargeable lithium batteries"; *Nature*, 2001, **414**, 359.

[10] M. S. Whittingham; "Electrical energy storage and intercalation chemistry."; *Science*, 1976, **192**, 1126.

[11] M. S. Whittingham; "Chemistry of intercalation compounds: metal guests in chalcogenide hosts"; *Prog. Solid State Chem.*, 1978, **12**, 41.

[12] B. L. Ellis, W. R. M. Makahnouk, Y. Makimura, K. Toghill and L. F. Nazar; "A multifunctional 3.5 V iron-based phosphate cathode for rechargeable batteries"; *Nat. Mater.*, 2007, **6**, 749.

[13] A. Ponrouch, D. Monti, A. Boschin, B. Steen, P. Johansson and M. R. Palacın; "Non-aqueous electrolytes for sodium-ion batteries"; *J. Mater. Chem. A*, 2015, **3**, 22.

[14] V. Palomares, P. Serras, I. Villaluenga, K. Hueso, J. Carretero-Gonzalez, T. Rojo; "Na-ion batteries, recent advances and present challenges to become low cost energy storage systems"; *Energy and Environ. Sci.*, 2012, **5**, 5884.

[15] V. Palomares, M. Casas-Cabanas, E. Castillo-Martinez, M. H. Man and T. Rojo; "Update on Na-based battery materials. A growing research path"; *Energy Environ. Sci.*, 2013, **6**, 2312.

[16] S. Kuksenko; "Aluminum Foil as Anode Material of Lithium-Ion Batteries: Effect of Electrolyte Compositions on Cycling Parameters"; Russian Journal of Electrochemistry, 2013, **49** (1), 67.

[17] K. Mizushima; P. C. Jones; P. J. Wiseman; J. B. Goodenough; "Li_xCoO_2 ($0<x\leq1$): a new cathode material for batteries of high energy density."; *Mater. Res. Bull.*, 1980, **15**, 783.

[18] C. Delmas, J. J. Braconnier, C. Fouassier, P. Hagenmuller; "Electrochemical intercalation of sodium in Na_xCoO_2 bronzes"; *Solid State Ionics,* 1981, **3–4**, 165.

[19] M. Dahbi, N. Yabuuchi, K. Kubota, K. Tokiwac and S. Komaba; "Negative electrodes for Na-ion batteries"; *Phys. Chem. Chem. Phys*., 2014, **16**, 15007.

[20] http://www.icispricing.com/il_shared/Samples/SubPage63.asp (Access July 2016)

[21] R. S. Carmichael, "Practical Handbook of Physical Properties of Rocks and Minerals"; CRC Press: Boca Raton, FL, 1989.

[22] N. Yabuuchi, K. Kubota, M. Dahbi, S. Komaba; "Research Development on Sodium-Ion Batteries"; *Chem. Rev.* 2014, **114**, 11636.

[23] A. Yamada, S. C. Chung and K. Hinokuma; "Optimized $LiFePO_4$ for Lithium Battery Cathodes"; *J. Electrochem. Soc.*, 2001, **148**, A224.

[24] P. Serras, V. Palomares, A. Goñi, I. Gil de Muro, P. Kubiak, Luis Lezama and T. Rojo; "High voltage cathode materials for Na-ion batteries of general formula $Na_3V_2O_{2x}(PO_4)_2F_{3-2x}$"; *J. Mater. Chem.*, 2012, **22**, 22301.

[25] H. Pan, Y. S. Hu and L. Chen; "Room-temperature stationary sodium-ion batteries for large-scale electric energy storage"; *Energy Environ. Sci.*, 2013, **6**, 2338.

[26] Z. M. Liu; X. Y. Wang; Y. Wang; A. P. Tang; S. Y. Yang; L. F. He; "Preparation of $NaV_{1-x}Al_xPO_4F$ cathode materials for application of sodium-ion battery"; *Trans. Nonferrous Met. Soc. China* 2008, **18**, 346.

[27] H. Zhuo; X. Wang; A. Tang; Z. Liu; S. Gamboa; P. J. Sebastian; "The preparation of $NaV_{1-x}CrxPO_4F$ cathode materials for sodium-ion battery"; *J. Power Sources,* 2006, **160**, 698.

[28] K. Chihara; A. Kitajou,; I. D. Gocheva; S. Okada; J. I. Yamaki; "Cathode properties of $Na_3M_2(PO_4)_2F_3$ [M = Ti, Fe, V] for sodium-ion batteries"; *J. Power Sources,* 2013, **227**, 80.

[29] R. A. Shakoor, D. H. Seo, H. Kim, Y. U. Park, J. Kim, S. W. Kim, H. Gwon, S. Lee and K. Kang; "A combined first principles and experimental study on $Na_3V_2(PO_4)_2F_3$ for rechargeable Na batteries"; *J. Mater. Chem.*, 2012, **22**, 20535.

[30] Y. U. Park; D. H. Seo; H. S. Kwon; B. Kim; J. Kim; H. Kim; I. Kim; H. I. Yoo and K. Kang; "A New High-Energy Cathode for a Na-Ion Battery with Ultrahigh Stability"; *J. Am. Chem. Soc.* 2013, **135**, 13870.

[31] M. H. Man, E. Gonzalo, G. Singh and T. Rojo; "A comprehensive review of sodium layered oxides: powerful cathodes for Na-ion batteries"; *Energy Environ. Sci.,* 2015, **8**, 81.

[32] C. Delmas, C. Fouassier and P. Hagenmuller, "Structural classification and properties of the layered oxides"; *Physica B+C*, 1980, **99**, 81.

[33] A. Mendiboure, C. Delmas and P. Hagenmuller, "Electrochemical intercalation and deintercalation of Na_xMnO_2 bronzes"; *J. Solid State Chem.*, 1985, **57**, 323.

[34] N. Yabuuchi, M. Kajiyama, J. Iwatate, H. Nishikawa, S. Hitomi, R. Okuyama, R. Usui, Y. Yamada and S. Komaba; "P2-type $Na_x[Fe_{1/2}Mn_{1/2}]O_2$ made from earth-abundant elements for rechargeable Na batteries" *Nature Materials,* 2012, **11**, 512.

[35] E. Peled, C. Menachem, D. Bar-Tow and A. Melman; "Improved Graphite Anode for Lithium-Ion Batteries"; *J. Electrochem. Soc*., 1996, **143** (1), L4.

[36] V. L. Chevrier and G. Ceder; "Challenges for Na-ion Negative Electrodes"; *J. Electrochem. Soc*., 2011, **158**, A1011.

[37] H. Kang, Y. Liu, K. Cao, Y. Zhao, L. Jiao, Y. Wang and H. Yuan; "Update on anode materials for Na-ion batteries"; *J. Mater. Chem. A*, 2015, **3**, 17899.

[38] H. Kim, J. Hong, G. Yoon, H. Kim, K. Y. Park, M. S. Park, W. S. Yoon, and K. Kang; "Sodium intercalation chemistry in graphite"; *Energy Environ. Sci.*, 2015, **8**, 2963.

[39] J. R. Dahn, U. von Sacken, M. W. Juzkow, and H. Al-Janaby; *J. Electrochem. Soc*., 1991, **138** (8), 2207.

[40] J. R. Dahn, R. Fong and M.J. Spoon; "Suppression of staging in lithium-intercalated carbon by disorder in the host"; *Physical Review B,* 1990, **42** (10) 6424.

[41] David Linden and Thomas B. Reddy, "Handbook of batteries"; McGraw-Hill, 3rd EdNew York, 2002.

[42] B. Jache and P. Adelhelm, "Use of Graphite as a Highly Reversible Electrode with Superior Cycle Life for Sodium-Ion Batteries by Making Use of Co-Intercalation Phenomena"; *Angewandte Chemie Int. Ed.,* 2014, **53** (38), 10169.

[43] B. Jache, J. O. Binder, T. Abe and P. Adelhelm; "A comparative study on the impact of different glymes and their derivatives as electrolyte solvents for graphite co-intercalation electrodes in lithium-ion and sodium-ion batteries"; *Phys. Chem. Chem. Phys.*, 2016, **18**, 14299.

[44] D. A. Stevens and J. R. Dahn; "High Capacity Anode Materials for Rechargeable Sodium-Ion Batteries"; *J. Electrochem. Soc.*, 2000, **147**, 1271.

[45] S. Komaba, W. Murata, T. Ishikawa, N. Yabuuchi, T. Ozeki, T. Nakayama, A. Ogata, K. Gotoh and K. Fujiwara; "Electrochemical Na Insertion and Solid Electrolyte Interphase for Hard-Carbon Electrodes and Application to Na-Ion Batteries"; *Adv. Funct. Mater.*, 2011, **21**, 3859.

[46] C. Bommier, T.W. Surta, M. Dolgos and X. Ji; "New Mechanistic Insights on Na-Ion Storage in Nongraphitizable Carbon"; *Nano Lett.,* 2015, **15** (9), 5888.

[47] J. Zhao, L. Zhao, K. Chihara, S. Okada, J.I Yamaki, S. Matsumoto, S. Kuze and K. Nakane; "Electrochemical and thermal properties of hard carbon-type anodes for Na-ion batteries"; *J. Power Sources,* 2013, **244**, 752.

[48] D. A. Stevens and J. R. Dahn; "The Mechanisms of Lithium and Sodium Insertion in Carbon Materials"; *J. Electrochem. Soc*., 2001, **148**, A803.

[49] K. Gotoh, T. Ishikawa, S. Shimadzu, N. Yabuuchi, S. Komaba, K. Takeda, A. Goto, K. Deguchi, S. Ohki, K. Hashi, T. Shimizu and H. Ishida; "NMR study for electrochemically inserted Na in hard carbon electrode of sodium ion battery"; *J. Power Sources* 2013, **225**, 137.

[50] C. K. Chan, H. Peng, G. Liu, K. McIlwrath, X. F. Zhang, R. A. Huggins and Y. Cui; "High-performance lithium battery anodes using silicon nanowires" *Nature Nanotechnology,* 2008, **3**, 31.

[51] J. W. Wang, X. H. Liu, S. X. Mao and J. Y. Huang; "Microstructural Evolution of Tin Nanoparticles during In Situ Sodium Insertion and Extraction"; *Nano Lett.*, 2012, **12**, 5897.

[52] M. K. Datta, R. Epur, P. Saha, K. Kadakia, S. K. Park, P. N. Kumta; "Tin and graphite based nanocomposites: Potential anode for sodium ion batteries"; *J. Power Sources* 2013, **225**, 316.

[53] A. Kohandehghan, K. Cui, M. Kupsta, J. Ding, E. Memarzadeh-Lotfabad, W. P. Kalisvaart and D. Mitlin; "Activation with Li Enables Facile Sodium Storage in Germanium"; *Nano Lett.*, 2014, **14**, 5873.

[54] Y. Kim, Y. Park, A. Choi, N. S. Choi, J. Kim, J. Lee, J. M. Ryu and K. T. Lee; "An Amorphous Red Phosphorus/Carbon Composite as a Promising Anode Material for Sodium Ion Batteries"; *Adv. Mater.*, 2013, **25**, 3045.

[55] X. Zhao, S. A. Vail, Y. Lu, J. Song, W. Pan, D. R. Evans and J. J. Lee; "Antimony/Graphitic Carbon Composite Anode for High-Performance Sodium-Ion Batteries"; *ACS Appl. Mater. Interfaces*, 2016, **8** (22), 13871.

[56] A. Darwiche, C. Marino, M. T. Sougrati, B. Fraisse, L. Stievano and L. Monconduit; "Better cycling performances of bulk Sb in Na-ion batteries compared to Li-ion systems: an unexpected electrochemical mechanism." *J. Am. Chem. Soc.*, 2012, **134**, 20805.

[57] C. Kim, K. Y Lee, I. Kim, J. Park, G. Cho, K. W. Kim, J. H. Ahn, H. J. Ahn; "Long-term cycling stability of porous Sn anode for sodium-ion batteries"; *J. Power Sources* 2016, **317**, 153.

[58] L. Baggetto, J. K. Keum, J. F. Browning and G. M. Veith; "Germanium as negative electrode material for sodium-ion batteries"; *Electrochem. Commun.*, 2013, **34**, 41.

[59] Z. Jian, B. Zhao, P. Liu, F. J. Li, M. B. Zheng, M. W. Chen, Y. Shi and H. S. Zhou; "Fe_2O_3 nanocrystals anchored onto graphene nanosheets as the anode material for low-cost sodium-ion batteries"; *Chem. Commun.*, 2014, **50**, 1215.

[60] M. Valvo, F. Lindgren, U. Lafont, F. Björefors and K. Edström; "Towards more sustainable negative electrodes in Na-ion batteries via nanostructured iron oxide"; *J. Power Sources*, 2014, **245**, 967.

[61] S. Hariharan, K. Saravanan and P. Balaya; "A rationally designed dual role anode material for lithium-ion and sodium-ion batteries: case study of eco-friendly Fe_3O_4"; *Phys. Chem. Chem. Phys.,* 2013, **15**, 2945.

[62] Y. Fu, Q. Wei, X. Wang, G. Zhang, H. Shu, X. Yang, A. C. Tavares and S. Sun; "A facile synthesis of Fe_3O_4 nanoparticles/graphene for high-performance lithium/sodium-ion batteries"; *RSC Adv.*, 2016, **6**, 16624.

[63] A. Maazaz, C. Delmas and P. Hagenmuller; "A study of the Na_xTiO_2 system by electrochemical deintercalation"; *J. Inclus. Phenom.,* 1983, **1**, 45.

[64] C. Delmas, F. Cherkaoui, A. Nadiri and P. Hagenmuller; "A nasicon-type phase as intercalation electrode: $NaTi_2(PO_4)_3$"; *Mater. Res. Bull.* 1987, **22**, 631.

[65] M. Zanini, J. L. Shaw and G. J.Tennenhouse; "The Behavior of Na - TiS_2 and Na - TiS_3 as Solid Solution Electrodes"; *J. Electrochem. Soc*. 1981, **128**, 1647.

[66] Z. Liang, P. Hui-Lin, H. Young-Sheng, L.Hong and C. Li-Quan; "Spinel lithium titanate ($Li_4Ti_5O_{12}$) as novel anode material for room-temperature sodium-ion battery"; *Chinese Phys. B,* 2012, **21**, 079901.

[67] A. Rudola, K. Saravanan, C. W. Mason and P. Balaya; "$Na_2Ti_3O_7$: an intercalation based anode for sodium-ion battery applications"; *J. Mater. Chem. A* 2013, **1**, 2653.

[68] P. Senguttuvan, G. Rousse, V. Seznec, J. M. Tarascon and M. R. Palacin; "$Na_2Ti_3O_7$: Lowest Voltage Ever Reported Oxide Insertion Electrode for Sodium Ion Batteries"; *Chem. Mater*. 2011, **23**, 4109.

[69] H. Pan, X. Lu; X. Yu, Y.S. Hu, H. Li, X. Q. Yang and L. Chen; "Sodium Storage and Transport Properties in Layered $Na_2Ti_3O_7$ for Room-Temperature Sodium-Ion Batteries"; *Adv. Energy Mater.* 2013, **3**, 1186.

[70] A. Rudola, K. Saravanan, S. Devaraj, H. Gong and P. Balaya; "$Na_2Ti_6O_{13}$: a potential anode for grid-storage sodium-ion batteries"; *Chem. Commun.*, 2013, **49**, 7451.

[71] M. Armand, S. Grugeon, H. Vezin, S. Laruelle, P. Ribiere, P. Poizot and J. M. Tarascon; "Conjugated dicarboxylate anodes for Li-ion batteries"; *Nat. Mater.*, 2009, **8**, 120.

[72] Y. Park, D.S. Shin, S. H. Woo, N. S. Choi, K. H. Shin, S. M. Oh, K. T. Lee, and S. Y. Hong; "Sodium Terephthalate as an Organic Anode Material for Sodium Ion Batteries"; *Adv. Mater.*, 2012, **24,** 3562.

[73] Y. Wang, K. Kretschmer, J. Zhang, A.K. Mondal, X. Guo and G. Wang; "Organic sodium terephthalate@graphene hybrid anode materials for sodium-ion batteries"; *RSC Adv.*, 2016, **6**, 57098.

[74] E. Castillo-Martínez, J. Carretero-González, M. Armand: "Polymeric Schiff bases as low-voltage redox centers for sodium-ion batteries."; *Angew. Chem. Int. Ed.*, 2014, **53**, 5445.

[75] M. Lopez-Herraiz, E. Castillo-Martinez, J. Carretero-Gonzalez, J. Carrasco, T. Rojo and M. Armand; "Oligomeric-Schiff bases as negative electrodes for sodium ion batteries: unveiling the nature of their active redox centers"; *Energy Environ. Sci*., 2015, **8**, 3233.

[76] J. Akimoto, K. Chiba; N. Kijima, H. Hayakawa, S. Hayashi, Y. Gotoh and Y. Idemoto; "Soft-Chemical Synthesis and Electrochemical Property of $H_2Ti_{12}O_{25}$ as a Negative Electrode Material for Rechargeable Lithium-Ion Batteries"; *J. Electrochem. Soc.* 2011, **158** (5), 546.

[77] K. Chiba, N. Kijima, Y. Takahashi, Y. Idemoto and J. Akimoto; "Synthesis, structure, and electrochemical Li-ion intercalation properties of $Li_2Ti_3O_7$ with $Na_2Ti_3O_7$-type layered structure"; *Solid State Ionics,* 2008, **178**, 1725.

[78] X. Liu, M. Krott, P. Müller, C. Hu, H. Lueken and R. Dronskowski; "Synthesis, Crystal Structure, and Properties of MnNCN, the First Carbodiimide of a Magnetic Transition Metal"; *Inorg. Chem.;* 2005, **44** (9), 3001.

[79] R. G. Pearson, Chemical Hardness, Wiley-VCH, Weinheim, Germany, 1997.

[80] M. J. Cooper; "The structures of some inorganic cyanamides. II. The structure of lead cyanamide"; *Acta Crystallogr*. 1964, **17**, 1452.

[81] M. Becker, J. Nuss and M. Jansen; "Crystal Structure and Spectroscopic Data of Silver Cyanamide"; *Z. Naturforsch. B,* 2000, **55**, 383.

[82] X. Liu, P. Muller, P. Kroll, and R. Dronskowski; "Synthesis, Structure Determination, and Quantum-Chemical Characterization of an Alternate HgNCN Polymorph"; *Inorg. Chem.*, 2002, **41** (16) 4259.

[83] Y. Yamamoto, K. Kinoshita, K. Tamaru and T. Yamanaka; "Redetermination of the Crystal Structure of Calcium Cyanamide"; *Bulletin of the Chemical Society of Japan,* 1958, **31**, 501.

[84] X. Liu, L. Stork, M. Speldrich, H. Lueken and R. Dronskowski; "FeNCN and $Fe(NCNH)_2$: Synthesis, Structure, and Magnetic Properties of a Nitrogen-Based Pseudo-oxide and -hydroxide of Divalent Iron"; *Chem. Eur. J.* 2009, **15**, 1558.

[85] K. Morita, G. Mera, K. Yoshida, Y. Ikuhara, A. Klein, H. J. Kleebe and R. Riedel; "Thermal stability, morphology and electronic band gap of Zn(NCN)."; *Solid State Sci.* 2013, **23**, 50.

[86] M. Becker and M. Jansen; "Synthese und Charakterisierung von Quecksilbercyanamid"; *Z. Anorg. Allg. Chem.* 2000, **626** (7), 1639.

[87] M. T. Nguyen, N. V. Riggs, L. Radom, M. Winnewisser, B. P. Winnewisser and M. Birk; "Molecular structure and spectroscopic properties of carbodiimide (HN=C=NH)"; *Chemical Physics*, 1988, **122**, 305.

[88] X. Liu, A. Decker, D. Schmitz and R. Dronskowski; "Crystal Structure Refinement of Lead Cyanamide and the Stiffness of the Cyanamide Anion"; *Z. Anorg. Allg. Chem.* 2000, **626** (1)**,** 103.

[89] H. D. Schädler, L. Jäger and I. Senf; "Pseudoelementverbindungen. V. Pseudochalkogene — Versuch der empirischen und theoretischen Charakterisierung eines Konzeptes"; *Z. Anorg. Allg. Chem*. 1993**, 619**, 1115.

[90] T. D. Boyko, R. J. Green, R. Dronskowski and A. Moewes; "Electronic Band Gap Reduction in Manganese Carbodiimide: MnNCN"; *J. Phys. Chem. C* 2013, **117**, 12754.

[91] X. Liu, , R. K. Kremer, M. Ahrens, C. Lee, M. H. Whangbo and R. Dronskowski; *J. Phys. Chem. C.,* 2008, **112** (29) 11013.

[92] M. Krott, X. Liu, B. P. T. Fokwa, M. Speldrich, H. Lueken and R. Dronskowski; "Synthesis, Crystal-Structure Determination and Magnetic Properties of Two New Transition-Metal Carbodiimides: CoNCN and NiNCN"; *Inorg. Chem.* 2007, **46**, 2204.

2.- Experimental: Synthesis methods and characterization techniques

In this work, two different families of compounds have been studied: $H_2Ti_3O_7$ (titanates) and transition-metal carbodiimides of formula T^MNCN. The different synthesis routes used to obtain the each desired product are explained in the following sections. The cell assembly and the different characterization techniques with the experimental conditions are described below.

2.1- Synthesis methods

2.1.1 Synthesis of $H_2Ti_3O_7$

The preparation of $H_2Ti_3O_7$ is not possible to be carried out by direct synthesis. That is why the most common synthesis route described in the literature is a two steps reaction: firstly the sodium titanate, $Na_2Ti_3O_7$ is synthesized; and from it, an ionic exchange of sodium ions by protons is performed in acidic media[1].

2.1.1.1 Precursor: Sodium titanate

Sodium titanate ($Na_2Ti_3O_7$) was synthesized by ceramic method and freeze drying. Both methods provide the aimed product. However, with freeze drying more amount of sample was prepared.

An aqueous solution was prepared using 10 mL of water and sodium carbonate ($Na_2CO_3H_2O$- SIGMA ALDRICH, CAS number 497-19-8) and 5% of excess and anatase (TiO_2- ALFA AESAR, CAS number 1317-70-0) as reactants was prepared to be used in the freeze drying process. This solution was stirred using 3 zirconia balls of 7 mm diameter in plastic jar with a Speed Mixer at 4000 revolutions per minute for 5 minutes. The procedure was repeated 3 times. The obtained homogenous solution was frozen with liquid nitrogen and placed inside the freeze drier (Figure 2.1a), where the temperature was set to -40 ^oC and the chamber was submitted to vacuum. After one day of evacuating at low temperature, the solution was heated till room temperature keeping the vacuum. The boiling of the solution was avoided (scheme of Figure 2.1b) and a good mixture of the powders was obtained. This way, the reactants were equally dispersed avoiding the aggregations formed when the water is boiled and keeping the structure of the freeze dried product. A pellet of this mixture was heated up to 800 ^oC for 12 hours[2]. This heating procedure was performed twice in order to obtain a $Na_2Ti_3O_7$ material as a single phase and with higher crystallinity. The characterization of this material is described in Chapter 4.

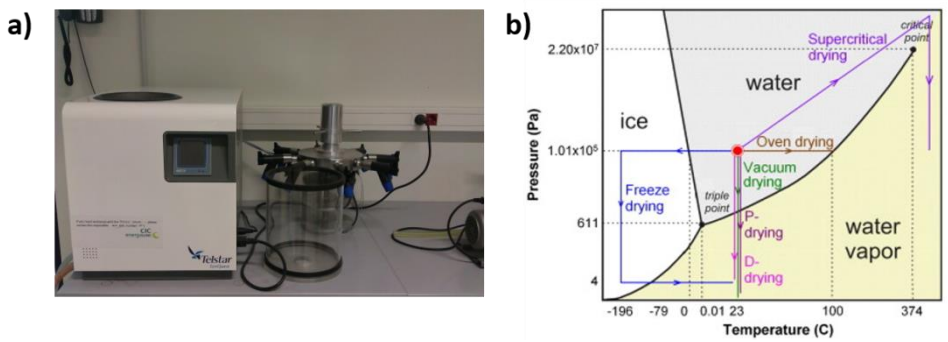

Figure 2.1. Freeze dryer used in the synthesis (a) and the schema of the phase diagram in function of temperature and pressure of the water (b).

2.1.1.2 Protonated titanate

Protonated titanate ($H_2Ti_3O_7$) was synthesized from $Na_2Ti_3O_7$ by ionic exchange in 200 mL in 0.1 M nitric acid solution and maintained at 60 ^oC for one day. Next day, the solution was filtered with an acid resistant Teflon filter (Santorius Stedim pore size 0.45 μm) under vacuum and the white powder was collected. The characterization of this sample indicated the presence of pure phases and it is compared with the precursor ($Na_2Ti_3O_7$) in Chapter 3.

2.1.2 Synthesis of transition metal carbodiimides

Transition-metal carbodiimides were synthesized by different routes. Manganese carbodiimide (MnNCN) was synthesized through two different routes. One is based on the solid state route by a stoichiometric mixture of zinc carbodiimide and manganese chloride as reported by *X.Liu et al.*[3]. The second method is performed through ionic exchange in organic media using lithium carbodiimide as precursor. Iron, cobalt and nickel[5] carbodiimide (FeNCN, CoNCN and NiNCN) were synthesized by Schlenk techniques following the synthesis routes described by *X.Liu et al.*[4] in the case of FeNCN and *M.Krott et al.*[5] for CoNCN and NiNCN. Solid solution carbodiimides containing two different transition metals were attempted for the first time also by Schlenk techniques from their respective hydrogenocyanamides. Copper and zinc carbodiimide (CuNCN and ZnNCN) were synthesized in aqueous solution at room temperature in agreement with the reported synthesis methods for these compounds by *X. Liu et al.*[6] and *K. Morita et al.*[7] respectively.

2.1.2.1 Precursors

2.1.2.1.1 Lithium carbodiimide

Lithium carbodiimide (Li_2NCN) was synthesized by organic addition[8] of 2 M n-butyllithium (n-BuLi) in cyclohexane (C_4H_9Li-SIGMA ALDRICH, CAS 109-72-8) to cyanamide (H_2NCN-SIGMA ALDRICH, CAS number 420-04-2) isolated in a flask with nitrogen atmosphere. A 15% of excess of n-BuLi was added because the molarity of the solution is usually lower than labelled. This flask was inside a bath of dry ice and acetone which yielded a temperature of -78 ^oC. The low temperature of the flask avoids the violent reaction of the n-butyllithium although the reaction takes much longer (few hours). After 4 hours, the reaction was completed and the flask was directly transferred to the Glovebox in order to avoid contact with air. There, by centrifugation, the lithium carbodiimide (yellowish powder) was separated from the organic solvent cyclohexane. The characterization of this compound is described in the annex.

2.1.2.1.2 Zinc carbodiimide

Zinc carbodiimide (ZnNCN) was synthesized by the addition of a solution of zinc chloride ($ZnCl_2$- SIGMA ALDRICH, CAS number 7646-85-7) in water and ammonia, into another solution of H_2NCN dissolved in water in stoichiometric ratio. The mixture was stirred for 3 hours stirring at room temperature the ZnNCN forming a white precipitate[7]. The white powder was filtered and the characterization of this compound is described in Chapter number 4. This compound was not only used as a precursor for other synthesis methods, but also tested as anode material for sodium and lithium ion batteries (Chapter 4).

2.1.2.2 Manganese carbodiimide

Manganese carbodiimide (MnNCN) was synthesized through two different routes.
The first one was performed by mixing synthesized ZnNCN ground with manganese chloride[3] ($MnCl_2$ – SIGMA ALDRICH, CAS number 13446-3-9). The mixture was compressed into a pellet and placed in a copper envelope. The envelope was heated till 600 ^oC for 36 hours under argon atmosphere. Figure 2.2 shows the different colours of the pellet before and after the treatment.

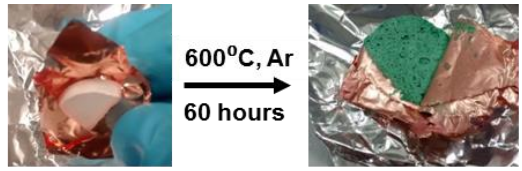

Figure 2.2. A mixture of manganese chloride and cyanamide pellet inside a copper envelope before (left) and after (right) the thermal treatment.

The second route consisted on an ionic exchange of stoichiometric amounts of Li_2NCN (0.163 g, 3 mmol) and $MnCl_2$ (0.377 g, 3 mmol) in 10 mL of THF as solvent (C_4H_8O-SIGMA ALDRICH, CAS 109-99-9) at room temperature. This new method of synthesis of MnNCN was performed inside the glove box (see Figure 2.3). After six hours stirring the resulting grey powder was centrifuged three times for 15 minutes and the THF was removed. The characterization of the synthesized powders from both synthesis routes is detailed in Chapter 5.

Figure 2.3. A mixture of manganese chloride and lithium carbodiimide inside the glovebox.

2.1.2.3 Iron, cobalt, nickel and $Co_{1-x}Fe_xNCN$ solid solution carbodiimides

Iron, cobalt and nickel carbodiimide were synthesized in a 2 step process by Schlenk techniques as *X.Liu et al.*[4] and *M.Krott et al*.[5] reported. The same procedure was followed for the synthesis of solid solutions of iron with cobalt. In the first step hydroge metal cyanamides (HT^MNCN) are formed. They are prepared by mixing the stoichiometric amount of chlorides ($FeCl_2$- SIGMA ALDRICH CAS number 7758-94-3, $CoCl_2$- SIGMA ALDRICH CAS number 7646-79-9 and $NiCl_2$- SIGMA ALDRICH CAS number 7718-54-9) and cyanamide from SIGMA ALDRICH in ammonia solution (25% in weight). This solution was prepared in Schlenk flask which allowed filtering inside the flask, avoiding the exposure to the air. It was important that water was degassed overnight. With that purpose, a nitrogen flow was passed at the same time that water was refluxed. The powder filtered inside a Schlenk flask (without exposure with the air) was transferred to the Glovebox. In

the second step, the prepared hydrogen carbodiimides were mixed with an eutectic mixture of lithium chloride: potassium chloride (LiCl- SIGMA ALDRICH CAS number 7447-41-8: KCl- SIGMA ALDRICH CAS number 7447-40-7) (56:44 in weight m.p=353 ^{o}C see Figure 2.4a) and heated up to 370 ^{o}C in vacuum inside a Schlenk ampoule (Figure 2.4b and Figure 2.4c). The obtained brown powders were washed with water for removing all the salts from the molten species. The characterization of these compounds is described in Chapter 5 for FeNCN, CoNCN and NiNCN; and in Chapter 6 for the solid solution samples.

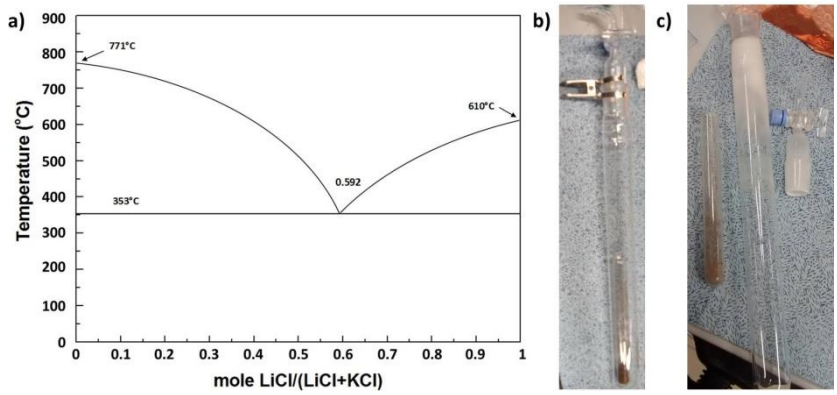

Figure 2.4. Phase diagram of LiCl:KCl (a), Schlenk flask assembled (b) and Schlenk flask piece by piece (c) with the synthesized powder of iron carbodiimide.

2.1.2.4 Copper carbodiimide

Copper carbodiimide was prepared in aqueous solution using the procedure described by *X. Liu et al.*[6]. Copper chloride ($CuCl_2$- SIGMA ALDRICH, CAS number 7447-39-4) were dissolved in 5 mL of water and it was mixed with of cyanamide in a 1:2 molar ratio, turning the solution into dark green due to the formation of $[Cu(NCNH_2)_2(H_2O)_2]^{2+}$ (Figure 2.5b). Then, 5 mL of an aqueous solution of 10 mmol of sodium sulphite (Na_2SO_3- SIGMA ALDRICH, CAS number 7757-83-7) were added in order to reduce the copper from oxidation state 2 to 1, appearing the compound $Cu(NCNH_2)Cl$ and getting the solution a light green color (Figure 2.5c). 15 mL of concentrated ammonia solution (25% weight) was used to keep the pH at around 10 obtaining the precipitation of the $Cu_4(NCN)_2NH_3$ compound (Figure 2.5d). The solution was left stirring overnight showing the oxidation of $Cu_4(NCN)_2NH_3$ (white compound precipitated in blue solution) to a black powder CuNCN (see Figure 2.5e). This powder was filtered applying vacuum and its characterization is detailed in Chapter 4.

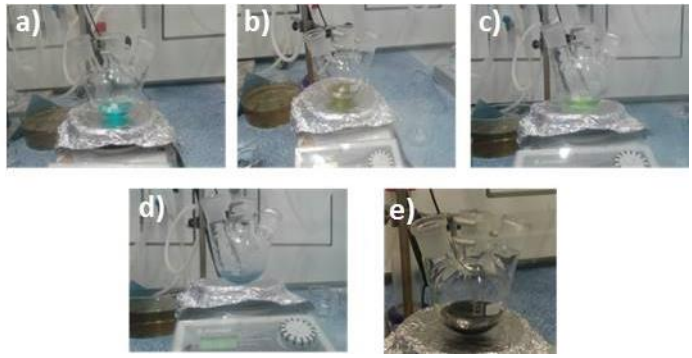

Figure 2.5. Synthesis of CuNCN step by step showing the different color of the solutions due to the different intermediates formed.

2.2- Cell preparation

2.2.1 Electrode preparation

Laminates. Electrode preparation was performed using copper or aluminium foil as current collector for measuring the materials for lithium or sodium ion batteries respectively. The slurry was prepared mixing 400 mg of material in the case of titanates and 300 mg in the case of carbodiimides. 10% of carbon SUPER C65 was added to the titanate phase. Carbodiimides needed more than 20% and a mixture of Ketjen black: Super C65 (50:50) was used as conductive carbon. In both cases 10% of PVdF was used as binder in order to improve the intergranular contact between the active material, conductive carbon and current collector. To prepare the slurry, the PVdF was dissolved in 2-3 mL of N-methyl-2-pyrrolidone in a vial with stirring for 3 hours. The mixture of active material and conductive carbon, which had been previously grinded, was added to the vial. After one hour stirring, the viscose solution was dropped to the copper or aluminium foil and with the desired thickness (usually 250 µm) was casted by doctor Blade. This laminate was left frying under vacuum and heated at 80 ^{o}C overnight.

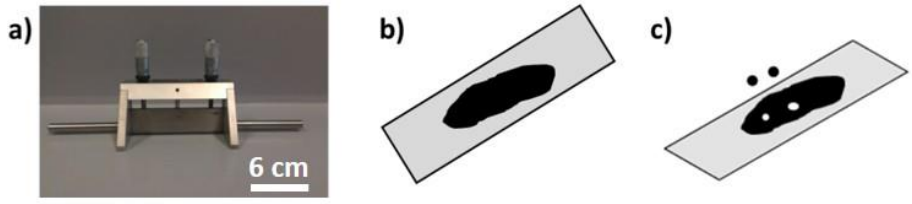

Figure 2.6. Photography of the Doctor Blade used for casting the laminates (a) and diagram of the shape of a laminate supported on aluminum foil current collector (b) and diagram of the same laminate punched to take the electrodes (c).

Finally, the laminates were punched with the desired size (7/16” for Swagelok cells and 1/2" for coin-cells) and the electrodes were pressed at 3 tons for 10 seconds. The electrodes were dried at 80^{o}C overnight and were transferred in the glovebox ready to assemble cells. Most of the laminates were prepared in the fumehood of the laboratory. However, laminates of iron, cobalt, nickel and solid solution carbodiimides were casted inside the glovebox. The loading mass of the electrodes differs in each kind of material. In titanates the mass loading was in the range of 1.8-5.4 mg and 1.1-4.2 mg in the case of carbodiimides.

2.2.2 Cell assembly

All the electrochemical measurements, apart from the full cells detailed in the last chapter, were carried out as half cells (the anode was always metallic lithium/sodium) and our active material, in spite of having application as anode when in a full cell, it was measured as a cathode. As metallic lithium and sodium as well as the electrolytes in the presence of water from the air, the cell assembly was performed in the glovebox. Once the cells were assembled and completely sealed, it was proceeded to carry out the electrochemical measurements. Two types of cells were used for these studies:

- 2.2.2.1 Swagelok type cell

Assembling the Swagelok cell consisted on: first, the electrode was placed above the stainless Steel plunger and then, a 1.3 cm diameter glass fibre Whatman GB-55 (separator) was added. After that, the glass fibre was soaked with 100 µL of electrolyte and the other plunger with metallic lithium/sodium was set taking care that there was good contact between the electrodes and the glass fibre. Metallic and polymeric Swagelok bodies have been used. For the metallic ones, kapton film had to be placed inside in order to avoid the shortcut of the prepared battery. Finally, the plungers were plugged into the potentiostat by appropriate cables. The reference and counter electrode were connected to the metallic lithium/sodium side and the working electrode was plugged into the side where the material to be tested is located. In the case of the three electrode Swagelok set up, the measurements were carried out connecting sodium or lithium as reference electrode, the counter electrode was connected to the cathode (layer oxide) for full cells and sodium or lithium for impedance and the carbodiimide as working electrode (iron carbodiimide for the full cell (Chapter 7) and copper carbodiimide for the impedance spectroscopy (Chapter 4).

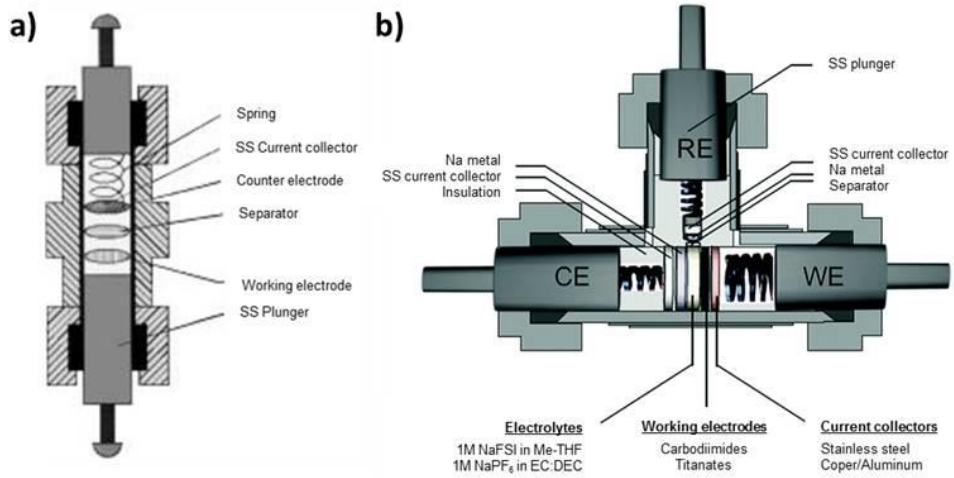

Figure 2.7. Two (a) and three (b) electrode Swagelok cell set up used for the galvanostatic; and full cell and impedance spectroscopy measurements respectively.

2.2.2.2 Coin-cell

For assembling a coin-cell, the Hoshen pieces were used with 2032 size which are employed for comercial batteries (Figure 2.8). For assembling a coin cell, first the can was placed on the floor of the glovebox and then the electrode ready to be tested was weighted and put above the can. After that, the glass fibre with 17" size was placed and soaked with 100 µL of electrolyte. Finallly, the spacer with the metallic lithium/sodium was added with the spring above and the cap with the gasket to close and seal the cell using a hand-operating closing tool.

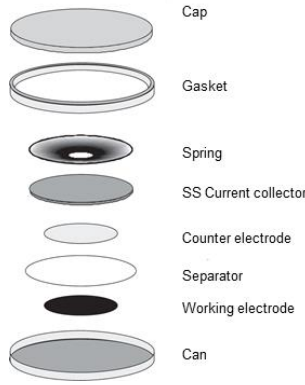

Figure 2.8. Parts of a coin cell experimentally used with the CR2032 size.

2.3- Characterization techniques

2.3.1 Diffraction

2.3.1.1 X-Ray Diffraction

X-Ray diffraction is a non-destructive technique which allows characterizing the crystalline structure of the studied materials. Each crystalline structure has its own X-Ray diffractogram and it allows determining the material´s structure.

X-Rays are one kind of the electromagnetic radiation of high energy and so low wavelength. When the X-Ray beam impacts with a systematically ordered array of atoms, some radiation crosses and the rest of radiation is diffracted by the electrons of the atoms of the crystalline structure. Most of the wave of the photons is dispersed interfering constructively or cancelling out (Figure 2.9). So that, some of the photons leaves in phase and its waves strengthen causing a diffracted X-Ray beam. When this beam is diffracted, the waves in phase, (with a phase difference proportional to 2π) the interference is constructive and results in a diffracted beam and a peak of diffracted intensity which appears at an angle θ according to Bragg´s equation (2.1).

$$n\,\lambda = 2\,d\,\sin\theta \qquad (2.1)$$

λ is the wavelength of the incident radiation, which in the case of X-Ray using a monochromatic copper electron anode, λ is 1.5406 Å.

n is an absolute number which indicates the diffraction order.

d_{hkl} is the interplanar distance between the planes responsible for that diffraction. The d_{hkl} can be calculated from the lattice paramters and symmetry of the crystal structure based on geometrical considerations.

θ is the angle that the beam forms with the reflection plane hkl.

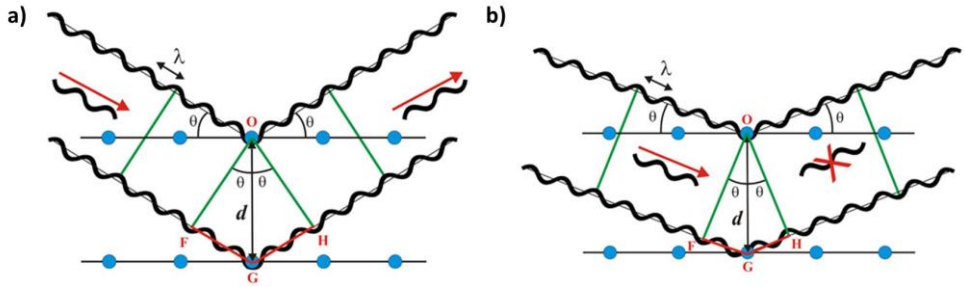

Figure 2.9. Constructive (a) and destructive (b) interference which follows and not follow Bragg´s law of diffraction respectively[9].

All the samples were prepared in a common poly-metylmetacrylate (PMMA) sample holder of the Company Bruker. About 50 mg of each sample were placed in the hole and it was flattened in order to avoid instrumental problems and obtain the best diffractogram. Samples were measured in a Bruker D8 Advance (Figure 2.10a) or Discover Diffractometer using Bragg-Brentano geometry using λ ($CuK_{\alpha1}$= 1.54056 Å, $K_{\alpha2}$= 1.54439 Å radiation with a LYNXEYE detector and LYNXEYE XE monochromator (λ=1.5406Å $CuK_{\alpha1}$ radiation) respectively.

Every synthesized powder was characterized by X-Ray Diffraction and it was determined whether the synthesized powder was obtained as a single phase or its crystallinity. In a diffractogram, many diffraction peaks (called reflections) are observed. Their 2θ Bragg position, width and intensity depend on the structure of the material under study. The main goal of this technique is the identification and the quantitative analysis of the synthesized samples. In these phases, instrumental factors, cell parameters, atoms positions, microstrain and particle size can be determined through X-Ray refinements.

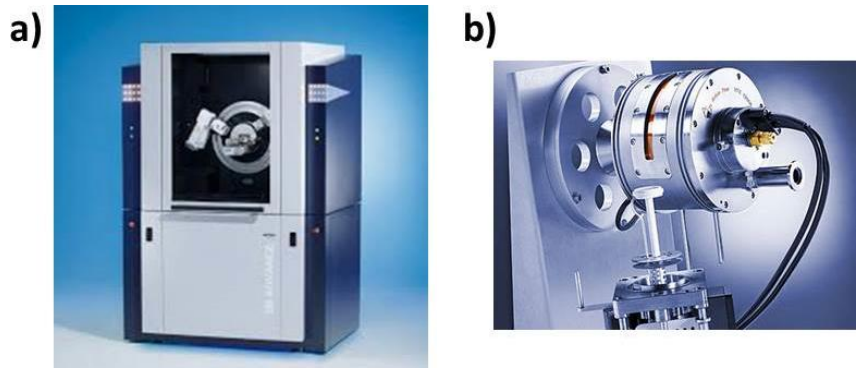

Figure 2.10. Bruker D8 Advance Diffractometer (a) which can connect many tools such as In-Situ XRD cell or Anton Paar Company HTK 1200N High-Temperature Oven-Chamber (b)[10].

For the **high temperature X-Ray diffraction** measurements, a HTK 1200N High-Temperature Oven-Chamber (Figure 2.10b) was used. These measurements were also carried out in inert atmospheres in order to avoid the influence of oxygen in the samples upon the increase of temperature. The gas flow was set up for not going directly to the sample and therefore preventing that the powder could fly in the Oven-Chamber ruining the measurement and damaging the chamber. In this study, the thermal evolution and stability of copper and zinc carbodiimide were analysed (Chapter 5) because they were the most crystalline carbodiimide samplesBoth carbodiimides were measured up to 800^{o}C from room temperature collecting a PXRD pattern every 100^{o}C. The sample holder was a small ceramic pot in order to reach high temperature without any reaction with the sample. About 30 mg of sample were needed for a good measurement.

XRD *In-Situ* Electrochemical cell was also assembled in order to measure how the structure of the material is changing upon cycling in a battery. For that purpose, a homemade-Swagelok cell based on a 1-inch Swagelok cell which fits in the sample position of Bruker D8 Advance was used. This cell has a transparent window which allows the X-Ray beam passing through and reaches the sample. Moreover, the window should keep the liquid electrolyte completely sealed. Thus a beryllium (Be) window sealed with a viton o-ring was used owing to their high mechanical strength and insulating properties. The limitation of this Be window is that at voltages higher than 3.5 Volts *vs* Na^{+}/Na the berillium is oxidized so for higher voltage measurements the window should be covered by aluminum, but the aluminum peaks would additionally interfere with the diffraction pattern of the material under study. Working electrodes were used in powder form with 65% active material and 35% carbon Super C-65 in the case of titanate and a mixture of Super C-65 and Ketjen Black (1:1) for the case of copper carbodiimide. Both powders were hand mixed in an agate mortar and dried at 80^{o}C for 12 hours before cell assembly. Two Whatmann glass fiber separators were placed for making sure there is no contact of any powder metallic sodium foil which acts as with the anode (and counter electrode). The 1 M $NaClO_4$ in EC:DMC was used for $H_2Ti_3O_7$ and 1 M NaFSI in Me-THF for CuNCN.

2.3.1.2 Neutron Diffraction

During the study of the synthesized samples, the X-Ray diffraction allows characterizing the phase and cell parameters of the synthesized sample. However, in order to refine the atomic positions, the lightest atoms, such as protons, are not able to be determined by X-Ray. This fact is because the X-Ray diffraction is produced through the scattering of x-rays with the electron cloud surrounding each atom. The contribution to the diffracted x-ray intensity is therefore larger for atoms with a large atomic number (Z) than it is for atoms with a small Z. As the lightest atoms have less electrons to scatter with X-Ray radiation, these atoms can be more precisely located through Neutron Diffraction technique.

Besides, Neutron Diffraction is produced by the interaction of the radiation (neutrons) with the nucleus of the atoms. As this radiation is not charged, unlike X-Ray, it can penetrate to the nucleus and it interacts with nucleus radiating scattered neutrons as a spherical wave. Since the interaction is nuclear, each element and its isotopes have different scattering amplitude[11] (Figure 2.12). This allows determining the position of atoms which cannot be located by X-Ray radiation. The main drawback of this technique is that is hard to access because it requires the use of big installations. In order to use this type of installations, applying for beamtime is usually requested and the proposal should be of interest enough to be accepted.

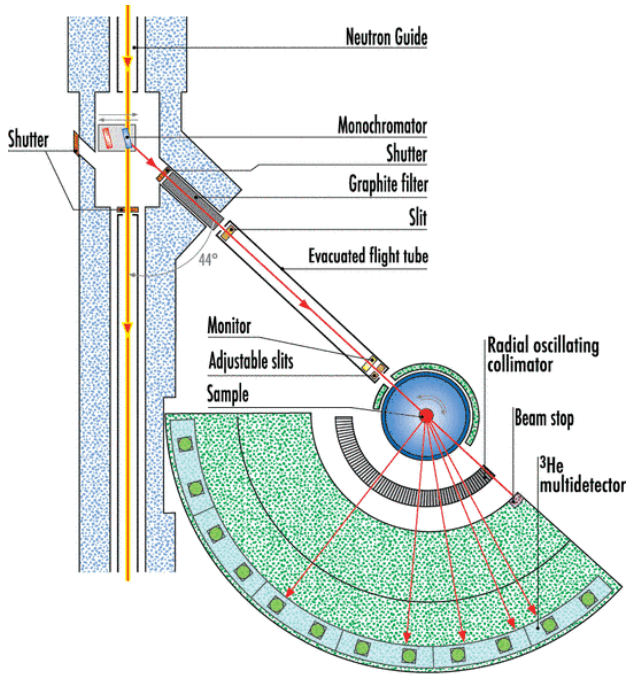

Figure 2.11. Instrument layout of D1B line at the Institue Laue-Langevin (Grenoble)[12].

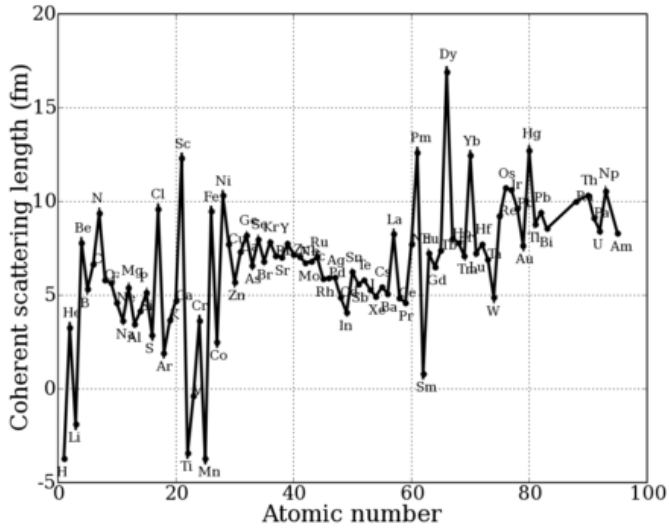

Figure 2.12. The relationship of the neutron scattering lenght with the atomic number (Z).

The determination of the proton positions of protonated titanate ($H_2Ti_3O_7$) were performed with data collected in the line D1B at the Institute Laue-Langevin in Grenoble. The polychromatic beam produced by the High-Flux Reactor (HFR) is modulated by the monochromator and this monochromatic beam is radiated into the sample covering the angular range 0.77º to 128.67º where the positive sensitive detector (PSD) collects the data. Experimentally, samples were measured using two different wavelengths (λ=1.28 Å and λ=2.52 Å). About 2-3 grams of sample were placed in a vanadium, since Vanadium nuclei hardly scatter neutrons. That is why it is often used as a container material despite the fact that vanadium is a strong scatterer of X-rays.

Rietveld refinements of the X-Ray diffraction and Neutron diffraction patterns were performed with Fullprof program[13,14]. The background was modelled with a linear interpolation between experimental points, while the peak shape was described by a Thompson-Cox-Hastings pseudo-Voigt function convoluted with axial divergence asymmetry function. For impurity phases only the unit cell and profile parameters were refined. Rietveld refinement method is based on the minimization the differences from the calculated structure and the experimentally diffractogram obtained in terms of intensity, widths and position of the peaks. The method tries to match the calculated to the experimental diffractogram through an iterative process providing the agreement factor that asses how good is the refinement of the samples.

2.3.2 Spectroscopy

2.3.2.1 Infrared spectroscopy

Infrared and Raman spectroscopies are two powerful techniques to observe the vibration of the molecular bonds based on the absorption and dispersion respectively. While in Infrared Spectroscopy the intensity of a peak is related with the change of the dipolar moment from ground to excited state, in Raman Spectroscopy the intensity of the peak is related to the polarity of the bonds. Both spectroscopies are complementary and are measured for energies in the range of wavelength of 10^{-2} to 10^{-4} cm^{-1} (Figure 2.13a).

In Infrared Spectroscopy, the frequency of the radiation is moved and the radiation absorbed (or transmitted) by the sample is measured. On the other hand, in Raman Spectroscopy, the sample is irradiated with a monochromatic light of frequency v (laser) causing two different types of dispersion: Rayleigh dispersion which is generated with the same wavelength than the incident beam; and Raman dispersion at different wavelengths[15] which results in the Raman spectrum. Carbodiimides show modes in Raman that are not active in IR and some modes in IR are not active in Raman. That is why these techniques could be complementary to each other. In carbodiimides the asymmetrical stretching modes are the most representative and are active in IR.

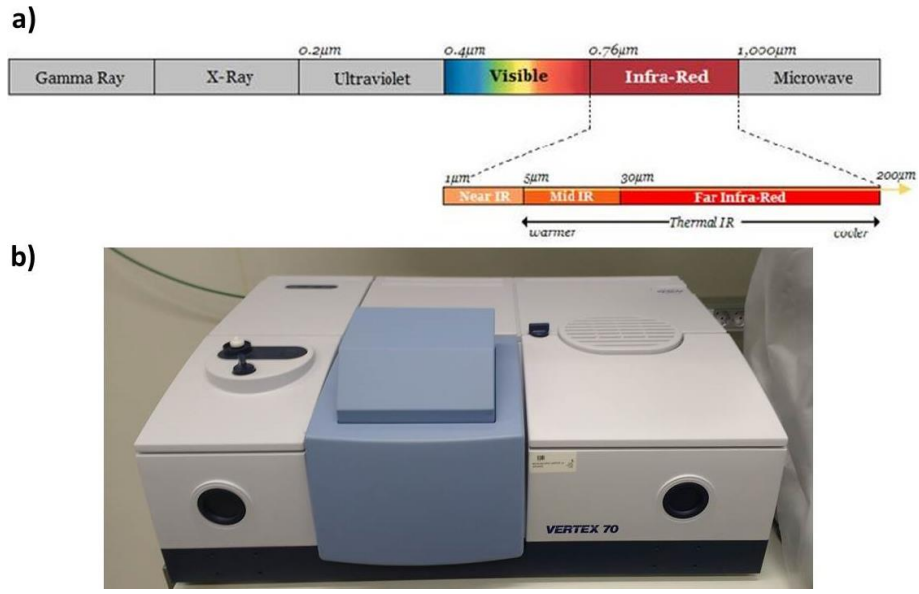

Figure 2.13. Regions of the electromagnetic spectrum and energy in wavelength units (μm) (a) and Vertex 70 Spectrometer (b).

In this thesis, Infrared Spectroscopy is a very important tool which helps to probe the characteristics bands of O-H bonds in the case of protonated titanate and N=C=N bond in the case of carbodiimides. A Bruker Vertex 70 Spectrometer (Figure 2.13b) was used in the study of the Infrared bands. Samples were placed in the diamond crystal and pressed measuring in the absorption mode in the 400-4000 cm-1 desired range of frequencies.

2.3.2.2 NMR spectroscopy

Nuclear magnetic resonance is a physical phenomenon based on the quantum-mechanical properties of each atomic nuclei. A lot of nucleus has a nuclear spin or nuclear angular moment and it is quantized. This moment can be described by the quantum spin number I and it can be 0, 1/2, 1, 3/2, 5/2…

If the value is 0 the nuclei is not active in NMR such as ^{12}C. On the other hand, if it is different from 0, the nucleus is active in NMR such as ^{1}H. The different states of nuclear spin of these nucleii are degenerated without applying a magnetic field. Nevertheless, after applying a magnetic field, the states of nuclear spin are not degenerated and when the nucleus absorbs the radiation of radiofrequency, the allowed transitions of nuclear spin states occur. Each nucleus absorbs at different radiofrequency so they have each own determined radiofrequency. For example in a 2.3 Tesla magnet, 1H absorbs at 100 MHz and 13C at 25 MHz. Moreover, the same nuclei which have different chemical environment cannot reach the same condition of resonance so different signals appear in the spectra separated by few hertz.. Each signal is described by its chemical shift, which consider the separation of frequency in hertz from a reference vs the total frequency in MHz. The integration of the signal area should be proportional to the amount of the nuclei that originate that signal.

In order to study well the NMR active nucleii, ideally they need to be abundant improving the signal/noise ratio. A larger relaxation time make the signal narrower which depends on the nucleus and its molecular environment. The interpretation of NMR spectra can also be aided by the splitting of the signal by a spin-spin coupling and the shift should be the same for both signals connected by the coupling constant J (few Hz). This spin-spin coupling can be homonuclear and heteronuclear and it is easily seen in liquid NMR but almost impossible in solid state NMR. The relative intensity of the splitting signals can be described by a nominal distribution (Pascual triangle).

In this thesis solid state NMR was used. Solid-state NMR spectra are very broad, as the full effects of anisotropic or orientation-dependent interactions are observed in the spectrum. The presence of broad NMR signals, once thought to be a hindrance actually provides much information on chemistry, structure and dynamics in the solid state. In

order to reduce broadening and improve resolution in the solid state, Magic Angle Spinning NMR is applied[16]. In MAS NMR, a sample is rotated (in a rotor which is the sample holder), rapidly around an axis at the magic angle θ_m= 54.74° with the static field causing effectively (Figure 2.14a) suppress chemical shift broadening as *E. R. Andrew et al.*[17]; *I. J. Lowe*[18] found yielding ($3\cos^2\theta - 1 = 0$). When the sample is set at the magic angle, the anisotropic part with fast rotation produces NMR sidebands. These sidebands are shifted away by a frequency equal to the spinning speed, and the spectrum consists of narrow lines at the isotropic shifts.

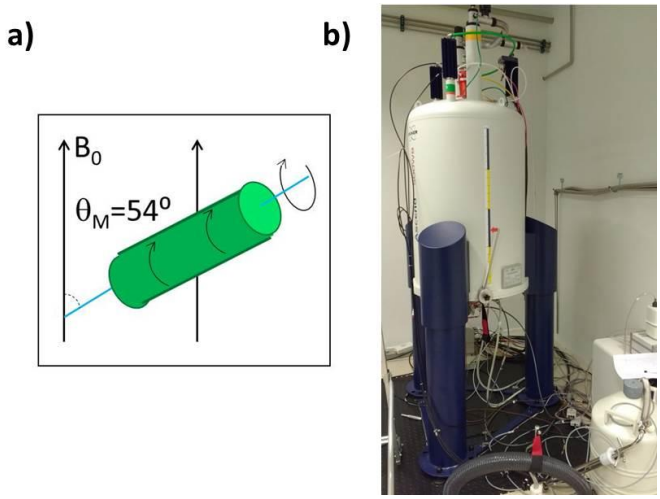

Figure 2.14. Schematic of a rotor spinning at the Magic Angle (a) and Brucker Ascend 500 MHz NMR equipment (b).

In this work, proton and sodium NMR signals of the protonated titanate were measured in order to combine the data with the structural study performed by X-Ray and Neutron Diffraction. ^{1}H and ^{23}Na solid state NMR data were collected on a Bruker 500 MHz spectrometer (Figure 2.14b) 11.6 Tesla, at an operating frequency of 500 MHz and 132 MHz for ^{1}H and ^{23}Na respectively. Rotors of 1.3 mm of diameter were filled with approximately 3 mg of sample and they were spun at the magic angle at a spinning rate of 50 kHz. A rotor synchronized Hahn echo (90^{o}-τ-180^{o}-τ-acq.) sequence was used with a 90^{o} pulse of 2.75 µs for ^{1}H nucleus and 1.5 µs for ^{23}Na nucleus and a delay of 40 s for both nuclei. 160 scans were collected for ^{1}H spectrum which was referenced to a secondary reference, deionized H_2O appearing the signal at 4.8 ppm. However, 1440 scans were collected per ^{23}Na spectrum referenced to a 1 M NaCl aqueous solution at 0 ppm. Fitting and integration of the spectra was performed using DMFit program[19].

Solid-State NMR can be useful in the analysis of structure and composition of various components of batteries, such as the electrolytes, binders and electrode materials. The diffusion of alkali ions can be calculated as well. The diffusion of alkali ions become more active at higher temperatures causing that the nuclear-spin interactions are averaged and

cancelled out. Therefore, the peaks become narrower allowing obtaining intrinsic characteristic of the material such as the activation energy and diffusion coefficient.

2.3.2.3 Mössbauer spectroscopy

The Mössbauer effect consists on the resonance emission and absorption of the nuclear ϒ-rays. The energy and the frequency of ϒ-radiation correspond to the transition of the elemental state to the excited states[20] (Figure 2.15a). Only few elements can be studied by Mössbauer spectroscopy such as ^{57}Fe, ^{119}Sn, ^{99}Ru and ^{197}Au.

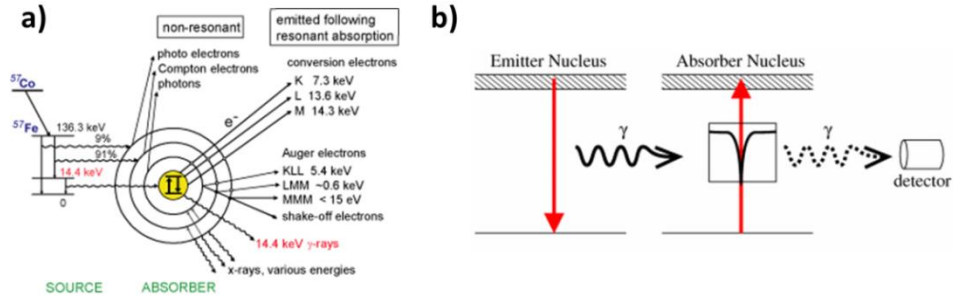

Figure 2.15. Schematic procedure of the radiation generated form the irradiation of the ^{57}Co source into a sample with ^{57}Fe which emitted ϒ-rays (a) and the schema of the Mössbauer spectrometer from the source to the ϒ-rays detector (b)**.**

In this thesis, only ^{57}Fe nucleus was studied. The equipment is made up of a radioactive source which in this case is ^{57}Co, a solid absorbent with the sample of ^{57}Fe and a ϒ-ray detector (Figure 2.15b). The process consists on incorporating ^{57}Co in stainless steel which is disintegrated by the capture of one extra-nuclear electron to obtain the excited state of ^{57}Fe which send out ϒ-radiation to go back to its fundamental state. If the ^{57}Fe of the source and absorbent do not have identical chemical composition, resonance absorption is taken place and the radiation cannot reach the detector. If not, there is not absorption and the radiation can reach the detector[21]. Moving the source at different speed causes that the energy of ϒ-radiation to be altered by Doppler Effect and each type of Fe, meaning Fe atoms in different environments and oxidation states) may show absorption at different speeds.

Measurements of absorption vs speed were carried out in transmission geometry and in both the antiferromagnetic and paramagnetic regime of solid-solution carbodiimides by collecting data both at room temperature and 70^{o}C. The measurements were performed by Prof. Jose Javier Saiz Garitaonandia in a home-made equipment at the University of Basque Country UPV/EHU.

2.3.2.4 Impedance spectroscopy

Impedance Spectroscopy is an electrochemical method that uses the current response under alternating current voltage to obtain the resistance, capacitance and inductance of the system under study. The simplest circuit follows Ohm´s law, which states that resistance is the ratio of voltage and current. Nevertheless, in alternating current (ac) circuits, two other circuit elements, capacitors and inductors, impede the flow of electrons giving rise to impdance. Impedance can be expressed as a complex number, where the resistance is the real component and the combined capacitance and inductance is the imaginary component. Capacitors and inductors affect not only the magnitude of an alternating current but also its time-dependent characteristics or phase.

The analysis of impedance is usually represented in Nyquist Plot (also known as Cole-Cole plot which looks like Figure 2.16a). It consists on the plot of the imaginary impedance component (Z") against the real impedance component (Z') at each excitation frequency.This kind of plot has often the shape of a semicircle which makes easier the observation of the ohmic resistance. The Nyquist plot of Figure 16a is fitted to obtain the equivalent circuit as can be seen in Figure 2.16b. Nevertheless, frequency values do not appear explicitly in the plot and the capacitance has to be calculated considering the frequency information therefore it is not possible to read it directly from the Nyquist plot, as it occurs with the ohmic and polarization resistance[22].

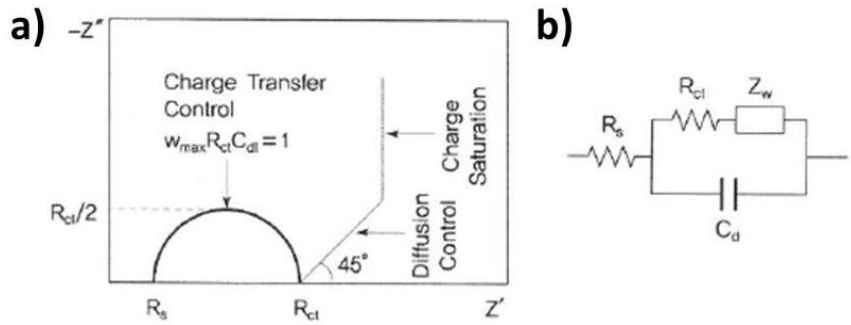

Figure 2.16. Nyquist plot of lithium secondary battery electrode (a) and the equivalent circuit (b) from ref.22.

In this work, the impedance spectroscopy was analysed qualitatively, looking for the differences in the resistance and impedance at full charge and discharge voltages of CuNCN (Chapter 4). Spectra was also refined by Boukamp software[23]. This was further related with the XPS analysis from the SEI layer decomposition products. Impedance was measured in a SP-200 potentiostat of Biologic company with one channel on a three electrode Swagelok cell with copper carbodiimide as working electrode and metallic sodium as counter and reference electrodes.

2.3.2.5 X-ray photoelectron spectroscopy (XPS)

X-ray photoelectron spectroscopy (XPS) is a quantitative spectroscopic technique that measures elemental composition, empirical formula, chemical composition and electronic state of the elements that exist within a material[24]. XPS is typically accomplished by exciting the surface of a sample with mono-energetic Al k_α x-rays causing photoelectrons to be emitted from the sample surface (typically 1-10 nm of the material surface is analysed). An electron energy analyser is used to measure the energy of the emitted photoelectrons. XPS requires ultra-high vacuum (UHV) conditions.

The energies of the photoelectric lines are well defined in terms of the binding energy of the electronic states of atoms. Since core level electrons in solid-state atoms are quantized, the resulting energy spectra exhibit resonance peaks characteristic of the electronic structure for atoms at the sample surface[25]. In the case of conducting samples, for which the detected electron energies can be referenced to the Fermi energy of the spectrometer, an absolute energy scale can be established, thus aiding the identification of species.

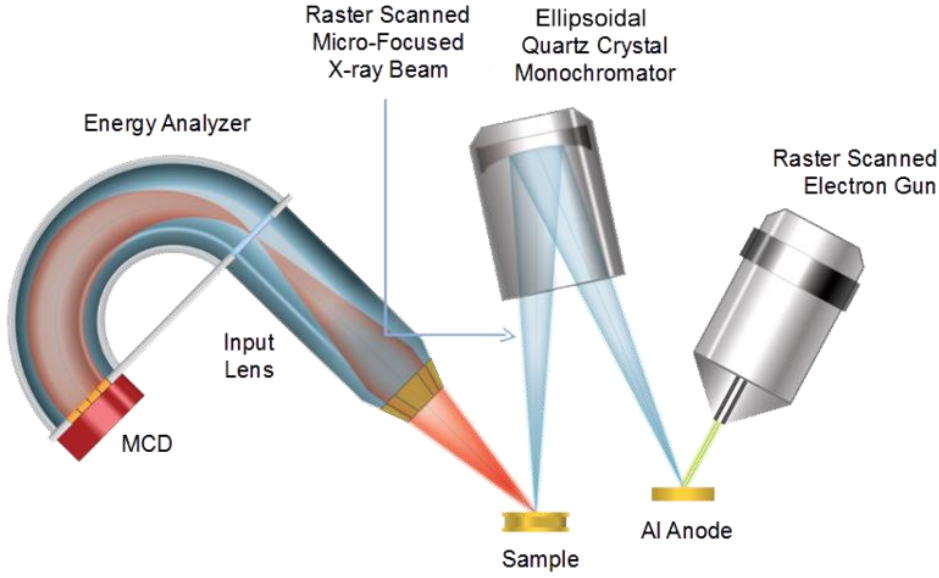

Figure 2.17. Schema of procedure of the XPS equipment.

Measurements of the copper carbodiimide examining principally the F 1s and S 2s orbitals were carried out by Dr. Ricardo Pinedo and Franziska Klein in a PHI5000 Versa Probe spectrometer using monochromatic Al Kα radiation (hv = 1486.6 eV) property of the Giessen University (Germany).

2.3.2.6 Electronic paramagnetic resonance (EPR)

EPR It is a very useful technique focus on the structural studies and the characterization of physic chemical properties. In this technique, in comparison with NMR, the electronic spins are taken part in the analysis and not the nuclear spin. EPR consists on the absorption of electromagnetic waves by the systems with unpaired spins under an applied extern magnetic field. Due to the high sensitivity of this technique with the magnetic field and morphologic characteristics, it is a suitable technique with the aim of analyse the physical properties.

It worth noting that unlike optic transitions, the magnetic component (not the electric) is the incident radiation which interacts with the system. Another difference with the optic spectrophotometer is that EPR works at constant frequency and it makes linear scans of static magnetic field. When the incident energy is equalize to the energy needed to change the orientation of the electron magnetic moment the resonance condition is taken place as it can be seen in the following equation 2.2.

$$h\nu = gB_o\mu_\beta \qquad (2.2)$$

Where h is the Plank´s constant (6.626 10^{-34} J·s), ν is the frequency at which the spectra was taken, μ_β is conversion constant called the Bohr magneton (9.274·10^{-28} J/G) and B_o is the magnetic field used.

The position of the signal in EPR is equivalent to g value and it allows characterizing the system and the area of the band of absorption is proportional to the number of spins that have resonance in the sample. The wideness of the signal can be big due to a very long relaxation time. In that sense, cooling the sample, the EPR signals have more intensity and make them narrower improving the resolution of the peaks if there are not saturation effects or antiferromagnetic interactions. Moreover, it can make that the signal of some compounds which saturate at room temperature due to their longer relaxation times. The interactions of the magnetic ion with its environment as a consequence of the transference of energy between the excited ions make wider the signal.

EPR measurements were carried out in a Bruker ELESYS spectrometer equipped with a Gaussometer Bruker BNM 200, a frequency meter of microwaves Hewlett-Packard 5352B and a Helium cryostat. These measurements were performed by the responsible of the equipment in the General Services of Research (SGIKER) at University of Basque Country (UPV/EHU).

2.3.2.7 Magnetic measurements: SQUID

The superconducting quantum interference device (SQUID) consists of two superconductors separated by thin insulating layers to form two parallel Josephson junctions. This device can be configured as a magnetometer and it is able to detect incredibly small magnetic fields.

Magnetic properties of solid solution samples were measured in a MPMS-7T, Quantum Design magnetometer. Susceptibility was measured heating from 5-400K after zero field cooling (ZFC) employing a constant external magnetic field of 1 KOe (0.1 Tesla). These measurements were carried out by Dr. Iñaki Orue, responsible of the Magnetic Measurements Platform of General Services of Research (SGIKER) at the University of Basque Country.

2.3.2.8 Inductively coupled plasma spectrometer- Atomic Emission Spectroscopy (ICP-AES)

An inductively coupled plasma spectrometer (ICP) is a tool for trace detection of metals in solution. A liquid sample is injected into argon gas plasma contained by a strong magnetic field. The elements in the sample are excited and the electrons emit energy at a characteristic wavelength as they return to their ground state. The emitted light is then measured by optical spectrometry.

Most ICP-AES instruments are designed to detect a single wavelength at a time (monochromator). Since an element can emit at multiple wavelengths, it is sometimes desirable to detect more than one wavelength at a time. This can be carried out by sequential scanning or by using a spectrometer that is designed to capture emissions of several wavelengths simultaneously (polychromator). Detection and quantification limits are typically range from parts per million (ppm) to parts per billion (ppb).

Transition-metals (Fe and Co) of solid solution carbodiimides were quantified by this technique. In order to measure the sample, acid digestion of the sample is needed. The measurements were carried out by the technician responsible of the ICP-AES spectrometer at RWTH Aachen University.

2.3.2.9 Thermogravimetric analysis- mass spectroscopy (TGA-MS)

Thermogravimetric analysis or thermal gravimetric analysis (TGA) is a method of thermal analysis in which changes in physical and chemical properties of materials are measured as a function of increasing temperature (with constant heating rate), or as a function of time (with constant temperature and/or constant mass loss). TGA can provide information about physical phenomena, such as second-order phase transitions, including vaporization, sublimation, absorption, adsorption, and desorption. Mass spectrometer is coupled to the equipment and allows identifying specific mass-ions generated with the mass losses of the thermobalance within a certain temperature range. The measurement was carried out in a STA 449 F3 SYSTEM CONNECTED TO QMS 403 AËOLOS (NETZSCH) spectrometer at CIC EnergiGUNE by the technician responsible of the equipment.

2.3.3 Electron Microscopy

Electron Microscopy is a type of microscope that uses a beam of accelerated electrons as source of illumination to create an image of the specimen. It is capable of much higher magnifications and greater resolving power than a light microscope, allowing it to see much smaller objects in detail. Both electron and light microscopes have resolution limitations, imposed by their wavelength as well as by the design of the microscope. The greater resolution and magnification of the electron microscope is due to the wavelength of an electron, its de Broglie wavelength, being much smaller than that of a light photon, electromagnetic radiation.

The electron microscope uses electrostatic and electromagnetic lenses in forming the image by controlling the electron beam to focus it at a specific plane relative to the specimen in a manner similar to how a light microscope uses glass lenses to focus light on or through a specimen to form an image.

Due to the strong interactions of electron with matter, gas particles must be absent in the column. The required high vacuum is maintained by a vacuum system typically comprising a rotary pump. Beams of these fast-moving electrons are focussed on an object and are absorbed or scattered by the object so as to form an image on an electron-sensitive photographic plate and more recently in CCD cameras.

During the development of this thesis two types of electron microscopes were used: Scanning Electron Microscopy (SEM) and Transmission Electron Microscopy (TEM).

2.3.3.1 Scanning Electron Microscopy

Scanning Electron Microsocopy (SEM) is a microscope which allows the observations and characterization of the surface of inorganic and organic material providing the morphologic information.

The operation of this process consists on the shift of the incident beam of electrons for making a scan. When the electrons go into the material, signals are generated allowing to obtain an image of the surface or the composition of the sample. The signals come from the secondary electrons, retrodispersed electrons and X-Rays (Figure 2.18 left).

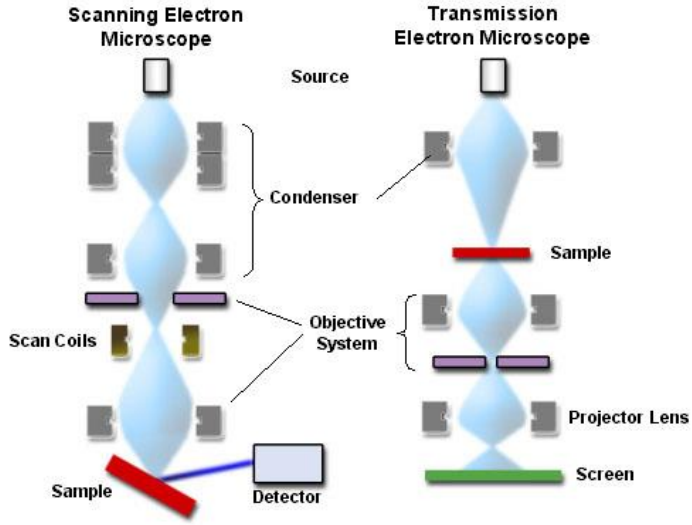

Figure 2.18. Schema of the SEM and TEM microscopes where the difference of the sample location is observed[26].

The microscope used in this thesis is a Quanta 200 FEG (FEI). The working voltages of the Quanta 200 FEG (FEI) scanning electron microscope can vary between 3kV (low vacuum mode) and 30 kV (high vacuum mode). Synthesized powdered samples were placed on a carbon tape to ground the sample, thus avoiding optical aberration effects due to sample charging by excess of electrons coming from the electron beam.

2.3.3.2 Transmission Electron Microscopy

Transmission Electron Microscopy (TEM) is similar to an optic microscope because it is based on the same manner of acting of an electromagnetic field through an electron beam (similar to the glass lenses through which passes the photon beam) as it can be seen in Figure 2.18 in the right. In the TEM, a thin crystal of the sample is irradiated with

an electron beam of constant current density (about 200KeV). Some of that electrons are transmitted, other part of electrons are dispersed and the rest have different interactions producing phenomena such as light emission, secondary electrons, Auger, X-Rays, etc. The transmission of the electrons is used for generating diffraction patterns and, focusing with the electromagnetic lens of the diffracted beams, for creating images directly from the material. The information of a short range crystalline structure and its microstructural defects can be obtained with this microscope, even like in SEM it is possible to determine the elemental composition of the sample taking advantage of the X-Ray emission.

The TEM measurements (images of the particles and electron diffraction) for the analysis of solid solution carbodiimides were carried out in the FEI Tecnai G2 is a 200kV field emission gun (FEG) high resolution TEM/STEM by Dr. Wei Zhang responsible of the platform at CIC Energigune. Samples were prepared in ethanol suspensions and placed in the TEM grids after sonication for 15 minutes. A Small amount of sample is needed for a good suspension.

2.3.4 Electrochemical measurements[22]

The cells assembled as described in section 3.2.2 (Cell assembly) were measured in order to study the electrochemical performance of the samples for sodium and lithium ion batteries. The main factors that are analysed in a battery are capacity, polarization, nominal voltage and cycle life and they are described in the following.

The capacity of a battery is the product of the total amount of charge, when completely discharged under given conditions, and time. Capacity linked to the voltage represents the energy that can be extracted from the battery under certain specified conditions. The temperature of a battery will also affect the energy that can be extracted from it. At high temperatures, the battery´s capacity is typically higher than at lower temperatures. The amount of charge or capacity that a material can store depends on the number of electrons involved (*n*) in the redox reactions, and the molecular weight (*MW*) of the compound. The Faraday constant (96485.33 Coulomb mol^{-1}) relates the three values. Equation 2.3 is used to calculate the theoretical capacity of the material for a supposed number of electrons involved but experimentally the capacity obtained is often lower than the calculated one.

$$C_{th} = \frac{nF}{3600\ MW} \qquad (2.3)$$

Overpotential is a lack or excess of electrode potential *vs* the equilibrium potential. When the current is flowing through the electrode material the observed potential is smaller (in discharge) or larger (in charge) than its equilibrium potential. This overpotential can be caused by three components: ohmic, activation and concentration polarization. Ohmic polarization is related to the iR drop and it decreases proportionally with the current density. Besides, activation polarization is related to the intrinsic properties of the electrode and is strongly influenced by temperature. On the other hand, concentration polarization comes from the concentration gradient of the reactants at the surface of active materials. It is important to know that these three types of polarization are difficult to be distinguished in a battery.

The nominal voltage of the battery is strongly influenced by the polarization. It is the voltage that is averaged from the total points of discharge. A typical example is the graphite which is cycled between 0.01-1.6 Volts *vs* Li^+/Li but it presents an average discharge/charge voltage of 0.2 Volts *vs* Li^+/Li.

The cycle life of the battery is the number of cycles that the battery achieves before depleting its capacity to 80%. A high performance battery should be able to keep the capacity for a long number of cycles. It is strongly dependant of the reversibility of the electrochemical processes. In the industrial level, the cycle life represents the number of cycles that the batteries do before falling below 80% of the initial capacity. In this thesis the materials were measured for 100 cycles as a standard measurement to study the capacity retention.

2.3.4.1 Galvanostatic measurements

The constant current method examines battery characteristics by measuring changes in voltage over time under a constant current. This kind of measurement can provide the capacity, reversibility, resistance and rate of diffusion.

2.3.4.1.1 Galvanostatic cycling

It is a galvanostatic electrochemical measurement based on continuous charging and discharging experiments in order to analyse the changes in voltage under a constant current for a given potential range. During the cycling, in the materials that are electrochemically active, the redox processes can be shown as small changes over time per cycle. This changes could appear in two different forms: i) like a plateau which represents a two phase reaction, this means that during the reaction part of the initial phase is changing to another strcuture or ii) like a slope corresponding to a solid solution

process where alkali ions are being gradually and topochemically inserted into the structure and causing a small change of the composition of all the material but without any change in the symmetry of the material (just causing small changes in the unit cell). Typically Voltage vs time, or voltage vs capacity is plotted. In Figure 2.19a it can be seen the galvanostatic cycling of the graphite/lithium cell for the first 4 cycles.

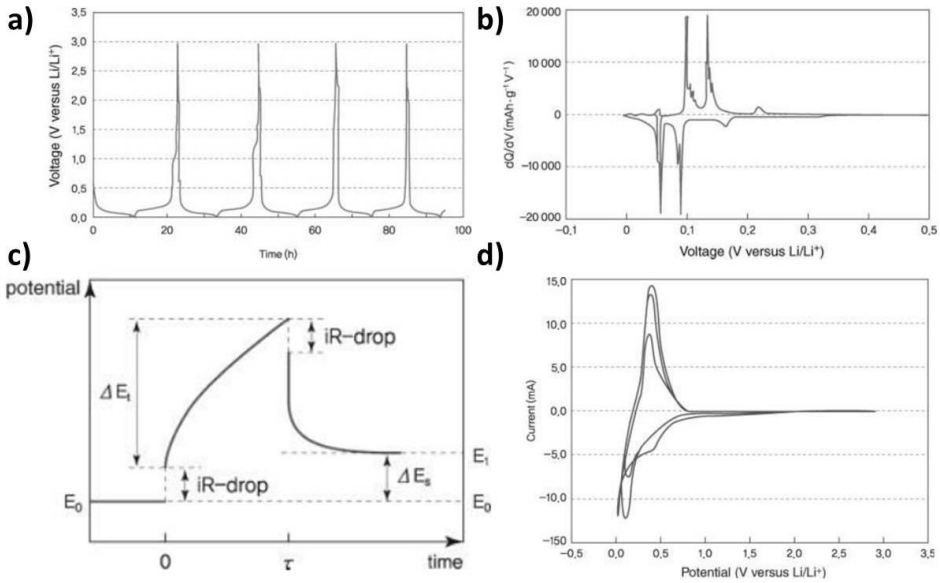

Figure 2.19. Voltage controlled constant current charge-discharge curve (a), the dQdV of the same cell (b), one step of a GITT experiment (c) and the cyclic voltammetry (d) of the graphite/lithium cell.

Moreover, the evaluation of reversibility of the redox process is analysed through the **coulombic efficiency** in each cycle, the ratio between the capacities on charge/discharge processes.

Differential capacity (δQ/δV): Differential capacity analysis is based on a mathematical operation from the galvanostatic measurement and is represented against voltage (Figure 2.19b). This graph is similar to cyclic voltammetry (CV) curve but this process is galvanostatic (constant current) while as it will be explained later, a CV is a potentiostatic (constant shift of voltage per time). The voltage at which the electrochemical reactions occur can be more easily detected in a differential capacity curves because in CVs the peaks can be shifted according to a scan rate due to the ohmic polarization.

2.3.4.1.2 Galvanostatic intermittent titration technique (GITT)

GITT is a type of constant current method that measures changes in open-circuit voltage induced by cutting off the current supply after applying constant current at each step during the charge and discharge process. During the constant current step the alkali ions are intercalated, resulting in concentration gradients at the surface and inner side of electrodes. Measuring the changes of voltage over time (Figure 2.19c), the rate of change in concentration can be calculated yielding the diffusion coefficient[22] from equation 2.4.

$$D^{GITT} = \frac{4}{\pi\tau}\left(\frac{m_B V_M}{M_B S}\right)^2 \left(\frac{\Delta E_s}{\Delta E_t}\right)^2 \qquad (2.4)$$

τ is the time that constant current is applied

m_B is the mass of the electrode material.

V_M is the molar volume of the electrode material.

M_B is the molar mass of the electrode material.

S is the electrode-electrolyte interfacial area.

ΔE_s is the change in voltage at each step

ΔE_t is the change in overall voltage under constant current.

2.3.4.2 Potentiostatic measurements

Constant voltage is an easier method than constant current for oxidative and reductive reactions to reach the electrochemical equilibrium.

2.3.4.2.1 Cyclic voltammetry

Cyclic voltammetry is an electrochemical analysis method that scans voltage with a constant scan rate of voltage for a given potential range of an electrochemical cell (see Figure 2.19d). The current needed for the system to reach equilibrium at the set voltage is recorded and the process is repeated for several cycles. It is recommended to use small scan rates (millivolts second^{-1}) in order to focus in detail on the analysis of the redox processes and avoid the high stress the electrodes can suffer in plateau processes.

This analysis is not a literally potentiostatic method, because the potential is not constant at all. However, as in this experiment measures the current response at a certain constant voltage, this technique was enclosed in this group.

This method can provide the information of potential, quantity of electricity and reversibility of redox reactions within the cell. However, using this method for obtaining quantitative data it is important to be aware of the IR drop and double layer charging processes.

2.3.4.2.2 Constant potential

Depending on the applied current, ion concentration gradients exist between the surface and the inner side of materials involved in intercalation. Unlike the electrode surface, charging is not fully complete within electrodes. In order to avoid this problem, a constant potential measurement is carried out after the galvanostatic charge or discharge. This method maximizes the energy storage capacity of batteries.

2.4- References

[1] J. Akimoto; K. Chiba; N. Kijima; H. Hayakawa; S. Hayashi; Y. Gotoh; Y. Idemoto; "Soft-Chemical Synthesis and Electrochemical Property of $H_2Ti_{12}O_{25}$ as a Negative Electrode Material for Rechargeable Lithium-Ion Batteries"; *J. Electrochem. Soc.* 2011, **158** (5) 546.

[2] S. Andersson and A. D. Wesley; "The crystal structure of $Na_2Ti_3O_7$"; *Acta Cryst.,* 1961, **14**, 1245.

[3] X. Liu, M. Krott, P. Müller, C. Hu, H. Lueken and R. Dronskowski; "Synthesis, Crystal Structure, and Properties of MnNCN, the First Carbodiimide of a Magnetic Transition Metal"; *Inorg. Chem.;* 2005, **44** (9), 3001.

[4] X. Liu, L. Stork, M. Speldrich, H. Lueken and R. Dronskowski; "FeNCN and $Fe(NCNH)_2$: Synthesis, Structure, and Magnetic Properties of a Nitrogen-Based Pseudo-oxide and -hydroxide of Divalent Iron"; *Chem. Eur. J.* 2009, **15**, 1558.

[5] M. Krott, X. Liu, P. Muller and R. Dronskowski; "Synthesis and structure determination of Co(HNCN)2 and Ni(HNCN)2"; *J. Solid State Chem.* 2007, **180,** 307.

[6] X. Liu, M. A. Wankeu, H. Lueken and R. Dronskowski "A Novel Method for Synthesizing Crystalline Copper Carbodiimide, CuNCN. Structure Determination by X-Ray Rietveld Refinement."; *Z. Naturforsch.* 2005, **60b**, 593.

[7] K. Morita, G. Mera, K. Yoshida, Y. Ikuhara, A. Klein, H. J. Kleebe and R. Riedel; "Thermal stability, morphology and electronic band gap of Zn(NCN)."; *Solid State Sci.* 2013, **23**, 50.

[8] X.Liu "Syntheses and Structures of Metal Cyanamide Compounds" University of Aachen, April 2002.

[9] http://www.xtal.iqfr.csic.es/Cristalografia/parte_05_5.html (Access August 2016)

[10] Instruction Manual, HTK 1200N High-Temperature Oven-Chamber, Anton Paar, Austria

[11] https://www.ncnr.nist.gov/resources/n-lengths/ (Access July 2016)

[12] https://www.ill.eu/instruments-support/instruments-groups/instruments/d1b/description/ (Access July 2016)

[13] H. M. Rietveld; "Line profiles of neutron powder-diffraction peaks for structure refinement*"; Acta Cryst*. 1967; **22**: 151.

[14] J. Rodríguez Carvajal; "Recent advances in magnetic structure determination by neutron powder diffraction" *Physica B* 1993; **192**, 55.

[15] K. Nakamoto; 2009, "Infrared and Raman Spectra of Inorganic and Coordination Compounds" Wiley,Hoboken, New Jersery, 6th Edition.

[16] A. Alia, S. Ganapathy, and H. J. M. de Groot;" Magic angle spinning (MAS) NMR: a new tool to study the spatial and electronic structure of photosynthetic complexes" *Photosynth Res.* 2009 Dec; **102** (2-3), 415.

[17] E. R. Andrew, A. Bradbury, R.G. Eades; "Nuclear Magnetic Resonance Spectra from a Crystal rotated at High Speed"; *Nature* 1958, **182**, 1659.

[18] I.J. Lowe; "Free Induction Decays of Rotating Solids"; *Phys Rev Let* 1959, **2**, 285.

[19] D. Massiot, F. Fayon, M. Capron, I. King, S. Le Calve, B. Alonso, J. O. Durand, B. Bujoli, Z. Gan and G. Hoatson; "Modelling one- and two-dimensional solid-state NMR spectra"; *Magn. Reson. Chem*., 2002, **40**, 70.

[20] G. Maddock; "Mössbauer Spectroscopy: Principles and Applications" Horwood Publishing, Chichester, 1997.

[21] V.Parish; "NMR, NQR, EPR and Mössbauer Spectroscopy in Inorganic Chemistry" Ellis Howood, Chichester, 1990.

[22] Jung-Ki Park; "Principles and Applications of Lithium Secondary batteries", Wiley-VCH Verlag &Co., Weinheim, Germany, 2012.

[23] B. A. Boukamp; "A nonlinear least squeares fit procedure for analysis of immittance data of electrochemical systems" Solid State Ionics, 1986, **20**, 31.

[24] http://www.nanolabtechnologies.com/instrument-xps-esca (Access July 2016)
[25] http://www.casaxps.com/ (Access July 2016)
[26] http://barrett-group.mcgill.ca/tutorials/nanotechnology/nano02.html (Access July 2016)

3. Structure resolution and insights on the electrochemical mechanism of $H_2Ti_3O_7$

In this chapter the structural and electrochemical characterization of $H_2Ti_3O_7$ are described. A combined refinement of powder X-Ray diffraction (PXRD) data, along with powder Neutron diffraction (PND) data at two different wavelengths provides us a more precise structure determination including the proton positions. Besides the physicochemical characterization by Scanning Electron Microscopy, InfraRed, and TGA, ^{1}H solid state NMR is critical in properly assigning and distinguishing the different types of protons. The electrochemical performance of the protonated titanate as electrode in sodium ion batteries was studied and the mechanism of the reaction of sodium insertion was deeply analyzed by *in-situ* XRD diffraction and *ex-situ* ssNMR. The understanding of the mechanism of reaction enables a cycle protocol which resulted in improved electrochemical performance *vs* other titanates.

3.1 Results and discussion

3.1.1. Structural and physicochemical characterization

3.1.1.1 Powder X-Ray Diffraction and Neutron Powder Diffraction

Rietveld refinements of $Na_2Ti_3O_7$ (Figure 3.1a) and $H_2Ti_3O_7$ (Figure 3.1b) confirmed that both materials were synthesized as pure phases. The refined lattice parameters for $Na_2Ti_3O_7$ are *a*=8.5619(5) Å, *b*=3.8005(4) Å and *c*= 9.1245(5) Å and *β*=101.595(3) º of the monoclinic $P2_1/m$ space group measured at room temperature. The data are in good agreement with those reported by *S. Andersson and A. D. Wadsley*[1]. Otherwise, $H_2Ti_3O_7$ was C-centered and belonged to the monoclininc *C*2/*m* space group with *a*=16.0243 (2) Å, *b*=3.7497 (6) Å and *c*= 9.1888 (4) Å and *β*=101.438 (3) º as lattice parameters. These parameters are in good agreement with those reported by *M. Gateshki et al.*[2] for this structure. The $H_2Ti_3O_7$ structure was previously reported without considering any protons in the structure[3]. Therefore, the refinement was based on the octahedral TiO_6 arranged in the same zig-zag $[Ti_3O_7]_n^{2-}$ layers of $Na_2Ti_3O_7$ but the hydrogen atoms were not located in the structure. The agreement factors of the Rietveld refinements of the powder X-ray diffraction data of sodiated and protonated titanates are listed in Table 3.1.

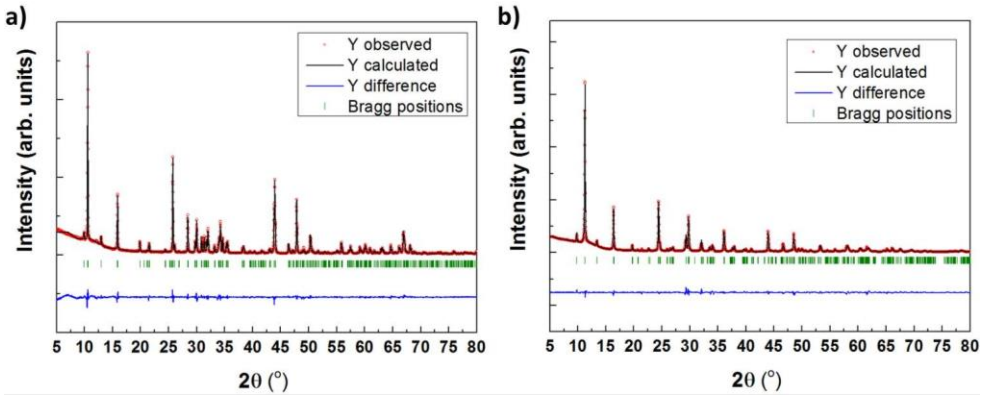

Figure 3.1. Observed (red dots), calculated (solid black line), and difference (blue bottom curve) patterns for the Rietveld analysis from the powder X-ray diffraction data of $Na_2Ti_3O_7$ (a) and $H_2Ti_3O_7$ (b). Green short vertical lines below the profile indicate the peak positions of all the possible Bragg reflections.

Table 3.1. Agreement factors obtained from the Rietveld refinements of the PXRD data of $Na_2Ti_3O_7$ and $H_2Ti_3O_7$.

$Na_2Ti_3O_7$		$H_2Ti_3O_7$	
R_p (%)	14.1	R_p (%)	14.4
R_{wp}(%)	16.3	R_{wp}(%)	17.0
R_{Bragg} (%)	5.11	R_{Bragg} (%)	5.26
χ^2	6.89	χ^2	8.41

According to PXRD analysis of the $H_2Ti_3O_7$, the study of the structure was not completed because protons had not been located yet. As hydrogen atoms were not possible to be located by XRD due to the insufficient scattering with X-Rays, complementary neutron diffraction measurements were carried out. Hydrogen has a large scattering interaction with neutrons (-3.74 fm)[4]. In addition, titanium and oxygen atoms have different scattering interactions being 3.63 fm and 5.80 fm respectively. Therefore, PND was the most suitable technique to obtain the position of the protons[5].

Combined Rietveld refinement of PXRD data and the PND patterns collected at two different wavelengths (λ=1.28 Å and λ=2.52 Å) was carried out without hydrogen atoms because there was not any information of how many and where they could be located (see Table 3.2). This Rietveld refinement was good in order to combine the information of the X-Ray (about Ti and O positions) and Neutron Diffraction, which also includes protons, since X-Rays do not provide information about them.

The differential Fourier map (see Figure 3.2) shows clearly two different protons and a weaker third one at x=0.5. The presence and location of three different protons are

pointed out in Figure 3.2. Another signal, similar to the assigned as H2 in Figure 3.2 was shown but it represented the same crystallographic site. The introduction of the three H^+ in the structure in the positions obtained from the Differential Fourier map analysis resulted in a better fit for the combined Rietveld refinement of X-rays and the two neutron diffraction patterns (see Figure 3.3). In addition, this fact can be observed comparing the agreement factors of the combined refinement without H and with protons (Table 3.2). The χ^2 of the Table 3.1 for $H_2Ti_3O_7$ is comparable to the combined refinement including protons (Table 3.2). However, the combined refinement without protons made worse the X-Ray refinement for the different contributions of the Neutrons where the scattering of protons had to be taken into account.

Table 3.2. Agreement factors of the Rietveld refinement of the combined PXRD and PND data of $H_2Ti_3O_7$ without/with adding the protons to the structure.

	Without protons			With protons		
	X-ray	**Neutron (λ=1.287 Å)**	**Neutron (λ=2.52 Å)**	**X-ray**	**Neutron (λ=1.287 Å)**	**Neutron (λ=2.52 Å)**
R_p	28.7	32.3	30.4	20.6	15.7	16.2
R_{wp}	32.3	29.2	27.5	21.9	14.4	11.0
R_B	19.5	25.6	22	7.95	7.36	7.55
R_F	11.6	17	17.9	6.87	4.88	8.06
χ^2	17.1	20.8	41.2	7.91	5.74	6.7
Global χ^2		26.7			7.03	

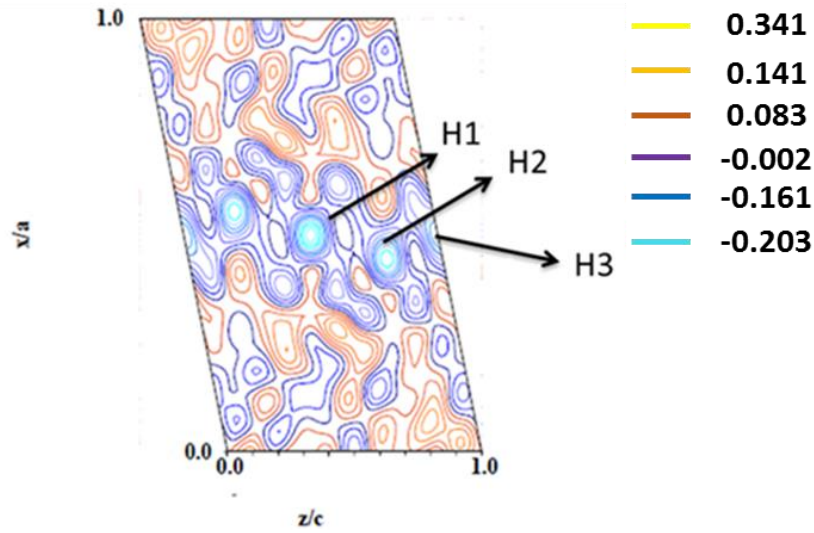

Figure 3.2. Proton (H1, H2 and H3) location from the Differential Fourier map at *ac* plane in the y=0.5 section. Blue lines represent negative intensity due to the negative proton scattering length for neutron radiation.

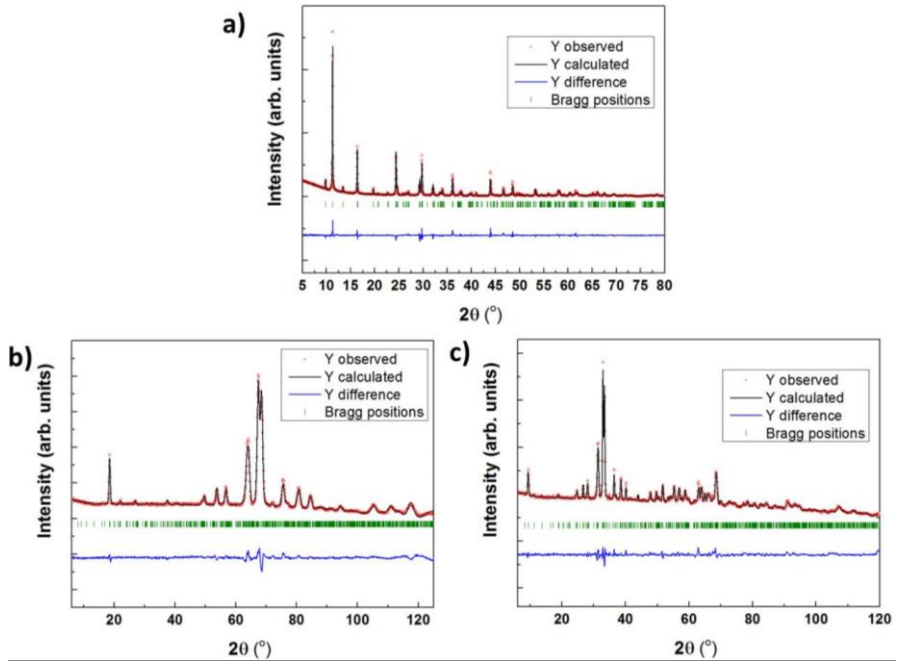

Figure 3.3. Rietveld refinement of X-Ray Diffraction (a), Neutron Diffraction with λ=1.28 Å (b) and Neutron Diffraction with λ=2.52 Å (c) where observed (red dots), calculated (solid black line), and difference (blue bottom curve) patterns are plotted with the Bragg positions in green vertical lines below diffractogram.

In the structure obtained from the refinement, the $[Ti_3O_7]_n^{2-}$ layers remained almost the same with the protons in the interlayer position from the GFourier (Figure 3.4a). In parallel with this study, *K. Kataoka et al.*[6] reported also the location of the protons by PND. In comparison with the reported values (Figure 3.4b), two important differences were observed (Table A3.1 and Table A3.2). First, they observed two types of protons; while in our analysis three kinds of protons were detected (their report did not consider H3). Second, the proton that was called as H1 was split in two positions to equalize the occupancy factors of both protons.

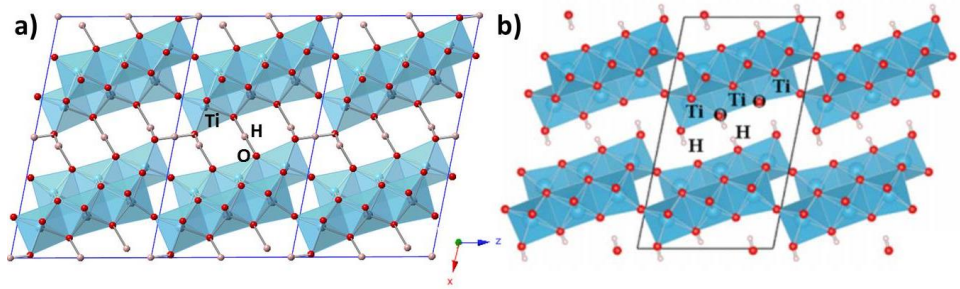

Figure 3.4. Structure obtained from the combined PXRD and NPD data of $H_2Ti_3O_7$ in this work (a) and the structure reported by Kataoka et al[7] (b).

The achieved thermal displacement parameters () were negative (-0.14 Å^2), but in fact negligible, for some of the oxygens and too large for protons (5.8 Å^2). The thermal parameters were refined as Biso which come from the positional displacement (U) as equation 3.1 shows[8]. These values are comparable to those reported by *Kataoka et al.*[7] (~5 Å^2) as it is observed in the comparison of Table A3.1. and Table A3.2. The higher resolution NPD pattern (λ=1.28 Å) was selected in order to go into more detail in the refinement of the proton positions and thermal displacements.

$$B_{iso} = 8\,\pi^2\,U^2 \qquad (3.1)$$

Microstructural parameters with strain broadening were added to the refinement. This fit significantly improved the agreement factors (Table 3.3) although the thermal displacement factor remained still large. By independent refinement of the thermal displacement factor of the three H atoms it was clear that H1 and H3 showed much larger values. Splitting of H1 into 2 positions, as *Kataoka et al.*[7] did, led to equivalent atoms 1 Å apart. Since both positions could not be simultaneously occupied, the site population was set to a half of its value. Anisotropic thermal parameters were considered for both H1 and H3 while H2 remained unsplitted with an isotropic thermal displacement of ~2.0 Å^2. The refinement of these parameters provided more precise –O-H distances. However, other atomic positions, interatomic distances and angles remain largerly unchanged (comparing Table A3.1 and Table A3.3 in the annex). The obtained distance between O4 and H1 (1.32 Å) was the suitable for an O-H bond which distances can vary from 0.9-1.3 Å.

Table 3.3. Agreement factors the refinement of PND data of wavelength of 1.28 Å introducing the strain microstructural parameters of $H_2Ti_3O_7$.

Neutron (λ=1.287 Å)	
$\mathbf{R_p}$	10.6
$\mathbf{R_{wp}}$	9.0
$\mathbf{R_B}$	4.3
$\mathbf{R_F}$	2.9
$\boldsymbol{\chi^2}$	2.29

The refinement was improved after applying these changes (Figure 3.5a) and the structure obtained from the refinement (Figure 3.5b) seems to be more reliable than the one obtained before introducing strain and H splitting. The resulting atomic position and interatomic distances are described in Table 3.4 and Table 3.5, respectively. The obtained atomic positions were in good agreement with the theoretical calculations using the projector augmented wave (PAW) method[9]. These calculations provided four different protons where two of them are in similar crystallographic position for H2. Therefore, the

positions of the protons obtained in the calculations are in good agreement with the neutron refinement described for this phase.

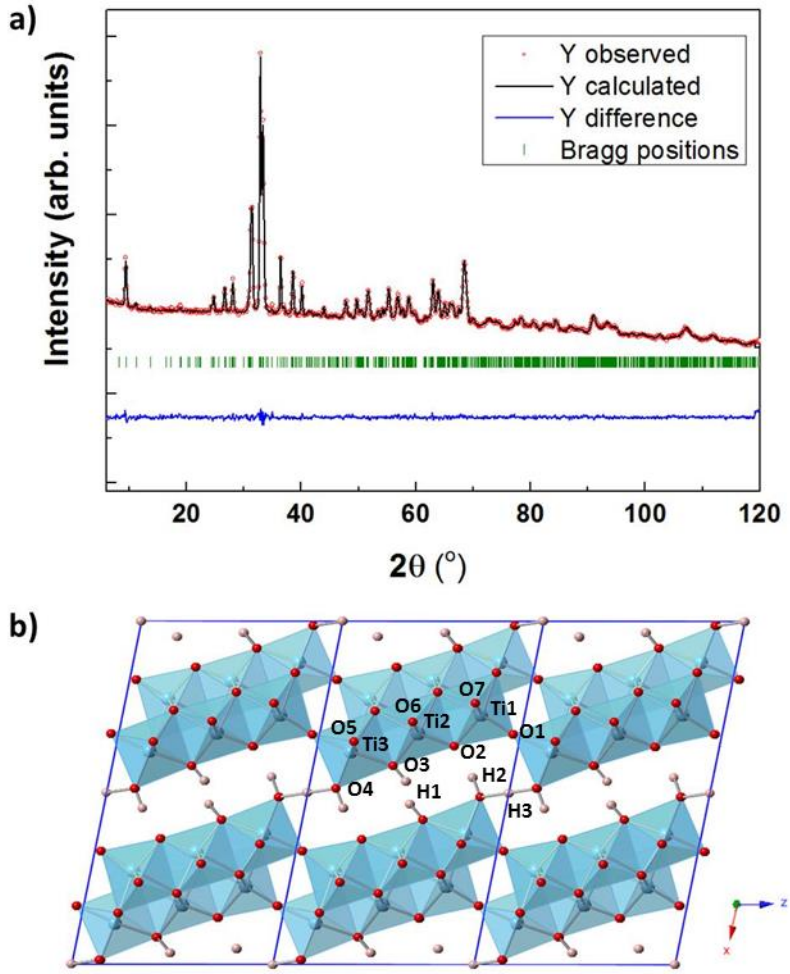

Figure 3.5. Rietveld refinement from the NPD data obtained at 1.28 Å wavelength for $H_2Ti_3O_7$ (a) and the structure (b) obtained from the refinement where red balls are the oxygen, blue octahedra are centered by titanium and white bonds corresponds to the hydrogen atoms. Here, the H1 is splitted and the Bisos for H1 and H3 are anisotropic.

Table 3.4. Atomic positions of $H_2Ti_3O_7$ as obtained from the refinement of PND data of wavelength of 1.28 Å introducing the strain microstructural parameters considering the splitting of H1 and the Baniso of H1 and H3 with space group C2/m.

Atom	Wyckoff position	*x*	*y*	*z*	Biso (Å^2)
Ti 1	4i	0.227(1)	0	0.214(2)	1.0 (3)
Ti 2	4i	0.173(1)	0	0.510(2)	0.7 (3)
Ti 3	4i	0.1206(8)	0	0.827(2)	0.2 (2)
O 1	4i	0.1706(5)	0	0.034(1)	0.3 (2)
O 2	4i	0.1350(6)	0	0.317(1)	0.7 (2)
O 3	4i	0.0788(8)	0	0.602(2)	1.0 (2)
O 4	4i	0.0128(7)	0	0.863(2)	1.8 (2)
O 5	4i	0.3504(5)	0	0.182(1)	0.5 (2)
O 6	4i	0.2927(5)	0	0.454(1)	0.2(2)
O 7	4i	0.2390(6)	0	0.747(1)	0.4 (2)
H 1	4i	0.035(6)	0	0.522(2)	Aniso
H 2	4i	0.046(1)	0	0.195(2)	2.0 (3)
H 3	2a	0	0	0	Aniso

Table 3.5. Distances of $H_2Ti_3O_7$ as obtained from the refinement of PND data of wavelength of 1.28 Å introducing the strain microstructural parameters considering the splitting of H1 and the Baniso of H1 and H3 with space group *C*2/*m*.

	d(Ti1- O) (Å)	d(Ti2-O) (Å)	d(Ti3-O) (Å)	d(H1-O) (Å)	d(H2-O) (Å)	d(H3-O) (Å)
O1	1.72 (2)	-	1.91 (2)	-	-	-
O2	1.91 (2)	1.76 (2)	-	-	1.64 (2)	-
O3	-	1.88 (3)	2.04 (2)	0.91 (6)	-	-
O4	1.97 (5)	-	1.82 (2)	-	-	-
O5	-	-	(2x) 1.938 (4)	-	0.98 (2)	(2x) 1.32 (2)
O6	2.06 (2)	(2x) 1.964 (6) 2.08 (2)	-	-	-	-
O7	(2x) 1.97 (2)	2.22 (3)	2.17 (3)	-	-	-
	1.933	1.978	1.967	**Average distances Ti-O in each octahedron**		

Once the refinement of the structure was completed (Figure 3.5 and Table 3.5), our neutron diffraction data obtained in D1B line of ILL were refined considering the atomic positions described by *K.Kataoka et al.*[7] (see Table 3.6). This refinement was carried out in order to see which structural model fitted better with our experimental data. Indeed the agreement factors of the refinement with the structural model published by *Kataoka et al.* [7] were considerably larger than those achieved with the atomic positions refined in this work and distances Ti-O and H-O seemed to be more reliable (Table 3.6) which confirmed that our model was a better approximation to the real structure.

Table 3.6. Agreement factors of the refinement of the NPD data taking into account the atomic positions obtained by us and *K. Kataoka* et al[7].

$H_2Ti_3O_7$ data of NPD from ILL (1.28 Å)		
Atomic positions	**Our refinement**	**K. Kataoka et al.**
R_p	2.3	8.2
R_{wp}	9.9	22.9
R_B	8.4	22.5
R_F	3.4	12.5
χ^2	2.02	12.48

The reason for not observing the third proton could be due to the fact that *K.Kataoka et al.*[7] used a shorter wavelength (1.80 Å), λ=1.8 Å vs λ=2.52 Å for one of our datasets, which made it less sensitive to the low angle reflections.

It is worth noting that the H2-O4-H3 angle, 102 º is very close to that found in water, 104.5 º as well as H2-O4 distance (0.99 Å). These structural characteristics could suggest that H2-O4-H3 angle can be attributed to be the water molecule leaving $H_2Ti_3O_7$ when it is heated obtaining firstly the $H_2Ti_6O_{13}$ and after $H_2Ti_{12}O_{25}$[10] phases consecutively.

In order to corroborate the validity of the model obtained from the refinement of the neutron diffraction data an analysis of he calculated bond valence sums (BVS) of titanium and hydrogen cations was carried out with Bond_Str. calculations from the Rietveld refinement of FullProf[11] program. BVS is a popular method in coordination chemistry to estimate the oxidation states of atoms. It is derived from the bond valence model, which is a simple yet robust model for validating chemical structures with localized bonds or used to predict some of their properties. The calculated valence from the refinement of the neutron diffraction data were: Ti1, 4.21(8); Ti2, 4.18(9); Ti3, 4.11(7); H1, 0.93(5); H2, 0.97(2); H3, 0.90(1). These values were mostly in agreement with the formal valence of Ti^{4+} and H^+. However, in the analysis of the *Kataoka et al.* [7] the calculated bond valence sums of, Ti1, Ti2, Ti3, H1 and H2 were +3.91(5), +4.45(9), +4.03(5) +1.04(2) and +1.03(2),, respectively. The quite large value in the case of Ti2 indicated a worst refinement of the data. In the analysis of the protons both refinements seem to be more or less similar, while the titanium values are closer to better values in the case of our refinement than the obtained by *K. Kataoka et al.*[7]. This suggested the correctly positioning the H in the structure leds to a more robust $[Ti3O7]^{2-}$ framework. A good refinement was obtained for these data. It is worth noting that deuterium has longer scattering interaction in neutron diffraction. Therefore, the deuteration of the samples would have attempted if the analysis had not succeeded.

3.1.1.2 Scanning Electron Microscopy

The microstructural morphology of protonated titanate was measured by Scanning Electron Microscopy. A homogeneous distribution of the particles was observed (see Figure 3.6a). Particles of $H_2Ti_3O_7$ showed platelet shape and 4 µm length as can be seen in Figure 3.6b. The shape and size of $H_2Ti_3O_7$ material was quite similar to its precursor ($Na_2Ti_3O_7$) as it can be seen in Figure 3.6c and Figure 3.6d.

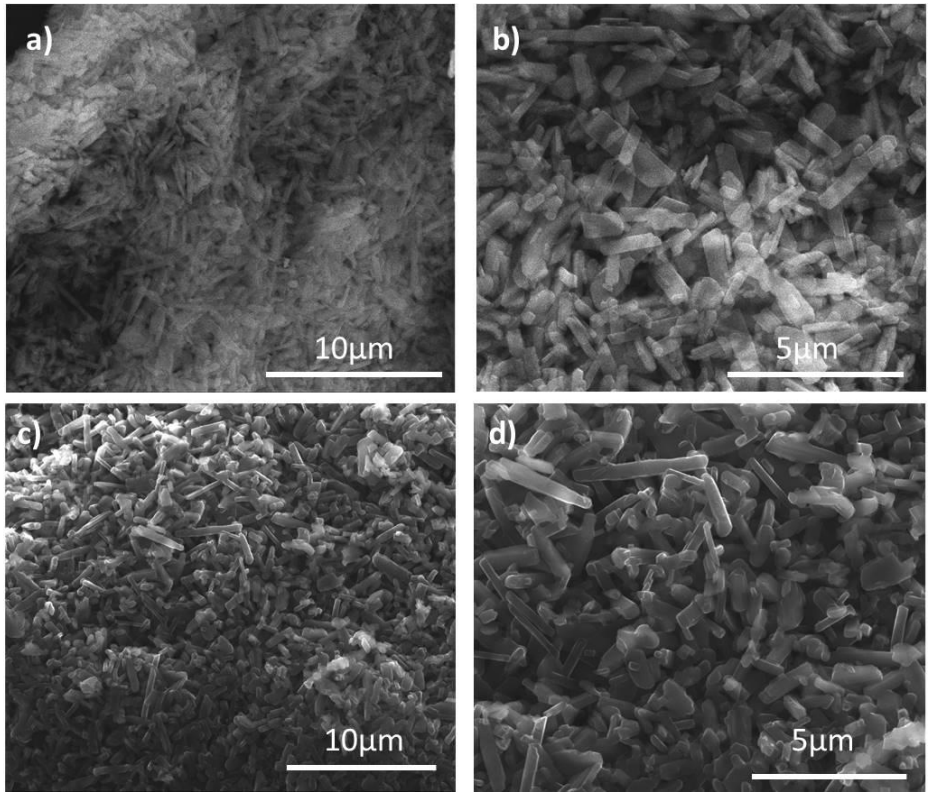

Figure 3.6. SEM images of the synthesized $H_2Ti_3O_7$ and $Na_2Ti_3O_7$ using 10000x (a,c), 20000x (b,d) magnifications respectively.

It is important to mention that the SEM images showed similar shape and size in spite of the acidic exchange in the synthesis of $H_2Ti_3O_7$.

3.1.1.3 Infrared spectroscopy

Infrared analysis of $H_2Ti_3O_7$ was carried out in order to identify the O-H bands that usually appear at around 3500-2900 cm^{-1}.

As it can be seen in Figure 3.7, two bands are observed in that region. One band appeared at 3188 cm^{-1} that it can be attributed to the shorter O-H distance and therefore the strongest O-H bond, i.e. the O3-H1 bond following the nomenclature assigned for the protons from the PND experiment. Other band less pronounced with two different tiny peaks was also observed at between 2990 cm^{-1} and 2920 cm^{-1}. These peaks of the band at 2900 cm^{-1} were assigned for the longest O-H bonds (the weakest O-H bonds). These peaks could correspond to the O4-H2 and O4-H3 bonds which were the weakest bonds. Therefore, the bands in the range of 3500-2900 cm^{-1} of IR spectrum could be assigned for the different O-H bonds in the structure. On the other hand, $H_2Ti_6O_{13}$ showed this band at higher values of wavelength (3320 cm^{-1}) indicating a stronger O-H bond[10].

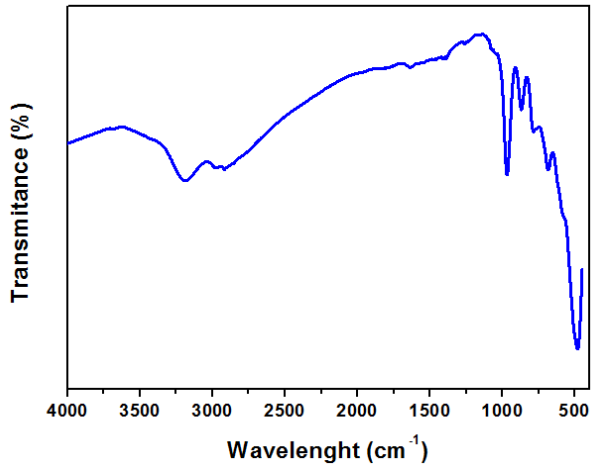

Figure 3.7. IR spectrum of $H_2Ti_3O_7$ measured after the drying process in order to avoid the signals from air moisture.

In the 500-1000 cm^{-1} range many different bands were observed. These peaks could be assigned to different types of Ti–O–Ti stretching vibrations of $H_2Ti_3O_7$ at room temperature[12].

3.1.1.4 Thermogravimetric analysis

Thermogravimetric analysis (or also called TGA) was carried out for $H_2Ti_3O_7$ phase first because it is important to know the thermal stability of the sample (in order to know up to which temperature the material is able to remove the adsorbed moisture without any structural change) and second to quantify the amount of water loss and thus confirm the stoichiometry of the compound. This knowledge could also help to store and handle the material in the appropriate way. In addition, this experiment could be useful. The calculation of the loss of weight was performed by the difference between the crucible with sample and the empty one. The analysis was carried out in air atmosphere in the range of 25 ^{o}C-800 ^{o}C (see Figure 3.8).

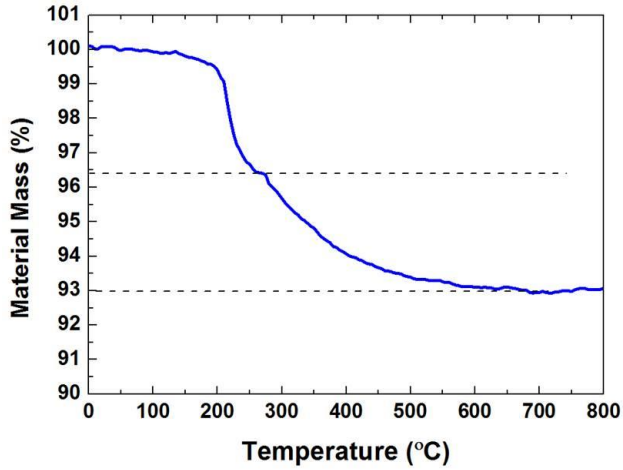

Figure 3.8. Thermogravimetric analysis of the $H_2Ti_3O_7$ sample from room temperature to 800 ^{o}C in air atmosphere.

The mass loss observed for $H_2Ti_3O_7$ was 7% (see equation 3.2) involving two different decompositions. These results were in good agreement with the values that *J. Akimoto et al.*[10] reported. At the first stage (up to 100 ^{o}C), a small decrease was observed. This amount could be assigned to the moisture present in the sample. The decomposition started at 120 ^{o}C likely forming $H_2Ti_6O_{13}$ compound according to a 3.6% of loss. This loss was attributed to half water molecule that was extracted from the structure. At 260 ^{o}C the second decomposition process started. In this case, the formed $H_2Ti_6O_{13}$ was decomposed yielding TiO_2 as final product by the continuous water loss (3.5% of mass loss) as can be seen in equation 3.3. In this process, it was probable that $H_2Ti_{12}O_{25}$ was formed as intermediate but it was not clearly observed in the analysis[10].

$$100 * \left(\frac{18\ g\ H_2O}{257.6\ g\ H_2Ti_3O_7} \right) = 6.99\ \% \qquad (3.2)$$

$$\mathbf{2\ H_2Ti_3O_7 \longrightarrow 2\ H_2Ti_3O_7 + H_2O\ (g) \longrightarrow 6\ TiO_2 + 2\ H_2O\ (g)} \qquad (3.3)$$

In conclusion, $H_2Ti_3O_7$ phase was considered as stable up to 120 ^oC and upon the increment of temperature the phase was losing water molecules forming $H_2Ti_6O_{13}$ as intermediate and yielding TiO_2, as confirmed by PXRD, as final product, stable from 550-600 ^oC up to 800 ^oC (last temperature of the analysis).

3.1.1.5 ^{23}Na and ^{1}H solid state NMR spectroscopy

The ionic exchange of Na by 1H was further confirmed by 23Na and 1H solid state Nuclear Magnetic Resonance. ssNMR is very powerful technique to identify the amount of the different types of atoms in this case sodium and hydrogen). Therefore, the possible presence of sodium ions that could be remained from the $Na_2Ti_3O_7$ (precursor) was analyzed using this technique.

The ^{23}Na ssNMR spectrum (Figure 3.9) shows that there was one signal at 7.2 ppm. This peak was assigned to less than 1% residual sodium as calculated (using DMFit program[13]) to remain in $H_2Ti_3O_7$ from the quantitative integration of the ^{23}Na-NMR signal. The reference used in the analysis of this spectrum was $Na_2Ti_3O_7$. The sodium signal presented in the protonated titanate ^{23}Na-ssNMR could be assigned to the sodium ions that could have in the surface of the synthesized sample after the ionic exchange. In addition, the narrowness of the peak was assigned to higher mobility of these sodium ions in the surface. This fact could indicate that the observed Na ions were not coming from the $Na_2Ti_3O_7$ structure. Therefore, the structural ionic exchange of Na^+ by H^+ was fully complete and confirmed by both PXRD and ^{23}Na-NMR techniques for the $H_2Ti_3O_7$ phase. In comparison with the signals of $Na_2Ti_3O_7$ observed in ^{23}Na-NMR spectrum reported by M.Zarrabeitia et al.[14], it did not fit with the observed signals in ^{23}Na-NMR spectrum of the $H_2Ti_3O_7$ phase. In ^{23}Na-ssNMR of $Na_2Ti_3O_7$, the two types of sodiums in $Na_2Ti_3O_7$ structure appeared at -18 ppm at 3 ppm.

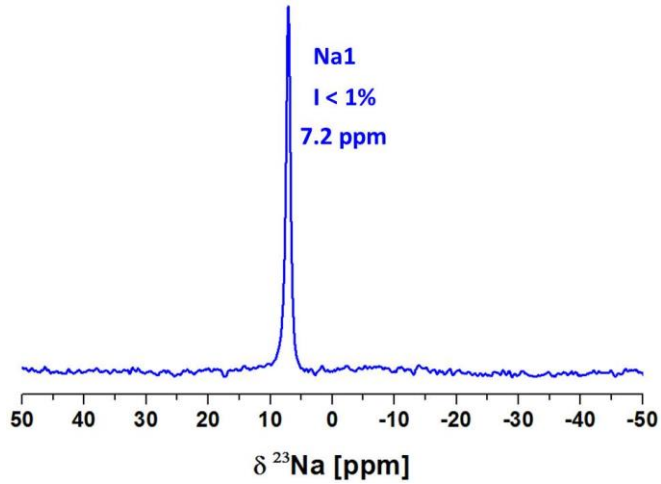

Figure 3.9. Magic angle spinning solid-state NMR spectra of $H_2Ti_3O_7$ ionic exchanged in acidic media from $Na_2Ti_3O_7$ for the core ^{23}Na.

Same rotor study for ^1H nucleus. In Figure 3.10 two signals can be resolved in the ^1H-NMR spectrum of $H_2Ti_3O_7$ at 11 and 13 ppm. The relative intensities of the two ^1H-NMR signals were integrated yielding 25% and 75% respectively. This ratio fully supported the existence of 3 different proton sites where two of them contributing to the same signal rather than two equally abundant protons proposed by *K. Kataoka et al.*[7].

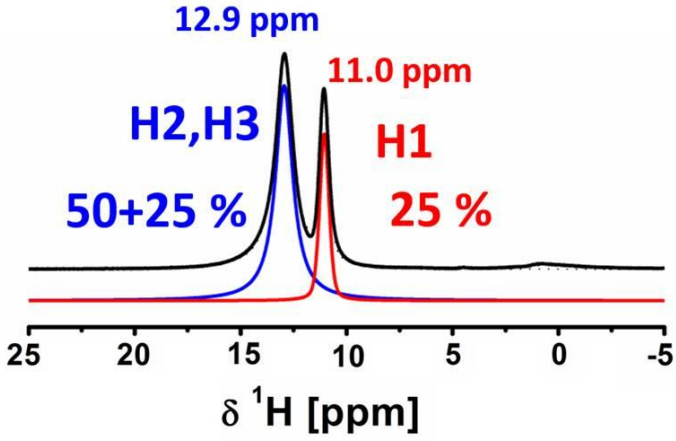

Figure 3.10. Magic angle spinning solid-state ^1H-NMR spectra of $H_2Ti_3O_7$ ionic exchanged in acidic media from $Na_2Ti_3O_7$.

The identification of the peaks was performed taking into account the Neutron Diffraction analysis. The signal at 11 ppm was assigned to H1 showing a population of 25%. This result was in good agreement with the occupancy observed in PND (0.25). The splitting observed for H1 in NPD would agree with the highest proton mobility and the narrowest of the ^{1}H-NMR signal. The signal at 12.9 ppm that corresponded to the 75% of the protons, could be assigned to the other two types of protons (H2 and H3) indicating the possible overlap of the signal because the similar environment of both protons. These two types of protons were bonded to same oxygen O4 (H2 and H3 with populations of 0.5 and 0.25 respectively).

In ^{1}H-NMR study of $H_2Ti_3O_7$, data were collected at much higher spinning rates (50 kHz) which yields much higher resolution spectra than the one previously reported (12 kHz) by *J.Akimoto et al.* [10]. This allowed deconvoluting the signals and integrating them in a better way, yielding a ratio of 1:3. This fact would support the structural model of 3 protons with total unit cell occupancies of 0.25 (H1), 0.5 (H2) and 0.25 (H3) as described in NPD refinement. So that, the integration of the ^{1}H-NMR data fully supports the existence of 3 different proton sites where two of them contribute to the same ^{1}H-NMR signal rather than two equally abundant protons. The chemical shift of these two H^+ signals is larger than the values of 5 and 9 ppm reported for the tunnel like ramsdellite type allotrope $H_2Ti_3O_7$ [9] or the only signal appearing at 10 ppm for the unique type of H^+ in $H_2Ti_6O_{13}$ [15]. This is indicative of a higher H^+ acidity in the layered $H_2Ti_3O_7$, whose most acidic protons should be those nearby the oxygen atom which is coordinated to only one titanium atom. This fact has not been observed neither in the ramsdellite phase nor the $H_2Ti_6O_{13}$ tunnel structure.

3.1.2 Electrochemical characterization

The electrochemical behaviour of $H_2Ti_3O_7$ in lithium ion batteries showed a plateau at 1.5 V *vs* Li^+/Li so considering the common reduction of voltage showed in sodium systems, it could be possible that the plateau of the insertion of sodium ions could be close to 1 V *vs* Na^+/Na. Based on the electronic configuration of the titanium ions $H_2Ti_3O_7$, three electrons can be taken part in the redox reaction from the 3 titanium ions (reduction from Ti^{4+} to Ti^{3+}). Nevertheless, looking at the literature, only 2 electrons usually are taking part in the battery tests[16,17].

In order to select the appropriate voltage range for measuring the $H_2Ti_3O_7$, several measurements were carried out. The material was discharged until 0.05 V *vs* Na^+/Na (green line in the voltage *vs* capacity plot of Figure 3.11). In the discharge, 4

electrochemical processes can be seen at 2 V *vs* Na^+/Na, 1.2 V *vs* Na^+/Na, 0.6 V *vs* Na^+/Na and 0.3 V *vs* Na^+/Na. At 2 V *vs* Na^+/Na, a solid solution process attributed to the insertion of sodium ions in the $H_2Ti_3O_7$ host occurred. The process at 1.2V *vs* Na^+/Na could be attributed to the reduction of Ti^{4+} to Ti^{3+} and only 1 titanium ion of $H_2Ti_3O_7$ is reduced according to its capacity (100 mAh/g). As *P. Senguttuvan et al.*[17] reported for $Na_2Ti_3O_7$, a semi-plateau appeared at 0.6-0.7 V *vs* Na^+/Na that could be attributed to the insertion of sodium ions into the C65 carbon that was used as conductive additive. At 0.3 V *vs* Na^+/Na, the plateau was really similar to the one observed in $Na_2Ti_3O_7$[17]. In this latter process, bigger contribution to the capacity by the formation of SEI layer formation was considered. However, during the charge process, it is clearly seen that there is not much reversibility in this battery. In order to attempt suppressing the plateau at 0.3 V *vs* Na^+/Na, a different battery (Figure 3.11 blue line) was assembled and cycled in the 0.4-3.0 V *vs* Na^+/Na voltage range. In blue line of Figure 3.11 can be easily seen that even the lowest voltage plateau was avoided, the reversibility was not good. However, the processes seemed to be more reversible than the green line of Figure 3.11a. Therefore, we selected region where was the plateau at 1.2 V *vs* Na^+/Na. $H_2Ti_3O_7$ (similar to those observed for P2-$Na_{0.66}[Li_{0.22}Ti_{0.78}]O_2$[18]) was cycled in the voltage range of 0.9-3.0 V *vs* Na^+/Na (Figure 3.11 red line). In δQ/δV plots (Figure 3.11b) can also be seen that above 2.2 V *vs* Na^+/Na there was not any redox process in the battery. That was the reason why the voltage range chosen to measure in detail the electrochemical properties of $H_2Ti_3O_7$ material was in the 0.9-2.2 V *vs* Na^+/Na.

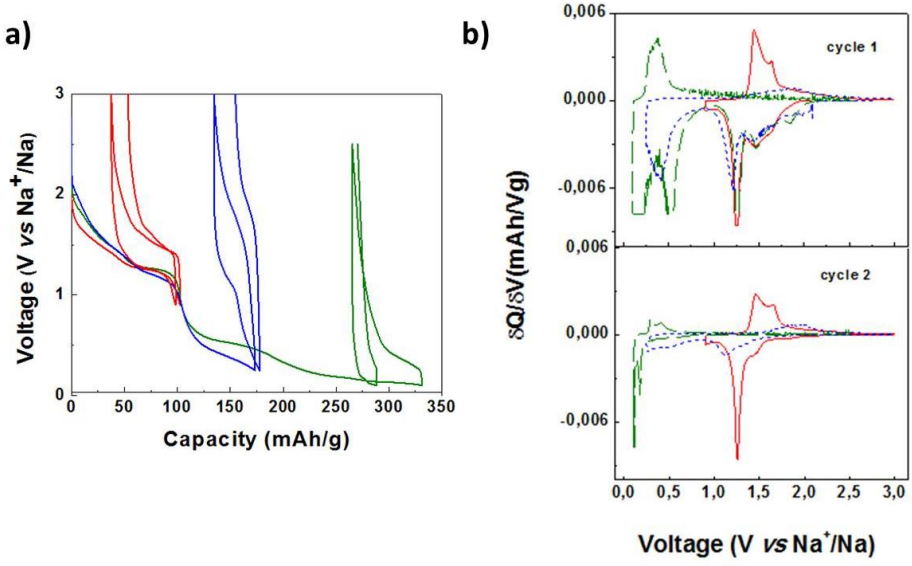

Figure 3.11. Electrochemical performance of $H_2Ti_3O_7$ vs Na^+/Na (a) and δQ/δV plot (b) of the first above and second bottom cycle of $H_2Ti_3O_7$ measured *vs* Na^+/Na. measured in different voltage ranges 0.9-3.0 V (solid red), 0.5-3.0 V (blue dots) and 0.05-2.2 V (dashed green).

Once the voltage range was selected, several electrolytes were tested in order to see which one worked with better performance for this material. It was checked sodium hexafluorophosphate ($NaPF_6$) and sodium perchlorate ($NaClO_4$) as salts, and ethylene carbonate (EC), dimethyl carbonate (DMC) and propylene carbonate (PC) as solvents. 1M $NaClO_4$ in EC:DMC mixture in a 1:1 ratio was selected as electrolyte as showed other titanates[18,19,20]. The electrochemical performance can be seen in Figure 3.12a. The polarization (0.2 Volts) was low but the reversibility of the profile was quite bad. $H_2Ti_3O_7$ was losing capacity every cycle as seen in Figure 3.12b. The irreversibility of the redox process of the titanium reduction/oxidation seemed to indicate that something was happening in the structure. For that reason, an *ex-situ* analysis was performed at the end of the discharge (0.9 V *vs* Na^+/Na). In the XRD of the electrode (Figure 3.13), we could observe that during the first discharge a big structural transformation had occurred. Comparing the diffractogram of the cycled electrode with the diffractograms of $H_2Ti_3O_7$ and $Na_2Ti_3O_7$, it can be seen that the structure at the end of the discharge had changed into $Na_2Ti_3O_7$–type structure.

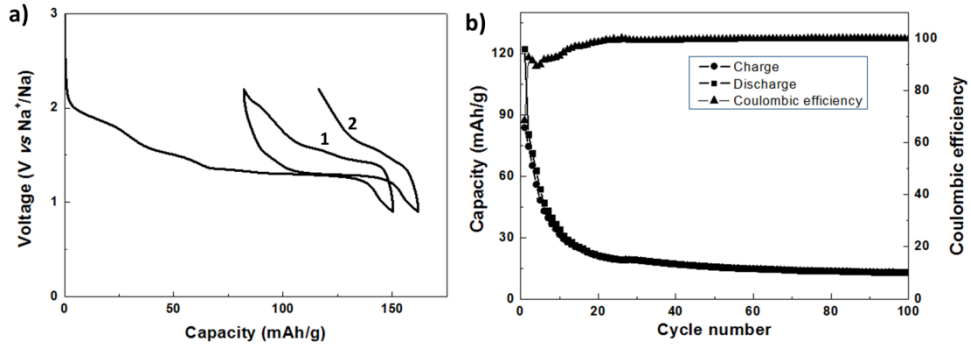

Figure 3.12. Galvanostatic discharge and charge in the first and second cycle of the voltage vs capacity discharge profiles (a) and cyclability of $H_2Ti_3O_7$ at C/10 rate for 100 cycles in the 0.9-2.2 V *vs* Na^+/Na voltage range for sodium ion batteries.

Seeing the low reversibility and the bad electrochemical properties, a CV and GITT experiments were carried out at very low rates (0.1 mVolt/s; and 15 minutes applying current before 2 hours relaxing respectively). In Figure 3.14a the cyclic voltammetry is observed. There it can be seen that the electrochemical process of the first discharge at 1.1 V *vs* Na^+/Na was shifted to 1.2 Volts *vs* Na^+/Na for the Ti^{4+}/Ti^{3+} reduction. During the charge, on the contrary, the voltage of the redox process decreased to 1.5 V *vs* Na^+/Na from 1.6 Volts *vs* Na^+/Na. In addition, in every cycle of the CV, the current that could be integrated from the peaks was becoming lower so the redox processes were not completely reversible in agreement with the cyclability observed in Figure 3.12b. The GITT of the first discharge (Figure 3.14b) helped to understand the first discharge processes. There were several solid solution processes from 2.2 V *vs* Na^+/Na to 1.4 V *vs*

Na^+/Na where the diffusion coefficient can be calculated following the Fick´s law of diffusion. In the solid solution region can be analyzed because the electrode diffusion was calculated without considering the effect of the interphase boundary movement on ion transport[21].

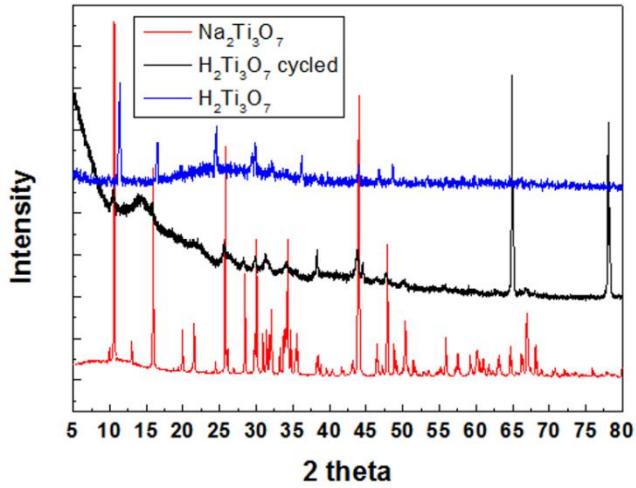

Figure 3.13. *Ex-situ* $H_2Ti_3O_7$ electrode (black line) and pristines $Na_2Ti_3O_7$ (red line) and $H_2Ti_3O_7$ (blue line) in the range of 5-80º of 2 theta after the first discharge to 0.9 Volts *vs* Na^+/Na.

In addition, there were two plateaux at 1.4 and 1.1 Volts *vs* Na^+/Na. These plateaux correspond to the reduction of titanium Ti^{4+}/Ti^{3+} and to the sodium insertion in the same locations than appear in the sodium titanate. These processes were involved in the structural transformation into $Na_2Ti_3O_7$-type structure at the end of discharge. Moreover, it is worth mentioning that the presence of two plateaux could be assigned for the insertion of each kind of sodium ion into the each different crystallographic site.

Also, through the zoom of GITT experiment (Figure 3.14c), the diffusion coefficient was calculated through the equation 3.4 where sodium ions can diffuse easily than the calculated by the same method for $Na_2Ti_3O_7$ by *A.Rudola et al.*[19]. While they obtained a diffusion coefficient of $3.48 \cdot 10^{-12}$ cm^2/s for $Na_2Ti_3O_7$, for $H_2Ti_3O_7$ a diffusion coefficient of $1.68 \cdot 10^{-11}$ cm^2/s was obtained, which is 5 times larger.

$$D^{GITT} = \frac{4}{\tau\pi}\left(\frac{V_{electrode}}{S_{electrode}}\right)^2\left(\frac{\Delta E_S}{\Delta E_t}\right)^2 = 1.68\,10^{-11}\ \mathrm{cm}^2/\mathrm{s} \qquad (3.4)$$

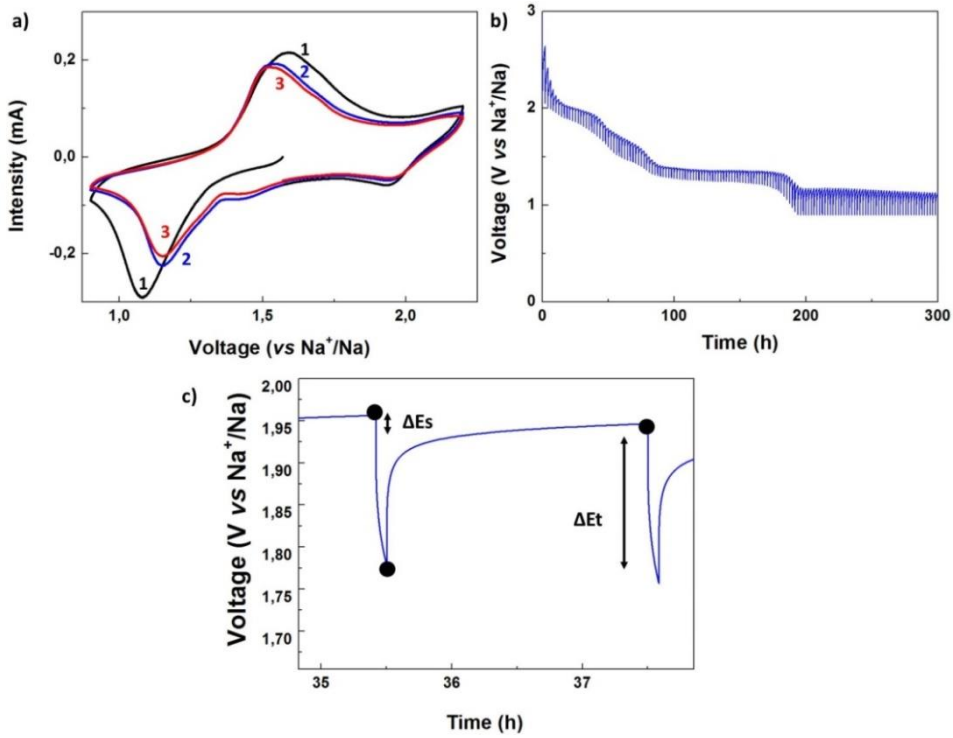

Figure 3.14. Cyclic voltammetry (a) and GITT experiment (b) and zoom of the GITT experiment of $H_2Ti_3O_7$ in the 0.9-2.2 V *vs* Na^+/Na voltage range for sodium ion batteries indicating the parameters used to calculate the diffusion coeficient.

In order to understand what was happening inside the battery and at which point of the discharge the structural change was occurring from $H_2Ti_3O_7$ like structure to $Na_2Ti_3O_7$ type structure, an *in-situ* XRD experiment was performed (Figure 3.15). In the *in-situ* XRD holder, mixture of $H_2Ti_3O_7$ and C65 was placed with two separators, electrolyte and sodium metal and then the cell was closed with the beryllium covered by aluminum disk. The material was discharged until 0.9 V *vs* Na^+/Na (thus avoiding the SEI formation and sodium insertion into the carbon) and it was seen that 1.2 Na^+ ions were sequentially added in the structure (Figure 3.15) down to this voltage. First of all, from 2.4 V *vs* Na^+/Na to 1.2 V *vs* Na^+/Na there were several processes of solid solution where 0.6 Na^+ ions were added to the host $H_2Ti_3O_7$ (δQ/δV plot), resulting in $Na_{0.6}H_2Ti_3O_7$ of $H_2Ti_3O_7$ type (*C*2/*m*). During cycling from OCV to 1.2 V *vs* Na^+/Na a solid solution process occurred. The diffractograms, in this range, exhibited a shift of the reflections indicating the insertion of Na^+ ions into the protonated titanate and were successfully refined with *C*2/*m* space group. At 1.2 V *vs* Na^+/Na, the plateau (two phase reaction) appeared. This plateau was characterized through δQ/δV plot as a very well defined sharp peak. At this stage, some reflections disappeared (such as the reflection at 2 theta values of 24º and 36º) and other

reflections continued shifting (as for example the reflection at 2 theta values of 12º and 17º). Moreover, reflections of a new phase appeared (as the reflections appeared at 27º, 28º or 31º of 2 theta). The appearance of the three processes during the plateau indicated that the intermediate compound of 1.2 V *vs* Na^+/Na ($Na_{0.6}H_2Ti_3O_7$) was transformed into $Na_2Ti_3O_7$ like the structure and the formed compound was also intercalating sodium ions. In this range, two phases were refined; the first one was based on $H_2Ti_3O_7$ like structure and another one, with $P2_1/m$ space group similar to the $Na_2Ti_3O_7$ structure. But looking at the difference between the initial and final state, it can be seen that the structure has turned from the monoclinic $C2/m$ into the $P2_1/m$ space group. The first diffractogram was easily fitted through Pattern Matching refinement included in Fullprof as the $H_2Ti_3O_7$ (Figure 3.16a). Trying to identify which phase was formed during the discharge, latest diffractograms were analysed. These patterns of the *in-situ* could be fitted using the $Na_2Ti_3O_7$ structure program as the refinement of Figure 3.16b shows. Contrary to what happens in $H_2Ti_6O_{13}$ where the two first intercalated lithium ions replace the protons with chemical reduction of the H^+ into H_2 (which evolves as a gas)[15], in $H_2Ti_3O_7$ the protons seem to remain in the structure during reduction and are mainly extracted upon oxidation. Indeed, for lithium ion batteries the H^+/Li^+ ion-exchange reaction occurs in the battery during cycling. In fact, the *ex-situ* XRD pattern of the $H_2Ti_3O_7$ electrode after cycling tests proved the formation of the isostructural layered $Li_2Ti_3O_7$[10].

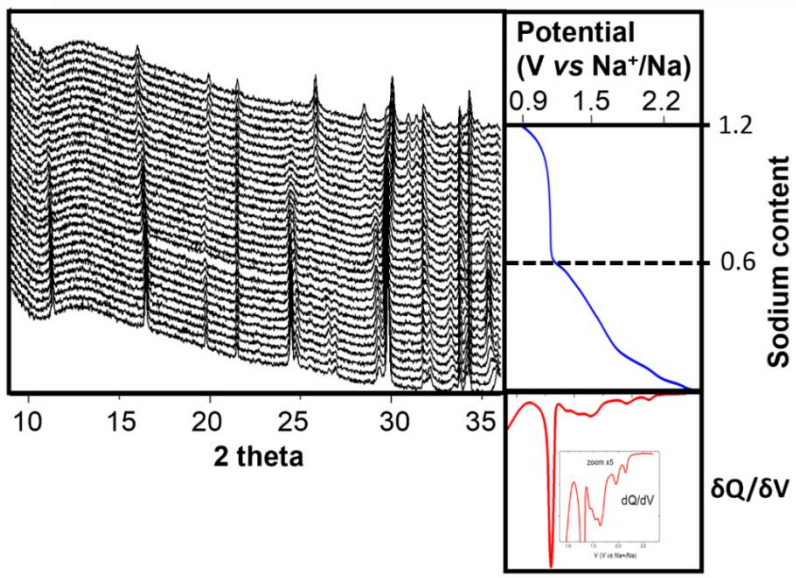

Figure 3.15. *In-situ* XRD diffractograms (black lines) in the range of 2 theta of 9-36º, galvanostatic discharge (blue line) in 0.9-2.4 V *vs* Na^+/Na range and δQ/δV plot (red) of $H_2Ti_3O_7$.

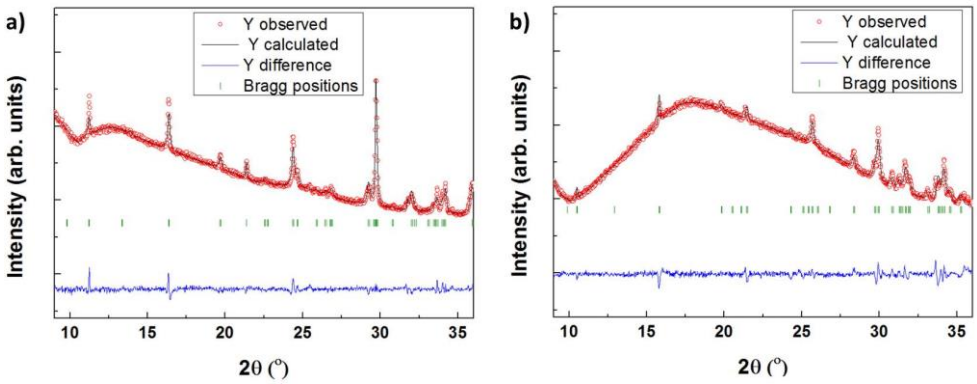

Figure 3.16. Profile Matching refinement of the first (a) and the last (b) diffractogram of *in-situ* measurement corresponding to $H_2Ti_3O_7$ like structure and $Na_2Ti_3O_7$ like structure.

The difference in the cell parameters obtained by the refinement of all the scans provided us the tendency upon scans. The cell parameter *a* is increasing during the sodium insertion up to approximately 0.8 sodium ions (see Figure 3.17) where the *a* parameter increased to 17 Å that would indicate the formation of the $Na_2Ti_3O_7$. This phase has an *a* cell parameter of 8.57 Å which was almost half of that of $H_2Ti_3O_7$. Therefore, the cell C-centered at *C*2/*m* of the pristine electrode was split in two cells crystallographically identical resembled into $P2_1/m$ space group.

So that, at this point is starting the transformation from $H_2Ti_3O_7$ to $Na_2Ti_3O_7$. This change is observed in the *β* angle as well. However, for *b* and *c* parameters remain almost unchanged due to the short variations as it can be seen in the red and blue lines of Figure 3.17.

The bad capacity retention could be explained by the structural transformation. According the structural transformation upon cycling at this range of voltage, it was considered that it could worth going to lower voltage and see how the behaviour of this material was. It should be the same than $Na_2Ti_3O_7$ but it had to be proved. Thus, after 1, 2, 3 and 4 cycles at the voltage range 0.9-2.2 V *vs* Na^+/Na; the voltage was reduced to 0.05 V *vs* Na^+/Na as it can be seen in Figure 3.18a. There is a big difference lowing to voltage to 0.05 V *vs* Na^+/Na from $H_2Ti_3O_7$ than after one cycle at higher voltage. It means that when $H_2Ti_3O_7$ is discharged to 0.05 V *vs* Na^+/Na, the structure does not have enough sodium as $Na_2Ti_3O_7$ to observe a reversible redox process at 0.3 V *vs* Na^+/Na. However, after one cycle at higher voltages in which most of the protons may come out, the sample is working as $Na_2Ti_3O_7$ showing almost the same electrochemical processes. In Figure 3.18b, it can be seen that the one that it was cycled twice at higher voltage and later cycled at lower voltages, seemed to be the better one in terms of capacity and cyclability. This improvement may be related to the sodium:hydrogen ratio content.

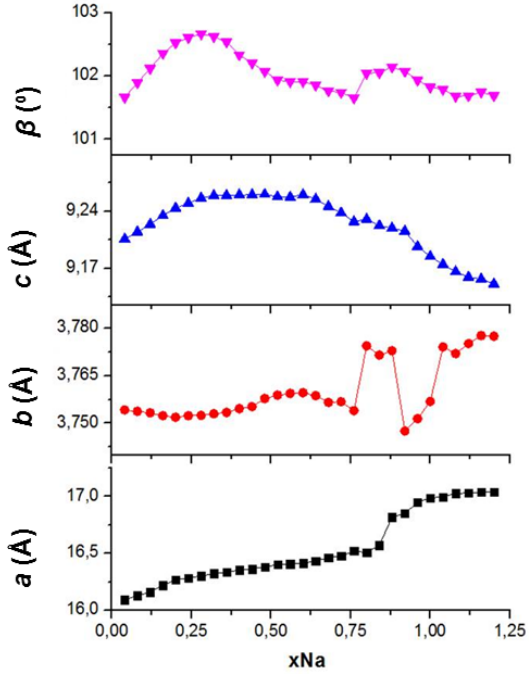

Figure 3.17. Difference in *a*, *b*, *c* and *β* cell parameters obtained from the Pattern Matching refinement of the *in-situ* cell.

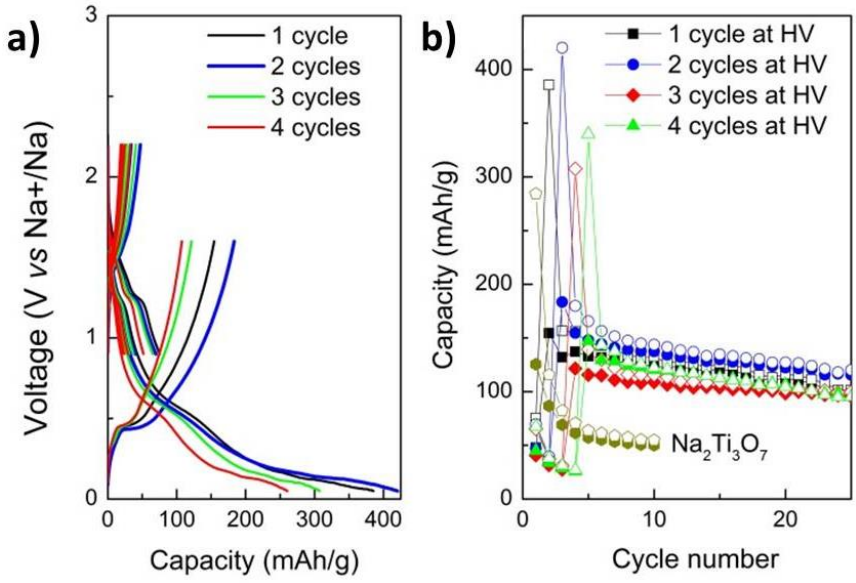

Figure 3.18. Galvanostatic discharge/charge profile (a) and cyclability (b) of the cells cycled at high voltage first for a different number of cycles and at the same voltage range as $Na_2Ti_3O_7$ afterwards**.**

In order to know clearly which was the composition of the titanate after that 2 cycles, an *ex-situ* ^{1}H-NMR experiment was carried out. The electrode cycled twice in the higher voltage range was cleaned removing the possible salts of the electrolyte using dimethyl carbonate. Afterwards, the electrode material was separated from the current collector and was placed into a 1,3mm rotor and in order to be able to quantify the amount of sodium and proton, the amount of sample was weighted (3.6 mg). This rotor was begun to spin at 50 KHz and after the proton signal was tuned at 500 MHz. In the experiment, two signals of proton were observed: one at 3.7 ppm and another at 11.0 ppm. There, it could be seen in Figure 3.19 that only one corresponded to one kind of proton left in the structure. It was observed that the H1 was still in the structure and the protons H2 and H3 had disappeared from the structure. Also, as the mass of the powder introduced in the rotor was weighted, it was possible to calculate the quantity of H1 remaining in the structure. However, the broad signal centred at 3.7 ppm which according to the literature could be assigned to dimethyl carbonate (DMC). This compound could appear due to the solvent used to remove the $NaClO_4$ salt was not completely evaporated.

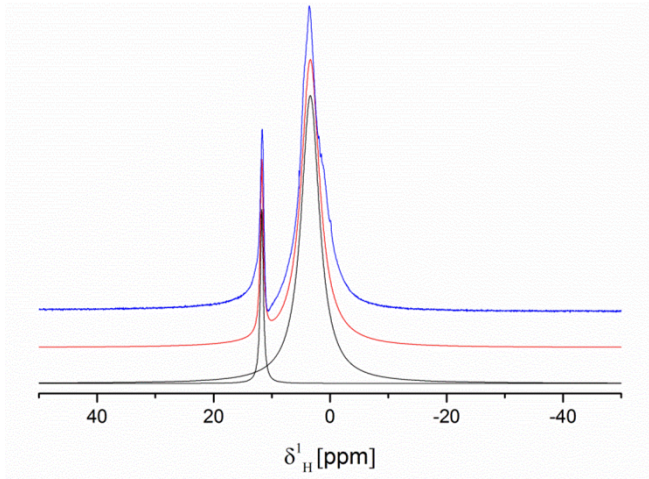

Figure 3.19. Experimental and fitting ^{1}H-NMR spectra of $H_2Ti_3O_7$ after two cycles in the 0.9-2.2 V *vs* Na^+/Na range where blue line is the raw data, the red line the calculated from the spectrum and the black lines the refinement of both peaks.

The signal appeared at 11.0 ppm corresponded to the H1 was fitted with DMFit program. The ^{1}H-NMR spectra was previously fitted for the $H_2Ti_3O_7$, so, as the same number of scans were carried out and knowing the weight of the material placed, from the intensity of signal the amount of the H1 could be determined. It was obtained that about 0.2 H^+ per formula unit was remaining in the structure. Nevertheless, it is not possible to determinate the exact amount of H^+ because it was calculated for the $H_2Ti_3O_7$ compound and the obtained compound had not the same stoichiometry. So the compound obtained

after cycling two times at high voltage should have a formula unit similar to $Na_{1.8}H_{0.2}Ti_3O_7$. This phase is cycling quite well, better than the $Na_2Ti_3O_7$ and it could be because at recent studies, it was shown that sodium titanate is not thermodynamically stable and it spontaneously protonated changing to mixed compositions of proton and sodium[23,24]. In these samples, it was observed that the plateau corresponding to the sodium insertion was in between the 0.3 V *vs* Na^+/Na of $Na_2Ti_3O_7$ to the 1.2 V *vs* Na^+/Na observed in this work for $H_2Ti_3O_7$.

For this material, the rate capability was carried out. The rate capability consists on applying different current densities in order to see how the material responded. If material is not very good electronic conductor the polarization will increase a lot at higher rates. It makes that some anodic materials which have the plateau close to 0 V *vs* Na^+/Na, such as hard carbon, at high rates are not able to intercalate sodium ions because sodium electroplating occurs before the sodium insertion into the carbon. Besides, applying high currents to the material makes the kinetics worse because the reaction has not enough time to take place. So the intrinsic characteristics of the material in terms of kinetics and sodium insertion voltage plateau are important to analyze the ability of the material to work at higher current rates. In this case, material worked quite well at high rates (1C) obtaining 100 mAh/g of capacity as it can be seen in Figure 3.20. From the second cycle at high voltage, the capacity was fading during the increment of the current as usually happens in this kind of experiment. Giving less time to the system to insert the sodium ions, the reaction was not completely occurred, so, that is the why the capacity decreased during the increment of the current. Moreover, it is important to mention that the material was able to recover the initial capacity (155 mAh/g) when cycling at low currents (C/10 = 20.8 mA/g) after the cycles at high current density. Also, when the voltage of the cell is decreased up to 0.05 V *vs* Na^+/Na, the increment of the SEI layer formation is clearly seen in the obtained discharge capacity (320 mAh/g). The reason of the increment of the SEI layer formation is that the voltage range in the first two cycles was quite higher compared to the third discharge. Therefore, electrolyte was not fully decomposed as *M. Muñoz-Marquez et al.*[25] reported for $Na_2Ti_3O_7$ and until 0.9 V *vs* Na^+/Na just NaF and NaCl were formed from pVdF and $NaClO_4$ respectively. However, reaching 0.05 V *vs* Na^+/Na sodium carbonate, PEO blocks and alkyl-carbonates were formed causing the increment of the capacity of the third discharge.

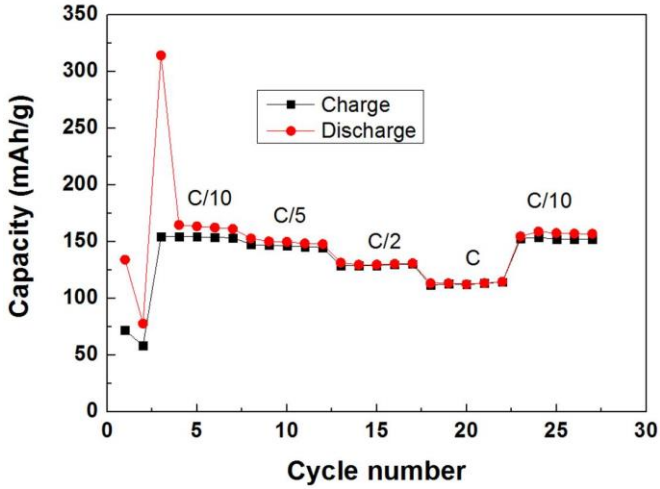

Figure 3.20. Rate capability of $H_2Ti_3O_7$ conditioning for 2 cycles at 0.9-2.2 V and then going down to 0.005-1.6 V. The first two cycles were perfomed at C/10 and different C-Rates were tested from C/10 to C in the range of 0.005-1.6 V.

Nevertheless, the reversibility of titanates did not seem to be the appropriate for an anodic material making this family of materials not the best candidates as anodes for sodium ion batteries, in spite the lower voltage plateau observed in $Na_2Ti_3O_7$. The big capacity fading observed in titanates could be improved by different sample handling. It was observed that using other synthesis parameters, such as another precursor (using sodium hydroxide instead of sodium carbonate) and different atmosphere (keeping the sample under argon atmosphere) or the use of Na-CMC (Carboxymethylcellulose) as binder in the electrode preparation; the capacity fading could be decreased and a 78% of the initial capacity (128 mAh/g) could be kept after 100 cycles[24]. Impedance measurements showed that the charge transfer resistance is smaller using the sodium hydroxide as precursor and handling the samples in argon atmosphere than in the conditions followed in this work. Moreover, during the charge, the charge transfer was decreasing according to the experiment of XPS due to the instability of SEI layer formed in the discharge process and partially dissolved during the charge.

Moreover, another critical point observed during the cycling was the SEI (solid electrolyte interphase) formed in the sodium insertion and deinsertion into the $Na_2Ti_3O_7$. This SEI layer formed upon cycling was studied by XPS. It was observed that as soon as the battery was assembled, the fluoride of the pVdF used as binder and the chlorine coming from the salt of the electrolyte ($NaClO_4$) reacted forming NaCl and NaF in the surface of electrode. At the end of discharge, it was observed that sodium carbonate and alkyl carbonates were formed from the decomposition of the solvents of the electrolyte and PEO

oligomers through the polymerization of the ethylene carbonate. Some of these components of the SEI layer were partially dissolved in the electrolyte during the charge process and some signals such as CF_2 block from the binder (pVdF) was partly reappearing after every charge step[25].

All the electrochemical results obtained in this work were in agreement with the different reports of this type of titanates[17,19,24]. The drawback of the capacity fading and the small capacity obtained caused that these titanates are not good candidates as anode materials for sodium ion batteries. This way, the need of finding a suitable anode for this technology makes necessary to explore new families of materials that can provide the required performance. This fact is the key in order to be competitive respect to lithium technology.

3.2 Conclusions

$H_2Ti_3O_7$ was successfully synthesized by ionic exchange from $Na_2Ti_3O_7$ and it was obtained as pure single phase confirmed by the Rietveld refinement of X-Ray Diffraction data. The GFourier study of the measurements of combined X-Ray and Neutron Diffraction of the phase $H_2Ti_3O_7$ allowed determining three types of protons and their positions in the structure. ^{1}H-ssNMR of the $H_2Ti_3O_7$ showed two signals that could indicate the presence of just two protons. However, through the quantification of the signals by DMFit program, we could conclude that one signal (11 ppm) could correspond to the proton centered in the unit cell (H1) and another signal (12.9 ppm) to the two more acidid different types of proton (H2 and H3). All the techniques together provided us enough information to identify the characteristics of the structure and in particular, the location of the protons.

The electrochemical performance of $H_2Ti_3O_7$ for sodium ion batteries did not accomplish the expectations that arouse given the previously reached performance as anodes for lithium ion batteries. Hugh capacity fading was observed and after the 10th cycle the material was not electrochemically active in the same voltage range. GITT experiment permitted to evaluate the kinetics of the reaction observing that the diffusion coefficient of Na ions was $1.68 \cdot 10^{-11}$ cm^2/s faster than in $Na_2Ti_3O_7$. When the material is discharged till 0.9 Volts, the structure turned into $Na_2Ti_3O_7$ like as shown by *in-situ* PXRD. By ^{1}H-NMR the remaining amount of proton after the two cycles in the range 0.9-2.2 V *vs* Na^+/Na in the structure was calculated: minimum 0.2 of H1/f.u so the structure would be similar to $Na_{1.8}H_{0.2}Ti_3O_7$. The cyclability of the battery with this composition had good performance and worked quite well at different rates showing that the material was very stable and could be suitable for sodium ion batteries if other issues related to SEI layer formation could be solved.

3.3 References

[1] S. Andersson and A. D. Wadsley; "The crystal structure of $Na_2Ti_3O_7$"; *Acta Crystallographica,* 1961, **14**, 1245.

[2] M.Gateshki, Q. Chen, L. M. Peng, P. Chupas and V.Petkov; "Structure of nanosized materials by high-energy X-ray diffraction: study of titanate nanotubes"; *Zeitschrift fuer Kristallographie*, 2007, **222** (11), 612.

[3] T. P. Feist and P. K. Davies; "The soft chemical synthesis of TiO_2 (B) from layered titanates"; *J. Solid State Chem.* 1992, **101,** 275.

[4] https://www.ncnr.nist.gov/resources/n-lengths/elements/h.html

[5] A. J. Ramirez-Cuesta, M. O. Jones and W. I. F. David; "Neutron scattering and hydrogen storage"; *Materials Today*, 2009, **12**(11), 54.

[6] K. Kataoka, N. Kijima, and J. Akimoto; "Ion-Exchange Synthesis, Crystal Structure, and Physical Properties of Hydrogen Titanium Oxide $H_2Ti_3O_7$"; *Inorg. Chem.* ,2013, **52**, 13861.

[8] J. Painter and E. A. Merrit; "Optimal description of a protein structure in terms of multiple groups undergoing TLS motion"; *Acta Cryst.*, 2006, **D62**, 439.

[9] M. Mori, Y. Kumagai, K. Matsunaga and I. Tanaka; "First-principles investigation of atomic structures and stability of proton-exchanged layered sodium titanate" ; *Phys. Rev B* 2009, **79**, 144117.

[10] J. Akimoto, K. Chiba, N. Kijima, H. Hayakawa, S. Hayashi, Y. Gotoh and Y. Idemoto; "Soft-Chemical Synthesis and Electrochemical Property of $H_2Ti_{12}O_{25}$ as a Negative Electrode Material for Rechargeable Lithium-Ion Batteries"; *J. Electrochem. Soc.* 2011, **158**, A546.

[11] J. Rodriguez-Carvajal; "Recent advances in magnetic structure determination by neutron powder diffraction"; *Physica B.,*1993, **192**, 55.

[12] S. Papp, L. Körösi, V. Meynen, P. Cool, E. F. Vansant and I. Dékány; "The influence of temperature on the structural behaviour of sodium tri- and hexa-titanates and their protonated forms"; *Journal of Solid State Chemistry,* 2005, **178**, 1614.

[13] D. Massiot, F. Fayon, M. Capron, I. King, S. Le Calvé, B. Alonso, J. O. Durand, B. Bujoli, Z. Gan and G. Hoatson; "Modelling one- and two-dimensional solid-state NMR spectra"; *Magnetic Resonance in Chemistry,* 2002, **40**, 70.

[14] M. Zarrabeitia, E. Castillo-Martínez, J.M. López Del Amo, A. Eguía-Barrio, M.A. Muñoz- Márquez, T. Rojo and M. Casas-Cabanas; "Identification of the critical synthesis parameters for enhanced cycling stability of Na-ion anode material $Na_2Ti_3O_7$"; *Acta Materialia*, 2016, **104**, 125.

[15] J. C. Pérez-Flores, F. García-Alvarado, M. Hoelzel, I. Sobrados, J. Sanz and A. Kuhn; "Insight into the channel ion distribution and influence on the lithium insertion properties of hexatitanates $A_2Ti_6O_{13}$ (A = Na, Li, H) as candidates for anode materials in lithium-ion batteries"; *Dalton Trans*., 2012, **41**, 14633.

[16] G. Rousse, M. E. Arroyo-de Dompablo, P. Senguttuvan, A. Ponrouch, J. M. Tarascon and M. R. Palacín; "Rationalization of Intercalation Potential and Redox Mechanism for $A_2Ti_3O_7$ (A = Li, Na)"; *Chem. Mater.*, 2013, **25** (24), 4946.

[17] P. Senguttuvan, G. Rousse, V. Seznec, J. M. Tarascon and R. M. Palacin; "$Na_2Ti_3O_7$: Lowest Voltage Ever Reported Oxide Insertion Electrode for Sodium Ion Batteries"; *Chem. Mater.,* 2011, **23**, 4109.

[18] Y. Wang, X. Yu, S. Xu, J. Bai, R. Xiao, Y. S. Hu, H. Li, X. Q. Yang, L. Chen and X. Huang; "A zero-strain layered metal oxide as the negative electrode for long-life sodium-ion batteries."; *Nat. Commun.* , 2013, **4**, 2365.

[19] A. Rudola, K. Saravanan, C. W. Mason and P. Balaya; "$Na_2Ti_3O_7$: an intercalation based anode for sodium-ion battery applications"; *J. Mater. Chem. A*, 2013, **1**, 2653.

[20] G. Yang, H. Song, M. Wu and C. Wang; "Porous $NaTi_2(PO_4)_3$ nanocubes: a high-rate nonaqueous sodium anode material with more than 10 000 cycle life"; *J. Mater. Chem. A*, 2015, **3**, 18718.
[21] Y. Zhu and C. Wang; "Galvanostatic Intermittent Titration Technique for Phase-Transformation Electrodes"; *J. Phys. Chem. C,* 2010**, 114,** 2830.
[23] J. Nava-Avedaño, A. Morales-Garcia, A. Ponrouch, G. Rousse, C. Frontera, P. Senguttuvan, J. M. Tarascon, M. E. Arroyo- de Dompablo and M. R. Palacin; "Taking steps forward in understanding the electrochemical behavior of $Na_2Ti_3O_7$"; *J. Mater. Chem. A*, 2015,**3**, 22280.
[24] M. Zarrabeitia, E. Castillo-Martínez, J.M. López Del Amo, A. Eguía-Barrio, M.A. Muñoz- Márquez, T. Rojo and M. Casas-Cabanas; "Towards environmentally friendly Na-ion batteries: Moisture and water stability of $Na_2Ti_3O_7$"; *Journal of Power Sources*, 2016, **324**, 378.
[25] M.A. Muñoz-Márquez, M. Zarrabeitia, E. Castillo-Martínez, A. Eguía-Barrio, T. Rojo, M. Casas-Cabanas; "Composition and Evolution of the Solid-Electrolyte Interphase in $Na_2Ti_3O_7$Electrodes for Na-Ion Batteries: XPS and Auger Parameter Analysis"; *ACS Appl. Mater. Interfaces,* 2015, **7**, 780.

4- Structural characterization and kinetic study of the conversion reactions of ZnNCN and CuNCN

In this chapter the structural and electrochemical characterization of copper and zinc carbodiimides are described. For the structural characterization, X-Ray Diffraction (at room temperature and upon the increment of temperature), Scanning Electron Microscopy and InfraRed Spectroscopy measurements were carried out. On the other hand, for electrochemical characterization galvanostatic charge-discharge and *ex-situ* XRD of discharged electrodes were measured in order to understand the mechanism of electrochemical reaction. In addition, for CuNCN, a detailed analysis of the Solid Electrolyte Interphase (SEI) layer formation and the irreversible capacity of the first cycle were performed. The study of SEI layer formation was carried out by SEM imaging of the electrode cross-section, XPS analysis and electrochemical impedance spectroscopy while potentiostatic measurements were performed to study the irreversibility.

4.1 Results and discussion

4.1.1 Structural and physicochemical characterization

4.1.1.1 Powder X-Ray Diffraction

XRD data were refined with the Fullprof Package program[1]. Zero, cell parameters, scale, background and atomic positions were refined simultaneously using Thompson Cox-Hastings pseudo Voigt function for the peaks fitting.

XRD diffractogram of ZnNCN powders exhibited narrow reflections suggesting that the material was highly crystalline. All reflections were in agreement with the reported[2] tetragonal single-crystal structure, *S.G. I*-42*d* (nº122). In ZnNCN, the unit cell comprises 8 formula units. The good fitting of the XRD pattern indicated that ZnNCN was synthesized as single phase (Figure 4.1a). Unit cell parameters, volume (and V/Z), molecular weight and the agreement factors obtained from the Rietveld refinement are shown in Table 4.1.

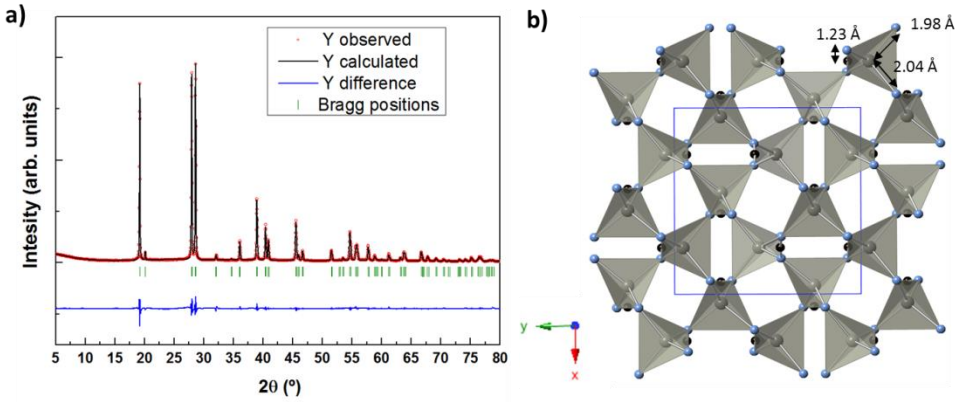

Figure 4.1. Observed (red dots), calculated (solid black line), and difference (blue bottom curve) patterns for the Rietveld analysis from the powder X-ray diffraction data of ZnNCN. Green short vertical lines below the profile indicate the peak positions of all the possible Bragg reflections (a). The structure obtained from the refinement for ZnNCN where light blue spheres are the nitrogen atoms, the black spheres are carbon atoms, grey spheres are zinc atoms and dark grey spheres are lead atoms in the YX plane (b).

In ZnNCN, Zn^{2+} were coordinated by 4 Nitrogen atoms forming tetrahedrons, as it can be shown in Figure 4.1b, as most of Zn^{2+} compounds. The oxidation state (2+) is the most common and stable for zinc.

Table 4.1. Cell parameters and agreement factors obtained from the Rietveld refinement method of ZnNCN**.**

Cell parameters		**Agreement factors from Rietveld**	
a=*b* (Å)	8.815(1)	R_p (%)	8.1
c (Å)	5.432(4)	R_{wp}(%)	10.1
Volume (Å^3)// V/Z (Å^3)	422.089(8) / 52.761	R_{Bragg} (%)	2.95
Molar mass (g/mol)	105.38	χ^2	4.54

The diffractogram of CuNCN was indexed with orthorhombic symmetry with space group *Cmcm* (nº63) in agreement with the literature[3]. In the case of CuNCN, the unit cell contains 4 formula units of CuNCN. The Rietveld fitting proves that CuNCN was synthesized as a single phase as it can be shown in Figure 4.2a and the obtained structure is shown in Figure 4.2b. Cell parameters, volume, molecular weight and agreement factors of the Rietveld refinement are listed in Table 4.2.

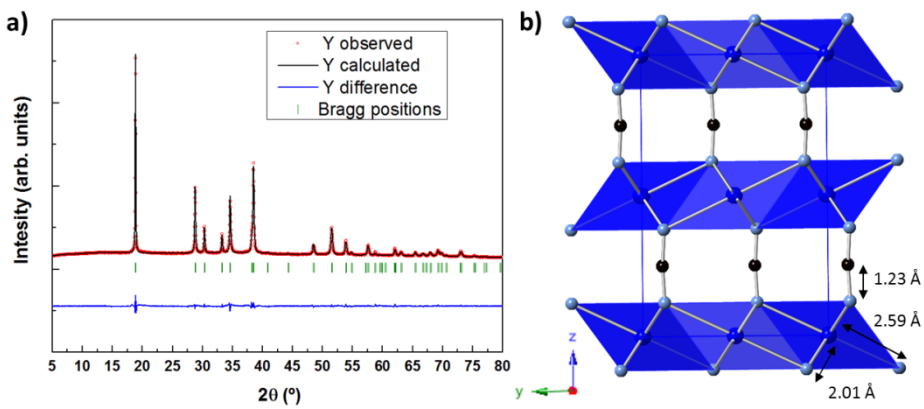

Figure 4.2. Observed (red dots), calculated (solid black line), and difference (blue bottom curve) patterns for the Rietveld analysis from the powder X-ray diffraction data of CuNCN. Green short vertical lines below the profile indicate the peak positions of all the possible Bragg reflections (a). The obtained structure for CuNCN from the refinement where light blue spheres are the nitrogen atoms, the black spheres are carbon atoms, the dark blue spheres are copper atoms and dark grey spheres are lead atoms in the YZ plane (b).

Table 4.2. Cell parameters and agreement factors obtained from the Rietveld refinement of CuNCN**.**

Cell parameters		**Agreement factors from Rietveld**	
a (Å)	2.991(1)	R_p (%)	11.9
b (Å)	6.207(1)	R_{wp}(%)	8.9
c (Å)	9.424(2)	R_{Bragg} (%)	3.31
Volume (Å^3)	174.942(6)	χ^2	7.01
Volume (Å^3)/Z	43.735	Molar mass (g/mol)	103.55

In the structure obtained from Rietveld refinement of CuNCN (see Figure 4.2b), Cu^{2+} were coordinated forming axially elongated octahedrons, with two different Cu-N distances. While the Cu-N distances of the equatorial plane of the octahedral were equal, the other two Cu-N distances were longer resulting in an elongation of the octahedral due to the presence of Jahn-Teller effect.

Jahn-Teller effect and transition-metal coordination discussion

Zn^{2+} has $3d^{10}$ electronic configuration so it has all the electrons of *3d* orbitals. Therefore, Zn^{2+} compounds, such as ZnNCN, are diamagnetic and usually colourless. There are, however, some exceptions of coulored Zn^{2+} compounds where the materials present charge transfer processes[4] such as zinc selenide and zinc telluride. In ZnNCN, zinc is coordined by four nitrogen atoms where two of them belong to the same carbodiimide chain and the other two to different NCN chains. This tetrahedron is not regular. It presents two different Zn-N distances: two nitrogen atoms are bonded to the zinc with a length of 1.98 Å and two other at a distance of 2.04 Å. The angle of the NCN group is 176.3 ° and the distances of N(1)-C and C-N(2) are also equal to 1.23 Å according to the carbodiimide configuration.

On the other hand, copper ions in CuNCN have $3d^9$ electronic configuration having one unpaired electron in the orbital e_g. In CuNCN, copper ions are octahedrally coordinated by 6 different Nitrogen atoms. NCN^{2-} is a π-donor ligand which makes the octahedral crystal field of copper smaller compared to other anions such as nitrate. Therefore, the electronic transition was less energetic causing the black colour than copper nitrate for example that exhibited blue colour. The octahedrons were elongated axially because of the presence of the Jahn-Teller distortion. This effect was due to the non-equal occupancy of energetic levels and the effect is stronger in compounds with an even number of electrons in the e_g orbitals, such as complexes of metals of high spin d^4, low spin d^7 and d^9 configurations. In fact, copper octahedra of CuNCN (Figure 4.2b) had in the equatorial plane four carbodiimide chains with an interatomic distances copper-nitrogen of 2.01 Å and two carbodiimide chains in the axial direction with Cu-N distances of 2.59 Å much longer than the equatorial. The obtained C-N distances were 1.23 Å, equal for N(1)-C and C-N(2), in agreement with a normal length for double bond. This value suggests that the coordination of NCN group is carbodiimide like, and not cyanamide like. The carbodiimide group is almost linear with an NCN angle of 173.7 °.

Both, Cu^{2+} and Zn^{2+}, are hard cations according to the Pearson´s HSAB principle[5], so they are only synthesized as carbodiimides and not as cyanamide.

4.1.1.2 Scanning Electron Microscopy

The microstructural morphology of copper and zinc carbodiimide was carried out by Scanning Electron Microscopy.

In the case of ZnNCN, optical aberrations were observed due to its low electric conductivity and sample had to be sputtered with gold in order to avoid overcharging. A homogenous distribution of particles assembled into bigger agglomerates was observed (Figure 4.3a) at low magnifications. Focusing in the agglomerates (Figure 4.3b), cauliflower like particles were shown. Increasing the magnification of the image was observed that these cauliflower like agglomerates were about 20 µm of size consisting of 4 µm faceted crystals.

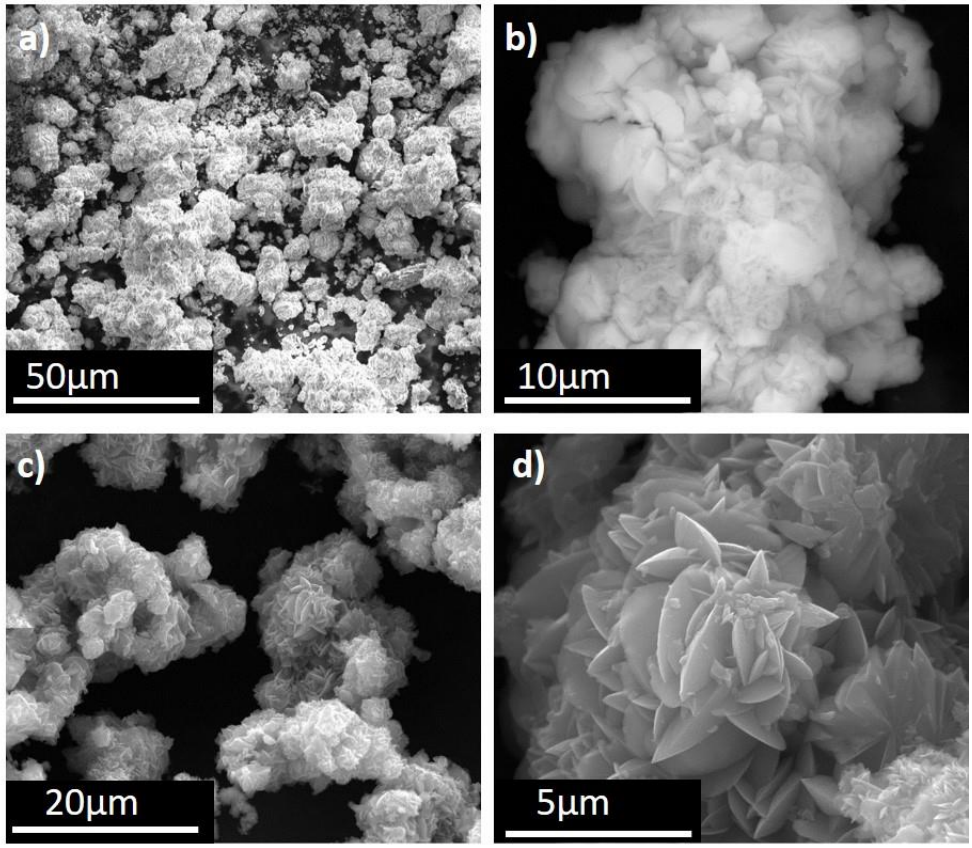

Figure 4.3. SEM images of the synthesized ZnNCN (a and b) and CuNCN (c and d).

In CuNCN sample, Figure 4.3c shows that the particles were homogenously distributed and forms some agglomerates. In Figure 4.3d can be seen the platelet shape of the particles were with ellipsoid form. The agglomerations were formed with desert rose like shape where the size of these ellipsoid platelets were around 3-4 µm of diameter.

The synthesized materials showed big differences in morphology although the similar synthesis methods. Different electrical conductivities were found for both compounds due to the need of the gold addition in ZnNCN in order to avoid the optical aberrations from sample charging.

4.1.1.3 Infrared spectroscopy

Infrared spectroscopy is the most powerful technique to distinguish carbodiimide and cyanamide functional groups of the synthesized compounds and it allows characterizing and comparing the observed bands in these compounds. ZnNCN and CuNCN were measured in order to look at the asymmetric stretching and deformation bands which were the IR active bands. These bands appeared around 2000 cm^{-1} and in the range 600-700 cm^{-1} respectively. In Figure 4.4, the most characteristic vibration modes in IR of cyanamide are shown. In cyanamide two groups were studied: NH_2 and the cyanamide ($N{=}C{-}N^{2-}$). Figure 4.4a, Figure 4.4b and Figure 4.4c show the asymmetrical stretching, symmetrical stretching and deformation respectively of the NH_2. Figure 4.4d, Figure 4.4e and Figure 4.4f describe the asymmetrical stretching, symmetrical stretching and deformation of the cyanamide group. According to the zone at which their bands appear, modes of NH_2 and carbodiimide group were above ordered from the least to the most energetic.

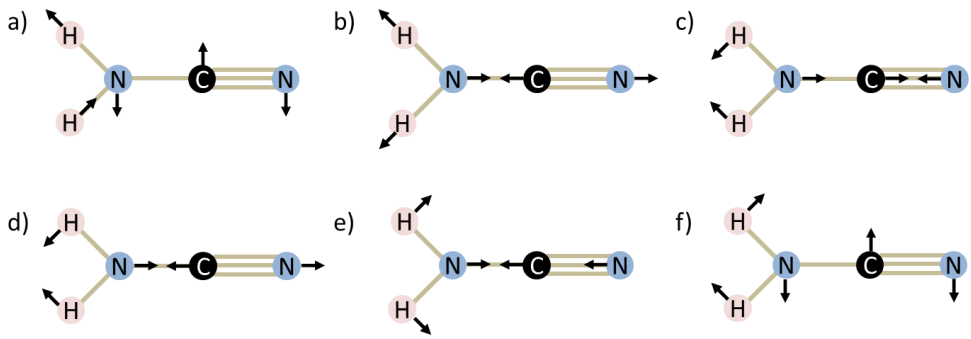

Figure 4.4. The IR active vibrational modes of cyanamide: asymmetrical (a), symmetrical (b) and deformation (c) of NH_2 and asymmetrical (d), symmetrical (e) and deformation of NCN group.

The infrared measurements of CuNCN and ZnNCN were carried out at room temperature and their spectra can be seen in Figure 4.5 where the frequencies were pointed out. The spectrum of cyanamide was also included for comparison because it was the precursor in the synthesis of both compounds. This experiment allowed understanding the differences in configuration of NCN bond between carbodiimide and cyanamide.

The most representative infrared bands that appeared in the spectra are summarized in Table 4.3. The spectra showed the most typical IR bands of carbodiimides in copper and zinc carbodiimides: the asymmetrical stretching (υ_{asy}) vibration at 2025 and 2044 cm^{-1} and the strong deformation (δ) at 594/687 and 672/695 cm^{-1} respectively. The obtained values of frequencies are in good agreement with the reported ones[6]. On the other hand, the IR spectra of cyanamide were quite different. The 6 described vibrational modes of cyanamide[7] were described in Figure 4.4 and were assigned in the spectrum Figure 4.5. The large shift in the asymmetrical stretching IR signal of H_2NCN was due to the cyanamide configuration[8] appearing at 2214 cm^{-1}. The symmetrical stretching of NCN appeared at 1151 cm^{-1}, being absent in CuNCN and ZnNCN. The deformation signal of NCN bond showed up at 600 cm^{-1}. Moreover, cyanamide presented the symmetrical and asymmetrical stretching of N-H bond at 3323 cm^{-1} and 3280 cm^{-1} respectively as well as the deformation at 1570 cm^{-1}.

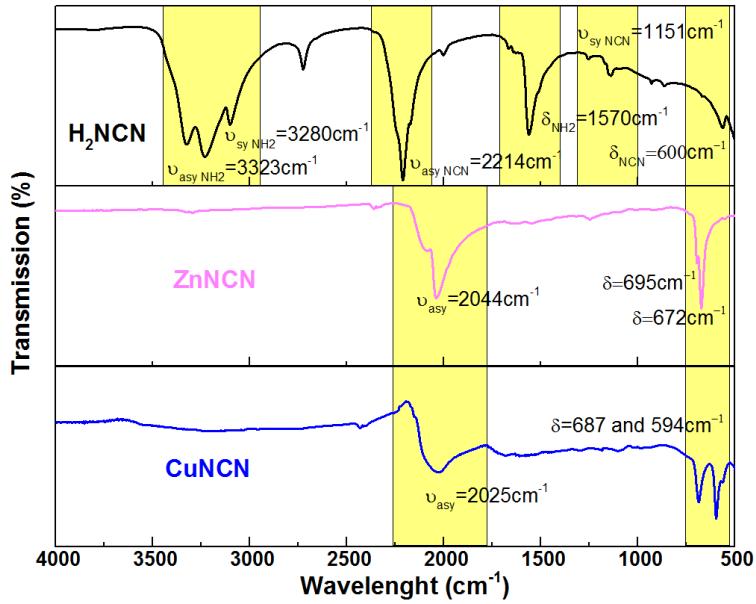

Figure 4.5. FTIR spectra in the range of 4000-500 cm^{-1} of H_2NCN (black), ZnNCN (pink) and CuNCN (blue) are represented respectively from top to bottom. Copper and zinc carbodiimides and cyanamide´s bands are pointed out with their values in cm^{-1} and yellow background.

Table 4.3. Cyanamide, zinc carbodiimide and copper carbodiimide most characteristics bands obtained from Infrared spectra.

Material	Group	$\upsilon_{asymmetrical}$ (cm^{-1})	$\upsilon_{symmetrical}$ (cm^{-1})	δ(cm^{-1})
H_2NCN	N-CΞN	2214	1151	600
	NH_2	3323	3280	1570
ZnNCN	N=C=N	2044	-	672/695
CuNCN	N=C=N	2025	-	594/687

Following Pearson´s HSAB theory, protons were hard acids so CuNCN and ZnNCN should have carbodiimide group ($^{-}$N=C=N^{-}). However, cyanamide adopted (NΞC-N^{2-}) form due to steric hindrance (small size of protons helps to be both atoms in the same side). In addition, this configuration made easier the hydrogen bonds formation.

4.1.1.4 Thermal stability

The thermal stability is usually determined by TGA/DSC experiments that make easier the analysis due to the coupled mass spectrometer. This detector allows identifying the loss of mass corresponding of a formation of gas species. However, regarding the literature for ZnNCN[2] the toxic dicyanogen[9] gas was formed by heating in air atmosphere. As the Thermogravimetric Analyzer did not have installed a safe system to evacuate the gas, the thermal stability of copper and zinc carbodiimide was measured by in-situ X-Ray Diffraction while heating. The temperature chamber was coupled to the diffractometer and a safe escape for the gas was set. Patterns were recorded with the samples at different temperatures in order to see at which temperature zinc and copper carbodiimides decomposed. The evolution of the diffractograms allowed us to know which species were forming during the increment of the temperature. Both materials were heated in the presence of air (oxidant) and nitrogen (inert) atmosphere.

XRD patterns of zinc carbodiimide were recorded from 30 to 800 ^{o}C every 100 ^{o}C with a 0.166 ^{o}C s^{-1} heating rate. Figure 4.6 shows that ZnNCN was stable in air until 400 ^{o}C. Above that temperature zinc carbodiimide started reacting observing a mixture of phases (ZnNCN and ZnO) at 400 ^{o}C. At 500 ^{o}C zinc oxide is the main phase with a small remaining of ZnNCN. At 600 ^{o}C zinc carbodiimide was completely transformed into zinc oxide.

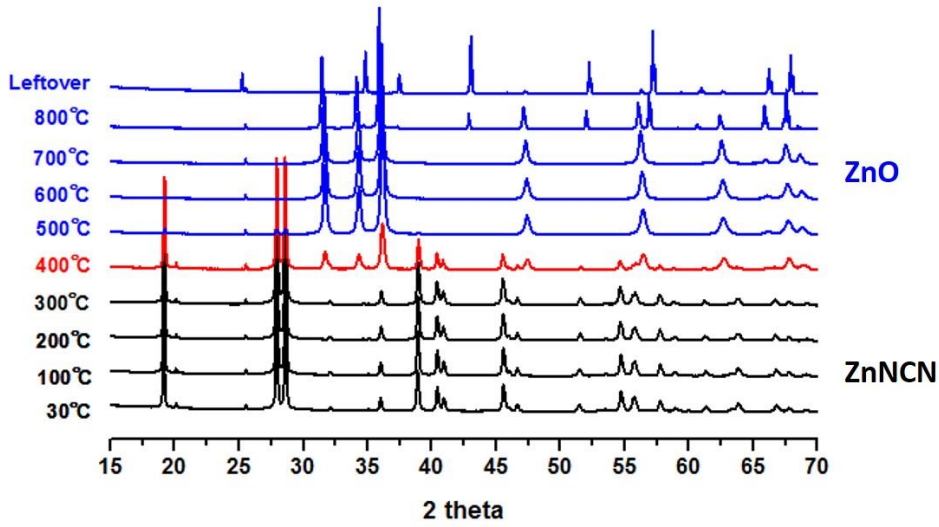

Figure 4.6. Diffractograms of ZnNCN in in the range 15-70 ^{o} from 30 ^{o}C (bottom) to 800 ^{o}C and leftover (top).

A pattern matching of the leftover was carried out in order to corroborate the formation of ZnO (see Figure 4.7). The peaks of zinc oxide became narrower due to the crystallization of ZnO upon the increment of the temperature. The formation of this phase could be attributed to the decomposition of carbodiimide group into dicyanogen gas and nitrogen gas (equation 4.1). Also there are three peaks corresponding to the aluminium holder of temperature chamber.

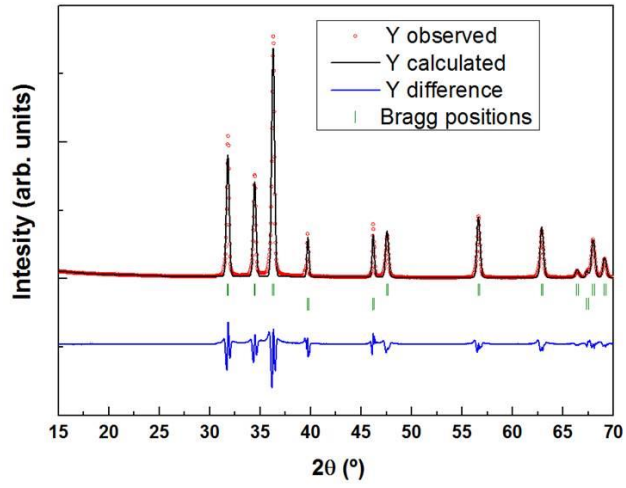

Figure 4.7. Observed (red dots), calculated (solid black line), and difference (blue bottom curve) patterns for the Pattern matching analysis from the powder X-ray diffraction data of the ZnO (leftover of ZnNCN in air atmosphere). Green short vertical lines below the profile indicate the peak positions of all the possible Bragg reflections.

$$2\ ZnNCN + O_2\ (g) \longrightarrow 2\ ZnO + N\equiv C\text{-}C\equiv N\ (g) + N_2\ (g) \qquad (4.1)$$

Measuring in inert nitrogen atmosphere, zinc carbodiimide was measured using temperature chamber (HTK1200 oven chamber) of Bruker D8 Discover diffractometer. XRD patterns were collected in 2θ steps of 0.019 º in the 15 º ≤2θ ≤ 70 º range, counting for 115.2 s per step (total time 30min.). Data sets were recorded from 30 to 800 ºC each 100 ºC with a 0.056 ºC s-1 heating rate. This material did not decompose up to 800 ºC in nitrogen atmosphere as it can be seen in Figure 4.8. This material was very stable in inert temperatures as *K.Morita et al.* reported[2]. They observed in TGA coupled with in situ mass spectrometry that above 800 ºC, ZnNCN decomposes yielding dicyanogen which signal is shown as m/z= 52, nitrogen (m/z=28) and metallic zinc at 900-1000 ºC.

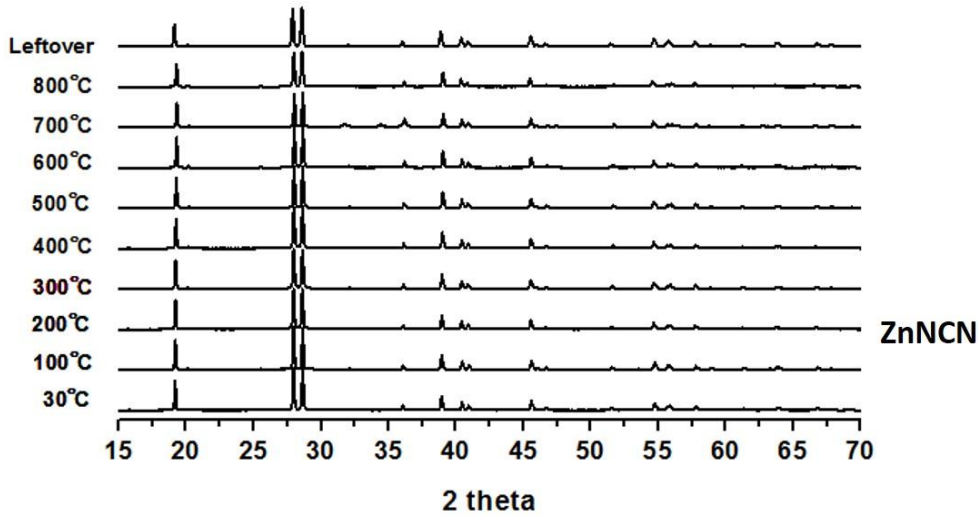

Figure 4.8. Diffractograms of ZnNCN in nitrogen atmosphere in the range 15-70 º from 30 ºC (bottom) to 800 ºC and leftover (top).

CuNCN was measured in the same conditions than ZnNCN in air atmosphere. Figure 4.9 shows that CuNCN material in air atmosphere was stable until 200 ºC. At that temperature, copper carbodiimide decomposed and transformed into copper oxide as the diffractograms of Figure 4.9 show. Again, the diffractogram of leftover was characterized as copper oxide by pattern matching with the Fullprof program (see Figure 4.10).

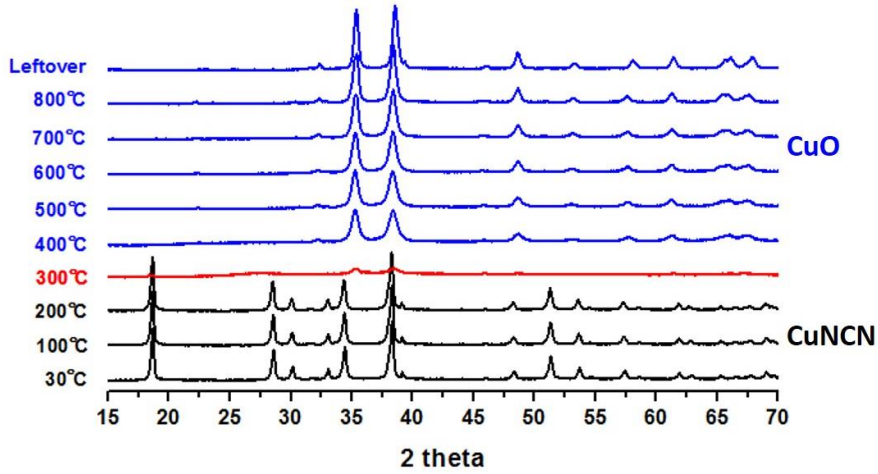

Figure 4.9. XRD patterns of CuNCN collected at different temperatures (30-800^{o}C) in the presence of oxygen and the leftover generated after cooling from 800^{o}C in the range 15-70 ^{o} of 2 theta to room temperature.

The peaks of copper oxide became narrower upon the increase of temperature. It means that CuO crystals grew as the temperature increased. It was likely that the carbodiimide group could decompose in dicyanogen gas and nitrogen gas (equation 4.2) as *K.Morita et al.* observed for ZnNCN[2].

$$2\ CuNCN + O_2\ (g) \longrightarrow 2\ CuO + N{\equiv}C\text{-}C{\equiv}N\ (g) + N_2\ (g) \qquad (4.2)$$

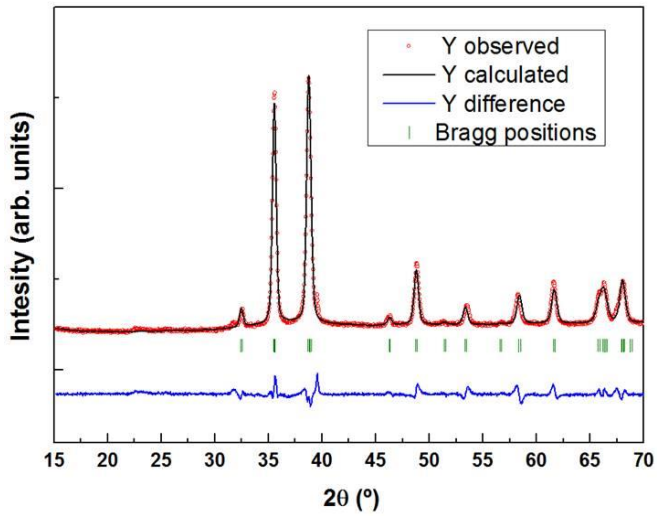

Figure 4.10. Observed (red dots), calculated (solid black line), and difference (blue bottom curve) patterns for the Pattern matching analysis from the powder X-ray diffraction data of the CuO (leftover of CuNCN measured in air atmosphere). Green short vertical lines below the profile indicate the peak positions of all the possible Bragg reflections.

CuNCN was also measured in nitrogen atmosphere following the same procedure than in ZnNCN. Figure 4.11 shows that CuNCN was stable until 200 ^{o}C. In the absence of oxygen, copper carbodiimide was decomposed at 200^{o}C and transformed into an intermediate phase, and finally into metallic copper at 400 ^{o}C, as it is shown in the diffractograms of Figure 4.11 and equation 4.3. A pattern matching was carried out in order to confirm the formation of metallic copper (see Figure 4.12). Appart from the peaks of metallic copper, there were some other small tiny peaks of copper nitride Cu_3N. Upon the increment of the temperature, the reflections of metallic copper were losing intensity and Cu_3N phase was increasing the intensity, so the copper nitride crystallized upon the increment of the temperature.

$$6\ CuNCN + 1/2\ N_2\ (g) \longrightarrow 3\ Cu + Cu_3N + 3\ (N\equiv C\text{-}C\equiv N)\ (g) + 3\ N_2\ (g) \quad (4.3)$$

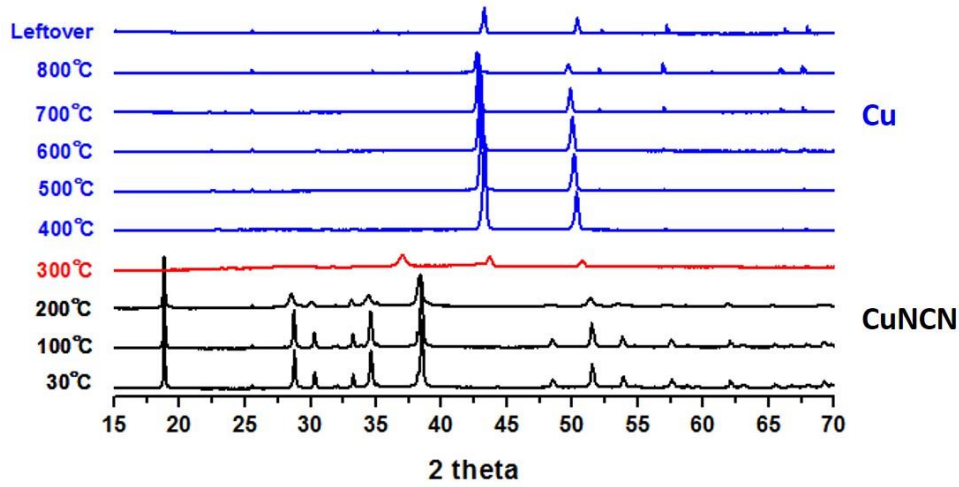

Figure 4.11. Diffractograms of CuNCN in nitrogen atmosphere in the range 15-70 ^{o} from 30 ^{o}C (bottom) to 800 ^{o}C and leftover (top).

The volume expansion of all compounds in the different atmospheres was analyzed at 200 ^{o}C. The election of that temperature was due to the fact that at 300 ^{o}C CuNCN was transformed into CuO and Cu in air and nitrogen atmosphere respectively. Therefore, the comparison of CuNCN and ZnNCN cannot be carried out above 200 ^{o}C. The percentages of the volume expansion experimentally observed are listed in Table 4.4.

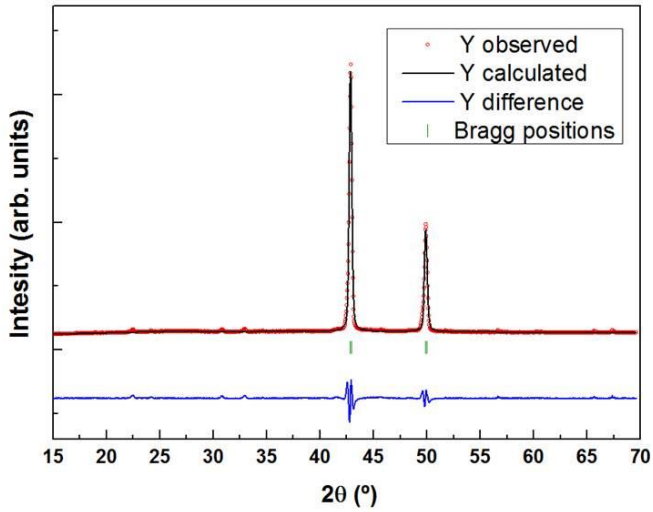

Figure 4.12. Observed (red dots), calculated (solid black line), and difference (blue bottom curve) patterns for the Pattern matching analysis from the powder X-ray diffraction data of the pattern at 700 ^{o}C of Cu (from CuNCN) in nitrogen atmosphere. Green short vertical lines below the profile indicate the peak positions of all the possible Bragg reflections.

Table 4.4. Volume expansion obtained by comparing the refined parameters by profile matching with the FullProf program of the PXRD data of CuNCN and ZnNCN at room temperature with those in air atmosphere and nitrogen atmosphere at 200^{o}C.

	Volume expansion	**Atmosphere**
CuNCN	0.25 %	Air
CuNCN	0.40 %	Nitrogen
ZnNCN	0.23 %	Air
ZnNCN	0.34 %	Nitrogen

Although very few data points are compared, it can be seen that CuNCN expanded a little bit more than ZnNCN, the expansion being larger under nitrogen than in air atmosphere.

4.1.2 Electrochemical characterization

Electrodes of zinc and copper carbodiimide were electrochemically tested in coin-cell type cells *vs.* Sodium and lithium Based on the electronic configuration of zinc and copper carbodiimide it is possible that a direct reduction from M^{2+} into M^{0} occurs and thus, two electrons take part in the reaction (with a capacity of 508 mAh/g and 517 mAh/g

respectively). However, since Cu^{+} is stable in a carbodiimide configuration, given the existence of $Cu_2(NCN)$ a two step reduction with topochemical intercalation could occur (with a capacity of 258 mAh/g). When zinc is reduced Zn^{2+} with $3d^{10}$ configuration can turn into Zn^{0} which both electrons going to the 4*s* orbitals. However, Cu^{2+} with $3d^{9}$ configuration turns into Cu^{0} with $3d^{10}$, $4s^{1}$ configuration.

4.1.2.1 ZnNCN

ZnNCN material did not seem an appropriate compound to have intercalation of Li and Na ions which could cause the reduction of Zn (II) to Zn (I). Compounds of Zn are usually of the cation Zn^{2+}, despite there are some exceptions of Zn^{1+} complexes[10].

For sodium ion batteries, in the capacity *vs* voltage plot (Figure 4.13a), a very long pseudo-plateau of about 500mAh/g was observed in the first discharge. This pseudo-plateau starts at 0.4 V *vs* Na^{+}/Na and finishes at 0.005 V *vs* Na^{+}/Na. Probably this plateau corresponded to the reduction of the Zn (II) to Zn (0). However, in the δQ/δV plot of the first discharge (b), a lot of peaks appeared in this region of voltage. This could indicate that there could be also some contribution of the insertion of sodium ions into the carbon, as well as electrolyte decomposition.

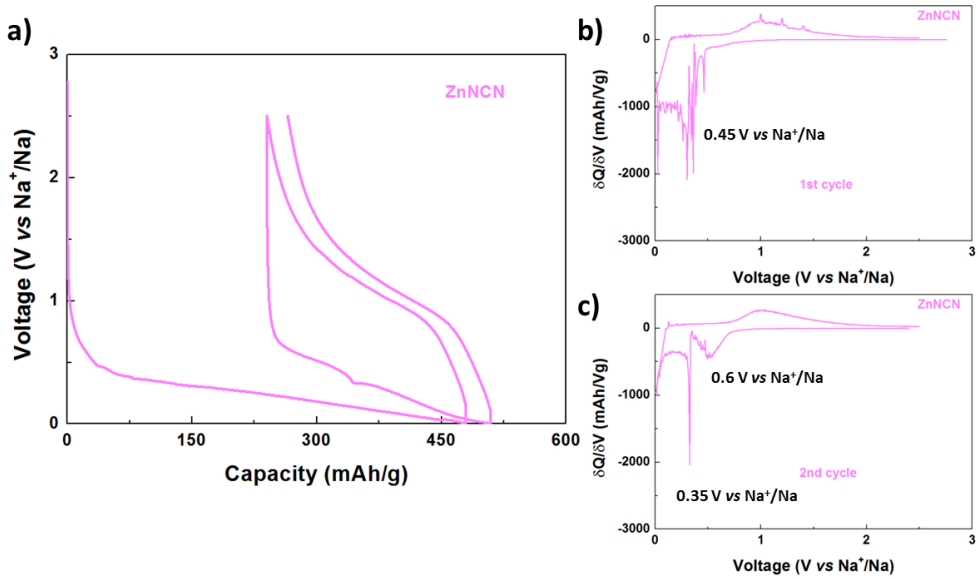

Figure 4.13. The first two galvanostatic cycles of ZnNCN in the plot Voltage *vs* Capacity in the voltage range 0.005-3.0 V *vs* Na^{+}/Na with 1 M NaFSI in Me-THF as electrolyte and using sodium metal as counter and reference electrode.

In the first oxidation, a capacity of approximately 250 mAh/g was achieved and a main process at 1.1 V *vs* Na^+/Na was observed in δQ/δV plot (b). In the first cycle some sharp peaks could be observed but they disappeared in the following cycles. The capacity obtained in the charge, 250mAh/g, did not correspond to theoretical capacity for two electron transfer for ZnNCN, 508mAh/g. As it can be seen in the first galvanostatic discharge, the plateau was cut off at 5 mV *vs* Na^+/Na. This could indicate an incomplete electrochemical process in the electrode. In addition, it was observed that ZnNCN needed addition of some high surface area carbon-Ketjen Black, because using just Super C65 as conducting additive was not enough to make ZnNCN electrochemically active. In the first cycle, there was an irreversible capacity of about 240 mAh/g which could be attributed to the irreversible process of the amorphization of the material in the first discharge. Indeed in the δQ/δV plot of the second cycle c) there were only three reversible processes. One small peak at 0.6 V *vs* Na^+/Na which can be assigned to the insertion Na^+ ions into the Super C65 carbon[11]. At 0.35 V *vs* Na^+/Na the most intensive peak that could correspond to the reduction of Zn(II) to Zn (0). And finally, the last peak at 0.05 V *vs* Na^+/Na could be assigned to the insertion of Na^+ ions into the Ketjen black carbon.

In order to identify the discharge product an ex-situ PXRD was performed. At 0.005 V *vs* Na^+/Na, the electrode was cleaned with the electrolyte solvent in order to remove the salts that could be deposited in the surface in the drying process. Once the electrode was clean and dried, it was placed in an air-sensitive sample holder. In the diffractogram (), no peak apart from those of copper foil was observed. This indicated that ZnNCN crystals reacted and nothing crystalline was formed during the discharge. In the study of the mechanism, the reduction of Zn (II) to Zn (I) forming a compound such as NaZnNCN was not considered[10]. That was the reason why the in-situ XRD was not performed for this material. There is no evidence of a new crystalline phase at the end of the discharge. This fact could be attributed to the amorphization of the material and the reduction of Zn (II) to Zn (0) at the end of the discharge.

The polarization in ZnNCN calculated from the δQ/δV plot (Figure 4.13b and Figure 4.13c) was 0.8 V. Polarization is a big drawback because it means that the Energy that needs to be supplied to the system during the charge is bigger than the energy recovered in the discharge. This polarization can be caused by mass transport limitations in the electrolyte and the solid phase of the electrodes, contact problems between the solid phases, or slow electrochemical reactions[12]. The contribution of each process depends on thermodynamic and kinetic properties of the material[13].

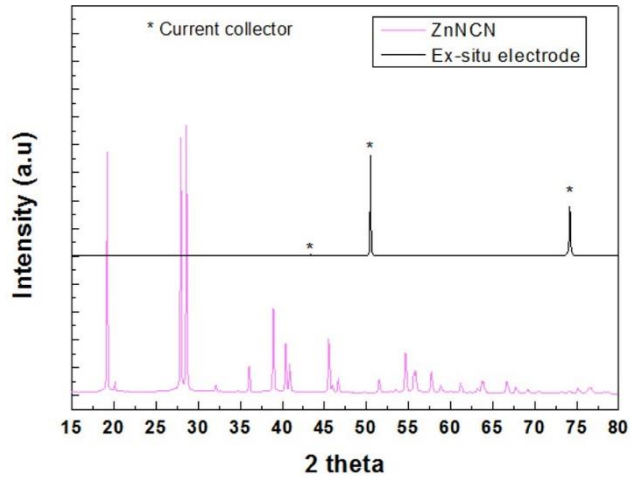

Figure 4.14. PXRD of ex-situ ZnNCN electrode in the range of 5-80 ^{o} of 2theta after the first discharge to 0.005 V *vs* Na^{+}/Na (black line) and the synthesized ZnNCN powder. In * are pointed out the copper foil reflections.

The long term cycling of ZnNCN for Na-ion batteries was measured in the voltage range of 0.005- 2.5 V *vs* Na^{+}/Na since no electrochemical activity was shown above 2.5 V *vs* Na^{+}/Na. The cyclability of ZnNCN was not very good. After 100 cycles, this material was able to keep just 40% of the capacity (100 mAh/g) from the second cycle (see Figure 4.15). The coulombic efficiency was higher than 99% from the fifth cycle.

In the study of ZnNCN material for lithium ion batteries (Figure 4.16a), there was a small plateau 150mAh/g at 0.9 Volts *vs* Li^{+}/Li and a large plateau of about 1000 mAh/g at 0.35 Volts *vs* Li^{+}/Li during the 1st discharge. These two plateaux were observed in δQ/δV plot (Figure 4.16b) with different intensity as corresponds to their different amounts of stored charge. The electrochemical process at 0.9 V *vs* Li^{+}/Li could be attributed to the adsorption of lithium ions in the carbon surface. The intensity of the corresponding peak was relatively small as can be seen in δQ/δV plot (Figure 4.16b). On the other hand, the peak corresponding to the lower voltage plateau was clearly shown in the Figure 4.16b. This plateau was assigned to the conversion reaction during the reduction of ZnNCN to metallic zinc and intercalation of the lithium ions into the graphene layers of the conductive carbon used as additive.

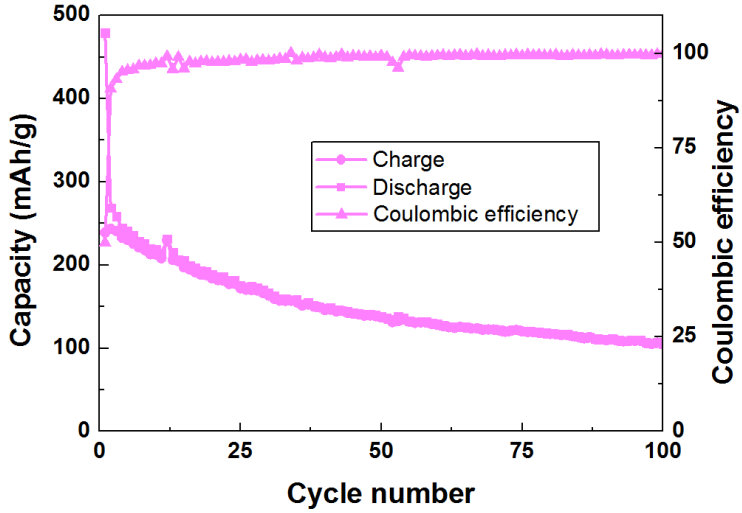

Figure 4.15. Cyclability of ZnNCN at C/10 rate for 100 cycles in the range of voltage of 0.005-2.5 Volts *vs* Na^+/Na using 1 M NaFSI in Me-THF and sodium as counter and reference electrode.

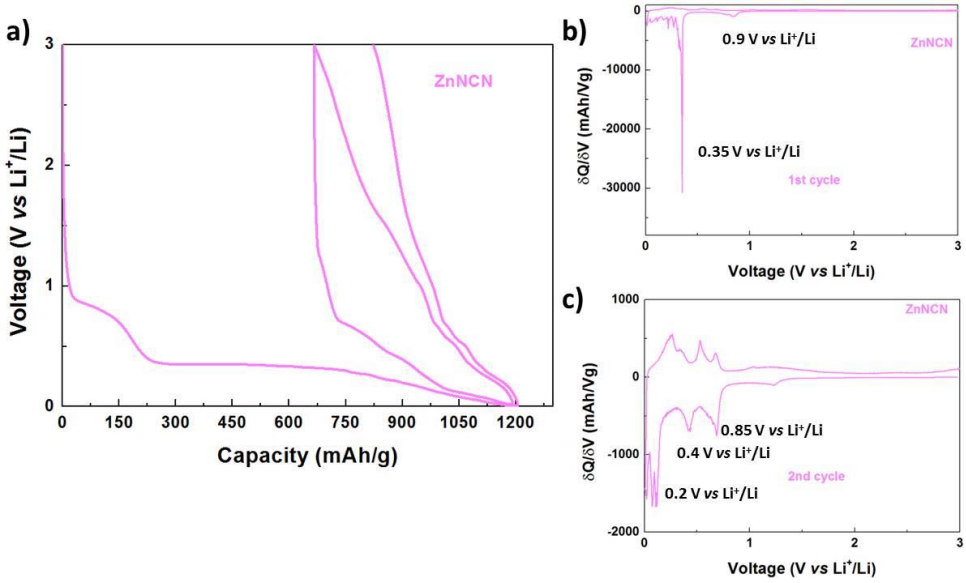

Figure 4.16. The first two cycles of CuNCN in the plot Voltage *vs* Capacity for Li-ion batteries (a) and first (b) and second (c) differencial capacity *vs* voltage plot (δQ/δV).

During the charge process, a capacity of 550 mAh/g was achieved which was almost the theoretical value (508 mAh/g) for the two electron conversion reaction. However, the electrochemical activity of the carbon was considered to be the reason for the extra capacity obtained. The high irreversible capacity of the first cycle was attributed to the

amorphization of the material which is an irreversible reaction in conversion systems and the irreversibility of the reaction of the lithium ions with carbon.

In order to check the contribution of the mixture of Ketjen black and Super C65, batteries using this material as working electrode were assembled and tested *vs* Li and *vs* Na. In Figure 4.17, it can be seen that the carbon mixture delivered high capacity (1600 and 1400 mAh/g respectively) in the first discharge, with a plateau at 0.9 Volts *vs* Li^+/Li. However, during the charge, the majority of the electrochemical activity was irreversible. This would explain the irreversible capacity observed. Taking that into account and that the percentage of carbon deployed with our materials was 20%, the influence in the electrochemical measurements of carbodiimides was not as big as in Figure 4.17 shows.

The capacity of ZnNCN material for lithium ion batteries faded almost 50% in the first 20 cycles. From the 20th cycle, the material was able to keep close to 200 mAh/g until 100th cycle as it can be seen in Figure 4.18. This capacity could be attributed mostly to the activity of carbon. This would mean that from the initial charge capacity (550 mAh/g), 200mAh/g were attributed to the mixture of carbons and 350 mAh/g to ZnNCN. The inactivity or electrical disconnections during the electrochemical process of some particles of ZnNCN could indicate the need amount of carbon was needed due to the bad electronic conductivity of ZnNCN material. Moreover, the coulombic efficiency was quite bad in the first cycle because the irreversibility of the redox reaction. Since 3rd cycle the coulombic efficiency was higher than 99%.

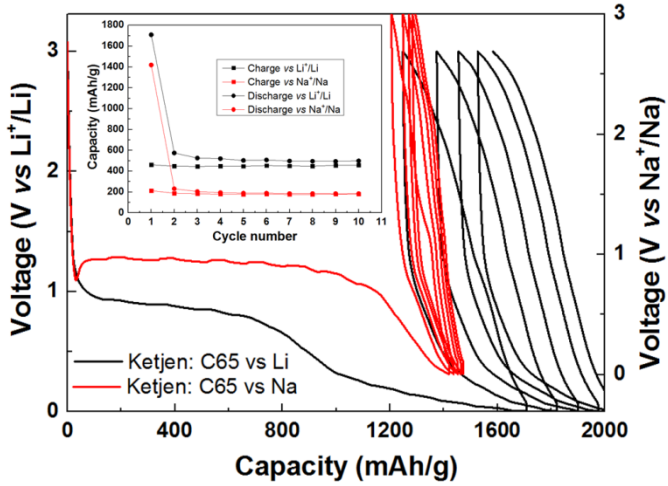

Figure 4.17. Voltage vs Capacity profile of the first five Galvanostatic cycles in the range 0.005–3.0 V *vs* Na^+/Na (red line and right scale) and *vs* Li^+/Li (black line and left scale) of a mixture of Ketjen black:C65 (50:50). The inset shows the capacity *vs* cycle number of the first ten cycles.

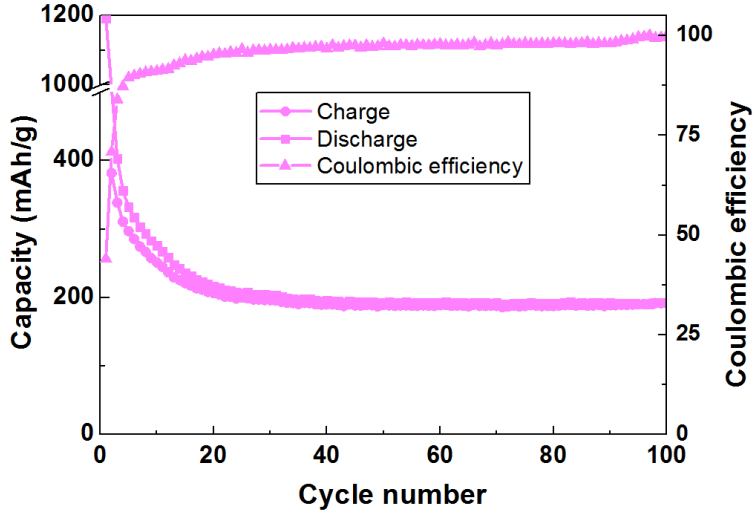

Figure 4.18. Cyclability of ZnNCN at C/10 rate for 100 cycles in the range of voltage of 0.005-3.0 Volts *vs* Li^+/Li using 1 M $LiPF_6$ in EC:DMC and lithium as counter and reference electrode.

In general ZnNCN show a reversible capacity below 1 A^+/f.u. both for Li and for Na According the bad cyclability and the low capacity values obtained in SIBs and LIBs, the volume expansion that this material could suffer in the electrochemical processes was calculated (see equation 4.4)[16,17]. Very small values were obtained for these types of systems (40.79%) compared to those observed in oxides with good cyclability such as CoO for LIBs. So this property seems not to contribute in the cyclability. Therefore, the low capacity obtained for ZnNCN was attributed to the bad electrical conductivity that could cause some disconnections making that not the whole material was active. However, the irreversibility could be attributed to the kinetics problems when ZnNCN was formed from the metallic zinc in Na_2NCN matrix.

$$\text{Volume expansion } (\%) = 100 \cdot ([V(Na_2NCN) + V(Mn)]/V(MnNCN)) - 100 \quad (4.4)$$

Electrochemical performance of ZnNCN indicated that ZnNCN was not a suitable candidate as anode because the large capacity fade observed in both sodium and lithium ion batteries.

4.1.2.2 CuNCN

4.1.2.2.1 Na-ion batteries

4.1.2.2.1.1 Galvanostatic cycling

The crystal structure of CuNCN seems to have layers separated enough (1.24 Å) for the topochemical intercalation of Li and Na ions which could cause the reduction of Cu (II) to Cu (I). The galvanostatic cycling for sodium ion batteries (see capacity *vs* voltage plot in Figure 4.19a) shows a small slope at 1.8 V *vs* Na^+/Na that could correspond to a solid solution process (insertion of about 0.10 Na^+ ions) during the first discharge. There was also a small plateau at 0.8 Volts *vs* Na^+/Na which could be attributed to the co-intercalation[18] of sodium ions solvated by one or several molecules of a high donor number solvent such as Me-THF (D.N.=18)[19] in the interlayers of the graphite and the carbon black used as conducting additive.

Finally a very large plateau of about 450 mAh/g, centered at 0.6 V *vs* Na^+/Na appeared where the reduction of copper (II) seemed to occur. The capacity obtained from the plateau indicated a process consistent with two electrons per CuNCN formula unit (517 mAh/g). Taking this into account, the redox reaction that was considered to take place was the reduction of Cu^{2+} to Cu^0. As the formation of copper-sodium alloys was not known a conversion or displacement reaction mechanism was suggested. However, on the first oxidation, around 300 mAh/g were achieved. As the theoretical capacity of Cu_2NCN is 258 mAh/g, it was considered that only one electron would be taking part in the oxidation reaction. The extra capacity obtained could be attributed to the electrochemical activity of the carbon. In following cycles, similar capacities were delivered (Figure 4.20). So, from the first discharge, it was considered that the reaction that could occur was the oxidation of metallic copper to Cu (I) compound, such as Cu_2NCN. Conversely, the reduction of Cu (I) complex into metallic copper in the discharge processes was suggested. This mechanism based on a one electron transfer reaction in copper compounds was deeply studied in both sodium[20,21] and lithium ion batteries[22] for copper oxide (CuO).

The polarization of CuNCN material can be seen in the $\delta Q/\delta V$ plots of the two first cycles (Figure 4.19b and Figure 4.19c). There can be also observed the difference between the galvanostatic discharge (copper reduction) process and the galvanostatic charge (copper oxidation) process. In the first cycle, the reduction peaks were at 1.8 V *vs* Na^+/Na according to the first slope process, a small peak at 0.8 V *vs* Na^+/Na for the probable sodium co-intercalation into carbon and a plateau at 0.6 V *vs* Na^+/Na attributed to the conversion reaction. During the first and main oxidation process at 1.2 V *vs* Na^+/Na (see

Figure 4.19b). However, in the second cycle, the polarization of this reaction was reduced because the reduction process was located at higher voltage (0.8 V *vs* Na^+/Na) as Figure 4.19c shows. In the comparison, in second cycle the polarization was reduced. Despite the drawback of polarization, materials that react trough conversion reactions, lead to transfer several electrons and they are good candidates for next-generation Electrochemical Energy Storage systems[23,24].

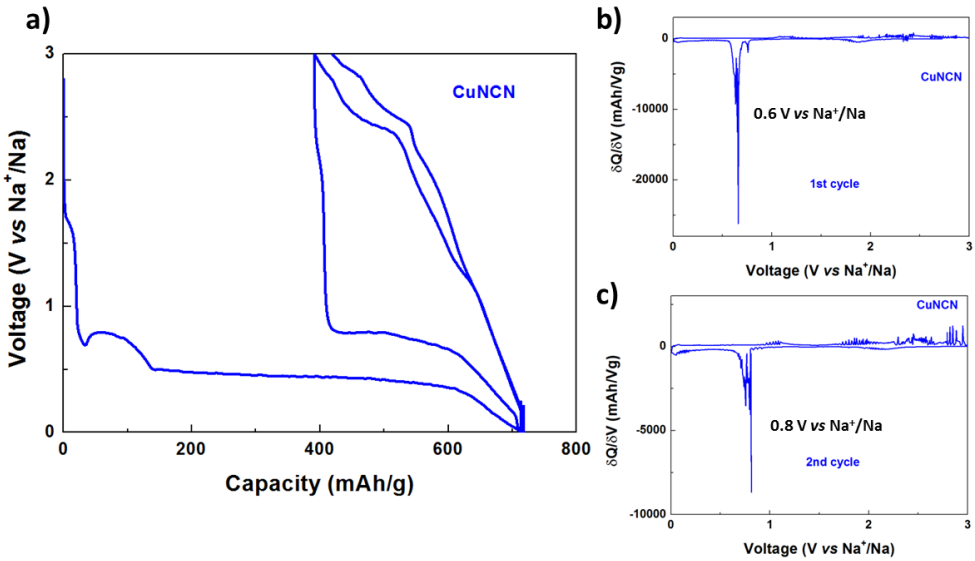

Figure 4.19. The first two galvanostatic cycles of CuNCN in the Voltage *vs* Capacity plot for Na-ion batteries (a), first (b) and second (c) differential capacity with respect to the voltage using sodium as reference in the 0.005-3.0 Volts *vs* Na^+/Na.

The observed increment of voltage for the reduction reaction from first to the second cycle was described in many studies of conversion materials[25,26]. Two main aspects could be the responsible of this fact. The first one was related to the possible amorphization of the material since materials in amorphous state can provide different properties than crystalline samples[23,27]. The second one, was based on the different electrochemical reaction of the two first discharges. In first discharge the CuNCN would be reduced to metallic copper, while in the second discharge the reaction could be the reduction of Cu (I) into metallic copper, provided that the charge reaction had formed Cu2NCN. If different processes were involved in 1st and 2nd discharge could increase the voltage as it can be observed in the common reduction potential tables[28].

CuNCN material exhibited quite good capacity retention being able to keep more than 78% of the capacity after one hundred cycles 220 mAh/g (see Figure 4.20). The coulombic efficiency was higher than 99% after the first three cycles.

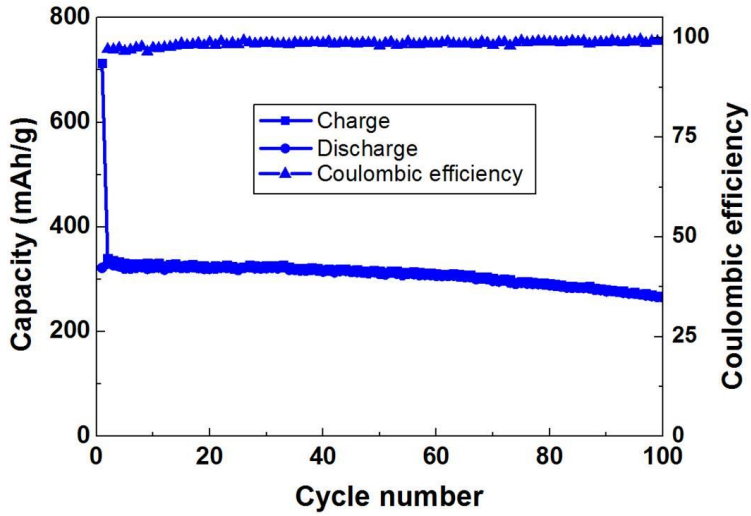

Figure 4.20. Cyclability of CuNCN at C/10 rate for 100 cycles using 1M NaFSI in Me-THF and sodium as counter and reference electrode in the 0.005-3.0 V *vs* Na^+/Na range. The coulombic efficiency is plotted as blue triangles.

4.1.2.2.1.2 Study of the mechanism of reaction

In order to demonstrate the suggested mechanism of conversion, *ex-situ* XRD of the electrode after the whole discharge was carried out. A coin cell with CuNCN as working material and metallic sodium as reference and counter electrode using 1M NaFSI in Me-THF as electrolyte was discharged to 0.005 V *vs* Na^+/Na. The coin cell was disassembled and the electrode was taken. The electrode was cleaned 3 times with Me-THF with the goal of removing all remaining possible salt deposited in the surface of the electrode. In order to avoid the air exposure, a sample holder was assembled in the glovebox and vacuum grease and kapton film were used to create an air-free atmosphere for the electrode. In Figure 4.21, it can be seen that just the copper foil reflections were observed.

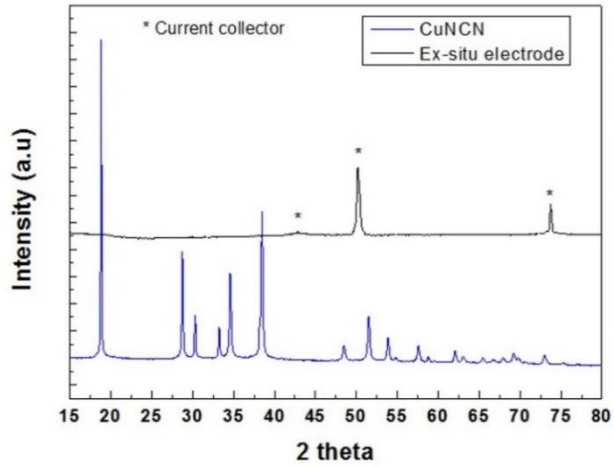

Figure 4.21. PXRD of ex-situ CuNCN electrode (black line) in the range of 5-80 º of 2 theta after the first discharge to 0.005 Volts *vs* Na^+/Na. Copper foil reflections are pointed out with * and synthesized copper carbodiimide was plotted in blue line**.**

As no crystalline phases were intermediate observed in the complete discharged electrode, an *in-situ* XRD experiment was performed to see whether any intermediate, such as NaCuNCN was observed. The *in-situ* cell was started to run at C/20 (21 mA/g), a bit slower than the tests that had been done for the electrochemical characterization in order to ensure to see all the changes that could occur in the material. Figure 4.22a shows the evolution of the diffractograms. Just reduction of the intensity of the reflections was shown and the apparition of another crystalline phase was not observed. The reduction of the peaks could be attributed to the amorphization of the material and the amorphization due to the conversion reaction. Moreover, at 44 º of 2 theta, a very broad peak appeared. This peak was observed at the end of the plateau of the discharge and increased its intensity during the CP process at 0.005 V *vs* Na^+/Na. That signal could be attributed to the (111) reflection of metallic copper confirming the conversion reaction (see equation 4.5). Nevertheless, the formation of Na_2NCN could not be confirmed by PXRD. In addition, after the charge, no reflections due to crystalline CuNCN nor Cu_2NCN did appear. It indicated that the oxidation of metallic copper to Cu (I) or Cu(II) complex occurred in within the amorphous form. Figure 4.22b, shows the top view of the in-situ XRD experiment. There it can be seen that the reflections decreased in intensity without any shift in 2 theta positions. The slope region of solid solution at 1.8 V *vs* Na^+/Na observed in Figure 4.19 was not negligible in the diffractograms of Figure 4.22a and Figure 4.22b indicating a small or inexistent process of insertion of sodium ions into CuNCN.

$$CuNCN + 2\,Na^{+} \longrightarrow Cu + Na_2NCN \quad (4.5)$$

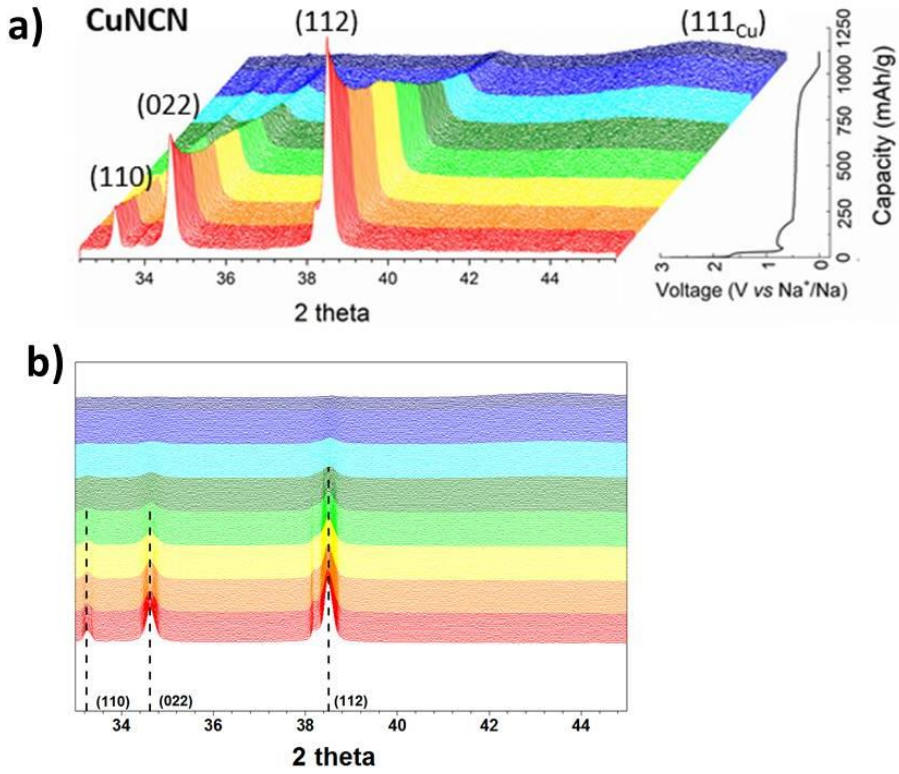

Figure 4.22. The evolution of the peaks of in-situ powder XRD data according to the first discharge of CuNCN down to 0.005 V *vs* Na^{+}/Na (a) and the top view of the in-situ XRD patterns highlighting the absence of shift (b).

Since the material losses its crystallinity after the firsts discharge, in order to analyse whether Cu^{2+} formed was upon charge, an EPR analysis was carried out in order in a CuNCN electrode after discharge and charge. The EPR of the charged electrode resulted in a very narrow signal for a g value of 2 that corresponded to free radical species which is commonly seen in carbons (see Figure 4.23a). Thus, this signal was attributed to the carbon used as conductive additive. A small wide signal was also observed at lower field which can be assigned to Cu (II) because the signal was centred at around 3200 Gauss. This signal was not well defined so it was decided to decrease the temperature in order to avoid the saturation effects and increasing antiferromagnetic interactions. The EPR signals increased in intensity and became narrower improving the resolution of the peaks. Since the temperature was set at 10 K the signal of the radical species was minimised and the signal corresponding to the Cu^{2+} was clearly observed. At room temperature, carbon

usually saturates the signal because they have longer relaxation times. This is the reason why its signal decreased upon lowering the temperature. The hyperfine structure (electronic spin S=1/2 –nuclear spin I=3/2) was relatively well resolved and 4 lines (2I+1) were obtained for each orientation of the applied magnetic field. In addition, the spectrum showed the common axial symmetry of the g tensor corresponding to a Cu^{2+} in a centre of the octahedra. The splitting generated by the hyperfine coupling also indicated that the Cu^{2+} ions were magnetically isolated which is different from the original compound CuNCN (Figure 4.23a), and probably these Cu^{2+} ions were mostly surrounded by diamagnetic Cu^{+} ions (Figure 4.23b). In the discharged electrode, the EPR spectrum did not show any signal of Cu^{2+}. This could be attributed to the complete reduction of all the Cu^{2+} nuclei. Therefore, the Cu^{2+} observed in the charged electrode (up to 3.0 Volts) was produced in the charge process and it was not a remaining amount of Cu^{2+} at the end of the discharge (Figure 4.23c).

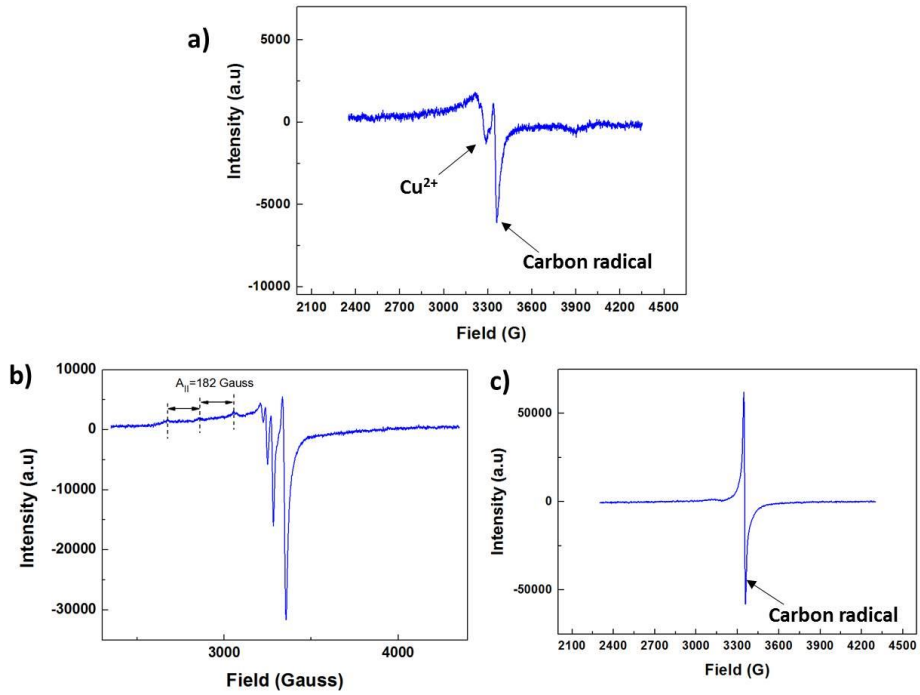

Figure 4.23. EPR spectrum of the pristine CuNCN electrode at room temperature (a), discharge up to 0.005 V *vs* Na^{+}/Na (b) and the charged up to 3.0 V *vs* Na^{+}/Na at 10 K (c).

The separation of these lines observed in the low field zone of the spectra (parallel region) was approximately 170 Gauss in agreement with the presence of 4 atoms of nitrogen linked to Cu^{2+} ions in the equatorial plane of the octahedral (Figure 4.23b). Anions with more electroattraction character such as fluorides (F^{-}) usually present lower values (120 Gauss).

4.1.2.2.1.3 Electrolyte decomposition

In this context, following the work reported by *F. Klein et al.*[24] on the mechanism of reaction of CuO for lithium and sodium ion batteries, monitoring the conversion reaction, SEI growth and dissolution on CuNCN electrodes have been attempted by means of *ex-situ* XPS measurements on cycled electrodes and SEM images of electrode cross-sections. Interestingly, these authors reported the dynamic evolution of the SEI in the Na systems, while a more static SEI was found for the Li ones. In addition, significant differences in the SEI composition of Na- (inorganic and layered) and Li-based (homogeneous but different ratio of inorganic/organic compounds) were observed.

Therefore, similar processes were expected for CuNCN electrodes in sodium ion batteries. This work has been conducted in collaboration with the group of Prof. Jürgen Janek in the Justus Liebig University in Giessen (Germany). Both XPS and SEM experiments were carried out by F.Klein and R. Pinedo. It must be noted, however, that in contrast to their previous work, in this one, no model CuO thin film electrodes were used and NaFSI in MeTHF was employed as electrolyte.

In the SEM images of the cross-section of the electrodes (Figure 4.24), no appreciable differences were observed between electrochemically discharged and charged samples. This feature could be caused by the different morphology and higher porosity of the CuNCN electrodes, which could favor the distribution of the SEI over the whole electrode and not only at the top surface.

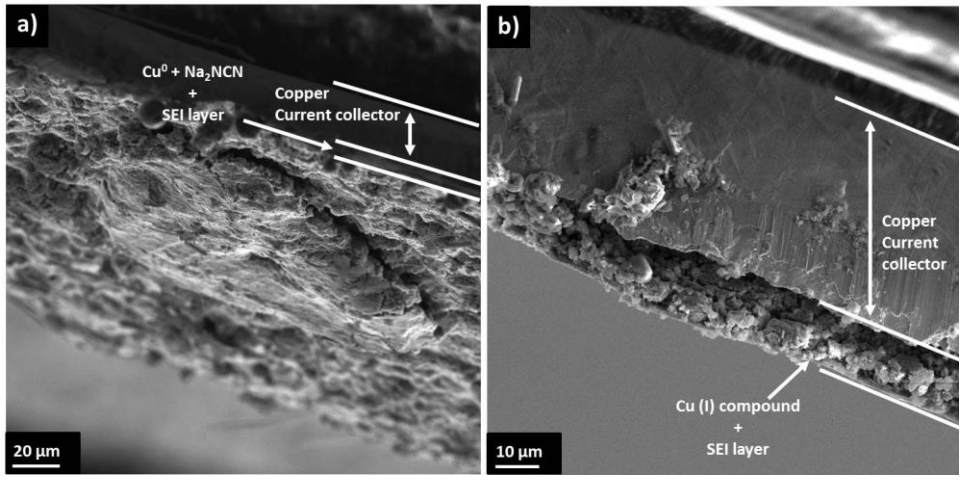

Figure 4.24. Cross-sectional SEM images of the CuNCN electrodes after discharge (a) and charge (b) in the first cycle.

In the XPS experiments, the stability of the CuNCN electrodes under Ar sputtering was firstly studied. Figure 4.25, reveals two important features: i) two different Cu species can be seen at the top surface and ii) Cu^{2+} species disappear after the Ar sputtering process. The latest can be easily observed in the Cu2p spectrum of the reference electrode before sputtering, where large satellite peaks (~ 9 eV higher than the 2p 3/2 signal) on the high binding energy side of the main photoelectron peaks are present. In contrast, these satellite signals are absent after sputtering, which implies the reduction of Cu^{2+} to lower oxidation states. Obviously this fact prevents us from monitoring the change of oxidation state along the electrochemical reaction by this technique.

The composition of the solid electrolyte interphase layer and its formation, which has not been specifically studied for this electrolyte (NaFSI in Me-THF) was studied by XPS. Firstly, *G. G. Eshetu et al.*[29] proposed a four electron reduction of LiFSI in lithium ion batteries, where the bisfluorosulfonyl imide group, in the presence of 4 electrons, is reduced in two steps, losing the fluoride groups. Therefore, the bisfluorosulfonyl imide group is reduced to bislithiumsulfonyl imide. Despite this drawback, LiFSI seems a good alternative to $LiPF_6$ due its higher conductivity and lower fluoride content. Recently, *F. Klein et al.*[24] studied the SEI growth for NaFSI in EC:DMC solvents using CuO as electrode material *vs* metallic sodium. There, only carbonates and NaF were observed. Taking into account the use of Me-THF as solvent[30], which is not known to decompose above 0 V *vs* Na^+/Na, it is possible that just NaF is present in the solid electrolyte interphase. Therefore, in this case the focus was on the F 1s and S 2p XPS signals. . XPS spectra of an electrode discharged down to 0.6 Volts *vs* Na^+/Na (Figure 4.26), shows that NaFSI salt is already decomposed, leading to the formation of NaF. The presence of some NaFSI, especially at the top surface can be explained by the partial stability of the salt after a certain thickness of SEI layer has been formed or by the incomplete removal of the salt after dissembling the cell. Upon cycling (in both discharged and charged states), the NaFSI signal completely disappears and only fluoride species are detected. A similar trend is noticeable from the S 2p signal (Figure 4.27a). Thus, at the top surface FSI- signals can be detected as the only sulphur species (Figure 4.27b). The sputtering process promotes the formation of a secondary species at 167 eV, as also reported by *K. Edstrom et al.*[31]. Moreover, and in contrast to LiFSI studies a third component emerges. The unequivocal identification of this component is quite challenging as several polysulfides species appear at similar binding energies (163-164 eV)[32] as Figure 4.27c shows. These species are also found after charge or several cycles.

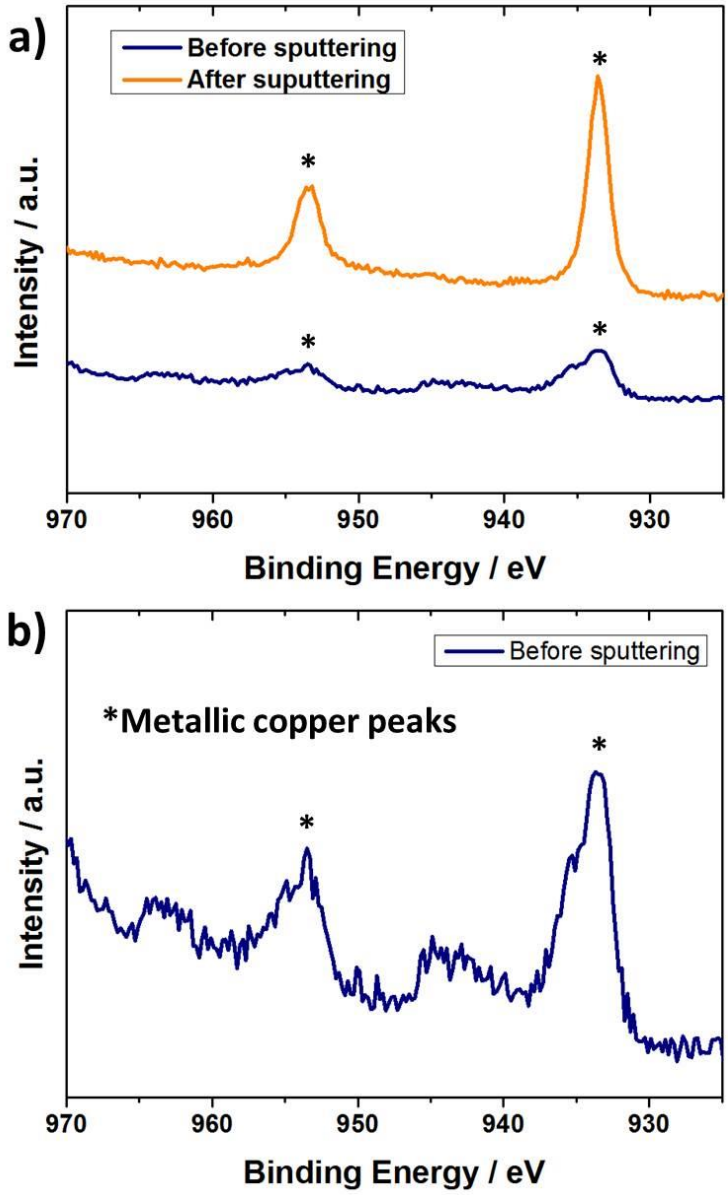

Figure 4.25. XPS experiment of the copper nuclei before (blue line) and after (orange line) the sputtering (a) and a different scale image of the before sputtering spectrum (b).

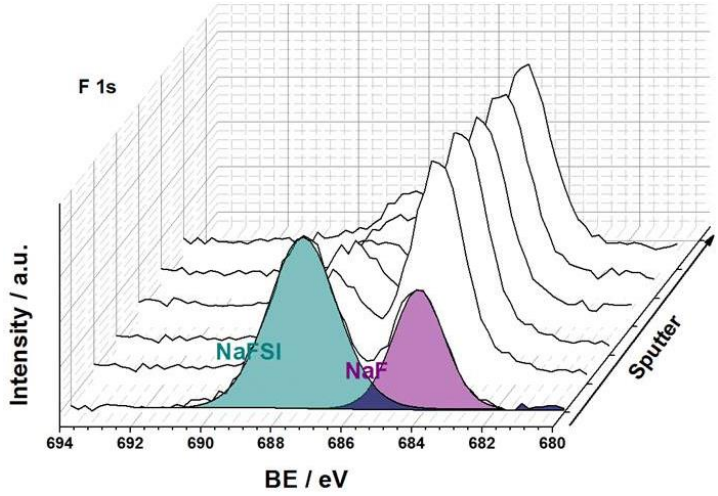

Figure 4.26. XPS measurements of CuNCN cycled electrode up to 0.6 Volts *vs* Na^+/Na for the Fluor nuclei and the sputtering to deeper layers of electrode.

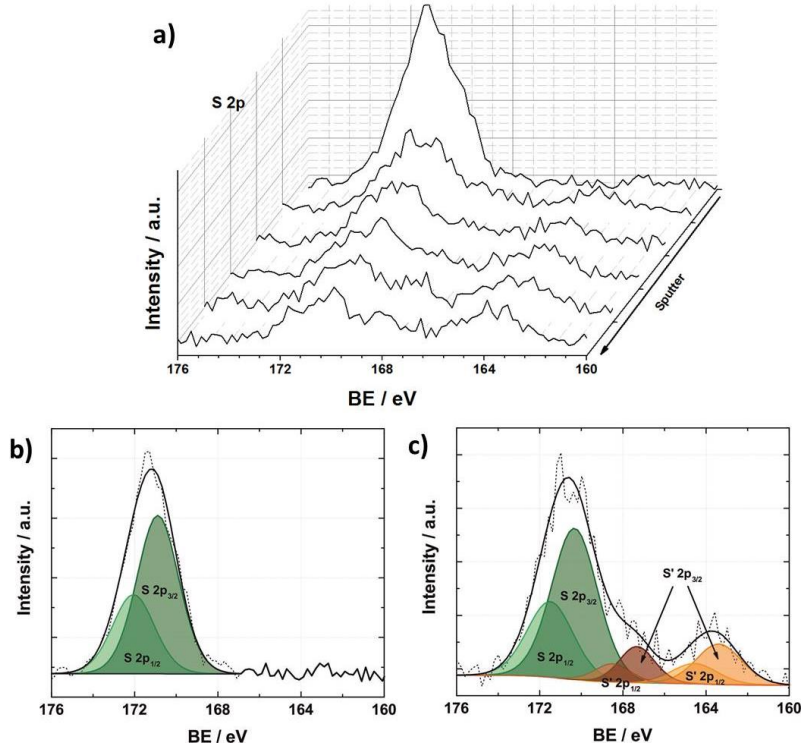

Figure 4.27. Evolution of the XPS measurements sputtered to different depths layers of a CuNCN cycled electrode down to 0.6 Volts *vs* Na^+/Na (a) and the deconvolution of the signals and fitting to the 2p orbital of sulphur for NaFSI spectrum in the surface (b) and deeper in the layer of the electrode (c).

Once it is known that the salt (NaFSI) is decomposed during the galvanostatic cycling, impedance measurements were carried out in the frequency range of 101 KHz to 5 mHz in order to evaluate the evolution of the conductivity of the cell when these compounds were formed. Firstly, it was shown in the left part of x-axis in (Figure 4.28a, Figure 4.28b and Figure 4.28c)that the resistance of the electrolyte was around 5 ohms. The analysis of the obtained semicircle was not deeply studied but it can be deduced that the resistance of the charge transfer and resistance due to the SEI layer could be both involved. The refinement of the impedance data was carried out by Boukamp software[33]. It was shown that the total resistance of both processes increased during the discharge process (from OCV to 0.005V) and it decreased during the charge (from 0.005V to 3 V vs Na+/Na) what could indicate the possible partial dissolution of the solid electrolyte interphase compounds (NaF or polysulfides), while the resistance from charge transfer could be similar at different stages (144 ohms) of the galvanostatic cycling. Moreover, it worth noting that below 20 Hz the solid state diffusion was observed and it is pointed out in Figure 4.28. The scheme of the sodium ion diffusion and corresponded with the circuit proposed is plotted in Figure 4.28d.

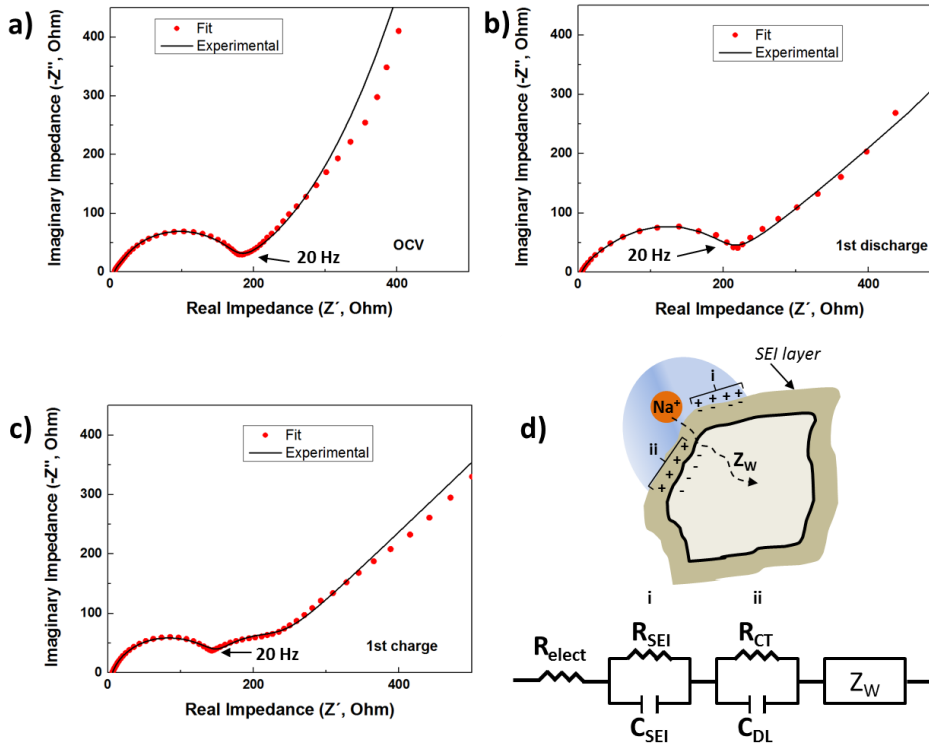

Figure 4.28. Nyquist plots of the CuNCN at different voltages: OCV (a), discharged up to 0.005 Volts *vs* Na^+/Na (b) and charged at 3.0 Volts *vs* Na^+/Na (c) with a scheme of the diffusion of Na ions (d).

4.1.2.2.1.4 Study of the irreversible capacity

Three causes can be envisaged for the observed low initial coulombic efficiencies: irreversible or non-electrochemical electrolyte decomposition, incomplete de-conversion due to the presence of inactive or electrically disconnected Na_2NCN/Cu regions, and incomplete de-conversion to the initial binary compound, but to other lower oxidation states such as Cu_2NCN. Arguments and reports for the three causes can be found when revisiting the literature on other conversion materials which denotes the lack of complete understanding about these processes. If the first two scenarios occur, the loss of capacity is irreversible; however, the rate capability (Figure 4.29) analyses have revealed that a certain fraction of the capacity can indeed be recovered after applying high rates (C) and decreasing again the current to C/10. Taking that into account, the third hypothesis, oxidation to Cu_2NCN, will be studied in detail following two different approaches. The first one requires the utilization of materials without intermediate oxidation states. In this context, NiO has been often denoted as a model electrode. However, even a metastable NiO_δ intermediate is formed upon reoxidation[34]. A second approach related to the kinetics of the reoxidation process was also evaluated. Thus, a constant potential (CP) step for 12 hours at 3 Volts *vs* Na^+/Na was introduced in the cycling procedure after the galvanostatic charge process (Figure 4.30a). This procedure has been previously deployed by the group of M. Winter to analyse the coulombic efficiency in $LiNi_{1/3}Co_{1/3}Mn_{1/3}O_2$ layered electrodes[35].

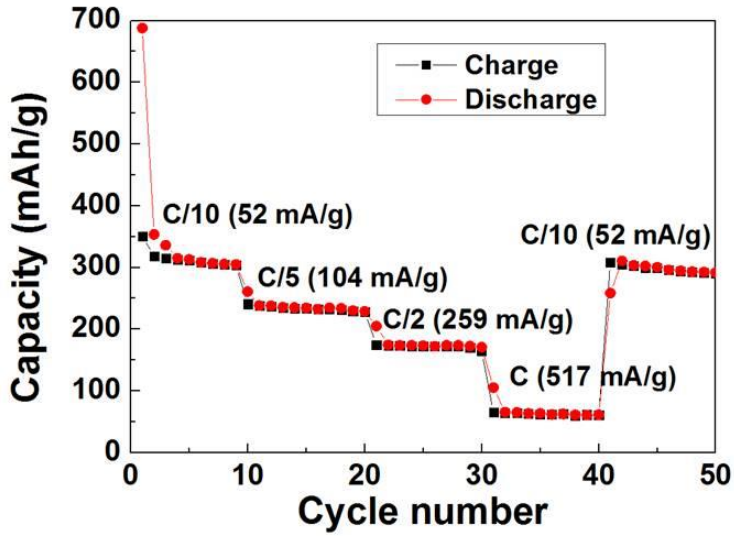

Figure 4.29. Rate capability of CuNCN cycled in the voltage range 0.005-3.0 Volts *vs* Na^+/Na for C/10, C/5, C/2 and C rates.

It must be once again noted that the first two mechanisms (electrolyte decomposition and electrically disconnection of active material) imply irreversible processes, and therefore, the capacity should not be recovered even under more favourable kinetic conditions. As shown in Figure 4.30a, potentiostatic experiment during charge allow extending the oxidation process, demonstrating that the underlying limiting factor for the Cu(0) → Cu^{2+} process is not completely irreversible and therefore more likely related to the incomplete conversion from Cu^{1+} → Cu^{2+}. 120 mAh/g are recovered during the constant potential step after the first charge, which corresponds to a 30 % of the charge capacity and a 17 % of the discharge capacity attained under conventional galvanostatic conditions. In order to further support the influence of the potentiostatic step on the re-oxidation of Cu, the CP step was also introduced during the subsequent cycles. After each CP on charge, the attained discharge capacity exceeds the one attained during the galvanostatic charge, demonstrating that the CP step has an effect on the conversion process. Moreover, the analysis of the current evolution during the CP step in the subsequent cycles reveals its progressive decrease with the cycle number (Figure 4.30b).

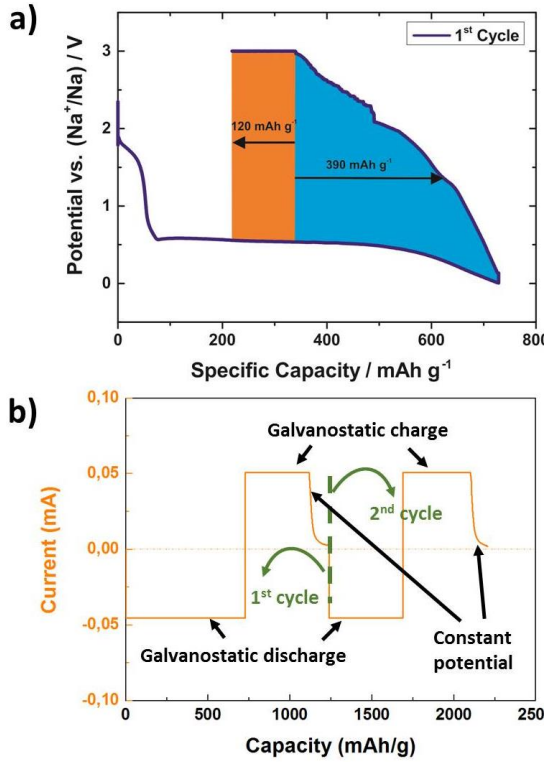

Figure 4.30. Galvanostatic discharge and charge and the following potentiostatic measurement at 3.0 Volts *vs* Na^+/Na (a) and the current evolution upon cycling using the constant potential after the galvanostatic cycle (b).

This progressive kinetic hindrance is consistent with the evolution of the SEI, and could explain the progressive intensity decay during the CP step until its stabilization in the 9th cycle. These measurements evidence the high influence of kinetics on the electrochemical performance of conversion systems and the inaccuracy of associating the low initial coulombic efficiency entirely to the irreversible processes. Thus, new systems with improved kinetics should be designed to partially overcome the low initial coulombic efficiency and the subsequent capacity loss from the second cycle on (Figure 4.31).

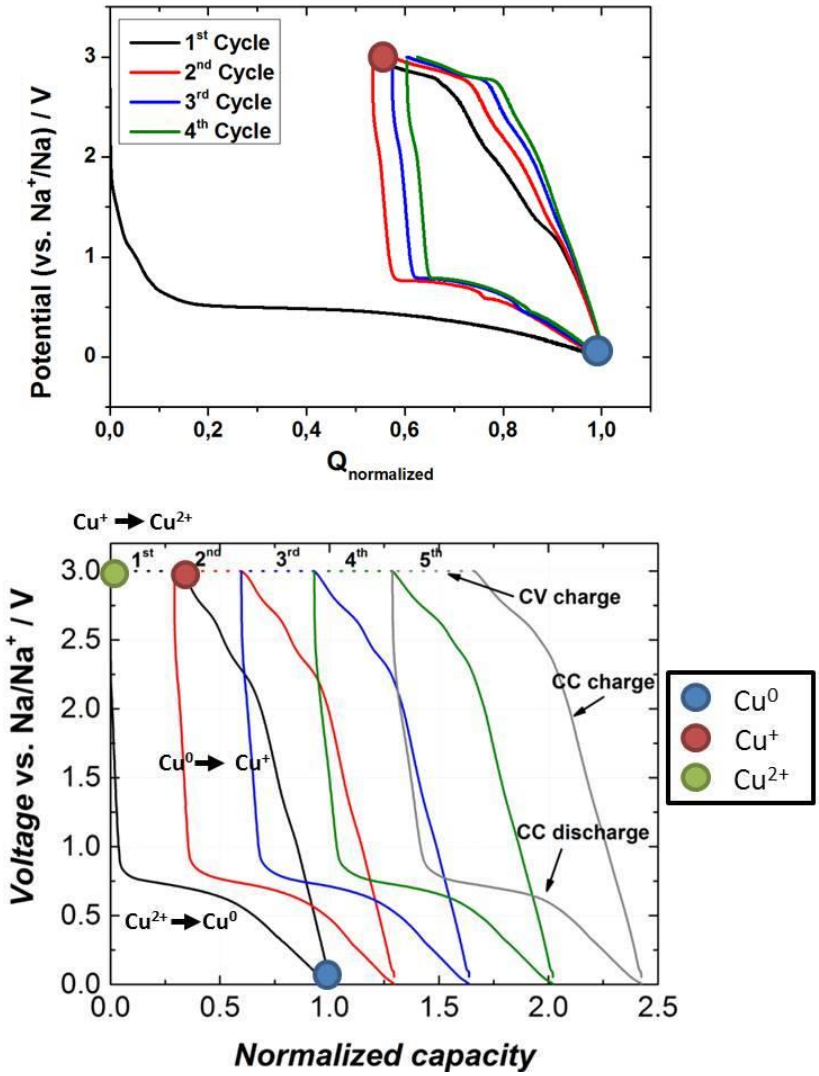

Figure 4.31. Cycling of the CuNCN for sodium ion batteries in the potential range of 0.005-3.0 Volts *vs* Na^+/Na (a) and the different cycling after constant potential at 3.0 Volts *vs* Na^+/Na (b).

According to the study of the mechanism through the different techniques, the suggested mechanism for the electrochemical reaction of CuNCN material with Na is described in Figure 4.32.

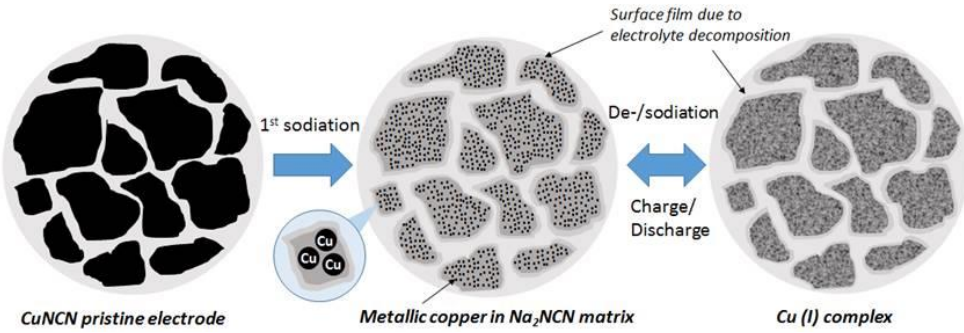

Figure 4.32. Sketch of the generally accepted reaction mechanism of conversion reactions using the example CuNCN/Na.

This mechanism consists on, the amorphization and the conversion reaction occurred forming copper nanoparticles dispersed in an amorphous matrix of Na_2NCN during the first sodiation. In this process material exhibited 700 mAh/g. This nanocomposite showed partial reversibility in the subsequent cycles (around 250-300 mAh/g). The reason of this partial reversibility is attiributed to the oxidation of metallic copper to Cu^+. The reaction is accompanied by side reactions with the electrolyte leading to surface film formation.

4.1.2.2.2 Li-ion batteries

In the study of CuNCN for lithium ion batteries (Figure 4.33a), it was observed that there was a small slope at 2.3 V *vs* Li^+/Li indicating insertion of 0.20 Li^+ ions like for sodium ion batteries. More noticeably, it also exhibited a big plateau of about 500 mAh/g at 1.4 V *vs* Li^+/Li which was also very clearly shown in the $\delta Q/\delta V$ plot of the 1st cycle (Figure 4.33b) This plateau was not reversible and from the second cycle the plateau disappeared (only appeared a bit in the second cycle (Figure 4.33c).). It could be attributed to the reduction of Cu (II) into Cu (0). Following the discharge, there were two slopes. In this region, the electrolyte decomposition and lithium ion insertion into the carbon must also be involved in this region. Upon charge, three sloppy processes seem to appear from the first cycle, as it happens in the measurement vs Na ion, corresponding to a reversible capacity of 350 mAh/g in the first cycle and decreasing to 250 mAh/g in the first ten cycles. However, in the second discharge there is almost only one sloppy curve that it is repeated in the following cycles.

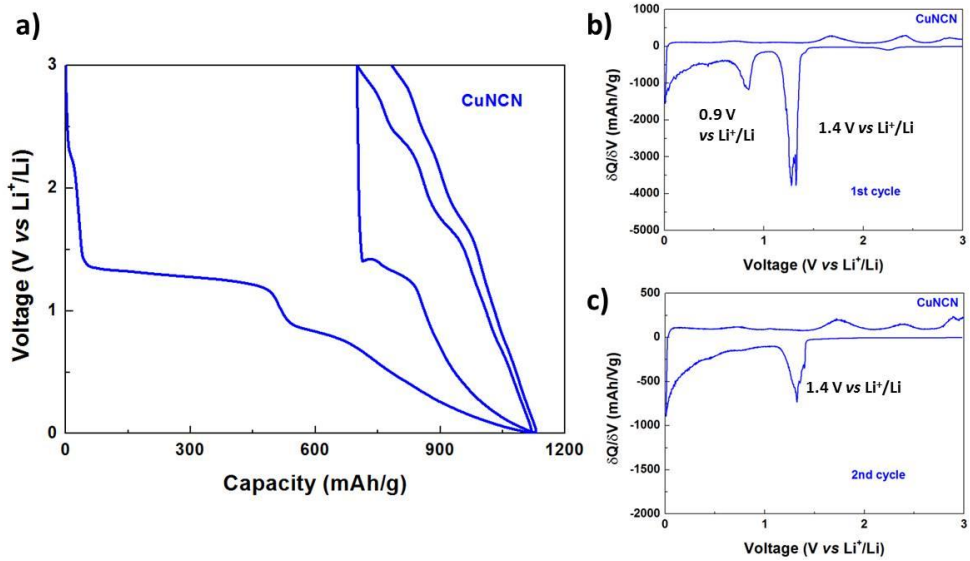

Figure 4.33. The first two cycles of CuNCN in the plot Voltage *vs* Capacity for Li-ion batteries (a), first (b) and second (c) differential capacity respect to the voltage (δQ/δV plot).

The polarization for LIB can be observed in the δQ/δV plot. The process at 0.9 V *vs* Li^+/Li disappeared in the second discharge (Figure 4.33c) but the reduction process was still at 1.4 V *vs* Li^+/Li although the intensity of the peak decreased. However, from 0.7 V *vs* Li^+/Li approximately, a charge transfer process starts that is similar in intensity in the first and second cycle suggesting that the products formed at the end of discharge are the same in every cycle.

The oxidation processes at 1.6 V *vs* Li^+/Li, 2.3 V *vs* Li^+/Li and 2.9 V *vs* Li^+/Li were easily observed both in the capacity *vs* voltage plot as well as in the δQ/δV plot. Moreover, these charge processes continued appearing upon cycling. Indeed the cyclability of this material was quite good for both sodium and lithium ion batteries keeping approximately 250 mAh/g form the tenth cycle until the hundredth cycle as it can be seen in Figure 4.34. From the tenth cycle, the capacity did not reduce upon cycling, but it even increased. Moreover, the coulombic efficiency was increasing in the first ten cycles and from there, CuNCN exhibited a coulombic efficiency larger than 98% in the 15^{th} cycle and higher than 99% from cycle 20^{th}.

The plateau observed in the first discharge at 1.4 V *vs* Li^+/Li, could be attributed to the reduction of Cu(II) to Cu(I). This way, this process could be reversible with the redox couple Cu(II)/Cu(I). In order to corroborate the reversibility of this plateau, batteries were assembled and cycled in the range of 1.0-2.5 V *vs* Li^+/Li (Figure 4.35a). It was observed that the plateau was not reversible and just 100 mAh/g of capacity were obtained (20 %

of coulombic efficiency). However, two processes at 1.7 V *vs* Li^+/Li and 2.3 V *vs* Li^+/Li were observed in charge as well as in the discharge at 1.5 V *vs* Li^+/Li and 2.1 V *vs* Li^+/Li, which were not clearly observed unlike the one cycled in the 0.005-3.0 V *vs* Li^+/Li range. In 1.0-2.5 V *vs* Li^+/Li range the battery had not almost capacity. It was closed to 20 mAh/g from the 5th cycle and at the end it had 10 mAh/g of capacity (Figure 4.35b).

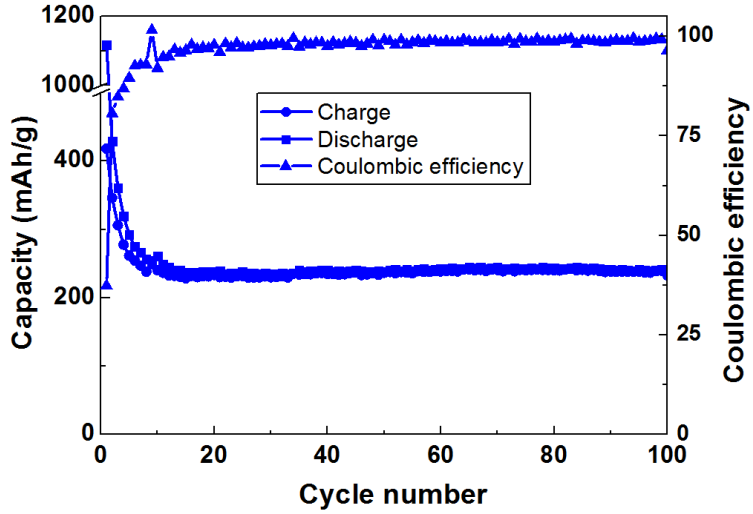

Figure 4.34. Cyclability of CuNCN at C/10 rate for 100 cycles using 1 M $LiPF_6$ in EC:DMC and metallic lithium as counter and reference electrode.

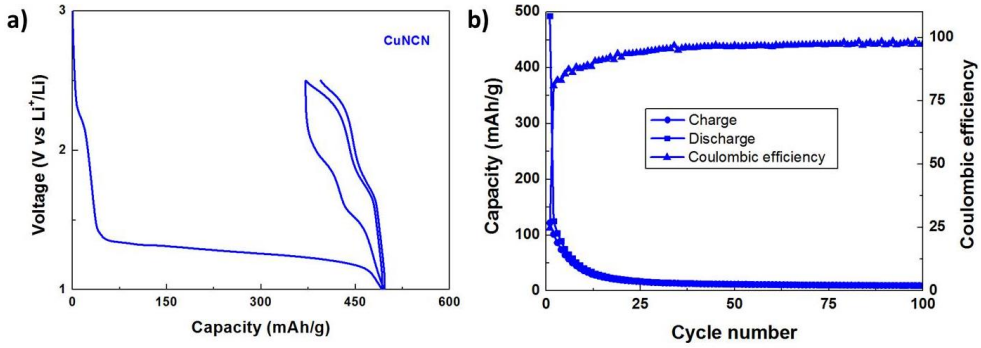

Figure 4.35. The first two cycles of CuNCN in range of Voltage 1.0-2.5 V *vs* Li^+/Li (a) and Cyclability of CuNCN at C/10 rate for 100 cycles in the same voltage range (b).

Therefore, these processes hardly contribute to the capacity of 250 mAh/g obtained in the 1.0-2.5 V *vs* Li^+/Li range. Nevertheless, it means that reactions at lower voltage of 1.0 V *vs* Li^+/Li, are mostly responsible to the capacity obtained in the range 0.005-3.0 V *vs* Li^+/Li.

4.2 Conclusions

ZnNCN and CuNCN were synthesized in aqueous media and characterized as a single phase confirmed by PXRD. Also, IR bands are in agreement with the reported values in the literature. The morphology of synthesized ZnNCN is based on 20 µm cauliflower like agglomerates made up by 4 µm faceted crystals. On the other hand, CuNCN forms small platelets of 3-4 µm of diamater that gather in a desert rose like aggregation. ZnNCN turns into ZnO from 400^{o}C in air while in nitrogen ZnNCN is stable up to 800^{o}C. Nevertheless, CuNCN is only stable up to 200ºC, while in air CuO is formed from 200^{o}C, but in nitrogen CuNCN turns into atmosphere CuO and small amount of Cu_3N at the same temperature.

The transition-metal carbodiimides $T^{M}NCN$ (T^{M} = Cu, Zn) have been evaluated as potential anodes for sodium and lithium ion batteries. ZnNCN experimented a big capacity fading and the whole material was not electrochemically active, while for CuNCN compound reversible capacities corresponding for $1e^{-}$ (258 mAh/g) process were found. These compounds insert Na through conversion reaction and the conversion mechanism was investigated for CuNCN. During the discharge, Cu metal was formed as observed by in-situ XRD diffraction *vs* Na^{+}/Na and show similar electrochemical behaviour in terms of capacity and hysteresis than commonly employed oxides (250 mAh/g and more than 1 V respectively). The incomplete conversion process has been unequivocally demonstrated by means of EPR measurements. Moreover, tests incrementing the C-rate from C/10 up to C have evidenced a kinetic limitation during the reoxidation process. This process has been further demonstrated by introducing a constant potential step after the galvanostatic charge process, evidencing that the loss of capacity is not caused, at least entirely by irreversible processes.

Given the similarities of carbodiimides to the oxide group, it seems that T^{M}(II) binary transition-metal carbodiimides operate through conversion reactions as demonstrated by in-situ powder XRD for CuNCN *vs* Na^{+}/Na.

4.3 References

[1] J. Rodriguez-Carvajal; "Recent advances in magnetic structure determination by neutron powder diffraction"; *Physica B.,*1993, **192**, 55.

[2] K. Morita, G. Mera, K. Yoshida, Y. Ikuhara, A. Klein, H. J. Kleebe and R. Riedel; "Thermal stability, morphology and electronic band gap of Zn(NCN)."; *Solid State Sci.* 2013, **23**, 50.

[3] X. Liu, M. A. Wankeu, H. Lueken and R. Dronskowski "A Novel Method for Synthesizing Crystalline Copper Carbodiimide, CuNCN. Structure Determination by X-Ray Rietveld Refinement."; *Z. Naturforsch.* 2005, **60b**, 593.

[4] J. Dreyhsig and B. Litzenburger; "Nature of optical transitions in the charge-transfer region of ZnS:Co and ZnSe:Co" *Phys. Rev. B.,* 1996, **54**, 10516.

[5] R. G. Pearson, "Chemical Hardness", Wiley-VCH, Weinheim, Germany, 1997.

[6] O. Reckeweg and A.Simon; "Azide und Cyanamide – ähnlich und doch anders"; *Z. Naturforsch*. 2003, **58b**, 1097.

[7] Hector Rubalcava; "Part I. The infrared spectra and structure of cyanamide. Part II. The infrared spectra of formamide, N,N-dideuteroformamide, and N-methylformamide." Dissertation (Ph.D.), California Institute of Technology, 1956.

[8] M. Davies and W. J. Jones; "The infra-red spectrum and structure of cyanamide and dimethylcyanamide" *Trans. Faraday Soc.*, 1958, **54**, 1454.

[9] Pradyot Patnaik, "A Comprehensive Guide to the Hazardous Properties of Chemical Substances", 3rd Edition, Wiley-VCH, Hoboken, New Yersey, 2007.

[10] Y. Wang, B. Quillian, P. Wei, H. Wang, X. J. Yang, Y. Xie, R. B. King, P. v R. Schleyer, H. F. Schaefer and G. H. Robinson; "On the Chemistry of Zn−Zn Bonds, RZn−ZnR (R = [{(2,6-$Pr^{i}_{2}C_6H_3$)N(Me)C}$_2$CH]): Synthesis, Structure, and Computations"; *J. Am. Chem. Soc.,* 2005, 127 (34), 11944.

[11] P. Senguttuvan, G. Rousse, V. Seznec, J.M. Tarascon and M.R. Palacín; "$Na_2Ti_3O_7$: Lowest Voltage Ever Reported Oxide Insertion Electrode for Sodium Ion Batteries"; *Chem. Mater*. 2011, **23**, 4109.

[12] Jung-Ki Park; "Principles and Applications of Lithium Secondary batteries", Wiley-VCH Verlag &Co., Weinheim, Germany, 2012.

[13] A. Nyman, T. G. Zavalis, R. Elger, M. Behm and G. Lindbergh; "Analysis of the Polarization in a Li-Ion Battery Cell by Numerical Simulations"; J*ournal of The Electrochemical Society*, 2010, **157** (11) A1236.

[16] L. Y. Beaulieu, K. W. Eberman, R. L. Turner, L. J. Krause and J. R. Dahn; "Colossal Reversible Volume Changes in lithium Alloys"; *Electrochemical and Solid-State Letters*, 2001, **4**(9), A137.

[17] F. Klein, B. Jache, A. Bhide and P. Adelhelm; "Conversion reactions for sodium-ion batteries" *Phys. Chem. Chem. Phys.,* 2013, **15**, 15876.

[18] B. Jache and P. Adelhelm, "Use of Graphite as a Highly Reversible Electrode with Superior Cycle Life for Sodium-Ion Batteries by Making Use of Co-Intercalation Phenomena"; *Angewandte Chemie Int. Ed.,* 2014, **53** (38), 10169.

[19] F. M. Kerton and R. Marriot; "Aternative Solvents for Green Chemistry" RSC Green Chemistry Series, Croydon (UK), 2013.

[20] I. Hasa, R. Verrelli and J. Hassoun; "Transition Metal Oxide-Carbon Composites as Conversion Anodes for Sodium-Ion Battery."; *Electrochim. Acta,* 2015, **173**, 613.

[21] H. Liu, F. Cao, H. Zheng, H. Sheng, L. Li, S. Wu, C. Liu and J. Wang; "In Situ Observation of the Sodiation Process in CuO Nanowires."; *Chem. Commun.* 2015, **51** (52), 10443.

[22] X. Wang, D. M. Tang, H. Q. Li, W. Yi, T. Y. Zhai, Y. Bando and D. Golberg; "Revealing the Conversion Mechanism of CuO Nanowires during Lithiation-Delithiation by in situ Transmission Electron Microscopy"; *Chem. Commun.*, 2012, **48**, 4812.

[23] P. Poizot, S. Laruelle, S. Grugeon, L. Dupont and J. M. Tarascon; "Nano-sized transition-metal oxides as negative-electrode materials for lithium-ion batteries"; *Nature* 2000, **407**, 496.
[24] F. Klein, B. Jache, A. Bhide and P. Adelhelm; "Conversion reactions for sodium-ion batteries" *Phys. Chem. Chem. Phys.,* 2013, **15** (3), 15876.
[25] P. G. Bruce, B. Scrosati and J. M. Tarascon; "Nanomaterials for Rechargeable Lithium Batteries"; *Angew. Chem. Int. Ed.;* 2008, **47**, 2930.
[26] J. Cabana, L. Monconduit, D. Larcher and M. R. Palacin; "Beyond Intercalation-Based Li-Ion Batteries: The State of the Art and Challenges of Electrode Materials Reacting Through Conversion Reactions" *Adv. Mater.* 2010, **22**, E170.
[27] Z. H. Stachurski; "On Structure and Properties of Amorphous Materials" *Materials,* 2011, **4**, 1564.
[28] A. J. Bard, R. Parsons, and J. Jordan, "Standard Potentials in Aqueous Solutions", Marcel Dekker, New York, 1985.
[29] G. G. Eshetu, S. Grugeon, G. Gachot, D. Mathiron, M. Armand and S. Laruelle; "LiFSI *vs.* $LiPF_6$ electrolytes in contact with lithiated graphite: Comparing thermal stabilities and identification of specific SEI-reinforcing additive"; *Electrochim. Acta* 2013, **102**, 133.
[30] L. W. Shacklette, J. E. Toth, N. S. Murthy and R. H. Baughman; "Polyacetylene and Polyphenylene as Anode Materials for Nonaqueous Secondary batteries" *J. Electrochem. Soc*. 1985, **132** (7), 1529.
[31] B. Philippe, R. Dedryvère, M. Gorgoi, H. Rensmo, D. Gonbeau, and K. Edström; "Improved Performances of Nanosilicon Electrodes Using the Salt LiFSI: A Photoelectron Spectroscopy Study"; *J. Am. Chem. Soc.* 2013, **135**, 9829.
[32] S. Wenzel, H. Metelmann, C. Raiß, A. K. Dürr, J. Janek and P. Adelhelm; "Thermodynamics and cell chemistry of room temperature sodium/sulfur cells with liquid and liquid/solid electrolyte"; *Journal of Power Sources* 2013, **243,** 758.
[33] B. A. Boukamp; "A nonlinear least squeares fit procedure for analysis of immittance data of electrochemical systems" *Solid State Ionics*, 1986, **20**, 31.
[34], U. Boesenberg, M. A. Marcus, A. K. Shukla, T. Yi, E. McDermott, P. F. The, M. Srinivasan, A. Moewes and J. Cabana; "Asymmetric pathways in the electrochemical conversion reaction of NiO as battery electrode with high storage capacity" *Scientific Reports* 2014, **4**, 7133.
[35] J. Kasnatscheew, M. Evertz, B. Streipert, R. Wagner, R. Klöpsch, B. Vortmann, H. Hahn, S. Nowak, M. Amereller, A.-C. Gentschev, P. Lamp and M. Winter; "The truth about the 1st cycle Coulombic efficiency of $LiNi_{1/3}Co_{1/3}Mn_{1/3}O_2$ (NCM) cathodes"; *Phys.Chem.Chem.Phys*. 2016, **18**, 3956.

5- Structural, electrochemical and thermodynamic studies of MnNCN, FeNCN, CoNCN and NiNCN

In this chapter the structural characterization of manganese, iron, cobalt and nickel carbodiimides is discussed and their electrochemical characterization as electrodes for Li and Na ion batteries is described and discussed in the context of the TMD stability of the different phases. For the structural study of these compounds X-Ray Diffraction, Scanning Electron Microscopy and InfraRed Spectroscopy techniques were used. In order to understand the mechanism of electrochemical reaction, galvanostatic cycling and *ex-situ* XRD measurements of discharged electrodes were carried out. At the end of this chapter, the electrochemistry and thermodynamics of all transition metal carbodiimides will be discussed. A comparison of the results obtained, including CuNCN and ZnNCN, with different oxides and other conversion materials will be also carried out.

5.1 Results and discussion

5.1.1 Structural and physicochemical characterization

5.1.1.1 Powder X-Ray Diffraction

The different synthesized MnNCN (described in Chapter 2) were characterized by X-Ray Diffraction. Different diffractograms were obtained for both synthesized samples. On the one hand, following the solid state synthesis reported by *X.Liu et al.*[1] a crystalline single phase was obtained as it can be deduced from the narrowness of the reflections of the diffractogram and through the Rietveld refinement analysis (Figure 5.1a). All reflections were in good agreement with the reported trigonal space group *R*-3*m*H (nº166) reported[2] from a single-crystal where the unit cell contained 3 formula units. The cell parameters, molar mass, volume (also per unit cell), T^M-N distances, ionic radius and electronic configuration of transition-metal ions are shown in Table 5.1.

The refined structure is shown in Figure 5.1b. The manganese cations are coordinated in octahedons by 6 nitrogens of different NCN chains. This octahedron is very regular where in the equatorial plane of the octahedra the four Mn-N distances are 2.262 Å and in the axial position of 2.261 Å. The reason for these regular octahedra being the absence of Jahn-Teller effect. In MnNCN, Mn^{2+} is high spin[1], thus there are five unpaired electrons with the energy levels (t_{2g} and e_g) both half occupied. The larger charge delocalization of $(NCN)^{2-}$ compared to the oxide group (O^{2-}) causes this bond between the transition metals and nitrogen to be more covalent. As a result, the T^M-N bond length was longer as can be seen in the

differences between d(Mn-O)=2.22 Å and d(Mn-N)=2.26 Å. Besides, the NCN^{2-} chain adopts the linear $[N=C=N]^{2-}$ carbodiimide shape with two C=N double bonds of 1.23 Å.

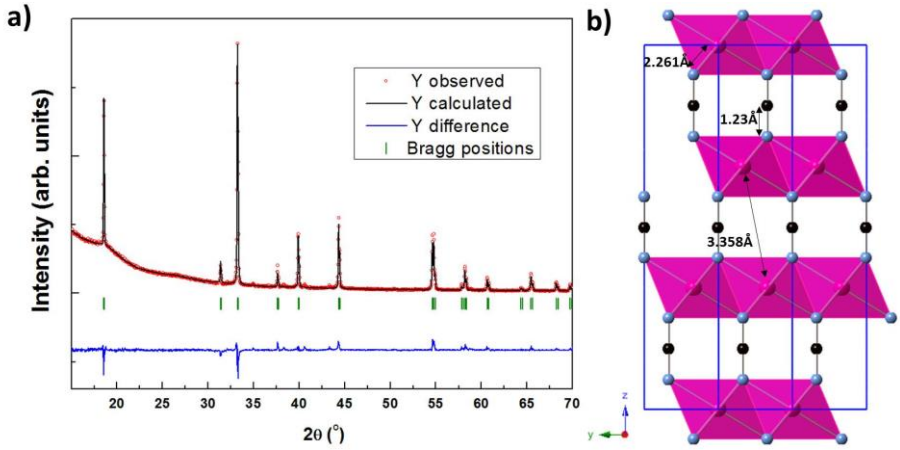

Figure 5.1. Observed (red dots), calculated (solid black line), and difference (blue bottom curve) patterns for the Rietveld analysis from the powder X-ray diffraction data of crystalline MnNCN. Green short vertical lines below the profile indicate the peak positions of all the possible Bragg reflections (a). MnNCN structure obtained from the refinement where the blue spheres are the nitrogen atoms, black spheres are the carbon atoms and purple octahedra are the MnN_6 block. Characteristic Mn-N, N-C and M-M distances are shown in MnNCN.

On the other hand, for manganese carbodiimide synthesized by organic media, just cell parameters were refined using Pattern matching fitting (Figure 5.2). The diffractogram showed very broaden peaks due to the low crystallinity of the sample. From the refinement, *a* = 3.3583(4) Å and *c* = 14.347(2) Å were obtained which agree with those of the crystalline sample (Table 5.1).

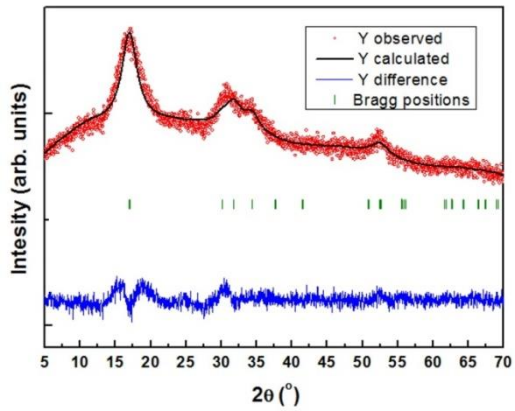

Figure 5.2. MnNCN synthesized in organic media. Observed (red dots), calculated (solid black line), and difference (blue bottom curve) patterns for the Pattern Matching analysis.

Iron, cobalt and nickel carbodiimides have a similar structure but with hexagonal symmetry. The X-ray powder diffractograms of the different carbodiimides were indexed using space group $P6_3/mmc$ (194) resembling the NiAs type structure. They were synthesized as pure phases (see Figure 5.3a for FeNCN and Figure A5.1 of the annex for CoNCN and NiNCN). The unit cell was made up by 2 formula units of MNCN (M=Fe[3], Co[4,5], Ni[5,6]). Their PXRD patterns showed narrow reflections indicating highly crystalline samples.

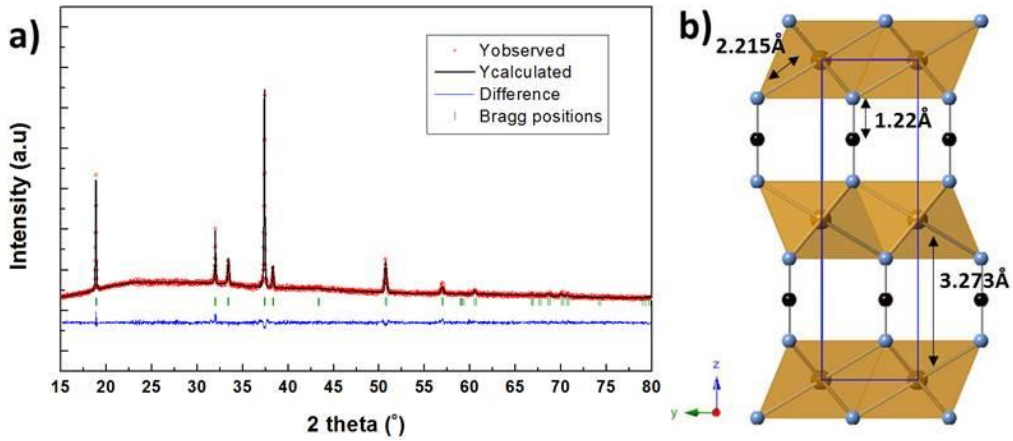

Figure 5.3. Observed (red dots), calculated (solid black line), and difference (blue bottom curve) patterns for the Rietveld analysis from the powder X-ray diffraction data of FeNCN and green short vertical lines below the profile indicate the peak positions of all the possible Bragg reflections (a) and the structure of FeNCN obtained from the refinement (b).

Table 5.1. Cell parameters and structural data obtained from the Rietveld refinement method of T^MCN (T^M=Mn^{2+}, Fe^{2+}, Co^{2+} and Ni^{2+}) and ionic radius from ref. 7.

	MnNCN	FeNCN	CoNCN	NiNCN
Space group	*R*-3*m*H	$P6_3/mmc$	$P6_3/mmc$	$P6_3/mmc$
Molar mass (g/mol)	94.94	95.85	98.93	98.71
***a=b* (Å)**	3.358 (3)	3.280 (2)	3.209 (3)	3.158 (2)
***c* (Å)**	14.337 (4)	9.404 (1)	9.381 (2)	9.249 (4)
***Y* (º)**	120	120	120	120
Volume (Å^3)	140.037 (4)	87.60 (1)	83.64 (2)	79.91 (6)
Volume/Z (Å^3)	46.679	43.8	41.82	39.96
Δdistance M-N (Å)	2.262	2.215	2.168	2.119
Ionic radius M^{2+} (Å)	0.83	0.78	0.745	0.69
Electronic configuration	$3d^5$	$3d^6$	$3d^7$	$3d^8$

The cell parameters; atomic positions and thermal parameters were refined for these carbodiimides obtaining the values represented in Table 5.1 and in Table A5.2, Table A5.3 and Table 5.4 of the annex. In $T^{M}NCN$, $(T^{M})^{2+}$ ions were coordinated in octhedra by six nitrogen atoms of different NCN chains with a unique Fe-N distance of 2.201 (6) Å, a Co-N distance of 2.168 (2) Å and a Ni-N distance of 2.119 (5) Å. Surprisingly, from the obtained structural data, big differences in the T^{M}-N distances were not obtained although a Jahn-Teller distortions should be observed for these compounds.

The N-C distances in the chain anion N=C=N changed slightly depending on the M^{2+} as well. In FeNCN the Fe-N distance is 1.220(4) Å, while for CoNCN the Co-N distance is 1.226(7) Å and the Ni-N is 1.233(2) Å. However, in all the structures the NCN angle was close to 180 ^{o}.

5.1.1.2 Scanning Electron Microscopy

The microstructural morphology of manganese, iron, cobalt and nickel carbodiimide particles was studied by Scanning Electron Microscopy.

In MnNCN sample, both types of synthesized powders were measured and particle sizes and shapes were very different. For the sample synthesized in organic media, the particle size was smaller (around 1µm) and its shape seemed homogeneous (see Figure 5.4a). In the more crystalline sample that was synthesized by the reported metathesis reaction[1], the particle size is bigger (4-5µm) and the particles have a regular bean like shape as can be seen in Figure 5.4b.

In the iron, cobalt and nickel carbodiimides different particle sizes were observed. For FeNCN the particle size was less than 1 µm (Figure 5.5a), while the cobalt carbodiimide showed a very regular platelet with bigger size (more than 5 µm) where the sides of the particle were well defined (Figure 5.5b). On the other hand, nickel carbodiimide showed more homogeneous shape with small wide rods particles forming aggregations of 6-7µm particles (Figure 5.5c).

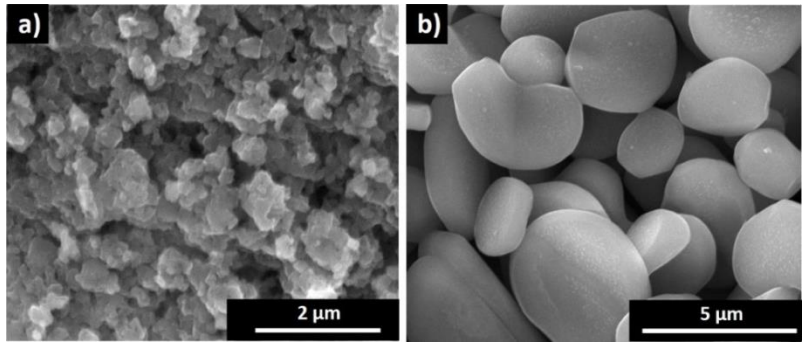

Figure 5.4. SEM of the different MnNCN synthesized samples where in (a) the MnNCN by the reported method and in (b) is the SEM image of the synthesized in organic media.

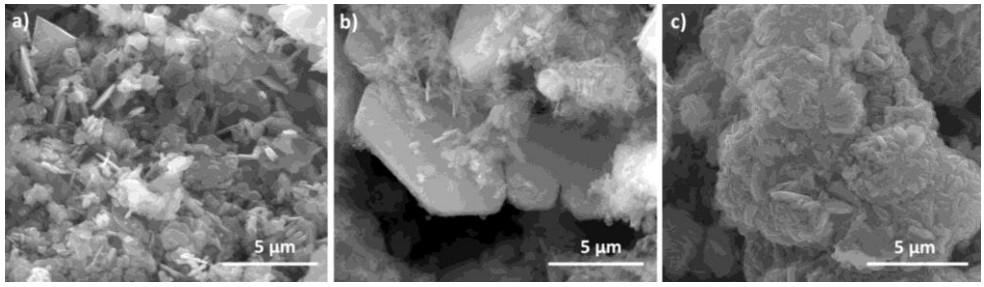

Figure 5.5. SEM images using 16000x magnifications of the synthesized FeNCN (a), CoNCN (b) and NiNCN (c) after cleaning once with deionized water.

The SEM analysis of the laminates performed inside the glovebox showed a very good homogeneity (see Figure 5.6) indicating that the electrochemical measurements of these materials could be carried out in correct conditions.

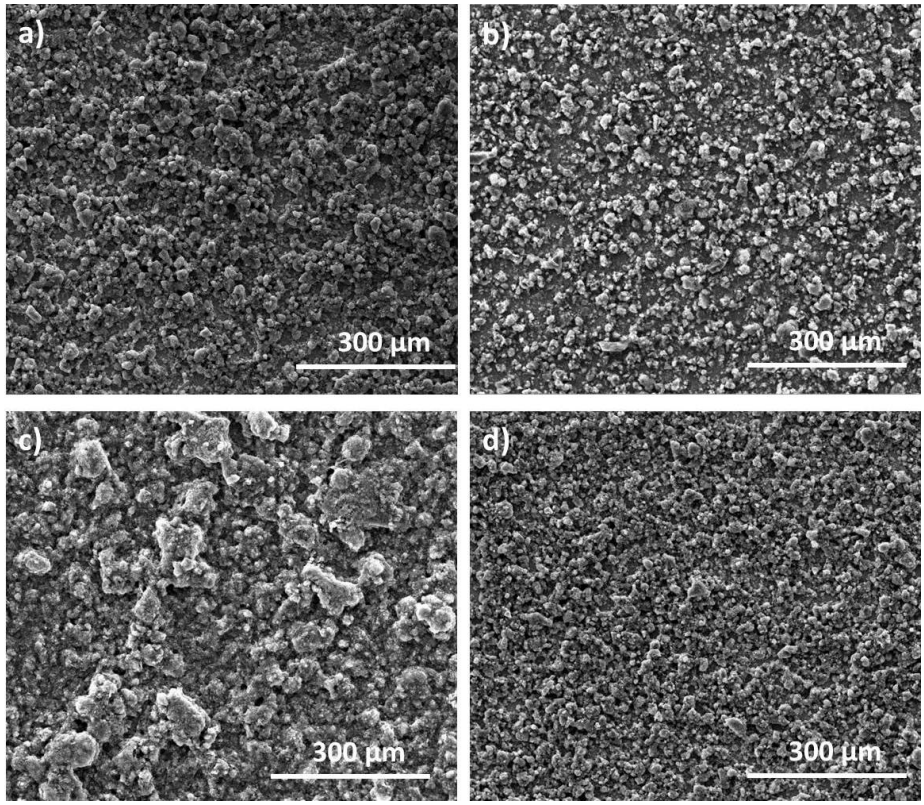

Figure 5.6. SEM images using 300x magnifications of the prepared laminates for the manganese (a), iron (b), cobalt (c) and nickel (d) carbodiimide.

It is important to note that although all the samples were synthesized in the same way, in the case of FeNCN and CoNCN several cleanings were needed to remove the mixture of salts (needles surrounding the particles), unlike the salts of nickel carbodiimide were only one washing was necessary.

5.1.1.3 Infrared spectroscopy

The FTIR spectra of the MnNCN, FeNCN, CoNCN and NiNCN compounds are shown in . Mn^{2+}, Fe^{2+}, Co^{2+} and Ni^{2+} metals, according to Pearson´s HSAB theory, are hard acids. This fact causes that their $T^{M}NCN$ phases crystallize in the carbodiimide like form, like CuNCN and ZnNCN and unlike proton or lead that prefer cyanamide-type NCN bond as discussed in Chapter 1 and Chapter 4.

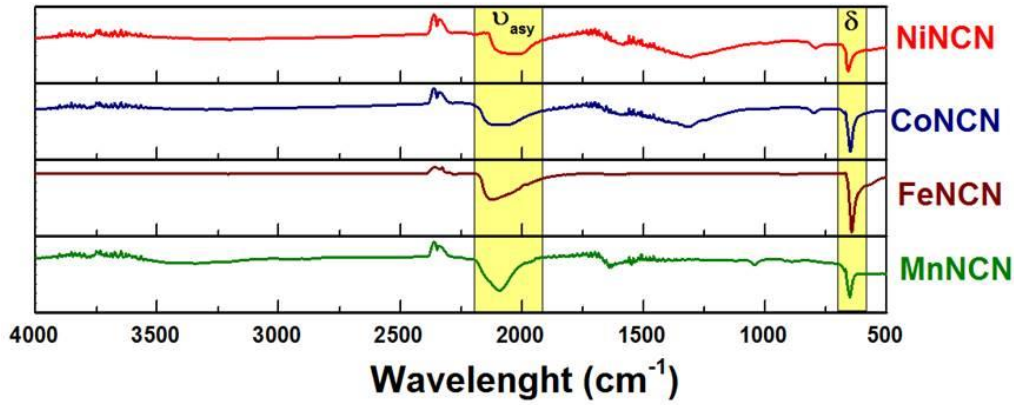

Figure 5.7. FTIR spectra in the range 4000-500 cm^{-1} of MnNCN (green), FeNCN (brown), CoNCN (blue) and NiNCN (red) are represented respectively from bottom to top.

The IR bands corresponding to the asymmetric stretching and deformation were assigned at around 2040-2130 cm^{-1} and 640-650 cm^{-1} respectively in good agreement with the reported values[1,3,4]. The distances of T^{M}-N and N=C bonds; the deformation and asymmetrical stretching from the spectra are listed in Table 5.2 for all the carbodiimides. The correlation between the bands and distances, for these compounds and including CuNCN[8] and ZnNCN[9] is shown in Figure 5.8. As can be seen a good correlation between the experimental frequencies of asymmetrical stretching and d(N=C) (Figure 5.8a) and deformation band with d(T^{M}-N) (Figure 5.8b) is observed.

Table 5.2. Frequency values of Manganese, iron, cobalt and nickel carbodiimide most characteristics bands obtained from Infrared spectra and the M-N and N=C distances obtained from the Rietveld refinement.

Material	$\upsilon_{asymmetrical}$ (cm^{-1})	δ(cm^{-1})	N=C distance (Å)	M-N distance (Å)
MnNCN	2049	650	1.230	2.261
FeNCN	2127	643	1.217	2.201
CoNCN	2089	648	1.226	2.168
NiNCN	2039	659	1.233	2.119

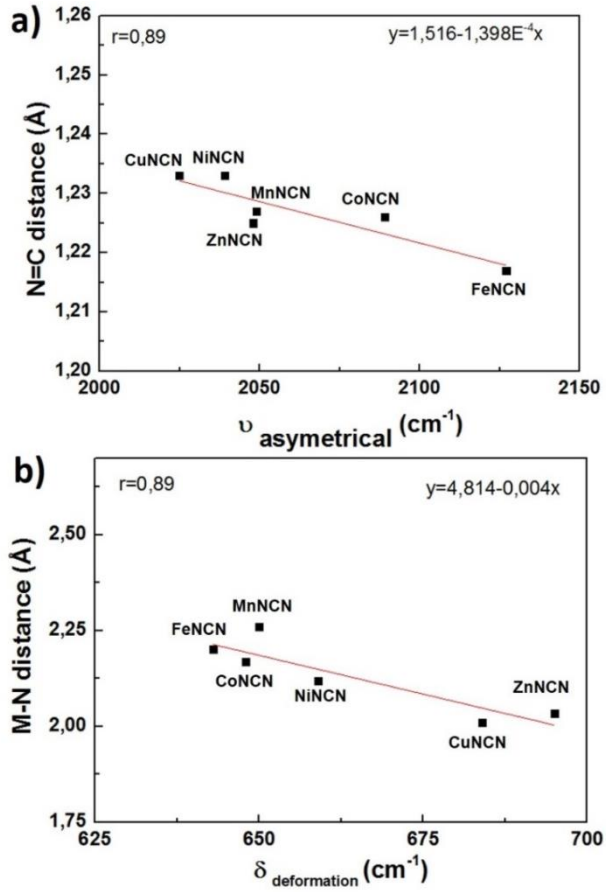

Figure 5.8. Correlation of the asymmetrical stretching and deformation with the interatomic N=C (a) and M-N (b) distances respectively.

There is a relationship between the frequency of the IR bands and the N=C and M-N distances, as both are related to the strength of these bonds. Specifically, comparing the isostructural compounds FeNCN, CoNCN and NiNCN a clear correlation could be obtained. While iron carbodiimide presented the longer Fe-N distance due to the smaller ionic radius and higher ionic character of the bond, CoNCN and NiNCN followed the same tendency. On the other hand, the analysis of MnNCN is more intriguing. The N=C distance is almost the same than in ZnNCN, which was the precursor used for its synthesis, and is in agreement with the tendency of FeNCN, CoNCN and NiNCN. Regarding to T^{M}-N distance, MnNCN show longer T^{M}-N distance due to its higher ionic radius (0.83 Å compared to the 0.6 Å of Zn^{2+}) and higher ionic character than ZnNCN. However, MnNCN did not follow the same tendency than FeNCN, CoNCN and NiNCN probably due to their different structure.

5.1.2 Electrochemical characterization

After the studies based on CuNCN and ZnNCN, it was considered the possibility that the $T^{M}NCN$ (T^{M}=Mn, Fe, Co and Ni) compounds could also experience a conversion reaction. Moreover, the reduction of these transition metals to T^{M} (I) oxidation state seems to be quite improbable expecting that all M^{2+} cations would be reduced to M^{0}. At the same time, two sodium/lithium ions could link with the carbodiimide group for a full displacement reaction where two electrons would be involved. Thus, a C-rate of 1C was calculated as the current needed to insert 2 alkali ions per transition metal in one hour. In the following we first compare the electrochemical performance of the MnNCN produced by different routes and next we compare the performance of the three isostructural members both for Na and Li ion batteries.

5.1.2.1 Manganese Carbodiimide

MnNCN crystalline sample was tested for sodium and lithium ion batteries. As it can be seen in Figure 5.9, crystalline manganese carbodiimide had a very large 1st discharge capacity at relatively low potential (0.8 V *vs* A^{+}/A for both SIB and LIB). Despite this high capacity (380 mAh/g for SIB and 1100 mAh/g for LIB) was observed, just 80 mAh/g and 250 mAh/g were reversible in the first charge for SIB and LIB, respectively. It seemed that manganese carbodiimide was electrochemically inactive. The electrochemical inactivity of MnNCN (which was previously reported by *B. Milke et al.*[10]) could be due to the proximity of the plateau to sodium and lithium electroplating. Therefore, it is important to attempt reducing the polarization of the electrode in order to see if a very low voltage plateau appeared. Indeed, the galvanostatic cycling looks quite similar to those of the carbons (previously discussed in Chapter 4), hence the electrochemical activity could come from the activity of the carbons. As both (Ketjen Black and Super C65) have partially graphitic structure, the co-intercalation[14] of sodium with solvent molecules, for SIB, and the intercalation of lithium ions in the interlayers, for LIB, could occur. Therefore, the electrochemical activity could be attributed to the insertion of sodium into the porous of the carbon being this mechanism not very reversible (red line of Figure 5.10). The irreversible capacity increased using Ketjen black because of its higher surface area compared to the Super C65[11]. For LIB, two different reactions occurred. At 0.8 V *vs* Li^{+}/Li, lithium ions were inserted into the porous of the Ketjen black and later at 0.2 V *vs* Li^{+}/Li lithium ions seemed to be inserted in between graphene layers. During charge, just the deinsertion of lithium ions of the porous was observed during the first discharge Moreover,

for SIB and LIB the electrochemical reactions were not reversible as it can be seen in the black line of Figure 5.10.

In order to reduce the polarization, the smaller particle size could be a good solution. This way, MnNCN synthesized in organic media was tested because of its smaller particle size as observed in the SEM images (Section 5.1.1.2). The smaller size could shorten the diffusion path of sodium and lithium ions[12]. As a result the polarization could be decreased making possible the observation of electrochemical activity in MnNCN.

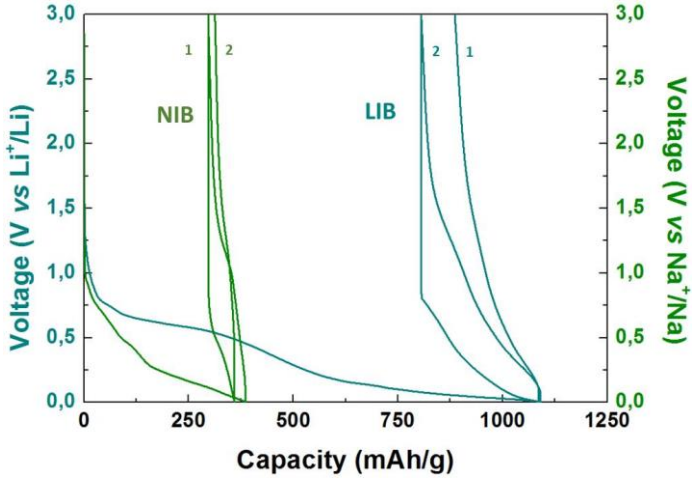

Figure 5.9. Electrochemical properties of MnNCN crystalline sample for sodium (bright green) and lithium (cyan) ion batteries.

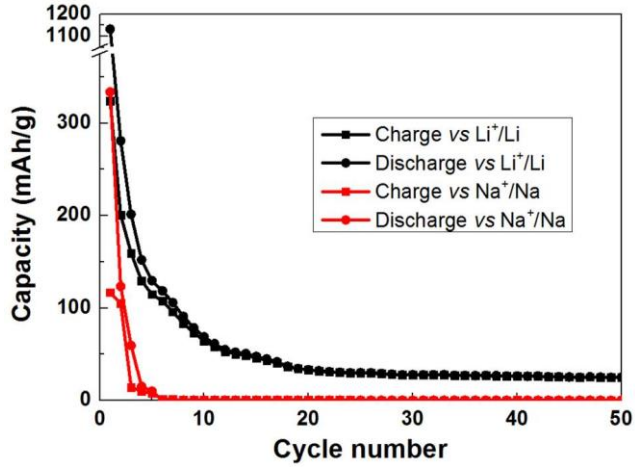

Figure 5.10. Cyclability of the crystalline manganese carbodiimide for sodium (red) and lithium (black) ion batteries.

Indeed a much larger reversible capacity was observed in the galvanostatic cycling of MnNCN synthesized in organic media, both for sodium and lithium ion batteries. For sodium ion batteries three different processes were observed in the first discharge (see Figure 5.11).

i) A solid solution process was observed at 1 V *vs* Na^+/Na and could be attributed to the adsorption of sodium ions on the carbon layers. ii) At 0.6 Volts *vs* Na^+/Na, a small plateau appears that can be attributed to the sodium co-intercalation[14] into the Ketjen Black particles (solvated with the solvent of the electrolyte which in this case is Methyl-THF). Iii) Finally, reaching 0.1 V *vs* Na^+/Na, a plateau, likely due to the conversion reaction of manganese carbodiimide with sodium, was shown. This plateau was very close to 0 V *vs* Na^+/Na, which can be the reason why it does not appear in the crystalline sample as Milke et al reported[10]. It is possible that through reducing the particle size of the crystalline sample by an intensive ball milling treatment, the overpotential coming from the activation polarization could be also be reduced. The processes that occur in the first discharge can be clearly shown in the δQδV plots of the first and second cycle (Figure 5.11b and Figure 5.11c). In contrast,, during the charge, it was observed that the process, where the conversion reaction was taking place at 2.4 Volt *vs* Na^+/Na, was somewhat reversible and highly contributed to the capacity.

A reversible capacity of 175 mAh/g was achieved for more than 100 cycles and the coulombic efficiency was higher than 99% from the second cycle onwards (Figure 5.12), which means that the main drawback of this material to be a suitable anode for sodium ion batteries was that it did not achieve the complete conversion reaction and intrinsic overpotential that this material exhibited.

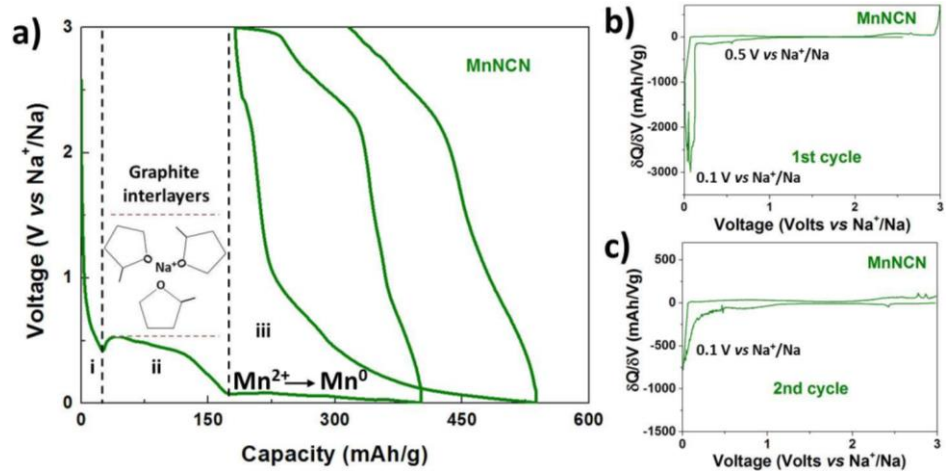

Figure 5.11. Galvanostatic cycling in the range of 0.005-3.0 Volts *vs* Na^+/Na of manganese carbodiimide synthesized in organic media and first (b) and second (c) differential capacity.

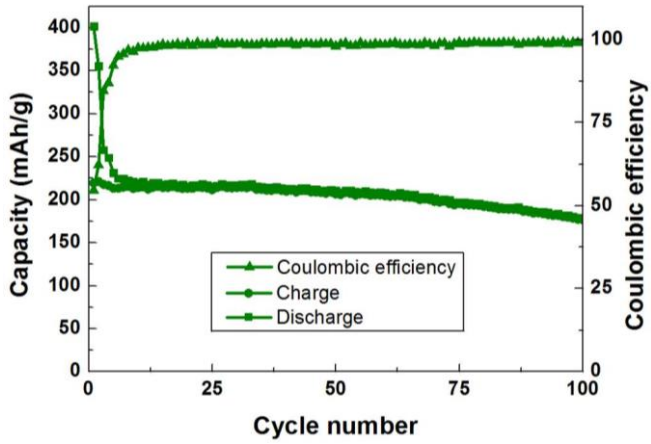

Figure 5.12. Cyclability of MnNCN synthesized in organic media for sodium ion batteries in the voltage range of 0.005-3.0 V *vs* Na^+/Na.

The capacity of 200 mAh/g obtained in the first charge, was quite lower than the theoretical capacity of this material (564.55 mAh/g) for the complete conversion reaction. This could be due to two different reasons: i) *carbon coating of the material*. A non-perfect carbon coating could cause an increment of the polarization and the material could not afford the complete electrochemical reaction. However, the discharge plateau was observed unlike in the crystalline sample. The cut off at 5 mV *vs* Na^+/Na were reached but the whole conversion reaction had not occurred. ii) The slower kinetic of the sodium ions in the conversion in comparison with the lithium analogue reaction. The conversion reaction was not fully accomplished despite the good cyclability of the cell.

In the *ex-situ* XRD analysis of the electrode, just the reflections of the current collector were observed (Figure 5.13). This fact could indicate that the material became amorphous during the first discharge.

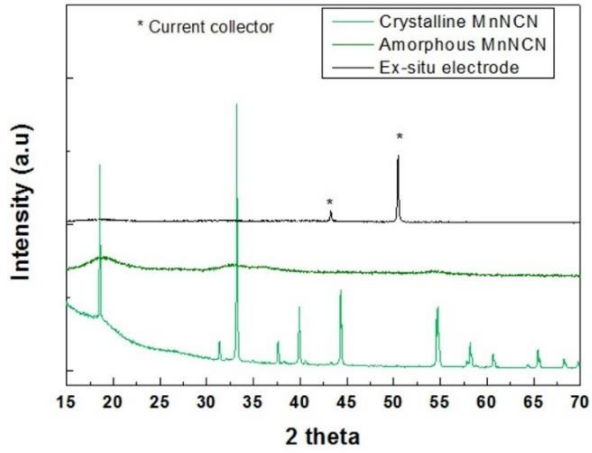

Figure 5.13. *Ex-situ* XRD pattern of MnNCN electrode discharged to 0.005 V *vs* Na^+/Na.

The good coulombic efficiency of the material presented could be due to the small volume expansion that the electrode suffered during the conversion reaction. This volume expansion was calculated taking into account the reported structures of manganese metal, sodium carbodiimide and manganese carbodiimide. The calculated expansion value of the electrode in sodium compound was about 66.76%, which is relatively small compared to the one experimented in oxides or fluorides[16].

In the case of lithium ion batteries, two reactions were clearly observed during the first discharge (see Figure 5.14). At 1 V *vs* Li^+/Li the adsorption of lithium ions in the carbon surface was observed. A plateau at 0.3 V *vs* Li^+/Li of about 850 mAh/g appears where the conversion reaction was taking place. Nonetheless, a reversible capacity of 550 mAh/g was achieved during the first charge. Upon cycling the capacity hardly faded during 100 cycles (Figure 5.15), being able to keep more than 500 mAh/g. The observed volume expansion for the electrode was calculated as 52.42%. This small volume expansion (compared to manganese oxide for example) can enhance the cyclability of the material. An irreversible capacity of 370 mAh/g was observed which was not coming from the displacement reaction. This fact can be attributed to the amorphization of the material as it was reported previously in several papers[17,18,19,20]. So, taking into account that in this material the percentage of carbon used was 20%, it seems that the fully conversion of manganese carbodiimide was reached. It is worth noting that the voltage of the plateau in the second cycle increased from 0.3 V *vs* Li^+/Li to 0.7 V *vs* Li^+/Li which is easily observed in the difference of δQδV plots of first and second cycle (Figure 5.14b and Figure 5.14c). This increment of the voltage was also previously observed for other conversion materials and is attributed to different properties of the materials in amorphous structure in comparison with the crystalline structure[19,20].

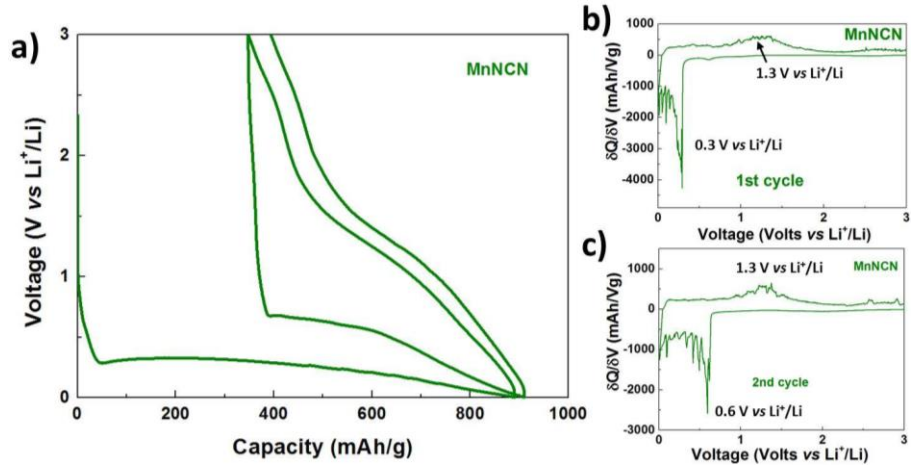

Figure 5.14. Galvanostatic cycling in the range of 0.005-3.0 Volts *vs* Li^+/Li of manganese carbodiimide synthesized in organic media and first (b) and second (c) differential capacity.

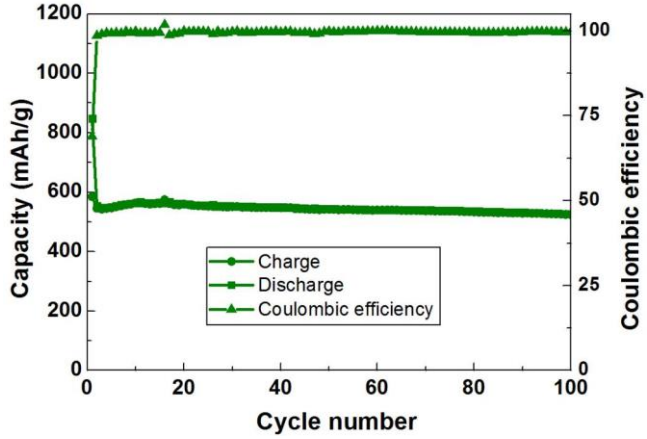

Figure 5.15. Cyclability of MnNCN synthesized in organic media for lithium ion batteries in the voltage range of 0.005-3.0 V.

Given the good electrochemical performance of this material for lithium ion batteries, the voltage range was decreased to 2 V *vs* Li^+/Li in order to check how the material could act as anode for a full cell study of lithium ion. The same behavior was observed in the first discharge process. However, reaching 2 Volts *vs* Li^+/Li (Figure 5.16a) during charge, the conversion reaction was not considered to be fully accomplished. In fact, during the charge, about half of the Mn^0 seemed to be converted into Mn^{2+}, as deduced from the obtained capacity to 300 mAh/g. As a result, during the second discharge, the length of the plateau was smaller causing an increase in the average voltage to 0.5 V *vs* Li^+/Li instead of the 0.4 V *vs* Li^+/Li of the sample that had been cycled up to 3 V *vs* Li^+/Li.

The average voltage during the charge is decreased from 1.6 Volts *vs* Li^+/Li to 1.05 Volts *vs* Li^+/Li in the sample cycled up to 2 V *vs* Li^+/Li. Notwithstanding, in Figure 5.16b it can be seen that the material was able to keep 78% of the first charge capacity up to 100 cycles (250 mAh/g) with a high coulombic efficiency (higher than 99% from second cycle).

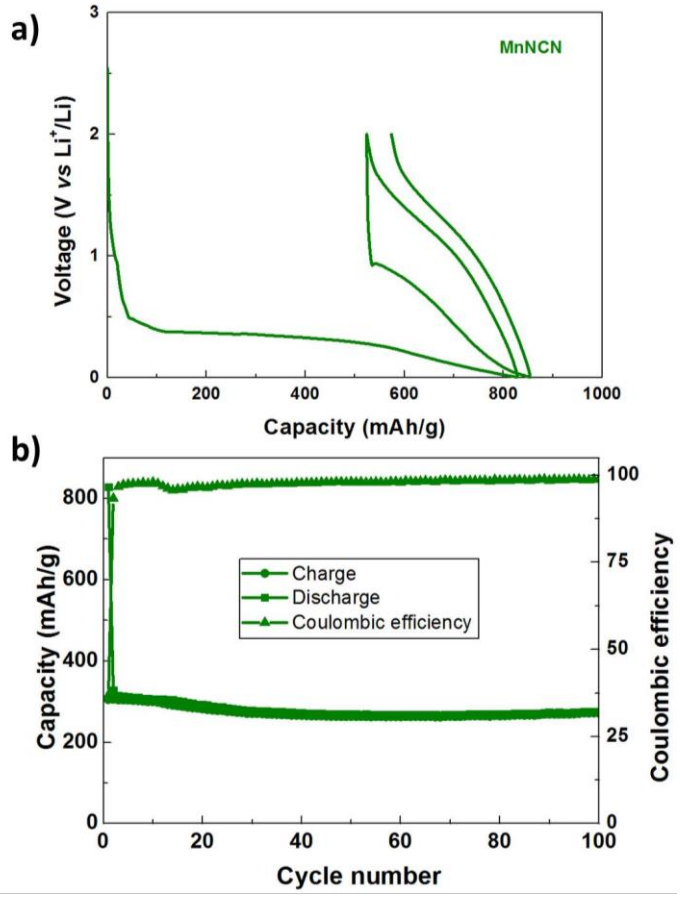

Figure 5.16. Galvanostatic cycling in the voltage range of 0.005-2.0 Volts vs Li+/Li of organic media synthesized MnNCN for lithium ion batteries.

In addition, as the average voltage of the cell was decreased and linked to the good capacity values; this material seemed to meet the requirements to be a suitable anode for lithium ion batteries. Even though, a very high first cycle irreversible capacity of this material (around 520 mAh/g) was observed if cycling only up to 2.0 Volts *vs* Li^+/Li. This fact however hindered the possible good performance of this material in a full cell test.

5.1.2.2 Iron, cobalt and nickel Carbodiimide

These transition metal carbodiimides have been electrochemically studied for the first time and the results were expected to be similar to those of the MnNCN phases. Considering that the simple transition-metal carbodiimides are not able to host lithium ions[21] and the metallic elements (Fe, Co or Ni) do not form alloys, a displacement reaction mechanism should be expected. Transition metal oxides which are analogues of carbodiimides such as FeO, CoO and NiO were described initially by *P. Poizot et al.*[19] as anode materials in lithium ion batteries working through a conversion mechanism. However, the electrochemical activity of these materials has not been reported yet for sodium ion batteries[22]. On the other hand, studies based on the higher oxidation states oxides such as α-Fe_2O_3 showed good electrochemical behavior as raw material[23] or anchored to graphene[24] in SIB. So that, the electrochemical performance of these transition metal carbodiimides were analyzed and compared with the reported electrochemical behavior of FeO, CoO and NiO in LIB.

Figure 5.17 shows the electrochemical performance of these transition metal carbodiimides at C/10 rate in sodium ion batteries. During the first discharge, there is a process at 1.5 V *vs* Na^+/Na due to sodium ion adsorption into the carbon layers, providing 30 mAh/g of capacity as it can be seen in brown line . At 0.8 V *vs* Na^+/Na an additional process seemed to take place, giving an irreversible 150 mAh/g of capacity. This process is not observed in the published study of the electrochemistry of FeNCN performed by M. Sougrati et al.[25]. Since they used PC (Propylen Carbonate) as solvent of the electrolyte which is not a high donor number thus blocking the co-intercalation into the graphite interlayers, we can deduce that this process is due to co-intercalation[14] of sodium, with the high donor number solvent that we are using into graphitic carbon. Finally, at 0.3 V *vs* Na^+/Na a large plateau of 400 mAh/g of capacity appeared which could be attributed to the conversion reaction (reduction of Fe^{2+} compound to metallic iron). This plateau presented the higher contribution to the capacity as it can be seen in δQδV plot (brown line of Figure 5.17). Iron carbodiimide showed similar galvanostatic discharge compared to the reported for FeO in LIB[19].

The galvanostatic curve of CoNCN was similar than for FeNCN. During the first discharge, (see blue line of Figure 5.17) a solid solution process appeared at 1.2 Volts *vs* Na^+/Na which could be attributed to the sodium adsorption into the carbon layer. At 0.8 V *vs* Na^+/Na the sodium co-intercalation[14] occurred in the same voltage as for FeNCN. At the end of the discharge, there was a plateau corresponding to the conversion reaction centered at 0.5 V *vs* Na^+/Na. This plateau was assigned to the reduction of CoNCN into metallic cobalt and forming the sodium carbodiimide matrix delivering 700 mAh/g of capacity a bit higher than theoretical (542 mAh/g). In the same manner, NiNCN had almost identical galvanostatic cycling compared to CoNCN in terms of shape and irreversible capacity of the first cycle.

During the first discharge (see Figure 5.17a), the same processes occurred. The solid solution process at 1.1 V *vs* Na^+/Na due to the sodium adsorption into the carbon layers and the sodium co-intercalation[14] at 0.85 V *vs* Na^+/Na. A plateau centered at 0.65 V *vs* Na^+/Na could be assigned to the conversion reaction where the reduction of NiNCN into metallic nickel and a sodium carbodiimide matrix occurred achieving a capacity of 600 mAh/g.

During the charge, two signals are shown in the δQδV plot obtained from the first galvanostatic cycle for these carbodiimides (Figure 5.17b) at approximately 1.3 and 1.9 V *vs* Na^+/Na. As *P. Poizot et al.*[19] described for transition metal oxide T^MO (T^M= Fe, Co, Ni) the fact that theoretical capacities were recovered indicated that two sodium ions took part in the electrochemical process. The second discharge was quite different and the voltage increased from 0.3 (0.5 or 0.65) V *vs* Na^+/Na in the case of FeNCN (CoNCN or NiNCN respectively) to 1.3 V *vs* Na^+/Na. This way, all the batteries worked in the same way and the processes occurred in all the charges and discharges at similar voltages (see Figure 17). However, the voltages of the discharge plateau for CoNCN and NiNCN from cycle number 10 decreased to 0.3 V *vs* Na^+/Na because the electrochemical activity was attributed to the carbon.

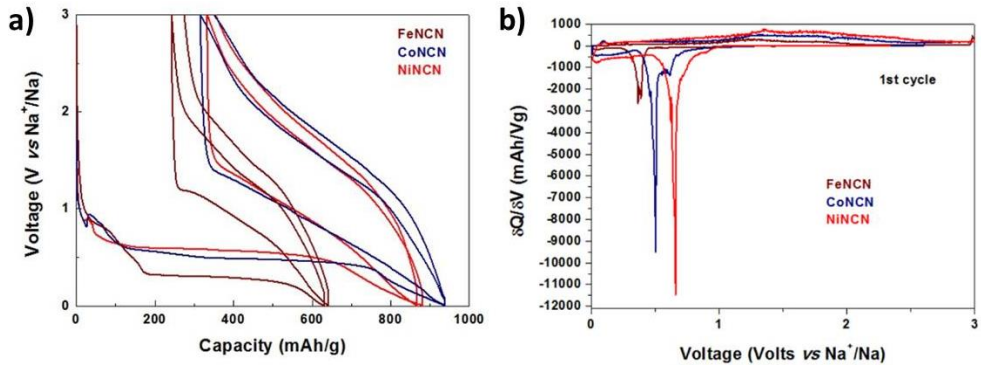

Figure 5.17. Galvanostatic 2 first cycles of iron (brown), cobalt (blue) and nickel (red) carbodiimide (a) and first cycle differential capacity (b) in the potential range of 0.005-3.0 Volts vs Na+/Na.

It is worth remarking that cyclability of FeNCN was quite better than that experimented by CoNCN and NiNCN although the galvanostatic cyclings were similar in all the cases. Iron carbodiimide was able to keep 320mAh/g after 100 cycles (approximately 80% of the initial capacity). The coulombic efficiency was around 99% from the third cycle (Figure 5.18a). This good cycling performance could be enhanced by the small volume expansion (77.96%) that the electrodes suffer upon cycling. This volume change was quite low compared to the compounds that operate at approximately same voltages. For example, sulphides, oxides and phosphides experiment an increment of volume of 100-200%, 150-250% and 200-400%, respectively[26]. Other compounds such as fluorides and chlorides present similar

volume expansion than carbodiimides but they operate at higher voltages. It is important to mention that the volume expansion could cause that active material particles loses contact from the composite electrode during the cycling. In the post-mortem analysis the detached metal particles could be mainly found close to the separator[27].

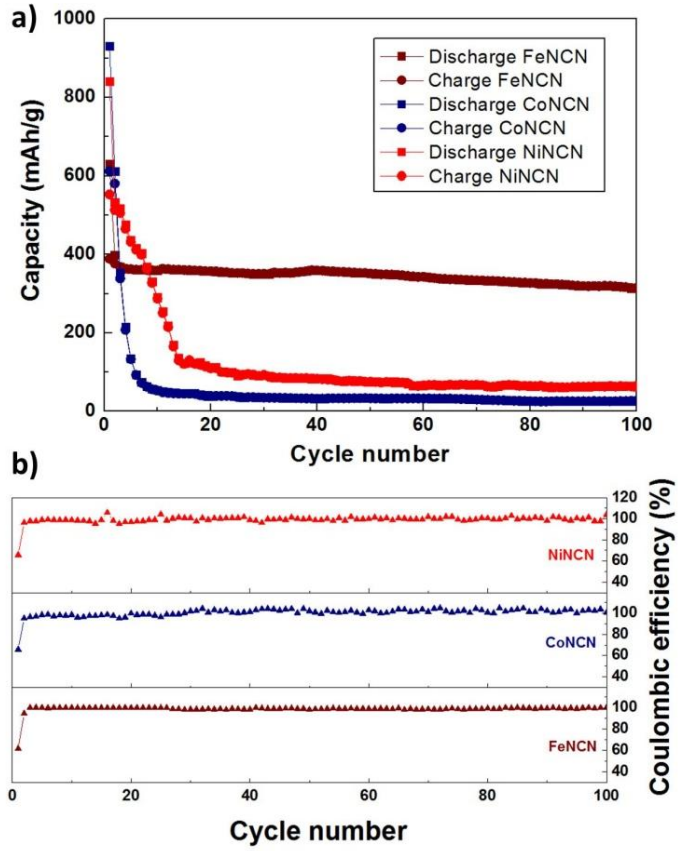

Figure 5.18. Cyclability of iron (brown), cobalt (blue) and nickel (red) carbodiimides (a) and their coulombic efficiency (b) for sodium ion batteries in the voltage range of 0.005-3.0 Volts *vs* Na^+/Na.

Contrary, in CoNCN and NiNCN, the capacity decreased drastically from 600 mAh/g and 550 mAh/g (close to 541.8 mAh/g and 543.1 mAh/g which are the theoretical capacity) to 100 mAh/g in less than ten and fourteen cycles (blue and red lines of Figure 5.18) respectively. The small capacity obtained after 20 cycles was solely attributed to the contribution of carbon into the capacity. In addition, the coulombic efficiency was higher than 93% for CoNCN while for NiNCN was around 95%. This bad cyclability was initially attributed to the higher volume expansion of CoNCN and NiNCN compared to the one experimented for

FeNCN (82.63% of CoNCN and 91.80% of NiNCN against 77.96% of FeNCN). However, transition metal oxides such as CoO[19] or Fe_2O_3[32], exhibited even higher volume expansion (around 150%) than CoNCN but the capacity retention was much better and just small fading appeared. Although the fact that CoO electrochemical activity has not been reported yet for sodium ion batteries, CoO for LIB showed very good cycling stability being able to keep 760 mAh/g for 100 cycles with a 2 µm-large particles. Therefore, the comparison with SIB was not easy to be carried out due to the different kinetics observed in sodium and lithium[33]. It would be interesting to compare how good would be the capacity retention of CoO in sodium ion batteries. A possible reason could be that the electrochemical reaction during the charge processes presented in CoNCN and NiNCN were more limited by the kinetics and the formation of CoNCN and NiNCN from Na_2NCN matrix is more difficult to take place[34]. As volume expansion did not seem to be the responsible of the capacity fading, several aspects can be the responsible of this loss or performance such as the particle size of the pristine electrode, the size of the metallic particles formed in the discharge[35], or the presence of inactive or electrically disconnected Na_2NCN/T^M regions.

The comparison of FeNCN, CoNCN and NiNCN showed that iron carbodiimide exhibited the best electrochemical properties. FeNCN presented the smallest polarization and the lower average voltage during the charge as well as good cyclability keeping 320 mAh/g after 100 cycles. Taking this into account, iron carbodiimide seems to be a promising candidate for anode material that work through conversion reaction in a sodium ion battery.

An *ex-situ* XRD analysis was performed in order to observe the reflections due to the metallic transition metals. However, no new crystalline phase was observed while the reflections of the pristine materials disappeared, as expected, at the end of the discharge. In the fully discharged electrode of FeNCN (Figure 5.19a) just metallic copper reflections coming from the current collector appeared. During charge, the reflections of FeNCN did not appear in the diffractogram (Figure 5.19b). Therefore, there was not any appreciable difference between both diffractograms even though the material was charged. For that reason, it was considered that the amorphization of the material was occurring during the discharge and the crystallinity of the FeNCN was not recovered. This was in agreement with the *in-situ* X-Ray Diffraction recently reported for the same material for lithium ion batteries[25] where the reflections disappeared during the discharge and they were not recovered in charge. Similar results were obtained for CoNCN and NiNCN (Figure 5.19c and Figure 5.19d for discharged electrodes).

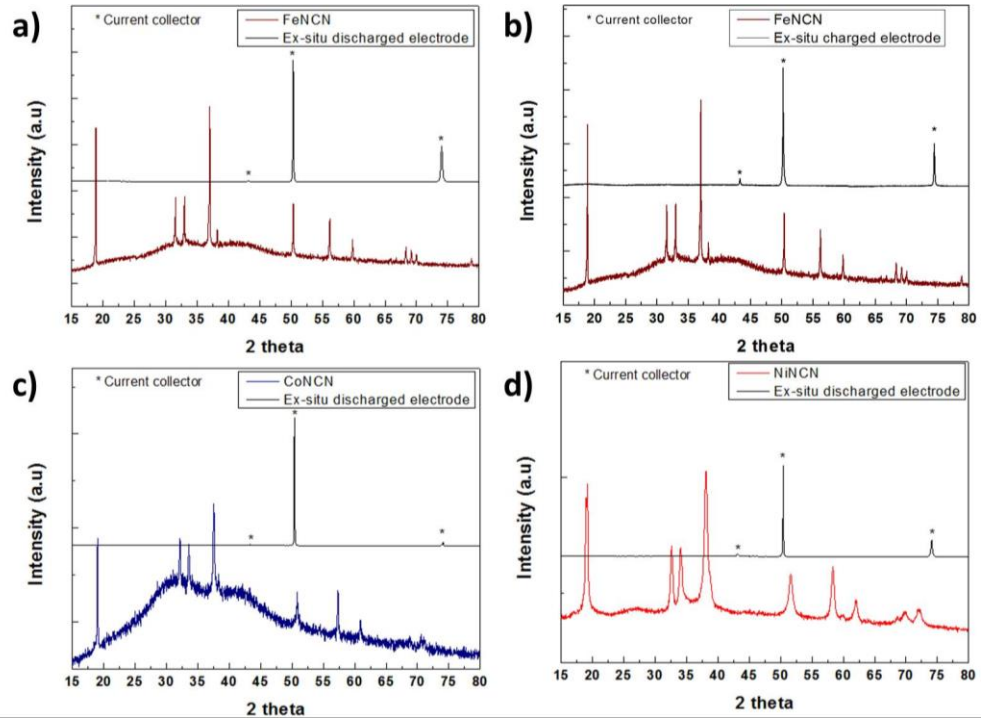

Figure 5.19. *Ex-situ* XRD for the discharge (a) and charge (b) of FeNCN and discharged electrodes of CoNCN (c) and NiNCN (d) with the respective synthesized powders.

For lithium ion batteries, two main processes occurred in the first galvanostatic discharge in iron, cobalt and nickel carbodiimides (Figure 5.20a). From 2 V *vs* Li^+/Li to 0.9 V *vs* Li^+/Li, a solid solution process was observed probably due to the adsorption of lithium ions in the carbon. This process was more pronounced for FeNCN because the plateaux of cobalt and nickel carbodiimide were at higher voltage and this process overlapped with the main redox process. This process was also observed for carbon measurement in Chapter 4 (Figure 4.17). A long plateau at 0.8 Volts *vs* Li^+/Li in the case of FeNCN, at 0.9 V *vs* Li^+/Li for CoNCN and at 1.05 V *vs* Li^+/Li in the case of NiNCN appeared. These plateaux could correspond to the conversion reaction of the transition metal carbodiimides reducing into metallic nanoparticles and embedded in a Na_2NCN matrix. A small *pseudo*-plateau at aproximately 2.1 V *vs* Li^+/Li during charge was observed for all the carbodiimides. These plateaux are more clearly identified in the $\delta Q/\delta V$ plots (Figure 5.20b). Reversible capacities close to the theoretical ones were obtained (540 mAh/g, 570mAh/g and 550 mAh/g for FeNCN, CoNCN and NiNCN respectively) in the first cycle. This electrochemical behavior of the first cycle was also in good agreement with those reported for oxides by *P. Poizot et al.*[19]. During the second discharge, the voltage of the plateau of these carbodiimides increased as it can be seen in Figure 5.20. This fact was attributed to lithium-driven structural modifications by TEM analysis in CoO by P. Poizot et al.[19].

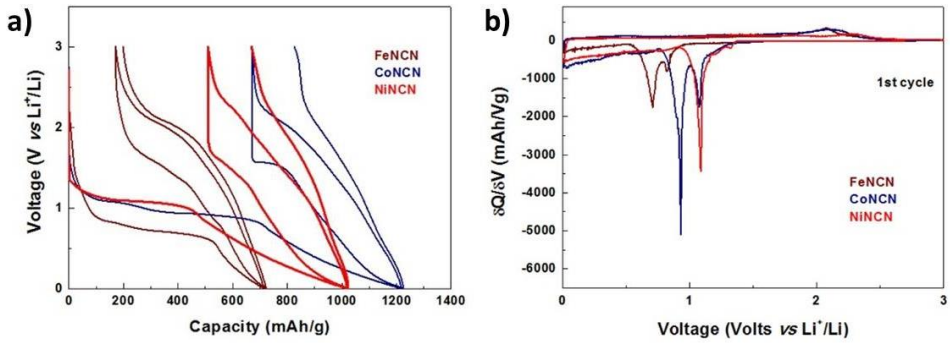

Figure 5.20. First two galvanostatic cycles (a) and first cycle differencial capacity (b) for sodium ion batteries of iron carbodiimide using metallic sodium as reference and counter electrode in range of the 0.005-3.0 Volts *vs* Na^+/Na.

The reaction mechanism of FeNCN has been recently reported by M. T. Sougrati et al.[25] The disappearance of the reflections during the discharge process did not allow characterizing the material by *in-situ* PXRD. However, Mössbauer *in-situ* analysis provided the information of the changes in the iron oxidation state and environment *in-situ* during the cycling. The main component of the pristine sample was a magnetic octet, due to the interaction of small quadrupolar moment with the low magnetic field presented in the sample as FeNCN is antiferromagnetic at room temperature (Zeeman Effect), where just five signals were resolved. Upon cycling, it was observed that the spectra changed to two different doublets which Sougrati et al suggested that was indicative that the full conversion to Li_2NCN/Fe^0had occurred. Besides, the lower value of hyperfine magnetic field could match with the amorphization of the FeNCN phase during the galvanostatic cycling. However, upon charge, it was observed that doublets which corresponded to iron nanoparticles were still presented in the charged electrode. This could explain why the full capacity of the plateau was not recovered during the charge.

It is worth noting that the cyclability was quite good for FeNCN; keeping after 100 cycles, a 80% of the initial capacity, i.e. 450 mAh/g (Figure 5.21a) while for FeO less than 50% of the capacity was achieved for the first 50 cycles[19] but the electrochemical curve is similar to iron oxide (FeO) as *M.V. Reddy et al*.[36] reported. For lithium ion batteries, the small volume expansion (62.56%) can be also the reason for the stability of the capacity that other compounds that work through conversion reaction do not reach. This volume change is quite low compared to the calculated for sulphides (55-125%), oxides (60-130%) and phosphides (125-250%)[16] all of which are compounds close to carbodiimides in terms of capacity and voltage plot. Other compounds such as fluorides and chlorides have lower volume expansion than carbodiimides in lithium ion batteries but they operate at higher voltages (such as 2.0-2.5 Volts *vs* Li^+/Li) so iron carbodiimide seems to be a promising candidate for lithium ion battery of the anodes working through conversion reactions as well.

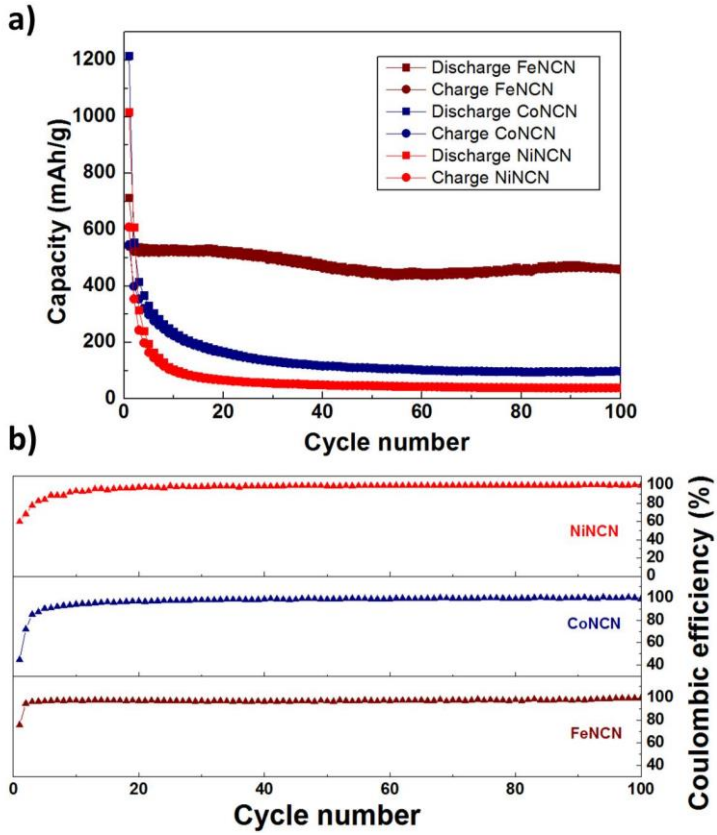

Figure 5.21. Cyclability of iron (brown), cobalt (blue) and nickel (red) carbodiimides (a) and the coulombic efficiency of the three materials (b) for lithium ion batteries in the voltage range of 0.005-3.0 Volts *vs* Li^+/Li.

The cyclability of CoNCN and NiNCN was as short as previously experimented in sodium ion batteries (Figure 5.21b y Figure 5.21c). Unlike the good cyclability of CoO in the study reported by *P. Poizot et al.*[19] in lithium ion batteries, a big capacity loss was observed for CoNCN and NiNCN in the first few cycles; obtaining in the first charge around 550 mAh/g. The capacity faded rapidly to 200 mAh/g in the cycle number 10 and even more rapidly for NiNCN, maybe due its larger volume expansion (75.02% for NiNCN instead of 66.67% of CoNCN). From cycle number 40 the capacity of both compounds was diminished to less than 100 mAh/g which could be mostly attributed to the carbon contribution. This carbon contribution was more or less stable up to one hundredth cycle. Concomitant to that capacity fading, the voltages of the discharge plateau of CoNCN and NiNCN decreased to 0.15 Volts *vs* Na^+/Na probably because the activity from cycle number 10 was mainly due to the carbon. Considering the overall electrochemical performance exhibited by cobalt and nickel carbodiimides, they do not seem suitable for secondary batteries because the reversibility of the redox reactions was really small. However, in the first cycle the capacity

is close to the theoretical one. Therefore, these compounds could be good anode materials for a primary battery for both sodium and lithium ion batteries in spite the fact that this was not the aim of this work. In LIB, the difference in cyclability could be attributed to the different particle size of the pristine materials in the electrodes or of the metallic particles formed during the first discharge which can cause difficulties in the conversion reactions.

5.1.3 Comparison of the electrochemistry of transition metal-carbodiimides

5.1.3.1 Electrochemical discussion

The electrochemical measurements of transition metal carbodiimides were all carried out in the same conditions, and considering the lack of crystallinity observed in all the materials at the end of the first discharge, it can be deduced that the same conversion reaction mechanism operates in all the compounds. However, different results in terms of polarization, capacity and average working voltage were obtained for each of them (Figure 5.22).

MnNCN has a voltage plateau very close to 0 Volts *vs* Na^+/Na and FeNCN, CoNCN and NiNCN exhibit a plateau at higher voltages, nevertheless this lower voltage goes with a very large polarization as observed in Figure 5.22 the largest among all T^MNCN. This fact also causes that MnNCN needs more conducting additive to reduce the ohmic polarization of the material and, in that way, avoid the possible sodium electroplating that can occur before the conversion reaction. This result is similar to that observed in the zinc carbodiimide compound. So, in order to have a comparative study of the electrochemistry of all the transition metal carbodiimides, Ketjen Black was added to all the carbodiimides when tested vs Na. It is important to note that this addition was not necessary for the studies in lithium. The kinetic of lithium ions leads to a reduction of the polarization. This fact avoids the problems experimented in SIB for making electrochemical active compounds that reacted by conversion reactions. Dealing with Ketjen black, the surface of the carbon increased a lot and a solid solution process is observed at the beginning of the electrochemical process. The adsorption of sodium and lithium ions into the carbon layers was considered in this work.

Overall, considering the average voltage of reduction (Figure 5.22a) and oxidation as well as their hysteresis, FeNCN exhibited the best electrochemical properties for Na-ion batteries which also shows the best cyclablitily and the smallest irreversible capacity in the first cycle

The electrochemical results of transition-metal carbodiimides are compared with analogue oxides (FeO, CoO and NiO) due to the similar electrochemical curves obtained in lithium ion batteries[19]. While the galvanostatic cycling and cyclability of FeNCN improved the electrochemical properties of FeO; cobalt and nickel carbodiimide show similar galvanostatic cycling in the first cycles but very bad cyclability. Two main reasons were considered to rationalize this phenomenon (process): i) the volume expansion whose the values are not so high (66-75% for LIB and 82-92% for NIB) but can have an important influence in the cyclability of these material; and ii) the different particle size of the metallic nanoparticles formed in the conversion reactions. These problem are related to the charge process because the subsequence discharge capacity achieves always similar values of capacity. In addition, the average voltage of the charge and discharge processes was decreased because from cycle number 20 the capacity was attributed to the carbon for CoNCN and NINCN. This voltage decrease was not observed in MnNCN and FeNCN for sodium and lithium ion batteries (Figure 5.22a and Figure 5.22b respectively). The different particle size of the pristine materials could enhance the irreversibility of the first cycle inCoNCN and NiNCN. Therefore, CoNCN and NiNCN are proposed as good anode materials for primary batteries of sodium and lithium ion.

Considering the previous results, we will consider that the FeNCN carbodiimide is a suitable material to be tested as anode in a full cell. As a result, this experiment was attempted and it will be described Chapter 8.

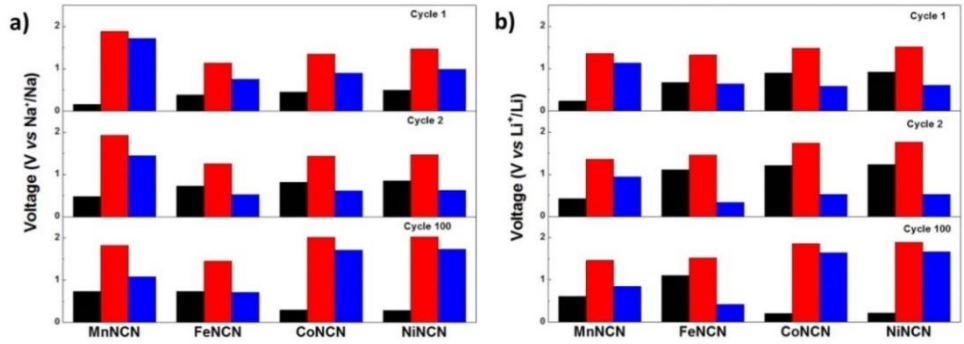

Figure 5.22. Bars diagram representing the average discharge voltage (black), charge voltage (red) and polarization (blue) in cycle 1 (above graph), cycle 2 (middle chart) and cycle 100 (bottom plot) of MnNCN, FeNCN, CoNCN and NiNCN for sodium (a) and lithium (b) ion batteries.

Considering the previous results we can deduce that in the case of carbodiimides amorphization of the material and formation of metallic nanoparticles and sodium or lithium carbodiimide matrix can occur in the first discharge. The conversion reaction of

these metallic nanoparticles inside the sodium/lithium carbodiimide matrix into amorphous transition metal carbodiimides could be the reason for the bad reversibility observed in the CoNCN and NiNCN phases. The major drawback of conversion reactions is their poor kinetics showed in the electrochemical reactions. This means that the rate at which lithium ions and electrons can reach the interfacial regions in the nanoparticle reacting with the active domains. This directly implies the large separation of the voltage in charge and discharge process causing a low energy efficiency of the electrodes. This drawback results in even worse electrochemical performance in SIBs.

XRD diffraction is not the best technique to follow the structural changes upon cycling due to the disappearance of the carbodiimide reflections in the fully discharged stage, which did not reappear after the galvanostatic charge. This is in agreement with the study by *P. Poizot et al.* [19] where the *in-situ* PXRD experiment only shows the diminishing of the cobalt oxide (CoO) reflections without reappearing after the charge process. This is attributed to the amorphization of the material which can cause the increment of the voltage observed in the second discharges of all the carbodiimides. In the case of the CoO electrodes during cycling, it is observed that a matrix of lithium oxide (Li_2O) is formed during the process.

5.1.3.2 Thermodynamic discussion

The electrochemical reactions proposed to take place with the carbodiimides in sodium and lithium ion batteries are described in Equations 5.1 and 5.2 respectively.

$$TMNCN + 2Na^+ + 2e^- \leftrightarrow Na_2NCN + TM \qquad (5.1)$$

$$TMNCN + 2Li^+ + 2e^- \leftrightarrow Li_2NCN + TM \qquad (5.2)$$

According to the second law of thermodynamics, all systems naturally tend to achieve the minimum of Gibbs free energy. Gibbs free energy is the thermodynamic potential which is minimized at chemical equilibrium and its kinetics are described by a constant (K) of the reaction. This constant is correlated with the voltage of the cell as indicated in Equation 5.4. So, the voltage and the Gibbs free energy of the electrochemical reactions are linked through Equations 5.3 and 5.4. The Gibbs free energy of the electrochemical reactions of transition-metal carbodiimides could easily be calculated through the theoretical values of the products and reactants. Unluckily, given the recent synthesis of transition-metal carbodiimides (first report in 2005) their Gibbs free energy had not been previously reported. Moreover, only one theoretical study reports the enthalpy of formation for T^MNCN (T^M= Mn^{2+}, Fe^{2+}, Co^{2+}, Ni^{2+}, Cu^{2+})[37]. That study predicts that these compounds are

metastable through the calculated enthalpy from the elemental state. This fact suggests that the preparation of these compounds could not be carried out from the starting elements. Therefore, in order to obtain these metastable compounds[1,3,4,5,8], the syntheses developed in this work have been performed from metastable intermediates. This fact is in agreement with the difficulties observed during the synthesis to obtain the hydrogen cyanamide of these compounds, especially in the preparation of $Fe(HNCN)_2$.

$$lnK = \frac{zFE}{RT} \qquad (5.3)$$

$$\Delta G_{reaction} = -RTlnK = -zFE \qquad (5.4)$$

As the calculations of the Gibbs Energy have not been performed yet for these compounds, the experimental electrochemical curves at room temperature have been studied in this work. Therefore, following the Gibbs energy -voltage correlation, it should be possible to calculate the Gibbs energy of T^MNCN (T^M= Mn^{2+}, Fe^{2+}, Co^{2+}, Ni^{2+}, Cu^{2+}), Na_2NCN and Li_2NCN from experimental voltage values. However, it is important to take into account that these calculations have one experimental error which is based on the intrinsic overpotential that these materials show in their electrochemical behavior. And it is worth noting that the overpotential observed in the materials which operate through conversion reactions can be very large.

In order to obtain the voltage from the electrochemistry, the most intense peaks of the first cycle δQδV of all T^MNCN (T^M= Mn^{2+}, Fe^{2+}, Co^{2+}, Ni^{2+}, Cu^{2+}) were considered (Figure 5.23). The approximate voltage values for sodium and lithium ion batteries are listed in Table 5.3 as well as the corresponding Gibbs free energies calculated from equation 5.5. Figure 5.23 shows a small increment of voltage with the number of 3*d* electrons from MnNCN to CuNCN. It is also important to mention that CuNCN in sodium ion batteries does not follow this tendency. This fact could be due to the higher polarization observed in the galvanostatic cycling. Also linked to the observed kinetic problems of CuNCN for SIB could explain the reason why this material does not follow the tendency while it is doing for LIB. The same tendency can be observed in lithium ion batteries. However, the voltage at which these batteries operate is higher than the sodium ion batteries and likewise the Gibbs free energy of the reaction with lithium is also larger. Figure 5.24 is a schematic overview summarizing the energies of reaction as deduced from the experimental electrochemical data, neglecting the contribution of the entropy. It is observed that the Gibbs energy values for the conversion reactions of Transition-Metal Carbodiimides for sodium ion batteries are quite similar to the theoretical/experimental enthalpy values reported by *M. Launey and R. Dronskowski*[37]. As the contribution of the entropy term to the Gibbs free energy is usually

much lower compared to the enthalpy term at room temperature, it can be considered correct that the enthalpy values are similar to the Gibbs energy of each Transition-Metal Carbodiimide (Equation 5.5 and 5.6).

$$\Delta G_{reaction} = \Delta H - T\Delta S \quad (5.5)$$

So if $\Delta S <<< \Delta H_f$:

$$\Delta G_{reaction} = \Delta H_f - T\cancel{\Delta S} = \Delta H_f \quad (5.6)$$

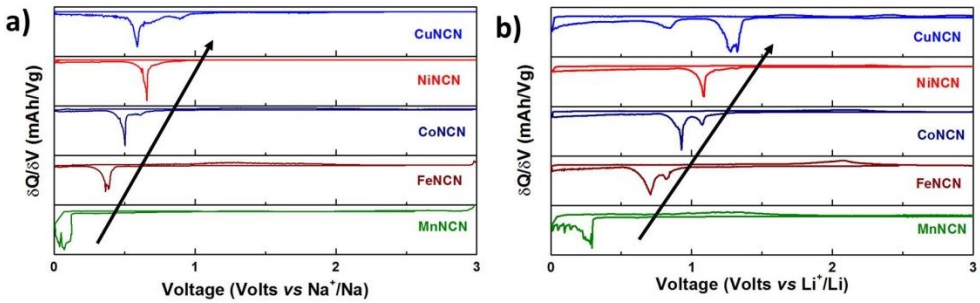

Figure 5.23. First cycle δQδV of T^MNCN (T^M= Mn^{2+}, Fe^{2+}, Co^{2+}, Ni^{2+}, Cu^{2+} and Zn^{2+}) for sodium (a) and lithium (b) ion batteries.

Table 5.3. Experimentally observed voltage of reduction of the Transition-Metal Carbodiimides in sodium and lithium ion batteries and the reported values for the theoretical enthalpy.

Material	**Voltage** V *vs* Na^+/Na	**ΔG** KJ/mol	**Voltage** V *vs* Li^+/Li	**ΔG** KJ/mol	**Voltage** V (Li-Na)	**ΔG (Li-Na)** KJ/mol	***ΔHf [37]*** *KJ/mol*
MnNCN	0.2	-38.6	0.3	-57,9	0.1	19.3	*44.8*
FeNCN	0.4	-77.2	0.75	-144.75	0.35	67.55	*77.3*
CoNCN	0.5	-96.5	0.9	-173.7	0.4	77.2	*101.5*
NiNCN	0.65	-125.45	1.1	-212.3	0.45	86.85	*123.8*
CuNCN	0.6	-115.8	1.25	-241.25	0.65	115.8	*144.8*

We can conclude from Table 5.3 that the Gibbs energy of Na_2NCN could be at slightly lower energy values than the elemental level indicating that the attainment of Na_2NCN from its elements is thermodinamicaly possible. Moreover, the similar values of $\Delta H_f \sim \Delta G$ and the effect of the overpotential indicate that Gibbs energy of Na_2NCN is negative. Hence, the formation of Na_2NCN from each Transition-Metal carbodiimide and elemental sodium is possible and spontaneous in the electrochemical cell, as experimentally shown in the discharge. The contrary is observed during the charge process.

These results can explain the electrochemically inactivity observed in crystalline manganese carbodiimide. The small difference in Gibbs energy of MnNCN and Na_2NCN, causes that the voltage of conversion reaction is close to 0 Volts, as it was observed experimentally. So that,

making a good carbon coating is very important and this could explain why when coating MnNCN just with Carbon Super C65, the electrochemistry did not work properly. The addition of Ketjen black, which shows higher conductivity and surface area[11] because its structure is very similar to graphite, is essential to make MnNCN electrochemically active because the better conductivity of the sample causes the reduction of the ohmic polarization of the MnNCN and avoids that the Mn^{2+} reduction to Mn^0 is taking place at higher voltages (0.2 Volts *vs* Na^+/Na) than the sodium electroplating. This problem is not appearing for lithium ion batteries due to the higher voltage (0.3 Volts *vs* Li^+/Li) at which the reaction takes place $\Delta G_{reaction} = \Delta H_f - T\Delta S = \Delta H_f$

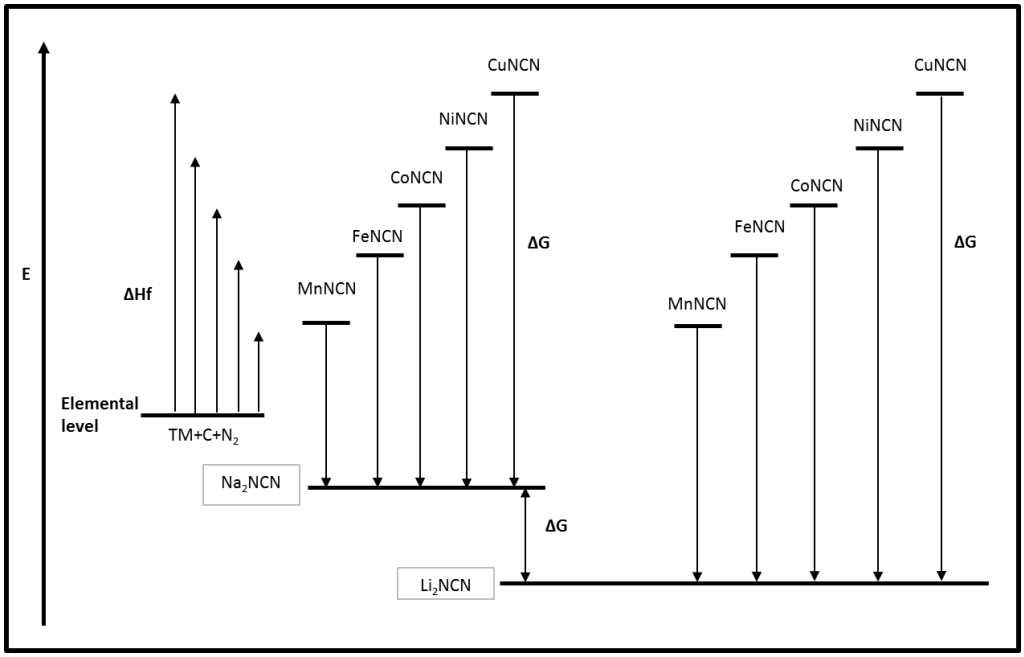

Figure 5.24. Schematic of the energy level of elements and transition-metal including those of sodium and lithium carbodiimides according to the observed electrochemical reduction of the Transition-Metal Carbodiimides.

$$Na_2NCN + 2\,Li^+ \leftrightarrow Li_2NCN + 2\,Na^+ \qquad (5.7)$$

As a result of these considerations, the formation of Na_2NCN and Li_2NCN has negative Gibbs free energy value so they should be spontaneously formed from their elements; however this synthetic route has never been attempted. Also, the difference in voltage between lithium and sodium carbodiimides (0.38 Volts) indicates that lithium carbodiimide is more stable than sodium carbodiimide and thus, if Na_2NCN were reacted with Li^+, Li_2NCN would form (equation 5.7). Moreover, the average difference in voltage between reacting with

lithium and with sodium is about 0.38 Volts (Figure 5.23) which is much smaller from the 0.96 Volts observed theoretically in the lithium *vs* sodium difference in oxides[16].

5.2 Conclusions

$T^{M}NCN$ (T^{M}= Mn, Fe,Co and Ni) were synthesized avoiding the exposure to the air by Schlenk techniques. The success of the synthesis was characterized through PXRD as a single phase and checking the -N=C=N- functionalities by IR bands which agree with the reported values in the literature for these compounds. It was observed by SEM that the cobalt and nickel carbodiimide have more regular platelet shape, while iron carbodiimide has more irregular shape, smaller particle size and heterogeneous distribution. The laminates of carbodiimides samples were homogeneous as it was proved by SEM measurements.

The electrochemical activity of these materials was proved and shown for the first time for SIB and LIB. Theoretical capacity values were reached in the first cycle for all of them considering a conversion reaction where 2 electrons per T^{M} are involved. Moreover, the voltages at which the processes are taking place (0.1-0.7 Volts for SIB and 0.3-1.25 Volts for LIB) are suitable for anode materials and agree with the thermodynamic discussion. However, the cyclability of the materials is quite different. Manganese and iron carbodiimide exhibited good cyclability being able to keep about 80% of the initial capacity in the cycle 100 for SIB and LIB. Nevertheless, in cobalt and nickel carbodiimides a high capacity fading was observed where capacity values drastically decreased from the theoretical values (~550 mAh/g) to the small capacity assigned to the carbon contribution in less than 20 cycles. *Ex-situ* XRD analysis of discharged electrodes did not provide any reflection of the reaction products, suggesting a conversion reaction mechanism. However, the similar electrochemical behavior of transition metal carbodiimide than the studied in the analogues transition metal oxides, allow us to guess what is happening inside the battery. So, this work suggests that in the first discharge the amorphization and conversion reaction was taken place and since then the electrochemical activity is attributed to the conversion process of amorphous material. The smaller polarization, less irreversible capacity in the first cycle and the good cyclability and capacity values make FeNCN a promising candidate as anode material for sodium ion batteries.

From the experimental voltages of reduction of the $T^{M}NCN$ (T^{M}= Mn^{2+}, Fe^{2+}, Co^{2+}, Ni^{2+} and Cu^{2+}) in the first cycle, an approximation of the values of the Gibbs free energy of reaction were performed. This study provides a good agreement with the theoretical/experimental enthalpy of formation of the $T^{M}NCN$. The formation of the discharged products (Na_2NCN and Li_2NCN) was concluded as thermodynamically favored.

5.3 References

[1] X. Liu, M. Krott, P. Müller, C. Hu, H. Lueken and R. Dronskowski; "Synthesis, Crystal Structure, and Properties of MnNCN, the First Carbodiimide of a Magnetic Transition Metal"; *Inorg. Chem.;* 2005, **44** (9), 3001.

[2] M. Krott, A. Houben, P. Muller, W. Schweika and R. Dronskowski; "Determination of the magnetic structure of manganese carbodiimide with diffraction experiments using polarized neutrons "; *Phys. Rev. B;* 2009, **80**, 024117.

[3] X. Liu, L. Stork, M. Speldrich, H. Lueken and R. Dronskowski; "FeNCN and $Fe(NCNH)_2$: Synthesis, Structure, and Magnetic Properties of a Nitrogen-Based Pseudo-oxide and -hydroxide of Divalent Iron"; *Chem. Eur. J.* 2009, **15**, 1558.

[4] M. Krott, X. Liu, P. Muller and R. Dronskowski; "Synthesis and structure determination of Co(HNCN)2 and Ni(HNCN)2"; *J. Solid State Chem.* 2007, **180,** 307.

[5] X. Tang, A. Houben, X. Liu, L. Stork and R. Dronskowski; "Crystal Structure Refinement of $M(NCNH)_2$(M = Fe, Co) Based on Combined Neutron and X-ray Diffraction Data"; *Z. Anorg. Allg. Chem.* 2011, **637,** 1089.

[6] M. Krott, X. Liu, B. P. T. Fokwa, M. Speldrich, H. Lueken and R. Dronskowski; "Synthesis, Crystal-Structure Determination and Magnetic Properties of Two New Transition-Metal Carbodiimides: CoNCN and NiNCN"; *Inorg. Chem.* 2007, **46**, 2204.

[7] L. H. Ahrens; "The use of ionization potentials Part 1. Ionic radii of the elements"; *Geochim. Cosmochim. Acta*, 1952, **2** (3), 155.

[8] X. Liu, M. A. Wankeu, H. Lueken and R. Dronskowski "A Novel Method for Synthesizing Crystalline Copper Carbodiimide, CuNCN. Structure Determination by X-Ray Rietveld Refinement."; *Z. Naturforsch.* 2005, **60b**, 593.

[9] K. Morita, G. Mera, K. Yoshida, Y. Ikuhara, A. Klein, H. J. Kleebe and R. Riedel; "Thermal stability, morphology and electronic band gap of Zn(NCN)."; *Solid State Sci.* 2013, **23**, 50.

[10] B. Milke, C. Wall, S. Metzke, G. Clavel, M. Fichtner and C. Giordano; "A simple synthesis of $MnN_{0.43}$@C nanocomposite: characterization and application as battery material"; *J. Nanopart. Res.* 2014, **16**, 2795.

[11] Jung-Ki Park; "Principles and Applications of Lithium Secondary batteries", Wiley-VCH Verlag &Co., Weinheim, Germany. 2012.

[12] J. Cui, C. Qing, Q. Zhang, C. Su, X. Wang, B. Yang and X. Huang; "Effect of the particle size on the electrochemical performance of nano-Li_2FeSiO_4/C composites" *Ionics* 2014, **20**, 23.

[14] B. Jache, J. O. Binder, T. Abe and P. Adelhelm; "A comparative study on the impact of different glymes and their derivatives as electrolyte solvents for graphite co-intercalation electrodes in lithium-ion and sodium-ion batteries"; *Phys. Chem. Chem. Phys.*, 2016, **18**, 14299.

[17] M. A. Lowe, J. Gao and H. D. Abruña; "*In operando* X-ray studies of the conversion reaction in Mn_3O_4 lithium battery anodes"; *J. Mater. Chem. A*, 2013, **1**, 2094.

[18] Y. Ma and S. H. Garofalini; *J. Am. Chem. Soc.*, 2012, **134** (19), 8205.

[19] P. Poizot, S. Laruelle, S. Grugeon, L. Dupont and J. M. Tarascon; "Nano-sized transition-metal oxides as negative-electrode materials for lithium-ion batteries"; *Nature* 2000 , **407** , 496.

[20] J. Cabana, L. Monconduit, D. Larcher and M. R. Palacin; "Beyond Intercalation-Based Li-Ion Batteries: The State of the Art and Challenges of Electrode Materials Reacting Through Conversion Reactions" *Adv. Mater.* 2010, **22**, E170.

[21] P. G. Bruce, B. Scrosati and J. M. Tarascon; "Nanomaterials for Rechargeable Lithium Batteries"; *Angew. Chem. Int. Ed.;* 2008, **47**, 2930.

[22] S. W. Kim, D. H. Seo, X. Mua and G. Ceder; "Electrode Materials for Rechargeable Sodium-Ion Batteries: Potential Alternatives to Current Lithium-Ion Batteries"; *Adv. Energy Mater.*, 2010, **2,** 710.

[23] S. Komaba, T. Mikumo, N. Yabuuchi, A. Ogata, H. Yoshida, and Y. Yamada;" Electrochemical Insertion of Li and Na Ions into Nanocrystalline Fe_3O_4 and α-Fe_2O_3 for Rechargeable Batteries" *J. Electrochem. Soc.*, 2010, **157**, A60.

[24] Z. Jian, B. Zhao, P. Liu, F. J. Li, M. B. Zheng, M. W. Chen, Y. Shi and H. S. Zhou; "Fe_2O_3 nanocrystals anchored onto graphene nanosheets as the anode material for low-cost sodium-ion batteries"; *Chem. Commun.*, 2014, **50**, 1215.

[25] M. T. Sougrati, A. Darwiche, X. Liu, A. Mahmoud, R. P. Hermann, S. Jouen, L. Monconduit, R. Dronskowski and L. Stievano; "Transition-Metal Carbodiimides as Molecular Negative Electrode Materials for Lithium- and Sodium-Ion Batteries with Excellent Cycling Properties"; *Angew. Chem. Int. Ed.*, 2016, **55** (16), 1.

[26] F. Klein, B. Jache, A. Bhide and P. Adelhelm; "Conversion reactions for sodium-ion batteries" *Phys. Chem. Chem. Phys.,* 2013, **15**, 15876.

[27] P. G. Bruce, B. Scrosati and J. M. Tarascon; "Nanomaterials for Rechargeable Lithium Batteries"; *Angew. Chem. Int. Ed.;* 2008, **47**, 2930.

[32] J. Zhang, T. Huang, Z. Liu and A. Yu; "Mesoporous Fe_2O_3 nanoparticles as high performance anode materials for lithium-ion batteries"; *Electrochemistry Communications,* 2013, **29**, 17.

[33] K. He, F. Lin, Y. Zhu, X. Yu, J. Li, R. Lin, D. Nordlund, T. C. Weng, R. M. Richards, X. Q. Yang, M. M. Doeff, E. A. Stach, Y. Mo, H. L. Xin and D. Su; "Sodiation Kinetics of Metal Oxide Conversion Electrodes: A Comparative Study with Lithiation" *Nano Lett.*, 2015, **15** (9), 5755.

[34] H. Jia, R. Kloepsch, X. He, M. Evertz, S. Nowak, Jie Li, M. Winter and T. Placke; "Nanostructured $ZnFe_2O_4$ as Anode Material for Lithium-Ion Batteries: Ionic Liquid-Assisted Synthesis and Performance Evaluation with Special Emphasis on Comparative Metal Dissolution" *Acta Chim. Slov*. 2016, DOI: 10.17344/acsi.2016.2243.

[35] F. Wang, R. Robert, N. A. Chernova, N. Pereira, F. Omenya, F. Badway, X. Hua, M. Ruotolo, R. Zhang, L. Wu, V. Volkov, D. Su, B. Key, M. S. Whittingham, C. P. Grey, G. G. Amatucci, Y. Zhu and J. Graetz; "Conversion Reaction Mechanisms in Lithium Ion Batteries: Study of the Binary Metal Fluoride Electrodes" *J. Am. Chem. Soc.*, 2011, **133** (46), 18828.

[36] M. V. Reddy, G. V. Subba Rao and B. V. R. Chowdari; "Metal Oxides and Oxysalts as Anode Materials for Li Ion Batteries"; *Chem. Rev.*, 2013, **113**, 5364.

[37] M. Launey and R. Dronskowski, "A Theoretical Study on the Existence and Structures of Some Hypothetical First-Row Transition-Metal M(NCN) compounds" *Z. Naturfosch.* 2005, **60b**, 437.

6- Structural and electrochemical characterization of $Co_{1-x}Fe_xNCN$

In this chapter, the structural and electrochemical characterization of the solid solution $Co_{1-x}Fe_xNCN$ (x=0.36 and x=0.46) are analyzed and compared to the end members x=0 and x=1). These compositions are herein reported for the first time and thus a more detailed analytical, structural study (including electron diffraction) and physicochemical characterization such as magnetic and Mossbauer measurements was performed. The goal of synthetizing these phases was to optimize the electrochemical performance by combining the good electrochemical stability of FeNCN for both SIB and LIB and the higher capacity observed in the first cycles for isostructural CoNCN.

6.1 Results and discussion

6.1.1 Elemental analysis

Both samples of the solid solution ($Co_{1-x}Fe_xNCN$) were analyzed by ICP-AES.. The stoichiometry of the samples was characterized as $Co_{0.54}Fe_{0.46}NCN$ and $Co_{0.64}Fe_{0.36}NCN$ after an acidic digestion of the samples.

The nominal amounts of iron and cobalt hydrogencynamide that were used for the reaction can be seen in Table 6.1 and compared with the experimental values obtained from ICP-AES.

Table 6.1. Comparison of the percentage of the weighted of cobalt and iron hydrogenocynamides compared to the observed by ICP-AES analysis.

Sample	Weighting proportion of Co	Experimental ICP-AES
$Co_{0.54}Fe_{0.46}NCN$	0.503	0.537
$Co_{0.64}Fe_{0.36}NCN$	0.670	0.640

The differences in these values could be attributed to the amount of each metal that could be lost during the washing procedure of unreacted precursors.

6.1.2 Structural and physicochemical characterization of $Co_{0.64}Fe_{0.36}NCN$ and $Co_{0.54}Fe_{0.46}NCN$

6.1.2.1 Powder X-Ray Diffraction

Powder X-Ray Diffraction patterns of the $Co_{0.64}Fe_{0.36}NCN$ and $Co_{0.54}Fe_{0.46}NCN$ samples were recorded at room temperature in the same conditions. This way, practically the same background was obtained making easier to compare the samples of $Co_{1-x}Fe_xNCN$ solid solution and the extremes FeNCN and CoNCN compounds (). However, it was observed that CoNCN exhibited a higher increment of the background due to the presence of fluorescence in the range 25-35 ° of 2 theta.

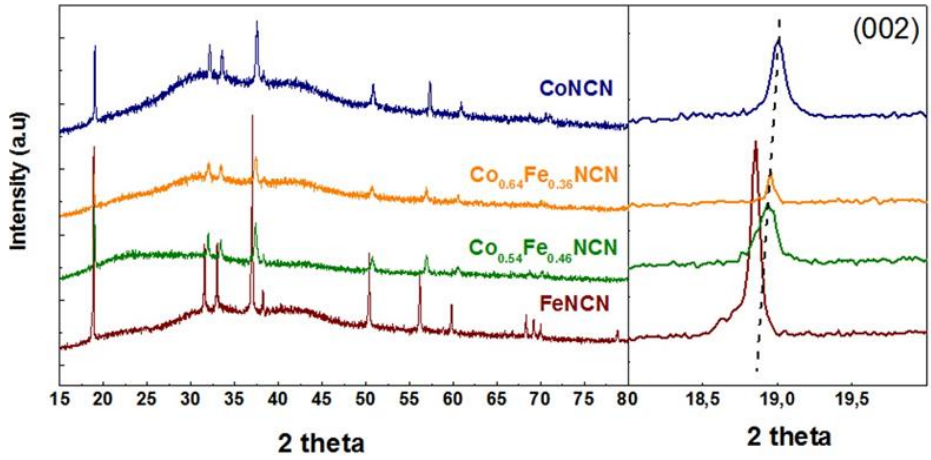

Figure 6.1. Diffractograms of FeNCN (brown), $Co_{0.64}Fe_{0.36}NCN$ (orange), $Co_{0.54}Fe_{0.46}NCN$ (green) and CoNCN (blue) and the shift of the peak corresponding to the (002) interplanar distance.

Synthesis of both phases were carried out using $Fe(HNCN)_2$ and $Co(HNCN)_2$ as precursors. The carbodiimide compounds ($Co_{1-x}Fe_xNCN$) resembled the NiAs structure with the space group $P6_3/mmc$ (nº194). Diffractograms were quite similar showing a shift of most of the peaks (see right side of Figure 6.1) due to the smaller cell parameters of CoNCN compared to FeNCN. Rietveld refinement of $Co_{0.64}Fe_{0.36}NCN$ and $Co_{0.54}Fe_{0.46}NCN$ show that these phases were obtained as single phases (Figure A6.1 of the annex).

Samples with more cobalt content ($Co_{0.64}Fe_{0.36}NCN$) showed that the reflections corresponding to the (002) interplanar distances were shifted to bigger 2 theta values compared to FeNCN (). Therefore, the reflections of the samples of $Co_{1-x}Fe_xNCN$ (x=0.36 and 0.46) corresponding to (002) interplanar distances were in between FeNCN and CoNCN.

As it can be seen in Figure 6.2, there is a relationship between the cell parameters and the content of each transition metal in the solid solution samples (indicating the existence of a solid solution). Small differences in the *a* and *c* cell parameters were found. The difference in the cell parameters of FeNCN and CoNCN were attributed to the higher ionic radius of Fe^{2+} than Co^{2+} (both in high spin configuration)[1] as can be seen in Table 6.2 and discussed in Chapter 5.

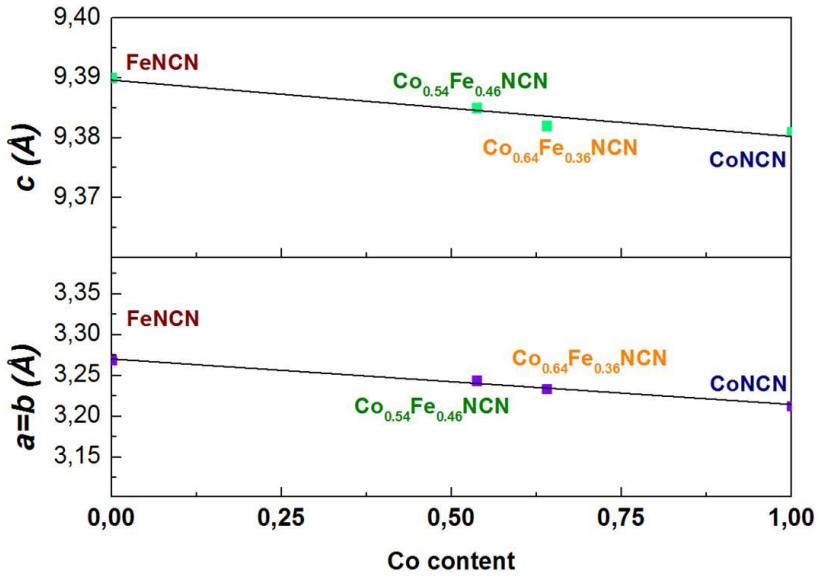

Figure 6.2. Plot of the relationship of the *a* and *b* cell parameters with the cobalt content in $Co_{1-x}Fe_xNCN$ (above) and the relationship with *c* cell parameter (bottom) according to Vegard´s law.

Table 6.2. Different in *a* (=*b*) and *c* cell parameters of $Co_{1-x}Fe_xNCN$ crystallized in $P6_3/mmc$ space group.

Material	*a*=*b* (Å)	*c* (Å)	Volume (Å^3)
FeNCN	3.269 (1)	9.390 (1)	87.60 (1)
$Co_{0.54}Fe_{0.46}NCN$	3.244 (2)	9.385 (8)	85.50 (2)
$Co_{0.64}Fe_{0.36}NCN$	3.234 (4)	9.382 (19)	84.93 (20)
CoNCN	3.213 (1)	9.381 (2)	83.64 (2)

In spite of the fact that there are few points representing the linear correlation of the cell parameters, $Co_{1-x}Fe_xNCN$ (x=0.36 and 0.46) samples matched quite well in linear interpolation. This is in agreement with the Vegard´s law and it suggests that samples with another composition in $Co_{1-x}Fe_xNCN$ would follow the tendency in the linear interpolation.

6.1.2.2 Transmission Electron Microscopy (TEM)

The morphology of the samples of $Co_{1-x}Fe_xNCN$ solid solution was analyzed by using TEM. In Figure 6.3a, it can be seen that the particles of CoNCN exhibited platelet form and more regular morphology. However, upon the increment of iron content in the solid solution the shape of particles changed to be less regular than the CoNCN counterpart. In Figure 6.3b and Figure 6.3c it can be observed that the heterogeneity increased with the amount of iron. Finally, in the FeNCN sample (Figure 6.3d) the regular shape of the platelets present in CoNCN was not observed and more heterogeneity of the particles was shown compared to CoNCN.

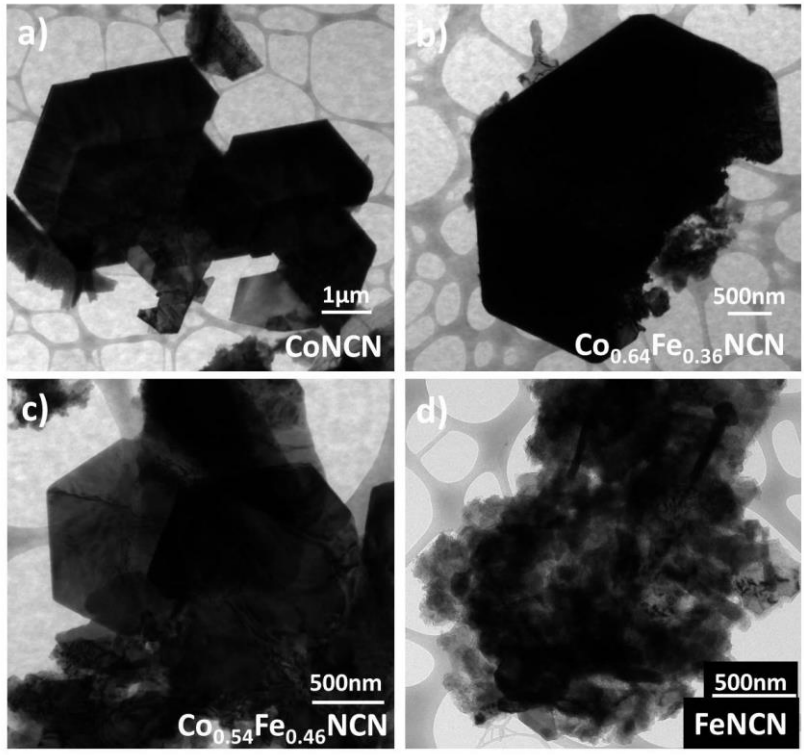

Figure 6.3. Low magnification TEM images of CoNCN (a), $Co_{0.64}Fe_{0.36}NCN$ (b), $Co_{0.54}Fe_{0.46}NCN$ (c) and FeNCN (d) where the morphology of particles is revealed.

From the electron diffraction, the characteristic planes of each sample were correspondingly indexed. The selected area for the electron diffraction patterns of the samples demonstrated that the recorded region was single crystal along the [001] direction for $Co_{0.64}Fe_{0.36}NCN$ (Figure 6.4a) and for $Co_{0.54}Fe_{0.46}NCN$ (Figure 6.4b). In order to compare both structures with the extremes of the solid solution, the characteristic planes were also indexed for CoNCN and FeNCN (Figure 6.4c and Figure 6.4d respectively).

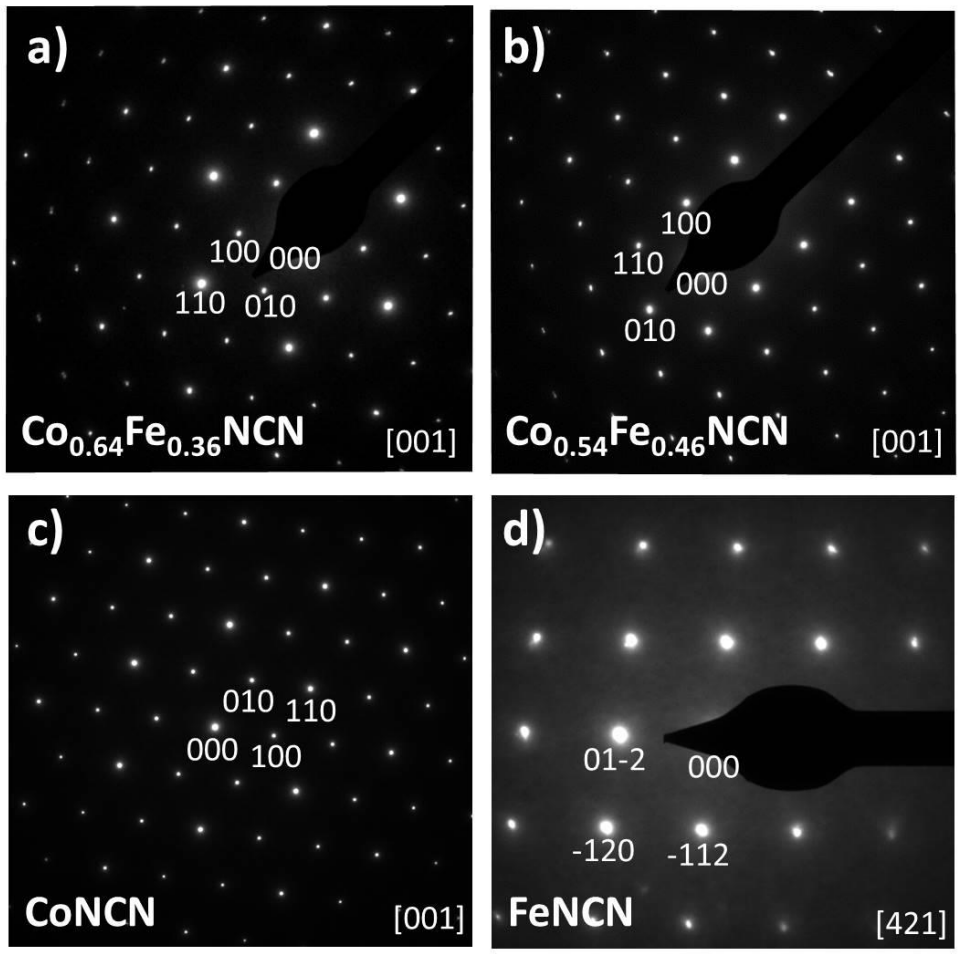

Figure 6.4. TEM images of $Co_{0.64}Fe_{0.36}NCN$ (a) and $Co_{0.54}Fe_{0.46}NCN$ (b) where the particle surface is observed and the electron diffraction of CoNCN (c) and FeNCN (d).

In addition, electron diffraction patterns did not show any extra reflection corresponding to a superstructure or any information about the ordering of Fe^{2+} and Co^{2+}. So, we concluded that there was a random ordering of these metal ions but there were not a large ordering of each metal as X-Ray diffraction just showed one phase.

6.1.2.3 Infrared spectroscopy

The infrared spectra of the $Co_{0.64}Fe_{0.36}NCN$, $Co_{0.54}Fe_{0.46}NCN$ were measured in order to see the most characteristic bands of carbodiimides.

The infrared spectra of solid solution samples including FeNCN and CoNCN samples for comparison are shown in Figure 6.5. The bands of the spectra of samples of the $Co_{1-x}Fe_xNCN$ solid solution were at similar values than FeNCN but some contributions in the position of the bands of CoNCN were also observed. The band corresponding to the asymmetric stretching of $Co_{0.54}Fe_{0.46}NCN$ appeared at 2125 cm^{-1} while $Co_{0.64}Fe_{0.36}NCN$ was shown at 2122 cm^{-1}. This could suggest that the C=N distances of NCN group was similar for all the described compounds. On the other hand, more differences in the deformation bands were observed. They appeared at around 650 cm^{-1}, close to the 648 cm^{-1} observed for CoNCN so the more cobalt content of these solid solutions could explain that the T^M-N distance should be more similar to the Co-N distance than the Fe-N distance.

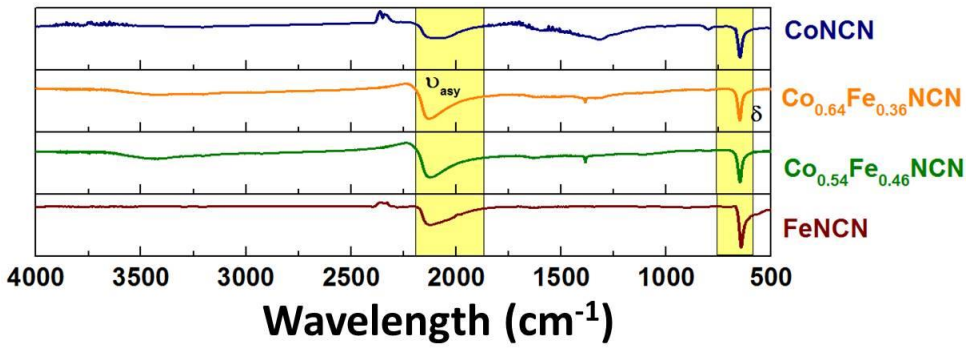

Figure 6.5. FTIR spectra in the range of 4000-500 cm^{-1} of CoNCN (blue line), $Co_{0.54}Fe_{0.46}NCN$ (green line), $Co_{0.64}Fe_{0.36}NCN$ (orange line) and FeNCN (brown line) are represented respectively from top to bottom.

As it was observed in the PXRD analysis, the more content of cobalt caused a decrease in cell parameters due to the smaller ionic radius. This fact affected in the T^M-N (T^M=Co or Fe) distance because was more similar to CoNCN than FeNCN. The higher values of frequency of deformation vibration mode observed for FeNCN could be attributed to the weaker Fe-N bond (bigger ionic radius and higher electropositivity of Fe^{2+}) compared to CoNCN.

6.1.2.4 Magnetic properties (SQUID)

The temperature dependence of the magnetic susceptibility for both samples of $Co_{1-x}Fe_xNCN$ solid solution showed small peaks. These peaks were just small changes in the tendency of the curve near room temperature. $Co_{0.54}Fe_{0.46}NCN$ showed (Figure 6.6a) this peak at 303K while $Co_{0.64}Fe_{0.36}NCN$ showed this peak at 283 K (Figure 6.6b). According to the literature, FeNCN[2] and CoNCN[3,4] showed Néel temperatures at 345 K and 252 K respectively (see Figure 6.7). Therefore, it was considered that the sample was antiferromagnetic ordered below 303 K and paramagnetic above that temperature.

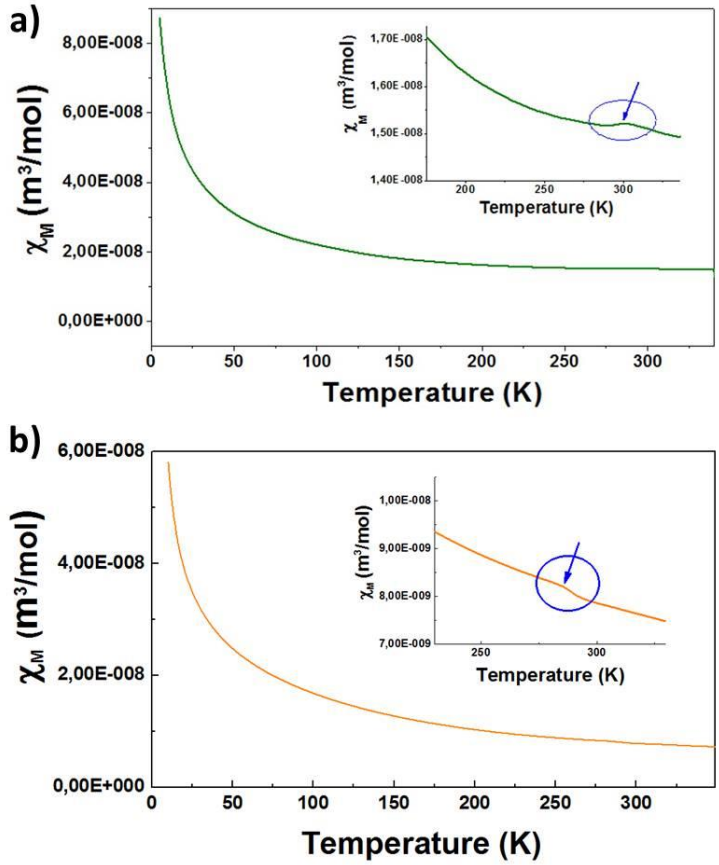

Figure 6.6. Field cooling using 1 KOe of magnetic field of $Co_{0.54}Fe_{0.46}NCN$ measured in the SQUID magnetometer with a zoom in the zone where the Néel temperatures seemed to appear.

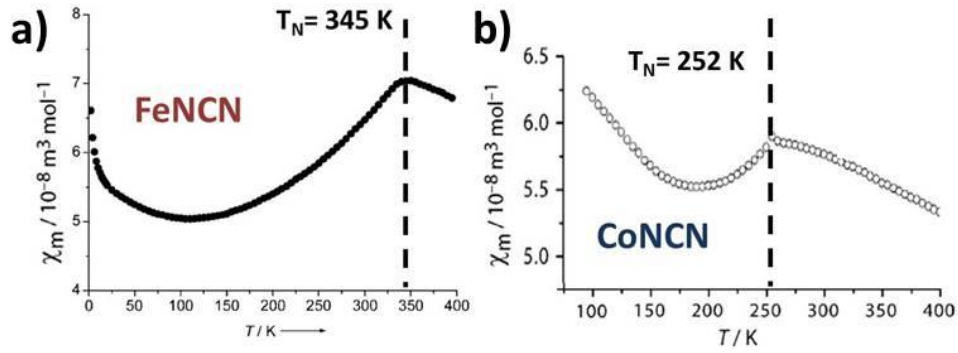

Figure 6.7. Iron[2] (a) and cobalt[3] (b) carbodiimide field cooling from 0 K and 100 K to 400 K respectively and the Néel temperatures pointed out for both compounds.

In the analysis of $Co_{0.64}Fe_{0.36}NCN$, similar conclusions could be obtained. The main difference was that sample was not antiferromagnetic at room temperature. This compound was antiferromagnetically ordered up to 283 K. Above that temperature, a paramagnetic behaviour was considered.

The bad resolution of these bands were in agreement with the mangetic properties experimented by FeNCN compound. In its measurement of susceptibility *vs* temperature, an increment of the magnetic field up to 1 Tesla and 2 Teslas was necessary in order to observe the transition temperature (Néel temperature) compared to the 1KOe (0.1 Tesla) used in this study[5].

Although the study of the magnetism of the samples of $Co_{1-x}Fe_xNCN$ solid solution did not provide a definitive result, the Néel temperature of these samples was considered to be 303 K and 283 K for $Co_{0.54}Fe_{0.46}NCN$ and $Co_{0.64}Fe_{0.36}NCN$ respectively.

6.1.2.5 Mössbauer spectroscopy

Mössbauer spectroscopy is a powerful technique to characterize compounds with nucleus such as iron or tin in the structure due to its high sensitivity to differences in the environment of Fe in the structure and its oxidation state.

The Mössbauer measurements of the samples of the $Co_{1-x}Fe_xNCN$ solid solution were carried out at room temperature. As it can be seen in Figure 6.8a, the spectrum of $Co_{0.54}Fe_{0.46}NCN$ showed the presence of a doublet and a quartet (but just a triplet is observed) not very well defined. This indicated that the magnetic ordering temperature was higher than room temperature. On the contrary, the spectrum of $Co_{0.64}Fe_{0.36}NCN$ (see

Figure 6.8b) exhibited the characteristic doublet of a paramagnetic state (just Quadrupole splitting) at same temperature. These results are in good agreement with the magnetic measurements described in the previous section, confirming that the Néel temperature should be lower than room temperature. It could also be observed that the doublet of the spectra of $Co_{0.64}Fe_{0.36}NCN$ was not as clear as that reported[5] for FeNCN above T_N (Figure 6.9). This could be due to the fact that the Néel temperature (283 K) is close to room temperature (~293 K).

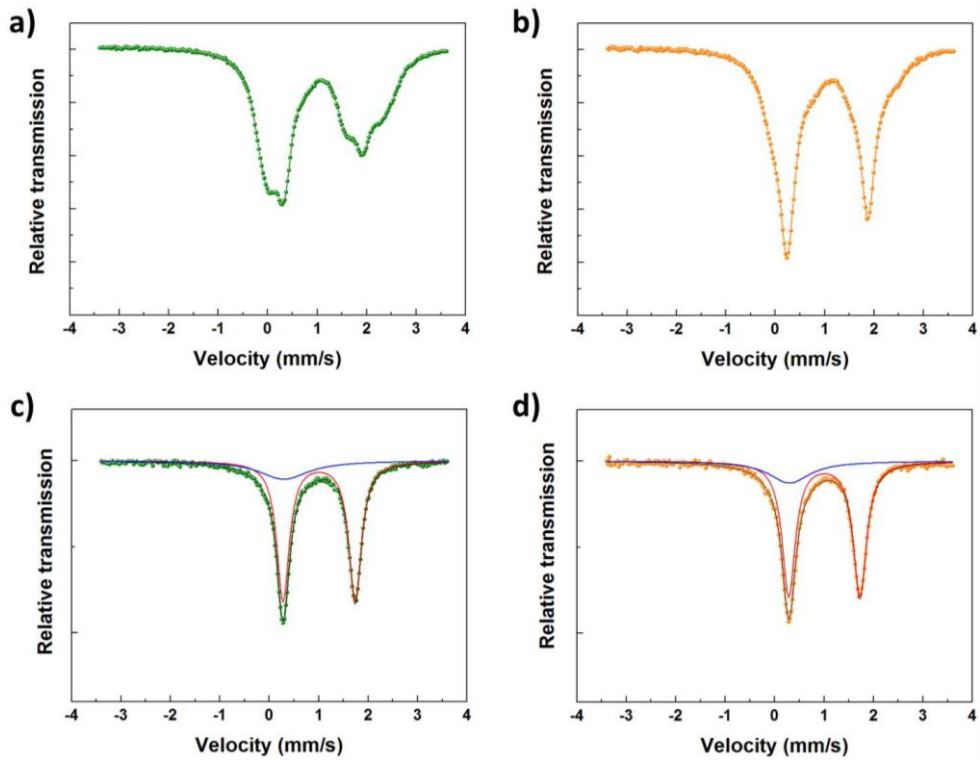

Figure 6.8. Mössbauer spectra of $Co_{0.54}Fe_{0.46}NCN$ at room temperature (a) and at 350 K (c) and $Co_{0.64}Fe_{0.36}NCN$ at R.T (b) and at 350 K (d) in the velocity range of -3.5 to 3.5 mm/s.

The Mössbauer spectra of both $Co_{0.54}Fe_{0.46}NCN$ and $Co_{0.64}Fe_{0.36}NCN$ at 350K, well above T_N, are shown in Figure 6.8 below. Both samples are in the paramagnetic state at this temperature (Figure 6.8c Figure 6.8d). The doublets of both samples were well defined and easier to be analysed allowing calculating the residual amount of Fe^{3+} that both solid solution samples could contain. In fact, both spectra were quite similar because both compounds were synthesized from the same precursors and crystallized into the same space group. There was just a small variation of iron content between the samples.

The spectra were fitted using the NORMOS program as a doublet state and the obtained parameters are given in Table 6.3. The ratio of Fe^{2+}/Fe^{3+} with about 20% of Fe^{3+} was achieved from the refinement. This Fe^{3+} could be attributed to the oxidation of the intermediate $Fe(HNCN)_2$ during its synthesis. This fact was in agreement with the same Fe^{3+} content found in both samples because the same precursors were used to synthesize both samples of $Co_{1-x}Fe_xNCN$ solid solution. In addition, from these refinements at 350 K the isomer shift and quadrupolar splitting were also calculated. It was considered that these percentages of Fe^{3+} were a bit higher than the reality because of the broadening of the fitted signal and this impurity was not observed in the X-Ray Diffraction (so the impurity should be very low or amorphous). The possibility that some Fe^{2+} was not fitted due to the different signal that can provide the sample with different order of Fe^{2+} and Co^{2+} in the structure was also considered.

In Table 6.3, it can be seen the difference between each kind of iron for both compounds. Fe^{3+} had a very small isomer shift due to the larger contribution of the electrons of the *s* orbital while Fe^{2+} had an isomer shift of 1mm/s because of the different high spin d^6 electronic configuration. The quadrupolar splitting is 0 mm/s for Fe^{3+} because the charge distribution is symmetrical and the gradient of electric field was practically 0. However, in high spin Fe^{2+} the gradient of electric field is not symmetrical due to the d^6 configuration and that is why there is a quadrupolar splitting and why it is quite large, and similar for both samples.

Table 6.3. Calculated isomer shift, quadrupolar splitting and percentage of each type of iron obtained from the refinement for the solid solution samples.

Sample	Type of iron	Isomer shift	Quadropolar splitting	Amount
$Co_{0.54}Fe_{0.46}NCN$	Fe^{2+}	1.01mm/s	1.46 mm/s	79.2%
	Fe^{3+}	0.30 mm/s	0.00 mm/s	20.8%
$Co_{0.64}Fe_{0.36}NCN$	Fe^{2+}	1.00mm/s	1.44 mm/s	79.6%
	Fe^{3+}	0.30 mm/s	0.00 mm/s	20.4%

Mössbauer experiment also confirmed that $Co_{0.54}Fe_{0.46}NCN$ was antiferromagnetic at room temperature and the Néel temperature was 303 K, while $Co_{0.64}Fe_{0.36}NCN$ was paramagnetic at room temperature and at 283 K became atiferromagnetically ordered.

These analyses were in agreement with the reported Mossbaeur spectra for FeNCN[5,6] showing two main different states at different temperatures (Figure 6.9). While above the Néel temperature (T_N= 345K) at 380 K, FeNCN exhibited a doublet indicating the paramagnetic state of the compound, below Néel temperature at 296 K a five-peak

spectrum with broad background was observed. These five peaks were attributed to a magnetic octet where just five lines were resolved.

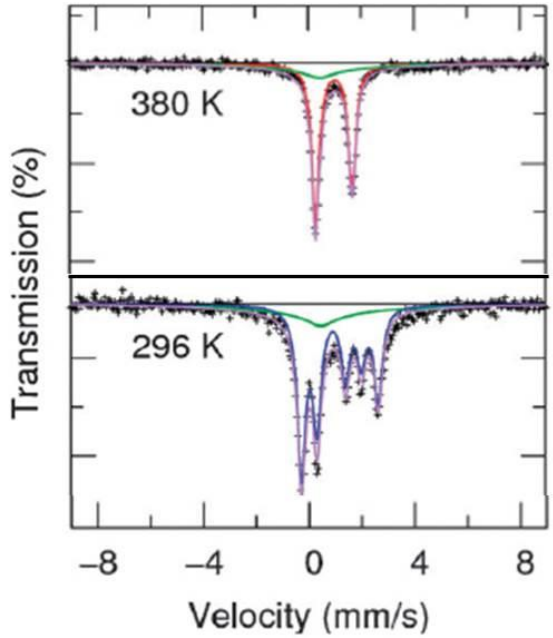

Figure 6.9. Mössbauer spectra of FeNCN at 296 K (below the T_N) and at 380 K (above T_N) from ref.6.

The difference in both spectra was the introduction of the antiferromagnetic interactions of the FeNCN sample at room temperature. When the magnetic hyperfine field was zero (paramagnetic state), the spectrum of FeNCN showed a doublet corresponding to the quadrupole moment generated by the electronic configuration of the iron in the sample as in the case at 380 K (graph at the top of Figure 6.9). This doublet appeared due to the splitting of the energy levels by the asymmetrical electric field generated. The asymmetric electronic charge distribution produced a quadrupole moment. In the case of ^{57}Fe which has I=3/2 as excited state, the energetic level of excited state is split in two due to the presence of quadruple splitting and two sub-states are created. So that, it is possible that two transitions can be observed in the Mössbauer spectra. Both transitions between energetic levels are equally permitted and the different in the intensity observed is related to the presence of some amount of Fe^{3+} that can be attributed to some impurities coming from the oxidation of precursor in the synthesis process. This contribution of the small amount of impurity is located in the peak close to 0 mm/s. Moreover, the shift (isomer shift) between the two peaks of the doublet is about 1.5-2.0 mm/s characteristic of a divalent iron. These are the reasons why this doublet is observed above Néel temperature of FeNCN at 380 K. However, below Néel temperature, at 296 K (Figure 6.9

at the bottom) the compound ordered antiferromagnetically and five peaks appear in the Mössbauer spectrum. As a result of the interaction between the nucleus and the weak magnetic field presented by FeNCN at room temperature the Zeeman Effect appeared. Therefore, ground state energetic level was split into two different sub-states due to the quadrupole moment. In addition, energetic levels were split into four different energetic levels due to the interaction with weak antiferromagnetic field that the material presented. As both electric gradient and magnetic field presented in the sample are small, there is not a bigger contribution of none of them so the degeneration of the levels result in a mixture of energetic levels where only 8 transitions are allowed. This is the magnetic octet that FeNCN exhibits at room temperature and M. T. Sougrati reported[6]. However, only five peaks are well defined which correspond to a doublet centered at 0 mm/s and a triplet at 2 mm/s. Owing to the mixture of the energetic levels of the excited state caused that the signals of the transitions that were similar are overlapped. These reported results for FeNCN matched with the results obtained for $Co_{0.54}Fe_{0.46}NCN$. However, $Co_{0.64}Fe_{0.36}NCN$ showed antiferromagnetic behaviour at room temperature so the doublet was shown in its spectrum.

6.1.3 Electrochemical characterization

In sodium ion batteries, both phases showed electrochemical activity (see Figure 6.10a). The shape of the galvanostatic curves in both compounds was similar to that observed for FeNCN. In the $Co_{0.54}Fe_{0.46}NCN$ sample, less first cycle irreversible capacity and lower voltage plateau were observed. The voltages of the plateaux were in between the voltage of the FeNCN and CoNCN. Accordingly, for $Co_{0.64}Fe_{0.36}NCN$, the first irreversible capacity is bigger than $Co_{0.54}Fe_{0.46}NCN$ probably due to the higher cobalt content. The mechanism of reaction of these compounds seemed to be similar to that in FeNCN and CoNCN where during the first discharge, the amorphization of the material and the conversion of the solid solution into metallic nanoparticles inside a Na_2NCN matrix occurred. In the charge, the re-formation of amorphous $Co_{0.54}Fe_{0.46}NCN$ and $Co_{0.64}Fe_{0.36}NCN$ was suggested. Nevertheless, the amorphous character of the phase caused that the plateau was not recovered during the charge process, as it occurred for the end members (Chapter 5) and therefore the electrochemical curve changed as the properties of one material can differ being crystalline or amorphous[7,8]. In the same context, the average voltage of both materials increased during the second discharge because in this step just the conversion reaction occurred. In addition, the second charge was almost the same than the first charge so after the first discharge, it seemed that same processes were taking place in all the discharges and the opposite process during the all the charges. In the first two galvanostatic cycles, it can be seen that the capacity was similar to the theoretical one for

each member of the solid solution. While for $Co_{0.54}Fe_{0.46}NCN$ (with theoretical capacity of 548 mAh/g) 540 mAh/g was obtained with an average voltage in discharge of 0.47 Volts *vs* Na^+/Na, for $Co_{0.64}Fe_{0.36}NCN$ (with theoretical capacity of 550 mAh/g) 545 mAh/g was achieved with an average voltage of 0.53 Volts *vs* Na^+/Na. The different voltages of both samples are clearly seen in the δQδV plots in the first cycle of both samples of $Co_{1-x}Fe_xNCN$ solid solution (Figure 6.10b).

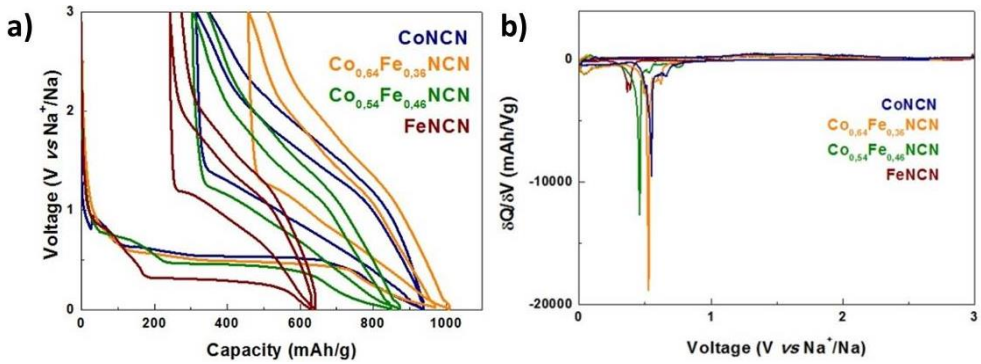

Figure 6.10. 2 first galvanostatic cycles of $Co_{0.54}Fe_{0.46}NCN$ (green line) and $Co_{0.64}Fe_{0.36}NCN$ (orange line) and the extremes of the solid solution (FeNCN in brown and CoNCN in blue) (a) and δQδV plot of the first galvanostatic cycle (b) for sodium ion batteries.

The capacity fading and coulombic efficiency of these materials improved in comparison with CoNCN and FeNCN. $Co_{0.64}Fe_{0.36}NCN$ was able to keep 435 mAh/g up to 100 cycles (Figure 6.11a) while the capacity in the cycle number 100 of $Co_{0.54}Fe_{0.46}NCN$ was 380 mAh/g (Figure 6.11b).

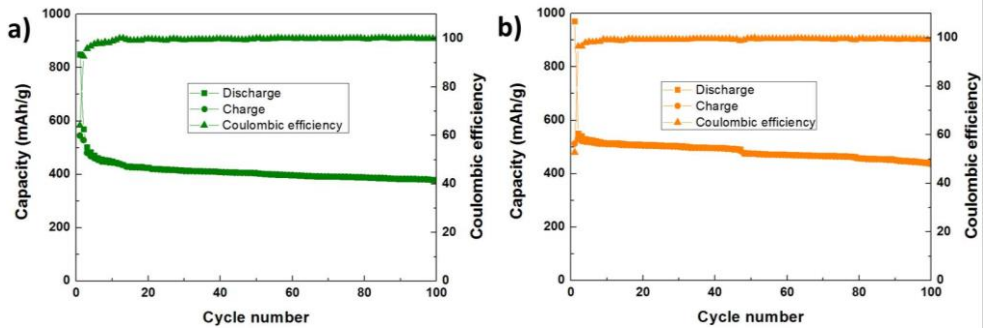

Figure 6.11. Cyclability of the first 100 galvanostatic cycles for $Co_{0.54}Fe_{0.46}NCN$ (green line at the top) (a) and $Co_{0.64}Fe_{0.36}NCN$ (orange line at the bottom) (b) for sodium ion batteries.

These results indicated that the capacity of FeNCN was increased for both samples and instead of a big capacity fading exhibited by CoNCN, stable capacities were achieved for $Co_{0.64}Fe_{0.36}NCN$ and $Co_{0.54}Fe_{0.46}NCN$. 80% and 70% of the initial charge capacity were kept respectively after 100 cyles. The addition of iron into cobalt carbodiimide caused a

reduction in the volume expansion of the electrode during the discharge process and the observed different morphology. They could be the main reasons for the decay of the capacity upon cycling. However, the coulombic efficiency of $Co_{0.64}Fe_{0.36}NCN$ and $Co_{0.54}Fe_{0.46}NCN$ was higher than 90% in the second cycle and it was increased to more than 99% from the cycle number 7 and 10 respectively. Therefore the overall expected enhancement of the electrochemical performance was achieved.

For lithium ion batteries, samples of $Co_{1-x}Fe_xNCN$ solid solution were also electrochemically active as it can be seen in Figure 6.12. In $Co_{0.54}Fe_{0.46}NCN$ sample less first cycle irreversible capacity and lower voltage plateau were obtained in comparison with $Co_{0.64}Fe_{0.36}NCN$ as it can be compared in Figure 6.12a and Figure 6.12b respectively. Nevertheless, contrary to what was observed for SIB, in LIB the hysteresis of the members of the solid solution was larger than in FeNCN and more similar to that of CoNCN. The mechanism of these compounds was probably the same than during the first discharge for CoNCN and FeNCN; and the amorphization occurred along with the conversion reaction of the solid solution samples into metallic nanoparticles inside theLi_2NCN matrix. In the charge, the re-formation of amorphous $Co_{0.54}Fe_{0.46}NCN$ and $Co_{0.64}Fe_{0.36}NCN$ was considered as the theoretical capacity was recovered. As it was observed in sodium ion batteries, the amorphization of the material could be the reason for the non-recovery of the plateau during the charge process. As a result, the electrochemical curve changed. Still, in the first two galvanostatic cycles, it can be seen that the obtained reversible capacity was similar to the theoretical one for each member of the solid solution. $Co_{0.54}Fe_{0.46}NCN$ material (with theoretical capacity of 548 mAh/g) achieved 526 and 525 mAh/g in the first and second cycle respectively, while $Co_{0.64}Fe_{0.36}NCN$ (with theoretical capacity of 550 mAh/g) exhibited 671 and 642 mAh/g. It is interesting to compare how the voltage is changing and the member of the solid solution with more iron content has lower voltage plateau than $Co_{0.64}Fe_{0.36}NCN$ as it can be seen in Figure 6.12b. This is in agreement with that described in the previous section for sodium ion batteries.

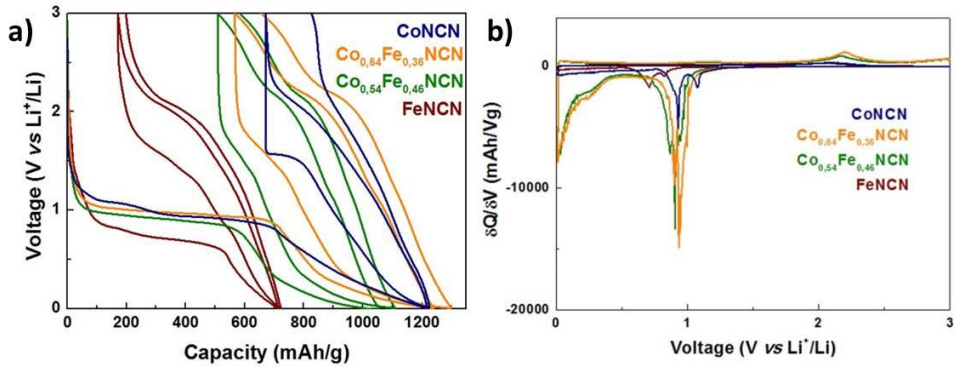

Figure 6.12. Galvanostatic 2 first cycles of $Co_{0.54}Fe_{0.46}NCN$ (green line), $Co_{0.64}Fe_{0.36}NCN$ (orange line) and the extremes of the solid solution (FeNCN in brown and CoNCN in blue) (a) and δQδV

plot of the first galvanostatic cycle for lithium ion batteries in the voltage range of 0.005-3.0 Volts *vs* Li^+/Li (b).

As in sodium ion batteries, the cyclability in lithium ion batteries was similar to that observed for FeNCN and quite better compared to the previously described for CoNCN.

$Co_{0.64}Fe_{0.36}NCN$ maintained 496 mAh/g up to 100 cycles (Figure 6.13a), while the capacity achieved in the cycle number 100 for $Co_{0.54}Fe_{0.46}NCN$ was 411 mAh/g (Figure 6.13b). In lithium ion batteries, the solid solution carbodiimides achieved stable capacities where $Co_{0.64}Fe_{0.36}NCN$ $Co_{0.54}Fe_{0.46}NCN$ kept approximately 80% of the initial charge capacity after 100 cycles. This result is quite interesting due to the bad capacity retention of the materials which react through conversion reaction. However, the coulombic efficiency of $Co_{0.64}Fe_{0.36}NCN$ and $Co_{0.54}Fe_{0.46}NCN$ was higher than 95% in the third cycle but it was increased to more than 99% from the cycle number 10 for both samples.

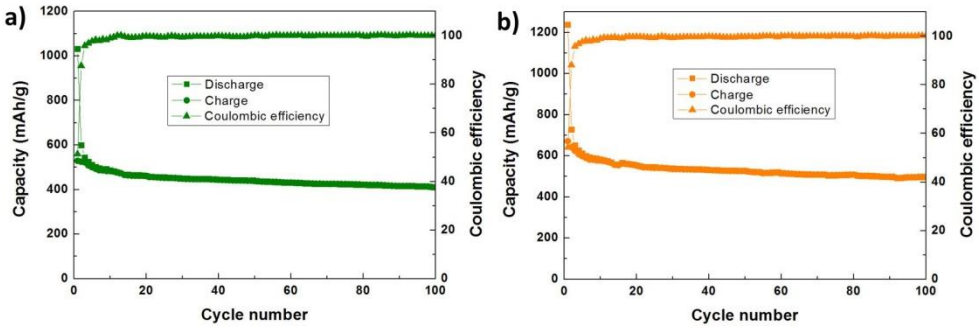

Figure 6.13. Cyclability of the first 100 galvanostatic cycles for $Co_{0.54}Fe_{0.46}NCN$ (green line at the top) (a) and $Co_{0.64}Fe_{0.36}NCN$ (orange line at the bottom) (b) for lithium ion batteries.

A comparison of the evolution of charge capacities for the 4 samples is shown in Figure 6.14. As can be seen, the reversibility of the samples from the solid solution ($Co_{1-x}Fe_xNCN$) was as good as the observed in Chapter 5 for FeNCN for both sodium and lithium ion batteries.

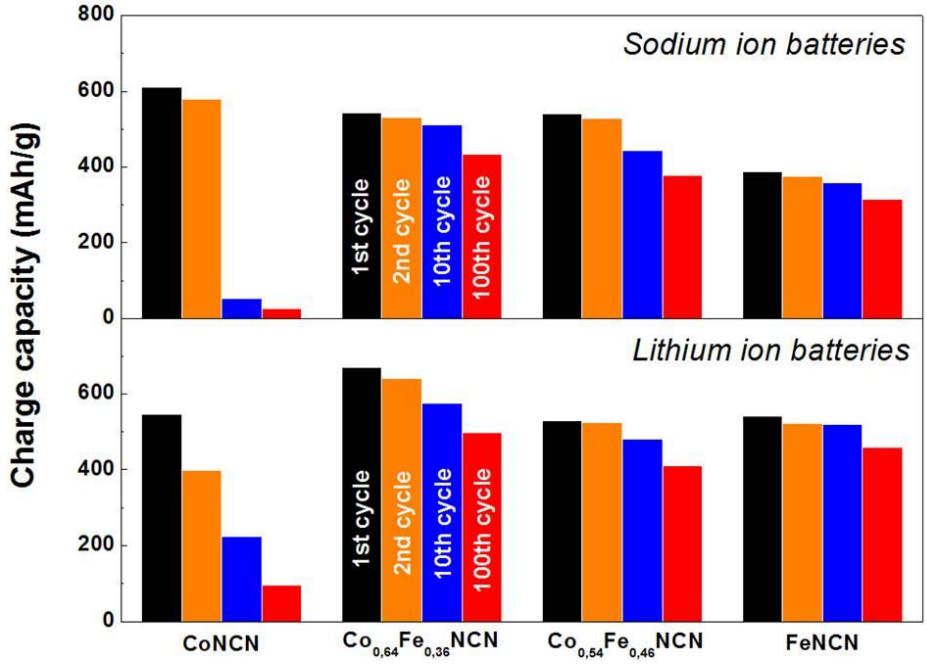

Figure 6.14. Bars diagram of CoNCN, $Co_{0.64}Fe_{0.36}NCN$, $Co_{0.54}Fe_{0.46}NCN$ and FeNCN indicating the charge capacity in first cycle (black), second cycle (orange), tenth cycle (blue) and one hundredth cycle (red).

The electrochemical behaviour of these samples is quite similar. However, they have important differences in capacity and voltage. Both samples from $Co_{1-x}Fe_xNCN$ solid solution samples improve electrochemical behaviour of the extremes FeNCN and CoNCN. More amount of cobalt in the samples provided better values in terms of capacity (see Figure 6.14) but $Co_{0.54}Fe_{0.46}NCN$ has lower average voltage in discharge and charge process. This makes that both compounds would be similar in terms of energy because the lower voltage plateau of $Co_{0.54}Fe_{0.46}NCN$ would equalize with the higher capacity of $Co_{0.64}Fe_{0.36}NCN$.

6.2 Conclusions

$Co_{0.64}Fe_{0.36}NCN$ and $Co_{0.54}Fe_{0.46}NCN$ were synthesized for the first time using Schlenk techniques in the same way than FeNCN and CoNCN. The success of the synthesis was characterized as a single phase by PXRD and checking the carbodiimide IR band are similar to cobalt and iron carbodiimide. The ICP-AES confirmed the exact amount of cobalt and iron in the sample as $Co_{0.64}Fe_{0.36}NCN$ and $Co_{0.54}Fe_{0.46}NCN$. TEM shows that the platelet shape was very regular for CoNCN, while the more amount of iron is involved, the more heterogeneity of the platelet is observed. Magnetic measurements show that $Co_{0.64}Fe_{0.36}NCN$ is practically in paramagnetic state at room temperature (T_N=283 K) unlike $Co_{0.54}Fe_{0.46}NCN$ which is in the antiferromagnetic state (T_N=303 K). Mössbauer spectroscopy required increasing the temperature in order to quantify the percentage of Fe^{3+}. The fitting indicates that 20% of the iron was Fe^{3+} for both samples..

The electrochemical activity of these materials was proved for the first time. For $Co_{0.64}Fe_{0.36}NCN$ and $Co_{0.54}Fe_{0.46}NCN$ samples, similar electrochemical behavior to FeNCN and CoNCN was observed. Close to theoretical capacities were achieved (~550 mAh/g) for both compounds in the first cycles. After 100 cycles, $Co_{0.64}Fe_{0.36}NCN$ is able to keep 435 mAh/g in sodium ion batteries and 496 mAh/g in lithium ion batteries. On the other hand, 380 mAh/g and 411 mAh/g were obtained in 100^{th} cycle for sodium and lithium ion batteries respectively in $Co_{0.54}Fe_{0.46}NCN$ sample. These samples showed the best electrochemical performance compared to the samples measured in this work

6.3 References

[1] L. H. Ahrens; "The use of ionization potentials Part 1. Ionic radii of the elements"; *Geochim. Cosmochim. Acta*, 1952, **2** (3), 155.
[2] X. Liu, L. Stork, M. Speldrich, H. Lueken and R. Dronskowski; "FeNCN and $Fe(NCNH)_2$: Synthesis, Structure, and Magnetic Properties of a Nitrogen-Based Pseudo-oxide and -hydroxide of Divalent Iron"; *Chem. Eur. J.* 2009, **15**, 1558.
[3] M. Krott, X. Liu, P. Muller and R. Dronskowski; "Synthesis and structure determination of Co(HNCN)2 and Ni(HNCN)2"; *J. Solid State Chem.* 2007, **180,** 307.
[4] M. Krott, X. Liu, B. P. T. Fokwa, M. Speldrich, H. Lueken and R. Dronskowski; "Synthesis, Crystal-Structure Determination and Magnetic Properties of Two New Transition-Metal Carbodiimides: CoNCN and NiNCN"; *Inorg. Chem.* 2007, **46**, 2204.
[5] M. Herlitschke, A. L. Tchougréeff, A. V. Soudackov, B. Klobes, L. Stork, R. Dronskowski, R. P. Hermann; "Magnetism and lattice dynamics of FeNCN compared to FeO"; *New J. Chem.* 2014, **38**, 4670.
[6] M. T. Sougrati, A. Darwiche, X. Liu, A. Mahmoud, R. P. Hermann, S. Jouen, L. Monconduit, R. Dronskowski and L. Stievano; "Transition-Metal Carbodiimides as Molecular Negative Electrode Materials for Lithium- and Sodium-Ion Batteries with Excellent Cycling Properties"; *Angew. Chem. Int. Ed.*, 2016, **55** (16), 1.
[7] Z. H. Stachurski; "On Structure and Properties of Amorphous Materials" *Materials,* 2011, **4**, 1564.
[8] P. Poizot, S. Laruelle, S. Grugeon, L. Dupont and J. M. Tarascon; "Nano-sized transition-metal oxides as negative-electrode materials for lithium-ion batteries"; *Nature* 2000, **407**, 496

7- Sodium ion full-cells development

7.1 Introduction

All the materials whose electrochemical performance has been studied in this work have been tested using metallic sodium as anode system. It was used because in principle it allows one to obtain the intrinsic properties of the materials with respect to a universal material so that data from different laboratories is comparable. However, metallic sodium is not the best option to act as anode for a commercial cell, and in fact the materials studied in this thesis are though as their replacement in a real cell. There are several reasons so as to why metallic sodium is not a good anode. The most important one is that the low melting point of sodium (around 98^{o}C) involves a significant safety hazard in devices designed for use at ambient temperatures using a Na metal electrode. Moreover, the high reactivity of metallic sodium with the organic electrolyte solvents and the dendrite formation during metallic sodium deposition are even more problematic than with metallic lithium anodes[1,2]. Therefore, there is a need of searching for a rechargeable battery based on two electrodes system where the anode should not be metallic sodium.

In the cathode side, sodium layer oxides seem to be the most suitable compounds because this family of materials has high tap density which leads to the better packing of the material in the device. The selection of one cathode is complicated, but there are several options and the decision is taken depending on both high capacity and higher average voltage. The selection of electrolyte is also quite hard because all materials work with different composition of electrolyte and the electrolyte which works better for the anode is not always working as well for the cathode electrode. So that, there are many differences between the electrolytes used in the reported full cells[3,4]. On the other hand, there is not a suitable anode for sodium ion batteries. Nevertheless, there has been a big development in anodes for sodium ion batteries. It seems that there are some good candidates such $Na_2Ti_3O_7$ with a plateau at 0.3 V *vs* Na^+/Na and a suitable capacity of 177 mAh/g or tin and antimony alloys that can deliver high values of capacity at relatively low voltage with good cyclability. Up to now, the best candidates are several types of hard carbons which can deliver close to 300 mAh/g with relatively low voltage plateau and small first irreversible capacity[5]. The success of Na ion batteries is strongly dependent on the development of safe and efficient anode materials. Most common studied full cell is based on hard carbons and layer oxides.

In order to test the electrochemical properties of the best studied anodes in a full cell, this chapter is going to give an overview of how the properties obtained in half cells impact into a full cell. In the previous chapters of this thesis, two families of compounds were studied: titanates and carbodiimides. So, one material of each family ($H_2Ti_3O_7$ and FeNCN) have been selected for the study in a full cell. While for intercalation compounds[6,7] there are many studies based on full cell especially for hard carbons[,8,9,10], fewer attempts were carried out in conversion systems[11,12].

As cathode, the layered sodium oxide with the formula $Na_{0.67}[Mg_{0.05}Ni_{0.25}Mn_{0.7}]O_2$ was selected due to the stability during the galvanostatic cycles and the high working voltage that this material exhibits. This cathode provided very good results when tested with hard carbon material in the laboratory by some other researchers at CIC EnergiGUNE[13]. Hence, a comparison is going to be performed between the hard carbon which is the most suitable anode material up to now, and the anodes studied within this thesis work. The energy obtained from the full cell can be obtained calculated by the equation 7.1 with the experimental values of capacity and voltage between the start and the end of the charge/discharge process (see Figure 7.1).

$$Energy(Wh/kg) = \int Capacity\ (Ah/kg)\, x\, Voltage\ (V) \quad (7.1)$$

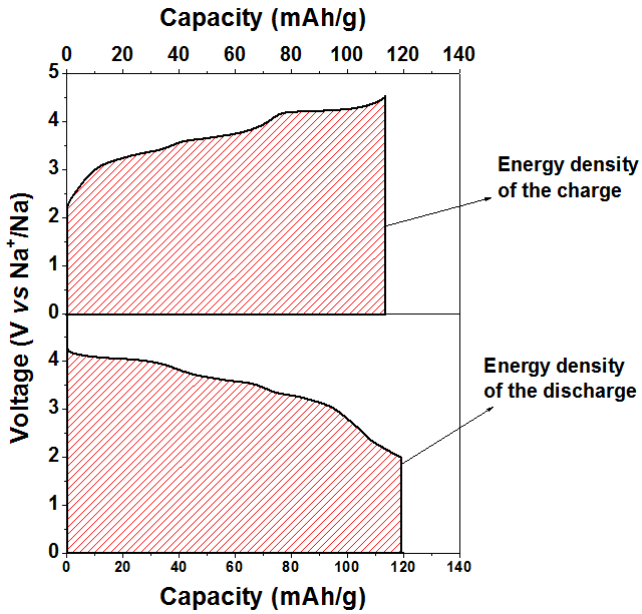

Figure 7.1. Integral of the electrochemical curves of a sodium ion battery describing the differences between the energy that is stored in the charge and that delivered during the discharge.

7.2 Results and discussion

7.2.1. Synthesis of sodium layer oxide: $Na_{0.67}[Mg_{0.05}Ni_{0.25}Mn_{0.7}]O_2$

The $Na_{0.67}[Mg_{0.05}Ni_{0.25}Mn_{0.7}]O_2$ was synthesized by ceramic method grinding in the mortar stoichiometric amounts of nickel (II), magnesium and manganese (III) oxides with sodium carbonate. The mixture was made as a pellet and was calcined up to 900^{o}C in the oven for 12 hours followed by a slow cooling process to obtain a single phase.

7.2.2. Structural characterization of P2-$Na_{0.67}[Mg_{0.05}Ni_{0.25}Mn_{0.7}]O_2$

The synthesized powder was characterized by powder X-Ray Diffraction through Rietveld Refinement Method[14](Figure 7.2a). A single phase with the *P*6$_3$/*mmc* space group with Mg, Ni and Mn randomly occupy the centre of octahedra has been observed[15]. The cell parameters and the agreement factors are listed in Table 7.1.

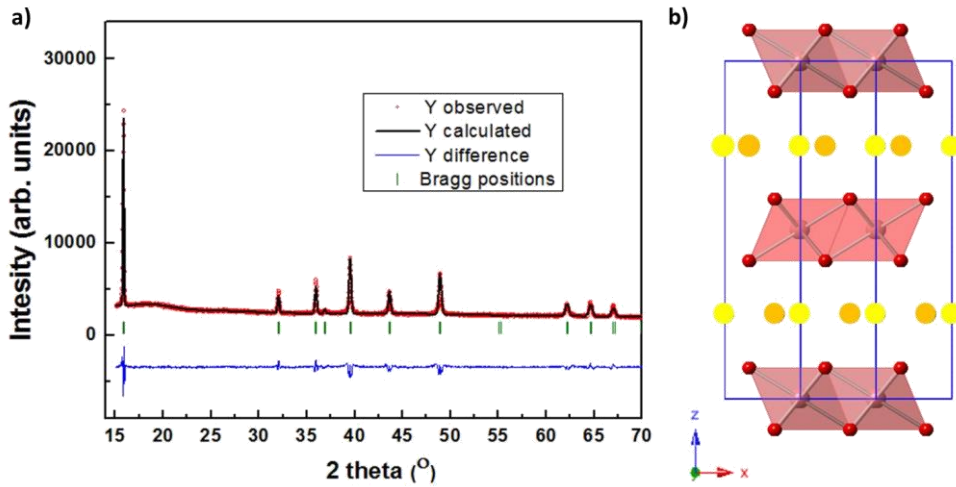

Figure 7.2. Rietveld refinement of the layer oxide P2- $Na_{0.67}[Mg_{0.05}Ni_{0.25}Mn_{0.7}]O_2$ where red dots are the experimental pattern, black line is the calculated pattern, blue line the differential of observed and calculated and the green ticks the Bragg positions (a). P2-$Na_{0.67}[Mg_{0.05}Ni_{0.25}Mn_{0.7}]O_2$ structure obtained from Rietveld refinement where yellow and orange balls are the different sodiums, red balls are oxygen atoms respectively and the octahedral centre in rose colour the manganese, nickel and magnesium atoms (b).

Table 7.1. Cell parameters and agreement factors obtained from the Rietveld refinement method of P2-$Na_{0.67}[Mg_{0.05}Ni_{0.25}Mn_{0.7}]O_2$.

Cell parameters		**Agreement factors from Rietveld**	
a=*b* (Å)	2.885(2)	R_p (%)	15.3
c (Å)	11.176(3)	R_{wp}(%)	12.3
Volume (Å^3)// V/Z (Å^3)	80.512(6)/ 40.256	R_{Bragg} (%)	5.27
Molar mass (g/mol)	101.76	χ^2	5.23

The the P2-$Na_{0.67}[Mg_{0.05}Ni_{0.25}Mn_{0.7}]O_2$ was selected among the sodium transition metal oxides because the doping in P2-$Na_{0.67}MnO_2$ with Mg reduced the amount of Mn^{3+} Jahn−Teller distortion and therefore, increased the structural stability of the compound. Moreover, Mg^{2+} doping prevents the Mn^{3+}/Mn^{4+} ordering in the structure during the charge/discharge processes because the high spin Mn^{3+} ions when replaced with Mg^{2+} partially transform into Mn^{4+} and thus there is a decrease in the number of Jahn-Teller active ions[16]. Ni^{+2} ions help to have higher operating voltage of the cell because of its high $Ni^{+2/}$ Ni^{+4} redox potential w.r.t Na^+/Na^0.

7.2.3. Electrochemical characterization of P2-$Na_{0.67}[Mg_{0.05}Ni_{0.25}Mn_{0.7}]O_2$

The molecular weight of this compound is 101.76 g/mol and it has a theoretical capacity of 176 mAh/g for the insertion of 0.67 Na^+ ions. From that amount of sodium, only 0.45 Na^+ ions were de/inserted in the range of voltage of 2.0-4.5 V *vs* Na^+/Na. An electrochemical test was performed in order to figure out the relation of mass balance in the full cell. A laminate with 76% wt. of layer oxide, 15% wt. C65 and 9% wt. of pvdF was prepared. The mass loading of the electrodes punched from the laminate were around 2.3 mg. The electrochemical behavior of the layer oxide was studied using 1 M $NaPF_6$ in EC:DEC (1:1 vol %) electrolyte and sodium as counter and reference electrode. The cathode was cycled between 2.0-4.5 *vs* Na^+/Na achieving a capacity of 120 mAh/g stable up to 100 cycles with very small polarization and very good capacity retention (see Figure 7.3 and Figure 7.4 respectively). From the cell, 0.5 mAh was obtained and this value was taken into account to make the mass balance calculations with the studied anodes. In the galvanostatic cycling, it can be seen that there are three processes at 3.4, 3.7 and 4.2 V *vs* Na^+/Na. In fact, in δQ/δV plot (Figure 7.3b) they are clearly shown, and the small polarization in each process was observed. 0.1 V of polarization were achieved in the processes at 3.4 and 3.7 V *vs* Na^+/Na^0 and 0.2 V for the process at 4.2 V *vs* Na^+/Na. These voltage plateaux could be attributed to the oxidation of Mn^{3+} to Mn^{4+}, Ni^{2+} to Ni^{3+} and the

transition from prismatic P2-type to octahedral/Prismatic OP4-type coordination[15]. It is very common that the layer oxides with P2-structure such as $Na_{0.67}Ni_{0.33}Mn_{0.67}O_2$ turn into O2-structure during the charge process at high voltages but the addition of magnesium caused the structural transition to OP4-structure instead of the common O2-structure.. The doping with Mg^{2+} smoothed also the charge/discharge curves and reduced polarization[16]. These processes were located at high voltage which is interesting in order to reach a high voltage difference between cathode and anode and therefore high energy density. All this properties made this cathode material appropriate for the assembly of a full cell using $H_2Ti_3O_7$ and FeNCN as anodes. For that purpose, $H_2Ti_3O_7$ and FeNCN were measured with the same electrolyte so as to see how much capacity was obtained in order to make a good mass balance between cathode and anode.

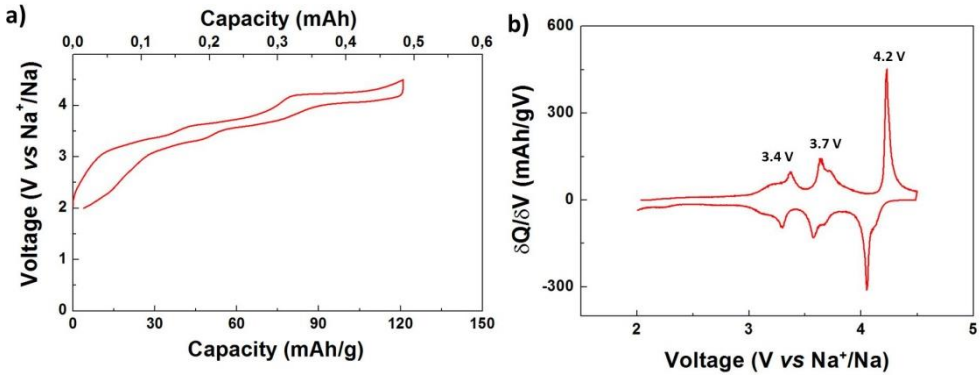

Figure 7.3. Capacity vs voltage profile (a) and δQ/δV plot (b) of $Na_{0.67}[Mg_{0.05}Ni_{0.25}Mn_{0.7}]O_2$ in the 2.0-4.5 V *vs* Na^+/Na range.

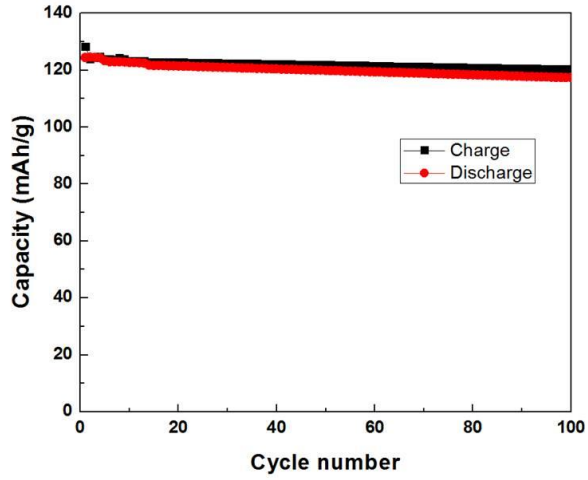

Figure 7.4. Cyclability for 100 cycles of the $Na_{0.67}[Mg_{0.05}Ni_{0.25}Mn_{0.7}]O_2$ in the range 2.0-4.5 V *vs* Na^+/Na.

7.2.4. Electrochemical studies for full-cell assembly

As discussed before, $H_2Ti_3O_7$ sample was also tested with the same electrolyte used for the cathode, and it was observed that the same electrochemical processes were taking part in the electrochemical discharge/charge as those described in Chapter 3. According to the electrochemical curve (see Figure 7.5), during the first two cycles, the plateau at 1.2 V *vs* Na^+/Na was observed. In that plateau, $H_2Ti_3O_7$ was likely transformed into $Na_2Ti_3O_7$-like structure. After these two cycles, the cell was discharged to lower voltage and cycled in the range 0.05-1.6 V *vs* Na^+/Na. In this range, a reversible capacity of 170 mAh/g was obtained with a very low voltage plateau (around 0.25 V *vs* Na^+/Na) which showed *ca.* 0.2 V of polarization. In the plateau of the discharge process the reduction of the titanium (from Ti^{4+} to Ti^{3+}) was occurred and during charge process the oxidation of the titanium (from Ti^{3+} to Ti^{4+}) was taking place.

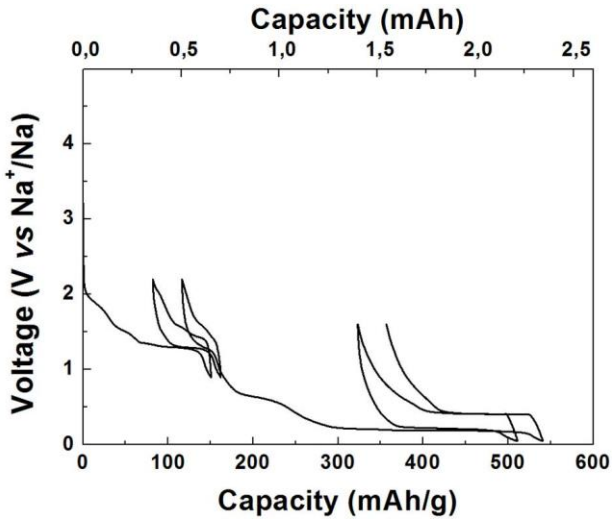

Figure 7.5. Electrochemical measurement of $H_2Ti_3O_7$ with 1M $NaPF_6$ in EC:DEC electrolyte in the ranges 0.9-2.2 V *vs* Na^+/Na (first two cycles) and 0.05-1.6 V *vs* Na^+/Na (3^{rd} and 4^{th} cycles).

FeNCN was tested with the same electrolyte, and the electrochemical behavior observed was similar to the obtained with 1M NaFSI in Me-THF electrolyte described in Chapter 5. However, it is important to mention that FeNCN did not show the pronounced process at 0.8 V *vs* Na^+/Na that was attributed to the co-intercalation process into the carbon by the Na ion solvated by Me-THF solvent, in the capacity *vs* voltage plot (Figure 7.6). During the discharge, the plateau of 400 mAh/g at 0.45 V *vs* Na^+/Na was observed. It was observed

that the cyclability of this material was very good. Besides, the coulombic efficiency of the iron carbodiimide is good, above 95% after the first cycle in which the coulombic efficiency was 78%. This indicated that appart from the electrolyte decomposition in first cycle; just the conversion reaction was occurred. The polarization of this compound was the main drawback in terms of energy because it implied a decrease of the average voltage of the cell.

However, this behavior shown in the half-cell did not imply that anode and cathode materials were going to work in the same way in the full-cell. Aspects, such as electrolyte decomposition and the voltage range where both materials were cycled, were determined by the full cell and they were monitored-by in a three electrode Swagelok cell with the layered oxide and the anode material ($H_2Ti_3O_7$ or FeNCN) as counter and working electrodes and using metallic sodium as the reference electrode.

As a general conclusion observed from the half-cell data, the most important problem derived from the anodes were the irreversible capacity of the first cycle due to the SEI layer formation. Nowadays, new studies are focused on compensating this extra capacity by mixing the cathode material with other compounds such as sodium azide[17]. The problem of using these azide compounds is the handling of the sample since azide compounds are explosive by abrasion.

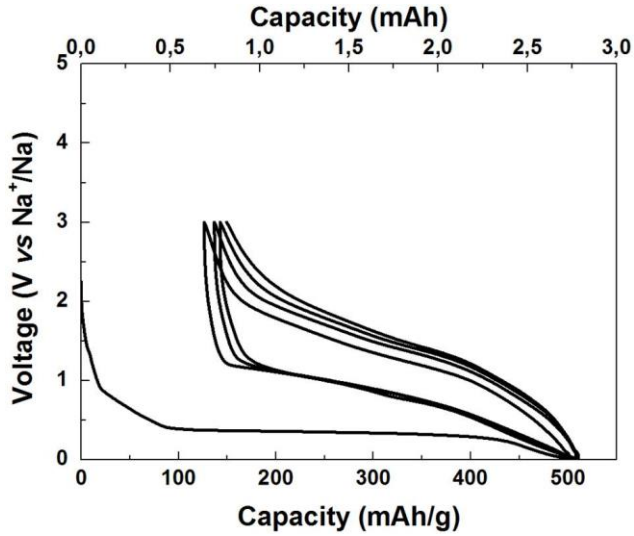

Figure 7.6. Electrochemical behaviour of FeNCN with 1M $NaPF_6$ in EC:DEC electrolyte in the ranges 0.005-3.0 V *vs* Na^+/Na for the first four cycles.

In this chapter, $H_2Ti_3O_7$ was precycled in order to take advantage from the good capacity retention of $Na_{1.8}H_{0.2}Ti_3O_7$ obtained after cycling two cycles in the 0.9-2.2 V *vs* Na^+/Na range. After these two first cycles at higher voltage, the full cell of $Na_{1.8}H_{0.2}Ti_3O_7$ was cycled in 0.05-1.6 V *vs* Na^+/Na voltage range for 100 cycles. Nevertheless, FeNCN was not precycled because the target of this study is to evaluate how the electrochemical properties of these materials impact in a final device, despite the fact that precycling could improve the results on FeNCN.

7.2.5. Electrochemical properties of $Na_{1.8}H_{0.2}Ti_3O_7$ in a full-cell

Presodiation of $H_2Ti_3O_7$ was performed in half cell in the following manner: $H_2Ti_3O_7$ electrode was cycled in a coin cell using 1M $NaPF_6$ in EC:DEC for two cycles at 0.9-2.2 V obtaining as a result the same plateau at 1.2 V *vs* Na^+/Na. This cycled electrode was taken from the half cell in the charged state at approximately 1.75V *vs* Na^+/Na and it was used as working electrode in a three electrode Swagelok cell where the cathode material $Na_{0.67}[Mg_{0.05}Ni_{0.25}Mn_{0.7}]O_2$ and metallic sodium was used as counter and reference electrodes respectively. The open circuit voltage of the cathode material in the cell was 2.73V *vs* Na^+/Na, so the starting voltage of the full cell was around 1 V *vs* Na^+/Na. While the anode was discharged to 0.05 V *vs* Na^+/Na, the cathode was charged up to 4.2 V *vs* Na^+/Na in the same process, so the full cell was charged up to 4.15 V *vs* Na^+/Na (Figure 7.7). This indicated that the sodium ions, which were deintercalated from the $Na_{0.67}[Mg_{0.05}Ni_{0.25}Mn_{0.7}]O_2$ causing the oxidation of the transition metals, were diffused through the electrolyte to the anode where titanium was reduced because of their intercalation. The excess of the cathode material (3 times more the amount of mass of the anode) compensated the higher capacity of the anode electrode compared to the cathode and the extra capacity of the anode could be attributed to the SEI layer formation. During the discharge process of the full cell, it was observed that the reversible capacity obtained in the anode was close to the theoretical value (178 mAh/g), taking the mass of the anode into the calculations. However, upon cycling a high capacity fading was observed during the first cycles and from the 5^{th} cycle onwards ~120 mAh/g(of anode) was obtained (Figure 7.7). Moreover, $Na_{1.8}H_{0.2}Ti_3O_7$, operates at low voltage with small polarization (about 0.25 V) which caused good electrochemical performance of the full cell. After ten cycles, a capacity of 0.17 mAh was obtained for this cell. This value was divided by the sum of the active mass of the anode (1.04 mg) and cathode (3.08 mg) in order to calculate the capacity of the cell in the discharge process of the full cell (41.2 Ah/kg). The integration of the electrochemical curve of the discharge provided 136 Wh/kg(of both active materials of cathode and anode) of energy as it can be seen in

Figure 7.8. Knowing the energy and capacity of the discharged curve, the average voltage was calculated as 3.3 V (see equation 7.2). This value is considered to be competitive for a sodium ion battery. Nevertheless, an anode with less capacity fading or better mass balance could provide higher amount of energy upon time which is desirable for these types of batteries.

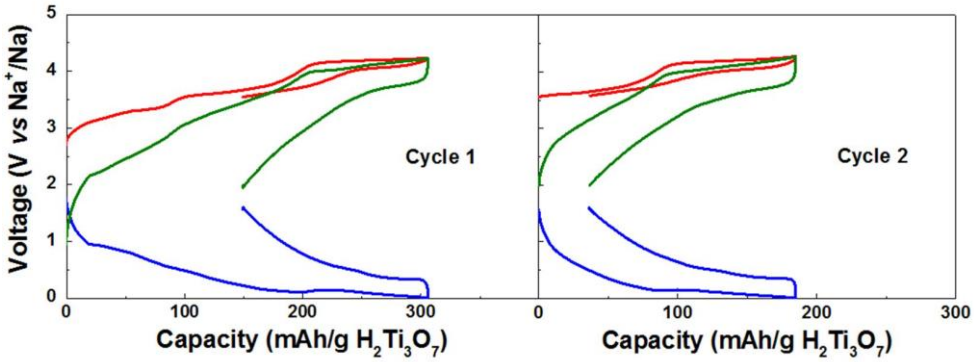

Figure 7.7. Electrochemical behaviour of the anode (blue line), cathode (red line) and the full cell (green line) of $Na_{0.67}[Mg_{0.05}Ni_{0.25}Mn_{0.7}]O_2$/ $Na_{1.8}H_{0.2}Ti_3O_7$ of the first and second cycle.

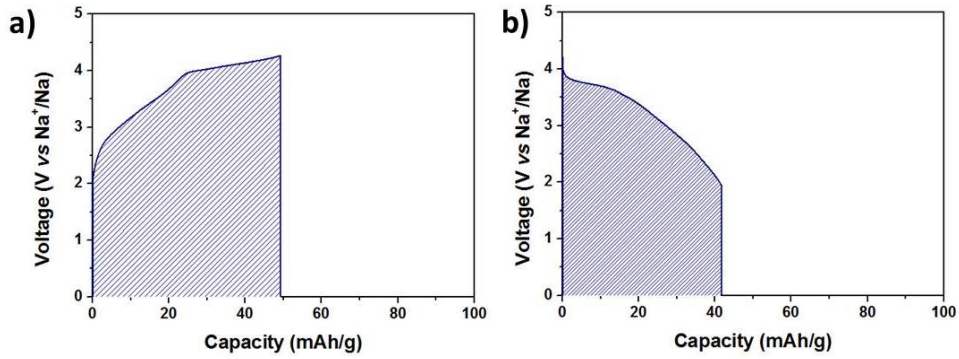

Figure 7.8. Calculation of energy density by the integration of the curve in the second charge (a) and second discharge (b) of $Na_{0.67}[Mg_{0.05}Ni_{0.25}Mn_{0.7}]O_2$/$Na_{1.8}H_{0.2}Ti_3O_7$.

$$41.2\ Ah/kg\ x\ 3.3\ V = 136\ Wh/kg \qquad (7.2)$$

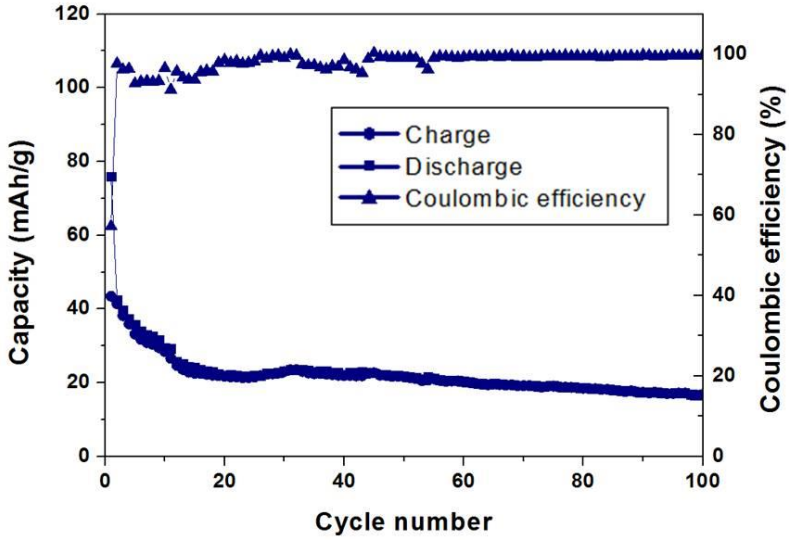

Figure 7.9. Cyclability in capacity values of the $Na_{0.67}[Mg_{0.05}Ni_{0.25}Mn_{0.7}]O_2/Na_{1.8}H_{0.2}Ti_3O_7$ cell for 100 cycles where the capacity was calculated by the sum of the anode and cathode masas.

7.2.6. Electrochemical properties of FeNCN in a full-cell

Iron carbodiimide/ P2-$Na_{0.67}[Mg_{0.05}Ni_{0.25}Mn_{0.7}]O_2$ full-cell was assembled obtaining 0.16 V of open circuit voltage (see Figure 7.10a). The ratio of electrode mass used in the development of the full cell was 6.2:1 (cathode:anode). As both electrodes were monitored, we could also see that the OCV was 2.63 V *vs* Na^+/Na and 2.79 V *vs* Na^+/Na for the anode and cathode respectively. From 0.16 V, the full-cell was charged up to 4.2 V. This voltage was obtained due to the charge of the cathode to close to 4.2 V *vs* Na^+/Na and the discharge of the anode to 0.01 V *vs* Na^+/Na. There, it could be seen that in the cathode three oxidation processes were observed like it was observed in the half cell while in the anode only the plateau due to the conversion reaction at 0.4 V *vs* Na^+/Na was observed. However, during the discharge process, the anode was charged to 3 V *vs* Na^+/Na and the cathode was discharged to 3.4 V *vs* Na^+/Na. Then, the first cycle irreversible capacity was observed. In the full-cell about 50% of the capacity was lost in the first cycle and the polarization contributed to the reduction of the full-cell voltage. The irreversibility of the first cycle could be "in principle" solved by the addition of the sodium azide or other sodium sacrificial salts to compensate the capacity from the SEI layer formation[17]. This way, the whole active material of cathode could be accessible in terms of capacity and a cathode:anode ratio smaller than 6.2:1 could be used. In the second cycle, the polarization of FeNCN decreased. As a result, the full-cell notably reduced its polarization increasing the average voltage (and therefore energy density)

(see Figure 7.10b and Figure 7.11). Upon cycling, the cell exhibited good capacity retention and high coulombic efficiency from the second cycle (Figure 7.12). It is worth mentioning that during the discharge of second cycle 157 Wh/Kg(of both active materials of cathode and anode) was achieved from the integration of the discharge in voltage *vs* capacity plot. From the energy and capacity values, 2.6 V as average voltage were obtained (equation 7.3). This value was smaller during the discharge because of the polarization, which decreased the average voltage from 2.9 V on charge to 2.6 V on discharge resulting also in a reduction of energy density or energy inefficiency of 10%.

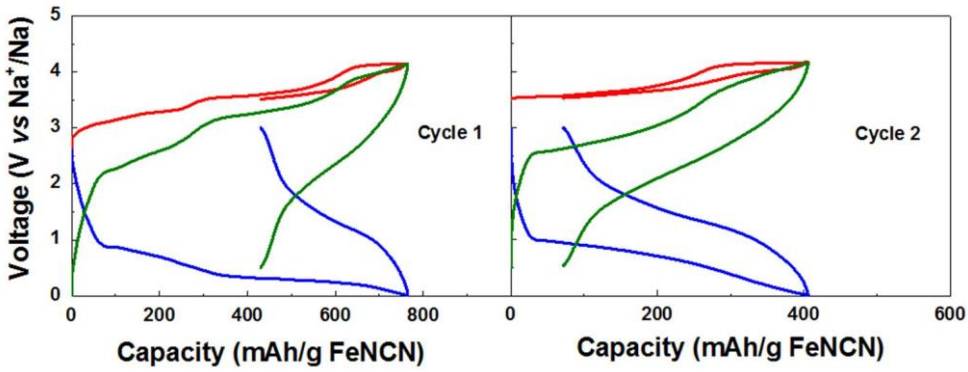

Figure 7.10. Electrochemical behaviour of the anode (blue line), cathode (red line) and the full cell (green line) of $Na_{0.67}[Mg_{0.05}Ni_{0.25}Mn_{0.7}]O_2$/ FeNCN for the first (left) and second (right) cycle of the cell.

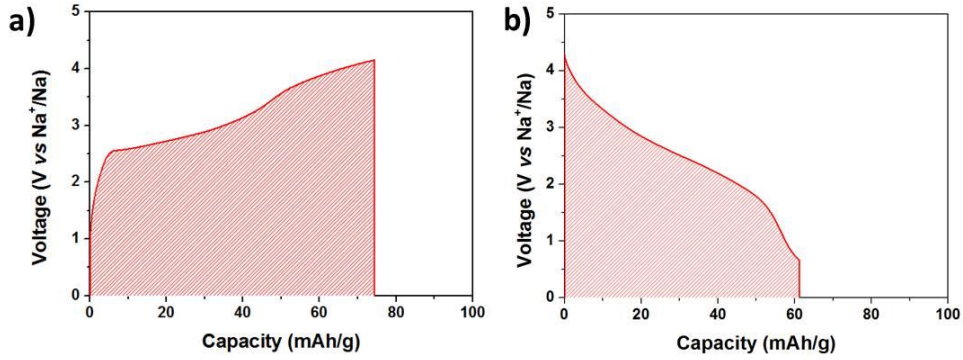

Figure 7.11. Calculation of the energy density in the second charge (a) and second discharge (b) of $Na_{0.67}[Mg_{0.05}Ni_{0.25}Mn_{0.7}]O_2$/ FeNCN.

$$60.4\ Ah/kg\ x\ 2.6\ V = 157\ Wh/kg \quad (7.3)$$

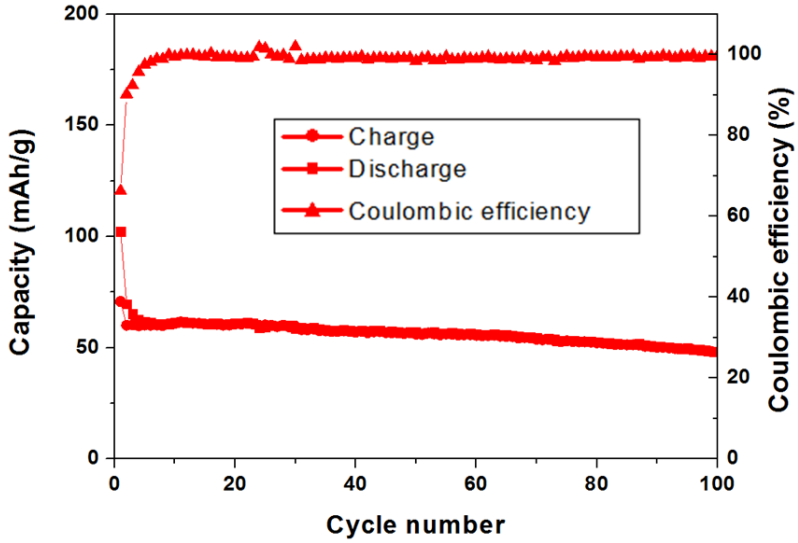

Figure 7.12. Cyclability in capacity values of the $Na_{0.67}[Mg_{0.05}Ni_{0.25}Mn_{0.7}]O_2$/ FeNCN cell for the first 100 cycles where the capacity was calculated by the sum of the anode and cathode masas..

In spite of high polarization and high irreversible capacity in the first cycle, the good capacity retention and high coulombic efficiency make the battery of carbodiimide very good candidate for a long-term stationary energy storage system. A pre-cycling could also improve the drawback of irreversible capacity of first cycle. However, this is not a solution for a real application because up to now, it is not possible to scale up making the pre-cycling process.

7.2.7. Electrochemical comparison of different anode compounds using P2-$Na_{0.67}[Mg_{0.05}Ni_{0.25}Mn_{0.7}]O_2$ as cathode.

In order to compare the material´s intrinsic electrochemical properties, the values obtained for the full cell using the same cathode material (P2-$Na_{0.67}[Mg_{0.05}Ni_{0.25}Mn_{0.7}]O_2$) with different anode materials are listed in Table 7.2. Up to this work, this cathode material was tested using metallic sodium[18] and hard carbon (CIC EnergiGUNE) as counter electrode. There, it can be observed that using metallic sodium as anode the full capacity of the cathode was reached and the voltage is the highest possible using this cathode for a sodium ion battery. Nevertheless, the formation of dendrites and the low melting point cause that the metallic sodium is not the ideal anode for an industrial final device as already discussed in this thesis despite it results in the higher capacity and voltage. Taking into account the literature about anode materials for sodium ion batteries, hard carbon

seems to be the most promising material due to its smallest first cycle irreversible capacity, low voltage plateau and good capacity retention compared to the rest of the studied anodes. Besides, experimentally it was observed that only 80 Ah/kg of capacity was found for the full cell from the first cycle with a voltage of 3.4 V. Therefore, the energy density obtained from the cell was 265 Wh/Kg. This was 60% of the energy that the full cell with metallic sodium provided but without the hazards derived from the use of metallic sodium. The good capacity retention of the layered oxide/HC full cell made hard carbon very promising material for sodium ion battery devices. In this context, the anode materials synthesized in this thesis were tested to see the differences with the, up to now, best candidates for Na-ion technology: hard carbons.

Table 7.2. Experimental values observed in the second discharge of the cells for P2-$Na_{0.67}[Mg_{0.05}Ni_{0.25}Mn_{0.7}]O_2$ using the anodes described below. The capacity calculation was performed using as mass the sum of anode and cathode (except metallic sodium, always in excess)**.**

Anode	Capacity (Ah/kg)	ΔVoltage (V)	Energy (Wh/kg)	Data
Sodium	123	3.7	455	[18]
Hard Carbon	77.8	3.4	265	CIC Energigune
$Na_{1.8}H_{0.2}Ti_3O_7$	41.2	3.3	136	This thesis
FeNCN	60.4	2.6	157	This thesis

An intercalation compound ($Na_{1.8}H_{0.2}Ti_3O_7$) and a material which works through conversion mechanism (FeNCN) were tested. In the titanate, the voltage is similar to the observed for the hard carbon. However, $Na_{1.8}H_{0.2}Ti_3O_7$ compound exhibited a polarization close to 0.2 V where in hard carbons the polarization is less than 0.1 V. For that reason the voltage observed in the full cell is lower than in hard carbons. Moreover, it showed higher first cycle irreversible capacity and so that, more cathode material was inactive after the first discharge. Besides, a high capacity fading was observed upon cycling which meant that the capability to store energy in decreasing. In spite of these electrochemical drawbacks, protonated titanate was able to store 136 Wh/kg which is the half of the energy observed for hard carbons. So, with the improvements in capacity retention that *M. Zarrabeitia et al.* described[19], these titanate materials could be competitive in comparison with hard carbons in terms of cyclability and capacity values. Only the first irreversible capacity could be a problem, but, as it was described above, new methods as the use of the azides are being developed.

On the other hand, the compound which works through conversion reaction (FeNCN) showed very good capacity retention which was similar, or even better, than hard carbon. Nevertheless, this compound had the same problem of first cycle irreversible capacity as

well as high polarization, which implied decreasing the voltage of the cell. In spite of these disadvantages, a capacity of 60.4 Ah/kg was obtained for more than 100 cycles with a 2.6 V of average voltage. Therefore, the energy density observed in the cell was 157 Wh/kg. So, despite the higher polarization and irreversible capacity, this anode worked better than titanate and the full cell of layered oxide and FeNCN delivered one third of the energy density than the full cell containing metallic sodium without any hazard problem.

7.3 Conclusions

Novel anode materials which work through intercalation, $H_2Ti_3O_7$, and conversion, FeNCN mechanism were tested against $Na_{0.67}[Mg_{0.05}Ni_{0.25}Mn_{0.7}]O_2$ in order to evaluate the differences in the electrochemical behavior between materials that operate through both mechanisms in a full cell.

The importance of the mass balance was corroborated when assembling the full cells in order to obtain the best results for both anode and cathode. In both $Na_{1.8}H_{0.2}Ti_3O_7$ and FeNCN it has been observed that the irreversibility of first cycle makes the cathode lose almost half of its capacity. So the values achieved from these cells in terms of capacity and energy are not as good as they could be. However, this fact does not affect to the average voltage observed in the cell. A precycling would be a good way to take advantage from the best properties of the anode materials avoiding the problems of the first cycle irreversible capacity. However, this step is currently not considered by industry.

$Na_{1.8}H_{0.2}Ti_3O_7$ has a plateau at very low voltage with 0.2 V of polarization causing that the difference of voltage with the cathode is bigger and therefore the energy of the full cell was about 136 Wh/kg in the second cycle. FeNCN contributes to the good capacity retention of the full cell although the high polarization and high first cycle irreversible capacity leading an energy density of 157Wh/Kg.

7.4 References

[1] D.A. Stevens and J.R. Dahn; "High Capacity Anode Materials for Rechargeable Sodium-Ion Batteries" *Journal of The Electrochemical Society*, 2000**, 147** (4) 1271.

[2] D. Kundu, E. Talaie V., Duffort and L. F. Nazar; "The Emerging Chemistry of Sodium Ion Batteries for Electrochemical Energy Storage" *Angew. Chem. Int. Ed.*, 2015, **54**, 3431.

[3] H. Kim, J. Hong, Y. U. Park, J. Kim, I. Hwang and K. Kang; "Sodium Storage Behavior in Natural Graphite using Ether-based Electrolyte Systems" *Advanced Functional Materials*, 2015, **25**, 534.

[4] S. Komaba, W. Murata, T. Ishikawa, N. Yabuuchi, T. Ozeki, T. Nakayama, A. Ogata, K. Gotoh and K. Fujiwara; "Electrochemical Na Insertion and Solid Electrolyte Interphase for Hard-Carbon Electrodes and Application to Na-Ion Batteries" *Adv. Func. Mat.,* 2011, **21**, 3859.

[5] D. A. Stevens and J. R. Dahn; "High Capacity Anode Materials for Rechargeable Sodium-Ion Batteries"; J. Electrochem. Soc., 2000, 147, 1271.

[6] S. Mukherjee, A. Bates, N. Schuppert, B. Son, J. G. Kim, J. S. Choi, M. J. Choi, D. H. Lee., O. Kwon, J. Jasinski and S. Park; "A study of a novel Na ion battery and its anodic degradation using sodium rich prussian blue cathode coupled with different titanium based oxide anodes" *Journal of Power Sources*, 2015, **286**, 276.

[7] J. Xu, C. Ma, M. Balasubramanian and Y. S. Meng; "Understanding $Na_2Ti_3O_7$ as an ultra-low voltage anode material for a Na-ion battery" *Chem. Commun.,* 2014*,* **50**, 12564.

[8] R. Dugas, B. Zhang, P. Rozier and J. M. Tarascon; "Optimization of Na-Ion Battery Systems Based on Polyanionic or Layered Positive Electrodes and Carbon Anodes" *Journal of The Electrochemical Society*, 2016, **163** (6), A867.

[9] J. Song, L. Wang, Y. Lu, J. Liu, B. Guo, P. Xiao, J. J. Lee, Z.Q. Yang, G. Henkelman and J. B. Goodenough; "Removal of Interstitial H_2O in Hexacyanometallates for a Superior Cathode of a Sodium-Ion Battery" *J.Am. Chem. Soc.* 2015, **137**, 2658.

[10] R. Alcántara, J. M. Jiménez-Mateos, P. Lavela and J. L. Tirado, "Carbon black: a promising electrode material for sodium-ion batteries" *Electrochem. Commun.***,** 2001, **3**, 639.

[11] S. M. Oh, S. T. Myung, C. S. Yoon, J. Lu, J. Hassoun, B. Scrosati, K. Amine and Y. K. Sun; "Advanced $Na[Ni_{0.25}Fe_{0.5}Mn_{0.25}]O_2$/C−$Fe_3O_4$ Sodium-Ion Batteries. Using EMS Electrolyte for Energy Storage" *NanoLetters* 2014, **14**, 1620.

[12] H. Ye, Y. Wang, F. Zhao, W. Huang, N. Han, J. Zhou, M. Zeng and Y. Li; "Iron-based sodium-ion full batteries" *J. Mater. Chem. A*, 2016, **4**, 1754.

[13] G. Singh, Private Communication.

[14] J. Rodriguez-Carvajal, "Recent Advances in Magnetic Structure Determination by Neutron Powder Diffraction" *Physica B*.,1993, **192**, 55.

[15] G. Singh, N. Tapia-Ruiz, J. M. Lopez del Amo, U. Maitra, J. W. Somerville, A. R. Armstrong, J. Martinez de Ilarduya, T. Rojo and Peter G. Bruce; "High Voltage Mg-Doped $Na_{0.67}Ni_{0.3-x}Mg_xMn_{0.7}O_2$ (x = 0.05, 0.1) Na-Ion Cathodes with Enhanced Stability and Rate Capability" *Chem. Mat.*, 2016, **28** (14), 5087.

[16] J. Billaud, G. Singh, A. R. Armstrong, E. Gonzalo, V. Roddatis, M. Armand, T. Rojo and P. G. Bruce, "$Na_{0.67}Mn_{1-x}Mg_xO_2$ ($0 \le x \le 0.2$): A High Capacity Cathode for Sodium-Ion Batteries"

[17] G. Singh, B. Acebedo, M. Casas-Cabanas, D. Shanmukaraj, M. Armand and T. Rojo "An approach to overcome first cycle irreversible capacity in P2- $Na_{0.67}[Fe_{0.5}Mn_{0.5}]O_2$" *Electrochemistry Communications* 2013, **337**, 61.

[18] P. F. Wang, Y. You, Y. Z. Yin, Y. S. Wang, L. J. Wan, L. Gu and Y. G. Guo; "Suppressing the P2–O2 Phase Transition of $Na_{0.67}Mn_{0.67}Ni_{0.33}O_2$ by Magnesium Substitution for Improved Sodium-Ion Batteries" *Angew. Chem.,* 2016, **128**, 1.

[19] M. Zarrabeitia, E. Castillo-Martínez, J. M. López Del Amo, A. Eguía-Barrio, M. A. Muñoz-Márquez, T. Rojo and M. Casas-Cabanas; "Identification of the critical synthesis parameters for enhanced cycling stability of Na-ion anode material $Na_2Ti_3O_7$" *Acta Materalia,* 2016, **104**, 125.

8- CONCLUSIONS AND PERSPECTIVES

The discussion of the results described in this work allows us obtaining the following conclusions:

- $H_2Ti_3O_7$ was synthesized as pure single phase. Three types of protons were determined by GFourier study from the measurements of combined X-Ray and Neutron Diffraction.
- The electrochemical performance of $H_2Ti_3O_7$ for sodium ion batteries did not meet the expectations that presented in lithium ion batteries although the higher sodium diffusion coefficient of $H_2Ti_3O_7$ compared to $Na_2Ti_3O_7$.
- An improvement of the cyclability and a decrease of the average working voltage was achieved when the transformation into $Na_2Ti_3O_7$ like structure ($Na_{1.8}H_{0.2}Ti_3O_7$).
- Transition-metal carbodiimides (T^M= Mn^{2+}, Fe^{2+}, Co^{2+}, Ni^{2+}, Cu^{2+}, Zn^{2+} and mixtures of Fe^{2+} and Co^{2+}) were obtained through different synthesis methods as single phases.
- The electrochemical activity of these materials was proved and shown for the first time as potential anodes for sodium and lithium ion batteries.
- The decomposition of NaFSI into NaF favours the formation of SEI layer formation in CuNCN electrode for sodium ion batteries.
- An incomplete conversion process and kinetic limitations were exhibited for CuNCN.
- CoNCN and NiNCN achieved large capacities in the first cycle consisting on a two-electron conversion process.
- Carbodiimides show higher capacities and smaller hysteresis, especially for FeNCN, CoNCN and NiNCN compared to the oxides. This means that carbodiimides improve the electrochemical performance in terms of energy density and efficiency.
- Iron carbodiimide seems to be a good candidate as anode material because of its lower voltage plateau, less irreversible capacity and good cyclability.
- Two different compositions of ($Co_{1-x}Fe_xNCN$) solid solution were successfully prepared. At room temperature, a different behaviour was exhibited by the $Co_{0.64}Fe_{0.36}NCN$ and $Co_{0.54}Fe_{0.46}NCN$ being antiferromagnetic and paramagnetic ordered, respectively, that can be attributed to the different magnetic ordered presented in FeNCN and CoNCN.
- Better electrochemical performance was achieved in samples of ($Co_{1-x}Fe_xNCN$) solid solution compared to the extremes of the solid solution.

- Sodium ion full-cells of $Na_{1.8}H_{0.2}Ti_3O_7$ and FeNCN were successfully assembled using P2-$Na_{0.67}[Mg_{0.05}Ni_{0.25}Mn_{0.7}]O_2$ as cathode. The higher energy density presented in the full-cell of FeNCN (157 Wh/Kg) than $Na_{1.8}H_{0.2}Ti_3O_7$ (136 Wh/Kg) makes iron carbodiimide a suitable anode for sodium ion batteries.

From the knowledge acquired during the development of this work, some perspectives are given in the field of sodium ion batteries:

- ✓ The research on anode materials continues being the key of the success of this technology. In the cathode part the use of analogues to lithium ion batteries provide similar electrochemical performance. However, there is not an anode material which can provide the good electrochemical properties of graphite in terms of capacity, cyclability and stability (also at high rates) for lithium ion batteries. Therefore, an anode material which meets the requirements is sought.

- ✓ There is a need to select an appropriate electrolyte that could be used in both anode and cathode electrodes. Nowadays, the research in electrode materials is focused on the electrochemical characterization of the cathodes or anodes separately. The selection of a unique electrolyte helps to standardise the study of the electrochemical properties of electrode materials. In addition, the study of a SEI layer of this electrolyte could help understanding some electrochemical processes, especially for anode electrodes.

- ✓ The good electrochemical properties reported for many electrode materials for sodium ion batteries in the literature should be tested in a full cell in order to corroborate how good their properties in a real cell are. The selection of the counter electrode would depend on the electrochemical properties obtained in the half cell level.

ANNEX

In this section, the supplemental information is provided in order to complete the information explained in the text. The atomic positions of the refinements described in the manuscript are listed below.

Chapter 2: Experimental

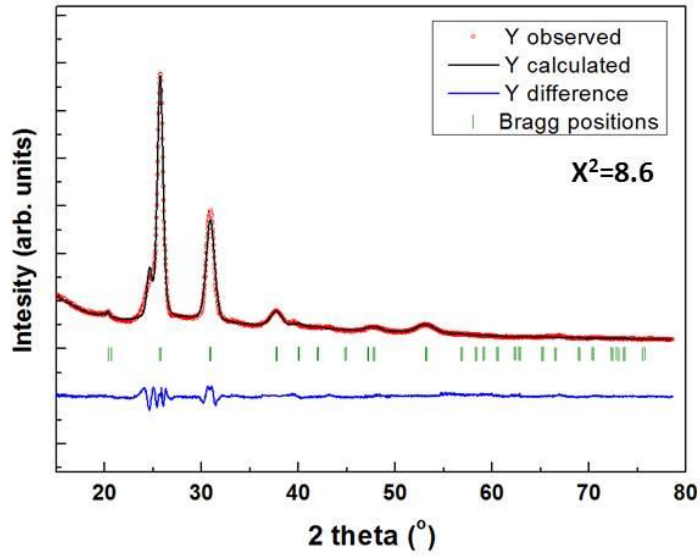

Figure A2.1. Pattern matching of XRD data of Li_2NCN with space group *I4/mmm* with the X^2 of the refinement in the graph.

Chapter 3: *Structure resolution and insights on the electrochemical mechanism of $H_2Ti_3O_7$*

Table A3.1. Atomic positions of $H_2Ti_3O_7$ as obtained from the combined refinement of PXRD and PND data with space group *C*2/*m* and the introduction of the 3 protons.

	Wyckoff position	x	y	z	Biso (Å^2)
Ti 1	4i	0.2288(6)	0	0.2140(10)	1.52(18)
Ti 2	4i	0.1715(7)	0	0.5107(11)	1.52(18)
Ti 3	4i	0.1254(6)	0	0.8297(10)	1.52(18)
O 1	4i	0.1684(9)	0	0.0330(19)	1.05(15)
O 2	4i	0.1339(10)	0	0.3161(18)	1.05(15)
O 3	4i	0.0813(11)	0	0.6076(18)	1.05(15)
O 4	4i	0.0096(10)	0	0.8606(18)	1.05(15)
O 5	4i	0.3505(8)	0	0.1763(15)	-0.14(11)
O 6	4i	0.2942(10)	0	0.4568(18)	-0.14(11)
O 7	4i	0.2355(9)	0	0.7456(17)	-0.14(11)
H 1	2c	0.00000	0	0.50000	5.8(7)
H 2	4i	0.036(2)	0	0.183(4)	5.8(7)
H 3	2a	0.50000	0.5	0.00000	5.8(7)

(Å)	d(Ti1-O)	d(Ti2-O)	d(Ti3-O)	d(H1-O)	d(H2-O)	d(H3-O)
O1	1.75(2)	-	1.86(2)	-	-	-
O2	1.94(2)	1.78(2)	-	-	1.79(3)	-
O3	-	1.84(2)	2.03(2)	(2x) 1.48(2)	-	-
O4	-	-	1.93(2)	-	0.76(3)	(2x) 1.32(2)
O5	2.05(2)	-	(2x) 1.917(4)	-	-	-
O6	2.27(2)	(2x) 1.960(5) (1x) 2.12(2)	-	-	-	-
O7	(2x) 1.974(5)	2.20(2)	2.06(2)	-	-	-

Table A3.2. Atomic Coordinates from the ref. 1, refined Isotropic Atomic Displacement Parameters ($Å^2$) and atomic distances for $H_2Ti_3O_7$ with our PND Data.

	Wyckoff position	*x*	*y*	*z*	Biso ($Å^2$)
Ti 1	4i	0.2333	0	0.2236	0.1(3)
Ti 2	4i	0.1643	0	0.4992	2.3(2)
Ti 3	4i	0.1259	0	0.8291	0.3(7)
O 1	4i	0.1694	0	0.0316	0.1(4)
O 2	4i	0.1345	0	0.3205	0.5(3)
O 3	4i	0.0740	0	0.5943	0.8(2)
O 4	4i	0.0091	0	0.8553	2.6(5)
O 5	4i	0.3512	0	0.1746	0.6(4)
O 6	4i	0.2964	0	0.4616	0.7(2)
O 7	4i	0.2394	0	0.7513	0.5(3)
H 1	4i	0.4720	0.5	0.4578	7.2(4)
H 2	4i	0.5439	0.5	0.1850	13.8(5)

(Å)	d(Ti1-O)	d(Ti2-O)	d(Ti3-O)	d(H1-O)	d(H2-O)
O1	1.858	-	1.855	-	-
O2	1.964	1.618	-	-	-
O3	-	1.834	2.155	(2x) 0.79	-
O4	-	-	1.935	-	(2x) 0.86
O5	2.029	-	(2x) 1.914	-	-
O6	2.223	(2x) 1.990 (1x) 2.213	-	-	-
O7	(2x) 1.930	2.390	2.084	-	-

[1] K. Kataoka, N. Kijima, and J. Akimoto; "Ion-Exchange Synthesis, Crystal Structure, and Physical Properties of Hydrogen Titanium Oxide $H_2Ti_3O_7$"; *Inorg. Chem*.,2013, **52**, 13861.

Table A3.3. Agreement factors, atomic positions and distances of $H_2Ti_3O_7$ as obtained from the refinement of PND data of wavelength of 1.28 Å introducing the strain microstructural parameters with space group *C*2/*m*.

Neutron (λ=1.287 Å)	
R_p	0.106
R_{wp}	0.090
R_B	0.043
R_F	0.029
$\chi 2$	2.29

	Wyckoff position	***x***	***y***	***z***	**Biso (Å^2)**
Ti 1	4i	0.225(1)	0	0.211(2)	0.1(2)
Ti 2	4i	0.173(1)	0	0.515(2)	0.4(3)
Ti 3	4i	0.122(1)	0	0.824(2)	0.4(2)
O 1	4i	0.1710(6)	0	0.035(1)	0.2(2)
O 2	4i	0.1339(6)	0	0.316(1)	0.1(2)
O 3	4i	0.0798(8)	0	0.604(2)	1.2(2)
O 4	4i	0.0132(8)	0	0.865(2)	1.7(2)
O 5	4i	0.3502(6)	0	0.180 (1)	0.5(2)
O 6	4i	0.2951(6)	0	0.457(1)	0.1(2)
O 7	4i	0.2371(6)	0	0.744(1)	0.3 (2)
H 1	2c	0	0	0.5	4.4(3)
H 2	4i	0.043(2)	0	0.193 (2)	4.4(3)
H 3	2a	0.5	0.5	0	4.4(3)

(Å)	**d(Ti1-O)**	**d(Ti2-O)**	**d(Ti3-O)**	**d(H1-O)**	**d(H2-O)**	**d(H3-O)**
O1	1.68(2)	-	1.94(2)	-	-	-
O2	1.91(2)	1.81 (2)	-	-	1.65(2)	-
O3	-	1.84 (3)	2.00(2)	(2x) 1.44(1)	-	-
O4	-	-	1.86(2)	-	0.96(2)	(2x) 1.30(2)
O5	2.08(2)	-	(2x) 1.931(4)	-	-	-
O6	2.31(2)	(2x) 1.948(5) (1x) 2.13(2)	-	-	-	-
O7	(2x) 1.991(5)	2.15(2)	2.12(2)	-	-	-

Table A4.1. Atomic positions of CuNCN obtained from the refinement of XRD data with space group *Cmcm*.

	Wyckoff position	x	y	z	Biso ($Å^2$)
Cu	4a	0.00	0.00	0.00	0.57(1)
N	8f	0.00	0.609(3)	0.383(5)	0.93(2)
C	4c	0.00	0.620(6)	0.25	0.87(1)

Table A4.2. Atomic positions of ZnNCN obtained from the refinement of XRD data with space group *I*-42*d*.

	Wyckoff position	x	y	z	Biso ($Å^2$)
Zn	8d	0.047(3)	0.25	0.125	0.43 (4)
N	16e	0.193(7)	0.070(1)	0.171(3)	0.82 (1)
C	8d	0.568(2)	0.25	0.125	0.56 (5)

Experiment of Cu+Na_2NCN battery

As the in-situ PXRD experiment suggested the formation of sodium carbodiimide and metallic copper in the first discharge of CuNCN, a battery using a stoichiometric mixture of these materials as working electrode was assembled. The first interesting observation was that the OCV was 1.6 Volts vs Na+/Na. This relatively "high" value could be attributed to the small carbon activity vs sodium as counter electrode. During the discharge process, just a process at 0.1 Volt vs Na+/Na (Figure A4.1 and Figure A4.2) was shown due to the insertion of sodium ions into the carbon used as additive. During the charge process in the δQ/δV the peaks observed at 1.1 and 2.2 Volts vs Na+/Na are similar to the processes observed in the oxidation of CuNCN during the cyclic voltammetry (where they are more clearly shown than in the δQ/δV) as it can be seen in Figure A4.2.

However, in the second discharge the plateau increased the voltage close to 0.8 Volts vs Na+/Na which agreed with the average voltage of the second discharge of CuNCN. This could indicate that the electrochemistry of metallic copper with sodium carbodiimide is very similar to that observed in CuNCN. It suggested that the reduction of Cu2+ of CuNCN into metallic copper and the oxidation to Cu^+ was proposed by the kinetic problems described in Section 4.1.2.2.1.4.

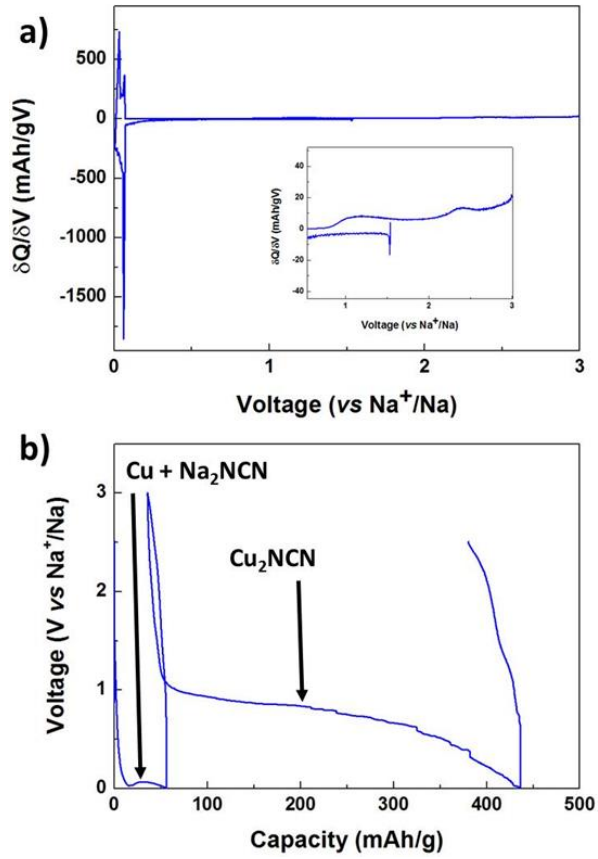

Figure A4.1. δQδV plot with the inset of the zoom of the charge (a) and the galvanostatic cycling of metallic copper and sodium carbodiimide in the 0.005-3.0 Volts vs Na+/Na voltage range (b).

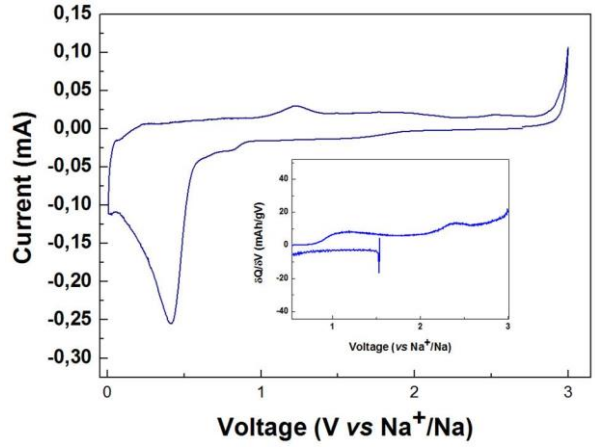

Figure A4.2. Cyclic voltammetry of CuNCN with the δQδV plot in the inset of the first charge of metallic copper and sodium carbodiimide in the 0.005-3.0 Volts vs Na+/Na voltage range.

Table A5.1. Atomic positions of MnNCN obtained from the refinement of XRD data with space group *R*-3*mH.*

	Wyckoff position	x	y	z	Biso ($Å^2$)
Mn	3a	0.33	0.67	0.67	0.25(5)
N	6c	0.00	0.00	0.584(1)	0.73(2)
C	3b	0.00	0.00	0.5	0.46(1)

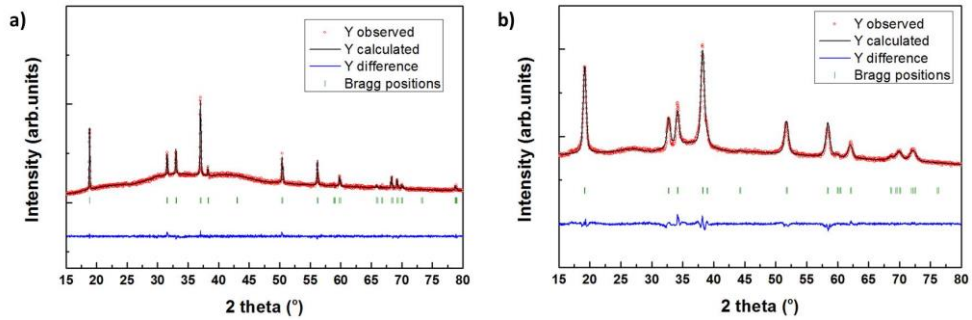

Figure A5.1. Rietveld refinement of CoNCN (a) and NiNCN (b) with space group *$P6_3/mmc$*.

Table A5.3. Rietveld refinement agreement factors for T^MNCN (T^M= Mn^{2+}, Fe^{2+}, Co^{2+} and Ni^{2+}) with space group *$P6_3/mmc$*.

Material	R_P (%)	R_{wp} (%)	R_B (%)	χ^2
MnNCN	12.12	9.98	4.36	2.92
FeNCN	6.37	7.25	2.12	1.71
CoNCN	7.42	8.02	2.98	3.59
NiNCN	24.45	30.89	7.67	4.23

Table A5.3. Atomic positions of FeNCN obtained from the refinement of XRD data with space group *P6$_3$/mmc*.

	Wyckoff position	x	y	z	Biso (Å^2)
Fe	2a	0.00	0.00	0.00	0.54(3)
N	4f	0.33	0.67	0.122(4)	0.62(7)
C	2c	0.33	0.67	0.25	0.50(4)

Table A5.4. Atomic positions of CoNCN obtained from the refinement of XRD data with space group *P6$_3$/mmc*.

	Wyckoff position	x	y	z	Biso (Å^2)
Co	2a	0.00	0.00	0.00	0.11(1)
N	4f	0.33	0.67	0.120(5)	0.24(1)
C	2c	0.33	0.67	0.25	0.13(3)

Table A5.5. Atomic positions of NiNCN obtained from the refinement of XRD data with space group *P6$_3$/mmc*.

	Wyckoff position	x	y	z	Biso (Å^2)
Fe	4a	0.00	0.00	0.00	0.32(4)
N	8f	0.33	0.67	0.118(2)	0.45(8)
C	4c	0.33	0.67	0.25	0.12(5)

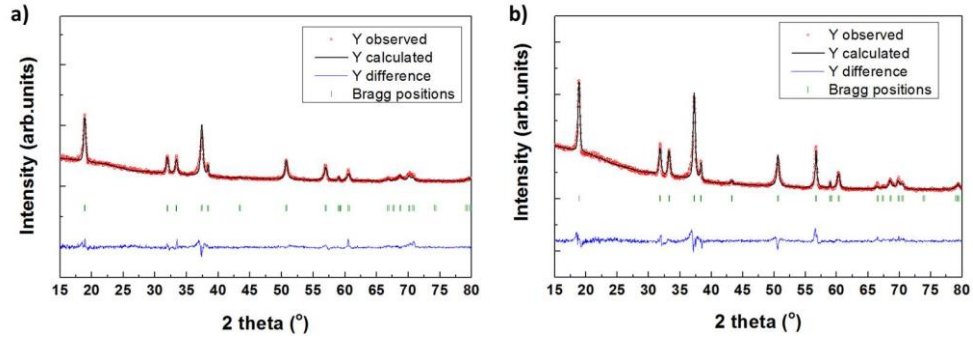

Figure A6.1. Rietveld refinement of XRD data of $Co_{0.64}Fe_{0.36}NCN$ (a) and $Co_{0.54}Fe_{0.46}NCN$ $Co_{0.64}Fe_{0.36}NCN$ (b) with same space group *$P6_3/mmc$*.

Table A6.2. Atomic positions of $Co_{0.64}Fe_{0.36}NCN$ obtained from the refinement of XRD data with space group *$P6_3/mmc$*.

	Wyckoff position	**x**	**y**	**z**	**Biso ($Å^2$)**
Fe	2a	0.00	0.00	0.00	0.75(4)
N	4f	0.33	0.67	0.121(6)	0.44(2)
C	2c	0.33	0.67	0.25	0.97(1)
Co	2a	0.00	0.00	0.00	0.82(6)

Table A6.3. Atomic positions of $Co_{0.54}Fe_{0.46}NCN$ obtained from the refinement of XRD data with space group *$P6_3/mmc$*.

	Wyckoff position	**x**	**y**	**z**	**Biso ($Å^2$)**
Fe	2a	0.00	0.00	0.00	0.67(4)
N	4f	0.33	0.67	0.122(3)	0.39(2)
C	2c	0.33	0.67	0.25	1.21(5)
C0	2a	0.00	0.00	0.00	0.79(6)